# DESIGN OF NANOMATERIALS FOR A REDUCED TOXICOLOGICAL IMPACT AND DEVELOPMENT OF NANOMATERIALS FOR UTILIZATION OF $CO_2$ BY OXIDATION-REDUCTION CHEMISTRY

by

**Michelle Najera**

BS in Chemical Engineering, University of California, Los Angeles, 2003

Submitted to the Graduate Faculty of

Swanson School of Engineering in partial fulfillment

of the requirements for the degree of

Doctor of Philosophy

University of Pittsburgh

2013

UNIVERSITY OF PITTSBURGH

SWANSON SCHOOL OF ENGINEERING

This dissertation was presented

by

Michelle Najera

It was defended on

April 18th, 2013

and approved by

Joseph McCarthy, PhD, Professor, Department of Chemical and Petroleum Engineering

Robert Enick, PhD, Professor, Department of Chemical and Petroleum Engineering

Melissa Bilec, PhD, Professor, Department of Civil and Environmental Engineering

Dissertation Director: Gotz Veser, PhD, Professor, Department of Chemical and Petroleum Engineering

**DESIGN OF NANOMATERIALS FOR A REDUCED TOXICOLOGICAL IMPACT AND DEVELOPMENT OF NANOMATERIALS FOR UTILIZATION OF $CO_2$ BY OXIDATION-REDUCTION CHEMISTRY**

Michelle Najera, PhD

University of Pittsburgh, 2013

This work is comprised of two distinct objectives: to study the nanotoxicity of complex nanomaterials and to develop nanomaterials for a process called chemical looping dry reforming (CLDR). For the first objective, nickel-containing nanomaterials (hollow Ni@$SiO_2$, non-hollow hNi@$SiO_2$, and Ni-$SiO_2$) were assessed as environmental contaminants. We hypothesized that incorporation of a silica support would stabilize the nickel nanoparticle and hence mitigate its toxicity. An initial assessment of agglomeration and dissolution indicated that nhNi@$SiO_2$ has smaller agglomerates, while Ni-$SiO_2$ allows for greater nickel ion shedding into solution. A toxicity screening was also done by 5-day nanomaterial exposures with zebrafish embryos. High survival of the zebrafish suggested a low toxic potential for silica-structured nanomaterials. However, nhNi@$SiO_2$ and Ni-$SiO_2$ materials stood out as having either slightly higher deformations or altered motility trends at high doses, respectively. Finally, elevated uptake of nickel following particle exposure suggested the possibility of internalization of the nanoparticle agglomerates.

While the toxic potential of complex nanomaterials was probed above, the potential value of such materials was also of interest. Hence, the efficacy of nanomaterials in a specific application was assessed as well. CLDR is a process in which $CO_2$ reacts with a metal oxide to

form CO. The metal oxide is regenerated back to a metal by reduction with a fuel (e.g., methane). The result is a cyclic process, which allows utilization of $CO_2$ (a greenhouse gas) by conversion to CO. Fe-based materials were selected as the most suitable for the process and core-shell, composite, and surface deposited nanomaterials were developed. According to comparison in thermogravimetric analysis (TGA), iron utilization of the nanomaterials was in the order of Fe@$CeO_2$ > Fe-$CeO_2$ > Fe-Barium hexa-aluminate > hollow Fe@$SiO_2$ > Fe@$SiO_2$. Among these, only the ceria-supported materials underwent an adequate extent of reduction with methane to complete the cyclic process. The ceria-supported materials also had superior oxidation capacity. Lastly, performance of the surface deposited Fe-$CeO_2$ in a fixed bed reactor was comparable that of the Fe@$CeO_2$ material, leading us to conclude that there was no observable benefit to the use of complex and costly core-shell structures for the CLDR process.

## TABLE OF CONTENTS

## LIST OF TABLES

## LIST OF FIGURES

# PREFACE

I would like to thank Gotz Veser for his patience and enthusiasm and his willingness to explore an entirely new field of research with nanotoxicity studies. Under your guidance I have become a stronger researcher and scientist. I hope you have continued success in your laboratory. I am also grateful to my committee for their support and advice.

I would like to thank the Mascaro Center for Sustainable Innovation (MSCI) for a awarding me a 3-yr fellowship and the Office of the Dean for a one-year fellowship, hence allowing me to complete this work. As part of the MCSI GAANN/IGERT program, I was able to make cross-disciplinary connections with several other students studying sustainability. These contacts allowed me to become more broadly aware of other sustainability-related research within the engineering school. Maintaining an underlying theme of sustainability in my dissertation work was extremely important to me personally. I am incredibly grateful for the financial support of MCSI, as this enabled me to steer this work to consider sustainability aspects, something that I think is extremely important for the field of chemical engineering to more fully embrace.

I would also like to acknowledge my lab mates. Lu Zhang laid the groundwork for our expertise in making core-shell nanostructures, and we are much indebted to her for our current knowledge of the microemulsion synthesis. I would also like to thank Saurabh for his collaboration with on developing and testing nanomaterials for chemical looping processes. Neha Nandakumur is gratefully acknowledged for her work as an undergraduate researcher conducting the an exergetic analysis on the CLDR process and Dr. Bob Enick and Dr. Vikas

Khanna are also acknowledged for their insightful discussions on exergy. Undergraduate Hannah Grace contributed excellent work to the development of materials for the CLDR process. Chris DiAndreth is gratefully acknowledged for conducting the preliminary studies that led to our pursuing an entire project to study the toxicity of nanomaterials. Sharlee Mahoney and Amey More are both acknowledged for being extremely helpful in the final phases of this work.

I thank Dr. Jill Millstone and Dr. Prashant Kumta for opening up their laboratories to me to conduct DLS and ICP studies, respectively. Finally, I gratefully acknowledge Dr. Edward Burton and his laboratory staff for supplying the resources and expertise from his laboratory to study the toxicity of nanomaterials using zebrafish embryos. I am specifically grateful to Qing Bai and April Perry for their contribution of handling the zebrafish husbandry for this work and Hubert Chow for his development of MATLAB tools for motility analysis.

I would like to thank my family for their love and support in this and all my endeavors. Thank you Brian, for you constant support and help during this process. I would not have wanted to finish this without you. And to my friends, especially those that provided me with occasional repose from work in the great outdoors, I cannot thank you enough for keeping me happy and healthy during the past 5 years.

# 1.0 INTRODUCTION

A central motivation that is captured in both projects in this work is to study nanomaterials from the standpoint of sustainability. A common model used for capturing the goals of sustainability is the 'triple bottom line.' This model assesses new products and processes based on their effect on people, profit, and planet (i.e., the social or human effects, cost, and the environment).

On one hand, nanomaterials have the potential to increase profits, especially for industrial processes, by enabling higher efficiency, better selectivity, or entirely new capabilities. One obvious example of this is with nano-catalysis, where unique populations of crystal structures that appear at the nano-scale are capable of excellent control over the desired reaction products. Our chemical engineering laboratory in fact specializes in developing complex nanomaterials and characterizing their behavior in chemical reactions of industrial relevance.

Nanomaterials could also provide an environmental benefit. Examples include nanomaterials for harnessing solar energy with photovoltaics, nanocatalysts that reduce polluting byproducts, and even the nanomaterials that can convert organic pollutants into less toxic chemical derivatives. As part of this dissertation work, nanomaterials were developed for a process that converts $CO_2$ to CO to be used downstream as an industrial feed gas. $CO_2$ is recognized as the biggest contributor to greenhouse gas, which has been proven to result in climate change. The development of this process and the nanomaterials it requires is hence aimed at mitigating these increasing anthropogenic $CO_2$ levels in the atmosphere.

Meanwhile, although naturally occurring nanomaterials have always existed, the introduction of *engineered* nanomaterials is relatively new, especially in terms of complex engineered nanomaterials containing two or more different components. From a human and environmental sustainability perspective, we have no prior experience for exposure to a nanomaterial that consists of two elements not typically associated with one another in nature and occurring at the nano-scale. Considering the growth of 'nano-enabled' products and processes, our knowledge of the potential toxicity (or even how to approach evaluating the toxicity) of these materials is fairly minimal.

Our work is focused on further developing of these two sides of the nano-regime in terms of both the potential benefits and the environmental risks of using complex engineered nanomaterials. To do this, for one project we designed nanomaterials that had the potential of address the challenging environmental problem of anthropogenic $CO_2$ emissions. Meanwhile, in a second project we developed a methodology to screen the toxicity of nanomaterials. In the bigger picture, it is possible that the value of a nano-enabled process could justify the use of nanomaterials, and so developing methods to classify toxicity becomes important. It is also possible that nanomaterials (even ones containing toxic components) could be designed in a way that makes them inherently less toxic. In this way, the benefits from a given nano-enabled process might be gained without the added risk of nanomaterial toxicity. Overall our goal in this work was to develop a better understanding of both sides of the nanomaterial debate in a way that can guide the further development of nanomaterials in order to enable us to benefit from them while simultaneously avoiding nanomaterial applications where toxicity is a concern.

# 2.0 ASSESSMENT OF TOXICITY FOR NANOMATERIALS

## 2.1 INTRODUCTION

Nanotechnology is predicted to be a 1 trillion dollar industry by 2015 (*1*) with over 1000 nano-enabled consumer products on the market (*2*). Nanomaterials refers to particles with one or more dimension measuring 1-100 nm (*3*). They are attractive for their large surface area, higher atom economies, and improved and catalytic reactivity and selectivity (*4-6*). Applications for *metal* nanomaterials, of interest in this work, have spanned electronics (*7*), storage (*8*), photonics (*9*), sensing (*10*), water treatment (*11, 12*), catalysis (*13*), drug delivery (*14-16*), medical imaging (*14, 17, 18*), and even construction (*19*).

However, concern has also mounted regarding the risk associated with a global accumulation of nanomaterials (*20-23*), especially with regard to toxic exposures from consumer products and biological applications (*24-26*). A toxicology risk is dependent on both the probability of exposure and the dose response measured from exposure to a material (*27*). A key concern stems from the possibility of nano-specific toxic mechanisms that cannot be extrapolated from toxicity of the analogous bulk material (*25, 28-30*). This is most likely occurs at diameters <20 nm (*28*). Yet this size range is also where the unique and desirable properties of nanomaterials discussed above are expected to emerge (*6, 28*). Hence there is a strong push for continued development and production of materials in these very small size ranges, despite a

parallel challenge of characterizing their exposure and toxic potential. In sum, while the use of nanomaterials could fundamentally alter how we benefit from the chemical and physical properties of materials, there is an equal need to characterize their behavior from the perspective of nanotoxicity.

The still nascent field of 'nanotoxicity' aims to develop methods to assess toxicity of nanomaterials. Currently, the toxicological understanding of nanomaterials is minimal, and often contradictory, and the field continues to grapple with how to effectively and efficiently study the growing number of nano-enabled materials being produced (*31-33*). Ideally, a robust and upfront physicochemical characterization of a new material would be used to *predict* the corresponding toxic potential and risk of that material. This sort of structure-to-activity relationship model is sometimes applied for new synthetic chemicals, but unfortunately even the long-established field of chemical toxicology is still developing these predictive tools (*34*). Moreover, they are not directly applicable to particle toxicity since they do not take into account behavior specific to particles, which can greatly modify final particle exposures. In fact, physicochemical analysis of nanoparticles goes beyond simple particle size and surface area measurements; it also should include measuring dynamic behavior specific to nanoparticles in natural systems, which introduces new challenges in creating experimental methods that are transferrable to a wide range particles sizes and types. Still, by describing the dynamic behavior of nanoparticles, such as dissolution and agglomeration, one can make connections between the structure and the expected behavior of materials in various biological exposure scenarios. More importantly, when armed with comprehensive physicochemical characterization data, the structure to activity (or toxicity) connections required for more predictive toxicology models might be revealed by correlation with biological assays.

Biological analysis typically requires an assessment using *in vitro* and *in vivo* methods to quantify potential risks (*29*). But conventional *in vivo* studies in mammals tend to be expensive and time consuming, and hence are not well matched to the rapidly developing field of engineered nanomaterials. On one hand, robust physicochemical characterization can aid in prioritization of such studies by identifying higher risk materials for further biological analysis. Zebrafish studies, on the other hand, have emerged in recent years as a comparatively fast and well-developed toxicological assessment with high-throughout tools (*35*) that might be able to meet the demand for toxicological screening of these new materials.

The zebrafish offers a uniquely accessible model for our studies since its biology presents many opportunities for experimental manipulations. Embryonic development is external, allowing the early development and organogenesis to be easily monitored via microscopy. Xenobiotic materials can be applied directly to the embryos without the requirement for complex in-utero delivery systems. Zebrafish are also prolific breeders; a single mating pair can generate 50-200 embryos so that statistically relevant sample sizes can hence be examined. This, combined with considerable development in the past 5 years in the use of zebrafish for abovementioned high-throughput toxicity screening, dramatically enhances the experimental power of biological assessment using zebrafish.

As an organism, zebrafish (*danio rerio*) offer a wealth of knowledge on morphology of development, organogenesis, organ system structure and function, and underlying molecular events of genome sequence and gene expression (*36*, *37*). The zebrafish shows striking genetic homology to higher vertebrate organisms, and the basic vertebrate body plan and many aspects of physiology are conserved through the vertebrate phylum (*36*). Embryogenesis in particular is quite sensitive to xenobiotic exposures that might otherwise be well tolerated. Early embryonic

development thus represents a special case of phylogenetically-conserved physiology, and it can hence be expected that the zebrafish model will be predictive of teratogenic effects of nanomaterials in higher vertebrates. Furthermore, exposure of zebrafish embryos to nanomaterials simultaneously encompasses several routes of exposure, thereby allowing elucidation of worst-case exposure scenarios in other organisms.

Most toxicological studies of nanomaterials to-date have focused on inhalation hazards (lung) since this is the most likely exposure route for workers in the materials manufacturing industry. But substantial risks have also been shown for both gastrointestinal and skin exposure (*38*) and the widespread use of nanomaterials will undoubtedly result in the accumulation of nanomaterials in waste streams, increasing the likelihood of other exposure routes. Aquatic organisms in particular are directly impacted by fresh water supplies contaminated with nanomaterials, and hence often serve as sentinels for the toxic compounds in the environment that pose a risk to humans (*39*). Unfortunately, there is minimal established knowledge with regard to aquatic exposure of nanomaterials (*40, 41*) and thus the use of an aquatic organism for these studies is highly relevant to the direct consequences of environmental contamination with nanomaterials.

In this work we aim to utilize the zebrafish model to ultimately test the toxicity of Ni-containing nanoparticles that are supported by silica. Nickel powders are frequently used as industrial catalysts, a field which could benefit greatly from implementation of nano-scaled materials. Furthermore, our silica-supported nickel nanoparticles can also be viewed as models for other complex nanomaterials, from which the potential toxicity might be estimated. Our hypothesis is that nanostructured encapsulation of nickel nanoparticles with amorphous silica can effectively mitigate toxicity. A brief review the state of the knowledge of the toxicity of nickel

and nickel nanoparticles is given below, with special emphasis on relevant zebrafish studies, where available.

Nickel is recognized as a toxin (*42-44*) and its toxicity has been confirmed in zebrafish studies, where soluble Ni was shown to delay hatching of embryos (*45, 46*) and to decrease locomotive activity at levels of 7.5 – 15 mg Ni/L (*47*). In one of the few nanotoxicological studies which aimed to investigate size effects using zebrafish, Ispas and coworkers found that Ni nanoparticles with diameters of 30, 60, and 100 nm had lethal concentration 50 (LC50) values of 328, 361, and 221 mg/L, respectively, suggesting that no clear systematic size effect exists for the toxicity of these Ni nanoparticles (*48*). However, it is likely that a more relevant size range for nanotoxicological effects is ≤ 30 nm given that the number of surface defects only increases significantly at ≤ 20 nm for spherical particles (*6*). Consistent with this, studies of sub-10 nm Ni particles with *Daphnia pulnex* (water flea) showed LC50 values after 48-hr exposures slightly above those for soluble Ni (*49*). The elevated toxicity of Ni nanoparticles compared to other metals in another study was purported to be a result of high dissolution of nickel into the media rather than due to the nanoparticles themselves, emphasizing the importance of a mechanistic understanding in our own nanotoxicity studies (*50*). Dissolution is often identified as a dominant mechanism for nickel nanoparticle toxicity, but nickel ions have a more difficult time crossing cellular membranes as compared to nickel nanoparticles, which can be taken up by endocytosis or phagocytosis (*51*). Hence, significant toxicity of nickel nanoparticles might be expected from 'Trojan-horse'-like coupling of uptake into cells followed by dissolution of the accumulated nickel nanoparticles (*52*). Beyond these studies, systematic Ni nanoparticle toxicity has not been studied in zebrafish, and most nanotoxicity studies to-date have not focused on particle diameters less than ~20-30 nm (*53*).

The use of a coatings to mitigate toxicity, has found some attention previously, although typically only for soft polymeric or surfactant coatings (*54, 55*). The use of (porous) oxide shells could result in much more robust shields by comparison. Silica coatings, in particular, are applicable to virtually any metal nanoparticle (*14, 56*) and are highly robust against thermal and mechanical stress. Porous silica coatings have been reported in a few cases for the intended use of mitigating nanoparticle toxicity (*57, 58*). Amorphous silica is generally considered biocompatible (*59*), although some *in vitro* studies challenge this view. For instance, while a study of fluorescently tagged silica nanoparticles shows no significant toxicity in zebrafish in the concentration range studied (0.0025 - 25 mg/L) (*60*), the presence of trace transition metals has been reported to increase ROS *in vitro* with lung epithelial cells (*61*). Similarly, conflicting reports exist on the size dependence of silica toxicity: In mouse keratinocytes, elevated toxicity is found via several different assays for 48 nm and especially for 30 nm silica particles in comparison to larger sizes (118 nm & 535 nm) (*62*). However, exposure of human epithelial cells to 15 and 46 nm amorphous silica results in low, but measurable, toxicities (*63*). One recent study also reports a significant impact of silica nanoparticle porosity in that mesoporous silica has less impact on cell function than non-porous silica nanoparticles, presumably due to lower cell-contactable surface area, despite a much larger total surface area (*64*). Given the highly porous nature of the silica coatings developed in our lab, this result suggests that porous silica coatings could indeed result in strongly reduced toxicity, as hypothesized.

Nanoparticles can be supported by either depositing them on the surface of silica structures or by encapsulating them within a silica shell (i.e. the so-called ‘core-shell’ structure). Metal@silica core-shell materials, in particular, have been proposed for a wide range of applications, including drug delivery (*65*), biomedical imaging (*15*), environmental remediation

(*66*), and catalysis (*67*). Meanwhile, the deposition-precipitation counter-part is more convenient from an ease of manufacture perspective and has been used more in industrial applications. By studying materials designed with three different methods of silica structuring, we aim to identify dominant relationships between each structure and toxic end points, allowing more over-arching conclusions regarding the best way to design complex structured materials with an inherently low toxicity. Complex multi-component materials have not been studied to the extent that well-dispersed, single component nanoparticles have. Realistically, very small (<20nm) and active nanoparticles, of interest for novel applications in the field of nanotechnology, will require a support to remain stable in nano-enabled applications. For this reason, the importance of studying the toxic potential of multi-component complex nanomaterials is clear when we consider of the next generation of nano-enabled products.

This study is compromised of the following specific objectives:

- Synthesis of Ni-containing nanomaterials with silica supports and material characterization of as-synthesized materials with TEM, EDX, XRD, and BET.
- *Abiotic analysis* of nanoparticle stability in representative media solutions, specifically with regard to aggregation and dissolution, using UV-Vis Spectroscopy, DLS, and ICP-AES.
- *In vivo* testing of the toxicity of Ni-containing nanomaterials with zebrafish larvae using end points of survival, developmental deformations, and motility, and measurement of nickel uptake using ICP-AES.

From a broader perspective our goal in this work was to develop a methodology capable of screening and studying the toxicity of nanomaterials. The project was a collaboration

between a synthesis and reactivity laboratory in chemical engineering and a laboratory in the department of neurology that specialized in behavioral animals models. Our fundamental approach was to learn how to design inherently less toxic complex nanomaterials while maintaining structures that were suitable for application in industrial processes.

## 2.2 METHODS FOR NANOTOXICITY STUDIES

**NOTE: The methods presented here are a detailed compilation of all of the procedures used for this chapter. A more concise or specific methods description is included in selected sections of this chapter.**

### Synthesis

Hollow Ni@$SiO_2$ core-shell materials were made using a one-pot reverse microemulsion synthesis adapted from Takenaka, et al. (*68*), consisting of several step-wise additions. First, 50 mL of cyclohexane (≥99% Sigma-Aldrich) and 10.5 g surfactant Brij 58 (≥99% polyethylene glycol hexadecyl ether, $M_n$ ~1124, Sigma-Aldrich) was refluxed at 50°C until the surfactant was fully dissolved. 1.5 mL of 1 M $Ni(NO_3)_2 \cdot 6H_2O$ (99.999%, Sigma Aldrich) was then added dropwise. The subsequent reduction with 1.5 mL hydrazine hydrate (Sigma-Aldrich) turned the microemulsion from green to purple, and the solution was then allowed to age for ~1 hour. Next, 3-5 g of tetraethylorthosilicate (TEOS, ≥99% Sigma-Aldrich) was added, followed by 3 mL of ammonium hydroxide (30%). It should be noted that the order of addition for TEOS and ammonia was reversed from that used in previous work (*69*) since a more stable microemulsion was observed with these conditions. After 2 hrs aging for $SiO_2$ shell growth via base catalyzed hydrolysis and condensation according to $Si(OCH_2H_5)_4 + 2\ H_2O \rightarrow SiO_2 + 4ROH$ (*70*). Finally, particles were precipitated with 2-propanol, collected via centrifugation, washed three times with 2-propanol, and dried in air. Crushed powder was placed in shallow ceramic boats and calcined in a Thermolyne 79300 tube furnace for 2 hrs at 500°C in air (flow rate 0.1 - 0.3 SLM). A slow ramp (<3°C/min) and a modest material amount (~1/2 batch size) was required to prevent

powder from exploding out of calcination boats during the fast oxidation of nickel occurring around 200-300$^{o}$C. Final batch sizes collected were ~0.7-1.0 g (for 1.5 mL Ni salt and 5 g TEOS), resulting in yields of ~90-100% for Ni and ~50-60% for Si after calcination.

Non-hollow nhNi@$SiO_2$ nanoparticles were made by a simple modification of the microemulsion method above. Hydrazine was excluded, and ammonia addition leads to a change in color from green to blue, indicating formation of a Ni-ammonia complex. The final material is comprised of a non-hollow silica sphere with embedded nickel nanoparticles. The collapse of the hollow interior probably results from a weaker interaction with the silica interface for the Ni-ammonia complex as compared to the Ni-hydrazine complex (*69, 71, 72*). Precipitated material is dried and calcined as described previously. However, in order to remove external nickel from the materials, calcined particles were reduced and etched in nitric acid. Specifically, 0.20 g of material was dispersed in a 1:1 volume dilution of nitric acid (Sigma, 70%) in DI water for 30 min. Etched materials were washed twice in water to neutral pH, dried, and calcined as above.

Nickel-free spherical $SiO_2$ particles were first synthesized and calcined using the hNi@$SiO_2$ microemulsion procedure described previously, except 1.5 mL DI water was added in place of the aqueous salt and hydrazine is excluded. A typical batch size was 1.3 g $SiO_2$ from 10 g TEOS, corresponding to ~50% yield for Si. Next, a deposition-precipitation method (modified from (*73*)) was used to deposit nickel nanoparticles on the surface of the silica spheres. 0.6 g of silica nanoparticles were dispersed in 15 mL of DI water by sonication, a Ni salt solution was added (0.55 g $NiCl_2$ in 10 mL DI water), and the mixture was again sonicated for 20 min. Ammonium hydroxide (30%, Sigma) was then added dropwise from a glass pipette (~5 mL, 52 drops, slowly over 20 min) until the pH of the solution was ~9.5. The material was mixed for 20

min, centrifuged, dried, calcined at 300$^{o}$C in air, rinsed two times in DI water, dried, and calcined again at 300$^{o}$C in air. Typical yields for Ni deposition on the material were 20-40%.

**Material Characterization**

All materials were characterized for particle size and morphology with transition electron microscopy (TEM, JEOL-2000FX electron microscope). Typical sample preparation consisted of grinding the sample in a mortar, ethanol dispersion, ~2 min sonication, and placing 1-2 drops of the dispersion on copper type-B support grid (Ted Pella, Inc.) to dry in air. Particle measurements of TEM images were done using ImageJ software (http://rsb.info.nih.gov/ij/). Crystal structure was determined with X-ray diffraction (XRD) (Phillips PW1830, USA). XRD was run in 'line focus' mode using a monochromatic Cu radiation at the wavelength of 1.54 Å. The beam voltage was 40kV at a current of 30mA. Diffraction patterns were recorded between 15 and 90° (2θ) in steps of 0.08° intervals with a 0.2 s counting time at each step. Scanning Electron Microscopy (SEM) equipped with EDX Genesis was used to determine elemental composition of samples at beam voltage of 15kV, spot size 4 (typically), collection time of 50-100 s, and a monitored dead times of 20-40%. An average of at least 3 measurements was calculated for each sample. Catalyst surface area and porosity were determined by Brunauer Emmett Teller (BET) analysis (Micromeritics ASAP 2020 surface area and porosity analyzer). Pre-treatment consisted of 2-3 hr degas at 200$^{o}$C under vacuum. Typically, a 6-point BET analysis was used for total surface area measurement and an 84-point $N_2$ BJH analysis with Halsey thickness curve correction and Kruk-Jaroniec-Sayari BJH correction for pore size and volume determination. Extended X-ray Adsorption Fine Structure spectra were collected at Argonne National Labs (ANL) Advanced Photon Source (APS) with the assistance of Jeffrey Miller. Several Ni-containing structures were analyzed and compared with standard of nickel

foil ($Ni^o$) and NiO powder. Oxidized and reduced samples were crushed and molded into a pellet for analysis. ANL clientele completed the curve fitting and analysis of the results on our behalf.

**Dynamic Light Scattering (DLS)**

Nanoparticle dispersions were tested with dynamic light scattering (Zetasizer Series Nano-ZS) to estimate the hydrodynamic diameter of the particles in E3 media (49 mM NaCl, 1.6 mM KCl, 3.3 mM$CaCl_2 \cdot 2\ H_2O$, 3.3 mM $MgSO_4 \cdot 7\ H_2O$, pH 7.4). This analysis works by measuring the velocity of particles undergoing Brownian motion under an applied electric field. Typically concentrations were ~0.05-0.5 g/L particles. The samples were first dispersed for ~2 min by sonication and then ~1 mL of dispersed solution was added to a plastic cuvette. The temperature was set to 25$^o$C and the stabilization period was 10 seconds. The refractive index of silica was used for all measurements. Three successive measurements were done, with the number of scans automatically determine by the instrument (usually 15-50 scans per measurement). The signal change was monitored for each successive scan as an indication of the occurrence of time-dependent agglomeration or gravitational settling. In response to indications of sedimentation, dispersions were pre-filtered with a 0.45 μm filter to verify the presence of large agglomerates and check for the presence of smaller particles, which would be masked by the signal from larger agglomerates.

**UV-Vis Spectroscopy**

Studies were done to measure any differences in settling behavior between each of the materials. Nanoparticles were dispersed in E3 media and deposited in a plastic cuvette to a liquid height of 1 in. Settling velocity and absorbance over time were related to agglomerate size by Stoke's law. Settling velocity and absorbance over time were related to agglomerate size by

Stoke's law. To do this, sedimentation was first measured by UV-visible spectroscopy at 287 nm. The downward velocity ($v_s$) of a particle subjected to gravitational and viscous drag forces can be described in relation to the particle radius (R), as shown in Figure 1 (*74*). The method assumes that the agglomerates are smooth spherical particles that do not change in size over time. Although this simplification is expected to introduce some error, it is nonetheless a convenient way to simultaneously measure sedimentation and estimate agglomerate size as a function of time and initial concentration, while not being limited to dilute the particle concentrations required for DLS.

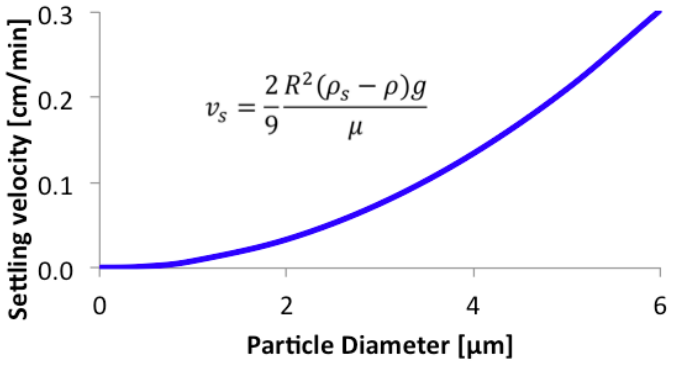


**Figure 1: Settling velocity as predicted by Stoke's law as a function of particle (or agglomerate) diameter, where $v_s$ is settling velocity, R is particle radius, $\rho_s$ and $\rho$ are densities of the solution and the particle, g is acceleration due to gravity, and $\mu$ is solution viscosity.**

## Inductively Coupled Plasma-Atomic Adsorption Spectroscopy (ICP-AES)

Trace metal ion concentration was measured under radial detection by ICP-AES (Thermo Electron Corporation iCAP6500 Duo Series ICP-OES Spectrometer). A standard curve was generated with at least 3 standard solutions that captured the sampling range. Standards were formulated from an ICP standard solution (Fischer Scientific) with 3% $HNO_3$ in deionized water.

A mean of 3 measurements are reported and an internal blank and standard were used in each sampling period.

**Dissolution**

The degree of nickel ion dissolution from the nanoparticles in E3 media was determined with ICP. Dispersions (typically, 50-200 mg Ni/L) were prepared in E3 media and separated into 10 mL aliquots for analysis at specific time points. Metal nanoparticles were removed from the dispersion by centrifugation followed by filtration (Amicon 10,000 molecular weight cut-off filters, ~3.1 nm). $HNO_3$ (Sigma, 70%) was added dropwise to the 5 mL of filtrate to a concentration of 3wt %. $NiCl_2$ solutions were tested as a control according to the procedure above, and a loss of only 1-2% of the original nickel concentration was measured, demonstrating the accuracy of the procedure used.

To calculate the amount of dissolved nickel available in each well [ng/well] (and hence available to each fish in each well) at a given dose, the following calculation was done:

*Concentration [mg Ni/L]* x *Well volume [L]* x *(1E6 ng/mg)*

For 24 well plates, 2.0 mL well volume was used, for 96 well plates 0.30 mL well volume was used. In both cases these were dispensed with a volumetric pipette.

Silica dissolution was measured according to ASTM D859-00. This procedure is designed to detect 'molybdate reactive' silica, which includes simple silicates, monomeric silica, silicic acid, and some undetermined amount of polymeric silica. The procedure used for nickel was also used here, in which dispersions of 50 or 200 mg Ni/L initial concentrations were separated into 10 mL aliquots for specific time points. Nanoparticles were removed from the dispersion by centrifugation followed by filtration (Amicon 10,000 molecular weight cut-off filters, ~3.1 nm). Filtrate was diluted to 25 mL (of higher) for analysis according to LOD

detection of 1-5 mg/L dissolved silica. By additional of several reagents according to the procedure, a color change occurs to green-yellow and then to blue. This color change is measured in UV-Vis and compared with a standard curve for concentration assessment.

**Zebrafish Embryo Exposures**

For in-vivo zebrafish studies, metal nanoparticles and homologous salt solutions were prepared in E3 media (49 mM NaCl, 1.6 mM KCl, 3.3 mM$CaCl_2 \cdot 2\ H_2O$, 3.3 mM $MgSO_4 \cdot 7\ H_2O$) at multiple concentrations. Dried nanoparticle powder was weighed according to a specific dose, added to E3 media, and sonicated ~20-30 minutes to disperse the powder as this time was expected to provide sufficient agglomerate dispersion (*75*). Serial dilutions were then prepared volumetrically using this first dispersion. To conduct exposures, 24 hours post fertilization (hpf) embryos were manually de-chorionated with tweezers and healthy fish was transferred to each well (1 fish/well) of 24-well or 96-well polystyrene plates. Residual water was removed with a pipette. Serial dispersions were re-dispersed by sonication for 1-2 minutes just prior to addition to each well. Fish were incubated for 5 days at 28.5$^{o}$C and analyzed visually each day for survival, developmental deformations, and motility. 6 – 18 embryos were typically tested at each dose, depending on the embryos available in a given clutch.

Negative controls of amorphous silica spheres at 750 – 6000 mg/L $SiO_2$ nanoparticles, corresponding to the highest estimated amount of silica at the highest dose of Ni@$SiO_2$ (400 mg Ni/L, 12 wt % Ni) were tested in 2 separate experiments to confirm $SiO_2$ particles were non-toxic in accordance with previous research (*59, 60*). No observable toxic effect was seen after these two exposures. Each test also included an internal negative control with E3 media. The homologous salt served as a comparator for metal toxicity (e.g., $NiCl_2$ for Ni-containing nanoparticles).

Speciation modeling was done to determine the effect of $NiCl_2$ on the pH of the media solutions using Visual MINTEQ, a program with a graphical interface built upon the U.S.E.P.A.'s MINTEQA2 speciation modeling tool. Results are shown in Figure 2, where an increase in $NiCl_2$ leads to a decrease in pH of 0.5 over the range of interest. The as-prepared pH for E3 media is near 6.93 without Ni according to MINTEQ, but it is adjusted to 7.4 following preparation. Thus we expected the pH to range roughly from 6.9 to 7.4 for $NiCl_2$-dosed media and our observations agree with this prediction. While we do not expect to see any observable effects on our 5 day study for pH values even as low at 5 (*76*), the pH of $NiCl_2$-dosed media was titrated with 0.01-0.1 M NaOH in E3 to achieve the desired media pH of 7.4.

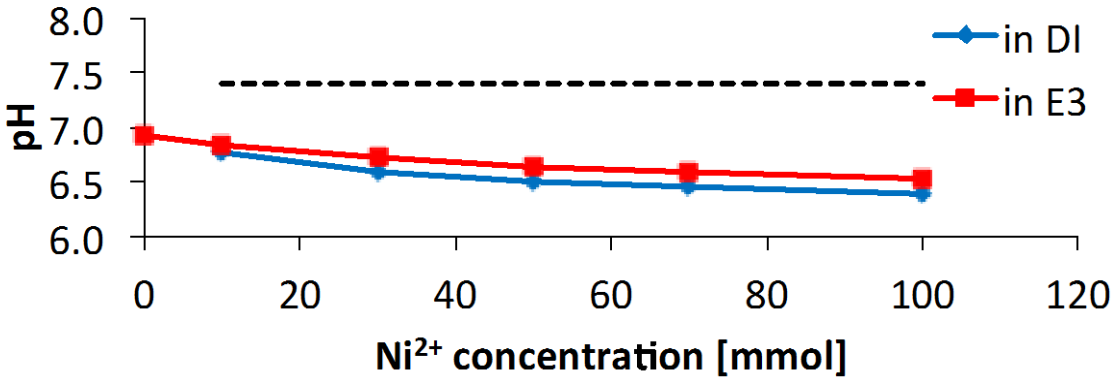


**Figure 2: pH dependence in water and E3 according to $Ni^{2+}$ concentration as modeled by MINTEQA2, showing a decrease by ~0.5 pH units with nickel addition.**

All zebrafish exposures were done under Institutional Animal care and Use Committee (IACUC) protocol 0802964A-1 approved 2/14/2008 or any subsequent revisions of this protocol.

**Uptake**

Surviving animals were collected upon termination of the experiment to measure cumulative metal uptake. Briefly, larvae were transferred to clean 12 well plates in groupings by dose and fresh E3 media was added (3 - 5 times, successively) to rinse residual particles from the

fish. Fish were sacrificed with a 10% bleach solution according to the operational protocol and again rinsed with E3 media. Residual media was removed and fish were dried in air. A digestion procedure by Borgmann et al., 2000 was used (*77*) beginning with addition of nitric acid (12.5 µL/fish, 70%, Fischer Scientific) followed by at least 1 week digestion and then addition of hydrogen peroxide (10 µL/fish, 30%, JTBaker), followed by 24 hrs digestion. Digestion reagents are not expected to contribute a significant amount of Ni to the sample and polypropylene storage containers used are expected to resist nickel adsorption (*78*). Resulting solutions were diluted up to 8 mL and the Ni concentration was measured in ICP.

Uptake [ng/fish] was calculated as follows:

*Concentration [mg Ni/L]* x *Dilution volume [L]* x *(1E6 ng/mg)* x *(1well/1fish)* / *# of fish*

**Swimming Analysis**

Zebrafish tracking was done at the completion of the five-day exposure experiment in dark (1-2 hrs), light (1-2 hrs), and 10 min light/dark cycles. Positional and time data collected in a video file for each fish was processed using LSRTrack and LSRAnalyze. These are MATLAB scripts developed within the laboratory of Edward Burton to quantify motility of zebrafish embryos from video files (*79, 80*). This analysis is performed on the raw data, allowing calculation of the velocity for each fish or mean velocities of each exposure dose at specific time points in the experiment.

## 2.3 ASSESSMENT OF THE EFFECT OF SILICA NANOSTRUCTURING ON THE ENVIRONMENTAL FATE OF COMPLEX NI-CONTAINING NANOMATERIALS IN MEDIA SOLUTIONS


### Abstract

There is an increasing interest in the use of nanoparticles for a range of applications, which is also coupled with a growing concern over the environmental risk associated with these materials (*21, 81, 82*). A key concern stems from the possibility of nano-specific toxic mechanisms that cannot be extrapolated from the toxicity of the analogous bulk material (*25, 28-30*). This is most likely occurs at diameters <20 nm (*28*). Yet this size range is also where many unique and desirable properties of nanomaterials are expected to emerge (*6*). Consequently, there is a strong push for continued development and production of materials in these very small size ranges, despite the parallel challenge of characterizing their exposure and toxic potential. Hence, while the use of nanomaterials could fundamentally alter how we benefit from the chemical and physical properties of materials, there is an equal need to better understand how to characterize their behavior from the perspective of nanotoxicity.

In practice, small nanoparticles (<20 nm) are unstable independent structures and require an added support to prevent agglomeration and inactivation (*83*). Few studies have been done on complex nanomaterials, despite the observation that toxicity can increase (*84, 85*) or decrease (*86*) as compared to single component structures. A study of the fate of silica-supported nickel nanoparticles in media solutions is presented here as a model for complex nanomaterials comprised of a toxic metal and a biocompatible support. In this evaluation, we have selected three nano-structured morphologies that are presently promising materials in nanotechnology.

These are hollow and non-hollow core-shell materials, consisting of nickel cores surrounded by silica shells, and surface-deposited materials in which nickel nanoparticles are instead deposited on a silica surface. In all cases the nickel nanoparticles are supported with amorphous silica.

To evaluate the environmental fate of nanomaterials, a complete understanding of the physicochemical characteristics is crucial (*33, 87-89*). Ideally, this type of characterization is performed *prior* to any toxicological testing in order to ensure appropriate dose and method for exposure, identify potential structure-to-activity relationships, and prioritize high risk materials for further evaluation (*53, 90*). Although the structure-to-activity relationship model has been applied for new synthetic chemicals (*34*), it is currently not directly applicable to particle toxicity. This is because is does not account for behavior specific to particles, which can greatly modify final particle exposures. In fact, a robust physicochemical analysis of a nanoparticle goes beyond simple particle size and surface area measurement; it also should include measuring dynamic behavior specific to nanoparticles in natural systems, which introduces new challenges in creating experimental methods that are transferrable to a wide range particles sizes and types.

Size, shape, surface area, surface chemistry, aggregation, agglomeration, sedimentation, and dissolution have all been identified as key material properties that can serve as indicators of nanotoxicity (*87*). Of these, agglomeration, sedimentation, and dissolution are poorly understood and have complex time-dependent behaviors that occur in increasingly relevant aqueous environments (*40, 41*). We have hence placed an emphasis on evaluating our silica-supported nickel-containing nanoparticles under the context of these behaviors in this study. We anticipated that through dynamic evaluation of agglomeration, sedimentation, and dissolution, important overarching relationships between structure and fate of the complex nanomaterials can be described and applied more broadly to other similar materials.

**Methods**

*Hollow Ni@$SiO_2$ (hNi@$SiO_2$)* materials were made using a one-pot reverse microemulsion synthesis adapted from Takenaka, et al. (*68*), consisting of several step-wise additions. First, 50 mL of cyclohexane (≥99% Sigma-Aldrich) and 10.5 g surfactant Brij 58 (≥99% polyethylene glycol hexadecyl ether, $M_n$ ~1124, Sigma-Aldrich) was refluxed at 50°C until the surfactant was fully dissolved. 1.5 mL of 1 M $Ni(NO_3)_2 \cdot 6H_2O$ (99.999%, Sigma Aldrich) was then added dropwise, followed by 1.5 mL hydrazine hydrate (Sigma-Aldrich) to form a nickel hydrazine complex. Next, 3-5 g of tetraethylorthosilicate (TEOS, ≥99% Sigma-Aldrich) was added, followed by 3 mL of ammonium hydroxide (30%). After 2 hrs of aging for silica growth, particles were precipitated with 2-propanol, collected via centrifugation, washed three times with 2-propanol, and dried in air. Crushed powder was placed in shallow ceramic boats and calcined in a Thermolyne 79300 tube furnace for 2 hrs at 500°C in air.

*Non-hollow Ni@$SiO_2$ (nhNi@$SiO_2$)* nanoparticles were made by a simple modification of the hNi@$SiO_2$ method. Hydrazine was excluded so that the ammonia addition instead leads to formation of a Ni-ammonia complex. Precipitated material was dried and calcined as described above. In order to remove external nickel from the materials, calcined particles were reduced and etched in nitric acid. Specifically, 0.20 g of material was dispersed in a 1:1 volume dilution of nitric acid (Sigma, 70%) in DI water for 30 min. Etched materials were washed twice in water to neutral pH, dried, and calcined.

For surface-deposited *Ni-$SiO_2$*, nickel-free spherical silica spheres were first synthesized and calcined using the microemulsion hNi@$SiO_2$ procedure except 1.5 mL DI water was added in place of the aqueous salt and hydrazine was excluded. A deposition-precipitation method

(modified from (*73*)) was used to deposit nickel nanoparticles on the surface of the silica spheres. 0.6 g of silica nanoparticles was dispersed in 15 mL of DI water by sonication, a Ni salt solution was added (0.55 g $NiCl_2$ in 10 mL DI water), and the mixture was again sonicated for 20 min. Ammonium hydroxide (30%, Sigma) was then added dropwise (~5 mL, 52 drops, slowly over 20 min) until the pH of the solution was ~9.5. The resulting material was mixed for 20 min, centrifuged, dried, calcined at 300$^{o}$C in air, rinsed two times in DI water, dried, and calcined again at 300$^{o}$C in air.

All materials were characterized for particle size and morphology with transition electron microscopy (TEM, JEOL-2000FX electron microscope). Typical sample preparation consisted of grinding the sample in a mortar, dispersed in ethanol, ~2 min sonication, and placement of 1-2 drops of the dispersion on copper type-B support grid (Ted Pella, Inc.) to dry in air. Particle measurements of TEM images were done using ImageJ software (http://rsb.info.nih.gov/ij/). Crystal structure was determined with x-ray diffraction (XRD) (Phillips PW1830, USA). XRD was run in 'line focus' mode using a monochromatic Cu radiation at the wavelength of 1.54 Å. The beam voltage was 40kV at a current of 30mA. Diffraction patterns were recorded between 15 and 90° (2θ) in steps of 0.08° intervals with a 0.2 s counting time at each step. Scanning Electron Microscopy (SEM) equipped with EDX Genesis was used to determine elemental composition of palladium-coated samples at beam voltage of 15kV, spot size 4 (typically), collection time of 50-100 s, and a monitored dead times of 20-40%. An average of at least 3 measurements was calculated for each sample. Catalyst surface area and porosity were determined by Brunauer Emmett Teller (BET) analysis (Micromeritics ASAP 2020 surface area and porosity analyzer). Pre-treatment consisted of 2-3 hr degas at 200$^{o}$C under vacuum. Typically, a 6-point BET analysis was used for total surface area measurement and an 84-point

$N_2$ BJH analysis with Halsey thickness curve correction and Kruk-Jaroniec-Sayari BJH correction for pore size and volume determination. Extended X-ray adsorption fine structure (EXAFS) spectra were collected at Argonne National Labs (ANL) Advanced Photon Source (APS). Ni-containing structures were analyzed and compared with standard of nickel foil ($Ni^o$) and NiO powder. Oxidized and reduced samples were crushed and molded into a pellet for analysis. ANL completed the x-ray adsorption near edge structure (XANES) curve fitting and analysis of the results on our behalf. Nanoparticle dispersions were tested by dynamic light scattering (DLS, Zetasizer Series Nano-ZS) to estimate the hydrodynamic diameter of the particles in E3 media (49 mM NaCl, 1.6 mM KCl, 3.3 mM$CaCl_2 \cdot 2\ H_2O$, 3.3 mM $MgSO_4 \cdot 7\ H_2O$, pH 7.4). The samples were first dispersed for ~2 min by sonication and then ~1 mL of dispersed solution was added to a plastic cuvette. The refractive index of silica was used for all measurements and three successive measurements were done at room temperature. Sedimentation was measured by UV-Vis spectroscopy. Nanoparticles were dispersed in E3 media and deposited in a plastic cuvette to a liquid height of 1 in. Settling velocity and absorbance over time were related to agglomerate size by Stoke's law. To do this, sedimentation was first measured by UV-visible spectroscopy (Figure 1). The downward velocity ($v_s$) of a particle subjected to gravitational and viscous drag forces can be described in relation to the particle radius (R), as shown in Figure 1 (*74, 91*). The Stokes equation is derived for the settling of smooth spherical particles, and the settling velocity of equivalently sized agglomerate fractals has been demonstrated to be higher due to permeability of the agglomerate pores (*92*). This effect becomes more pronounced as agglomerate size increases, since the added drag forces due to surface roughness become more outweighed by decreased packing density (and hence larger pores). The net result is that agglomerate size estimates will be slightly overestimated by this

analysis. However, this method it is nonetheless a convenient way to simultaneously measure sedimentation and estimate agglomerate size, while not being limited to dilute the particle concentrations required for DLS.

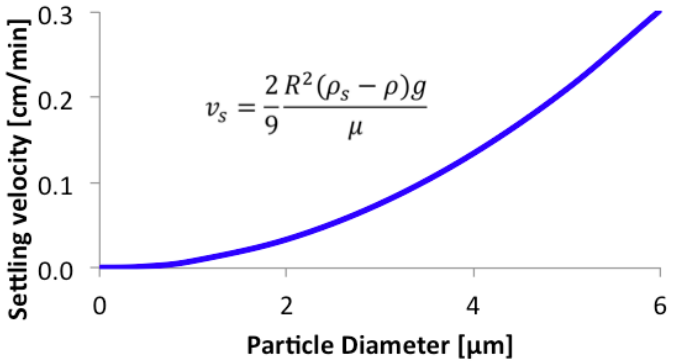


**Figure 3: Settling velocity as predicted by Stoke's law as a function of particle (or agglomerate) diameter, where $v_s$ is settling velocity, R is particle radius, $\rho_s$ and $\rho$ are densities of the solution and the particle, g is acceleration due to gravity, and $\mu$ is solution viscosity.**

Trace metal ion concentration was measured under radial detection by ICP-AES (Thermo Electron Corporation iCAP6500 Duo Series ICP-OES Spectrometer). A standard curve was generated with at least 4 standard solutions that captured the sampling range. Standards were formulated from a stock standard solution (Fischer Scientific) with 3 wt. % $HNO_3$ in deionized water. A mean of 3 measurements are reported and an internal blank and standard were used during each sampling period. The degree of nickel ion dissolution from the nanoparticles in E3 media was determined with ICP. Dispersions (typically, 50-200 mg Ni/L) were prepared in E3 media and separated into 10 mL aliquots for analysis at specific time points. Metal nanoparticles were removed from the dispersions by centrifugation followed by filtration (Amicon 10,000 molecular weight cut-off filters, ~3.1 nm). $HNO_3$ (Sigma, 70%) was added dropwise to the filtrate to a concentration of 3wt %. Silica dissolution was measured according to ASTM D859-

00. This procedure is designed to detect 'molybdate reactive' silica, which includes simple silicates, monomeric silica, silicic acid, and some undetermined amount of polymeric silica. The procedure described above for nickel was also used here, in which dispersions of 50 or 200 mg Ni/L initial concentrations were separated into 10 mL aliquots for collection at specific time points. Nanoparticles were removed from the dispersion by centrifugation followed by filtration (Amicon 10,000 molecular weight cut-off filters, ~3.1 nm). The filtrate was diluted to detection limit of 1-5 mg/L of dissolved silica as needed. By additional of several reagents according to the procedure, a color change occurs to green-yellow and then to blue. This color change is measured in UV-Vis and compared with a standard curve for concentration assessment.

**Results**

TEM images of the Ni-containing nanomaterials synthesized for this study are shown in Figure 4 and basic material characteristics are given in Table 1. The nickel nanoparticles were all similar in size (near 2 nm) and nickel content was ~5-10 wt. %. The BET surface areas were ~200-300 $m^2/g$ and the silica structure was mesoporous with pore diameter ~0.7 nm. The primary particles were spherical and <60 nm and hence, in the absence of agglomeration, are optimum size for endocytotic uptake (*93-95*). While occasional necking between adjacent particles in TEM indicated the presence of some aggregation in the as-synthesized material, analysis by SEM showed some particle clusters of <1 μm coexisting with solitary particles, emphasizing that the material remains in the nano-range in the dry powder form.

The silica matrix is porous and amorphous while the nickel particles are crystalline. Further characterization of the material crystal structure is included here since crystallinity can be a factor in particle dissolution (*96, 97*). XRD analysis of Ni-$SiO_2$ corresponded with nickel silicate ($NiSiO_3$) and NiO (Figure 5). However, for both hNi@$SiO_2$ materials and nhNi@$SiO_2$

the peaks were much less distinct, and only a correlation to Ni was identified. Further analysis was done by EXAFS for these samples and XANES peaks of the hNi@$SiO_2$ and nhNi@$SiO_2$ do both correspond with NiO. However, oscillations in the EXAFS spectra at >8.37 kEV (see Figure 6 for nhNi@$SiO_2$ as an example) also suggested the presence of Ni silicates (*72*).

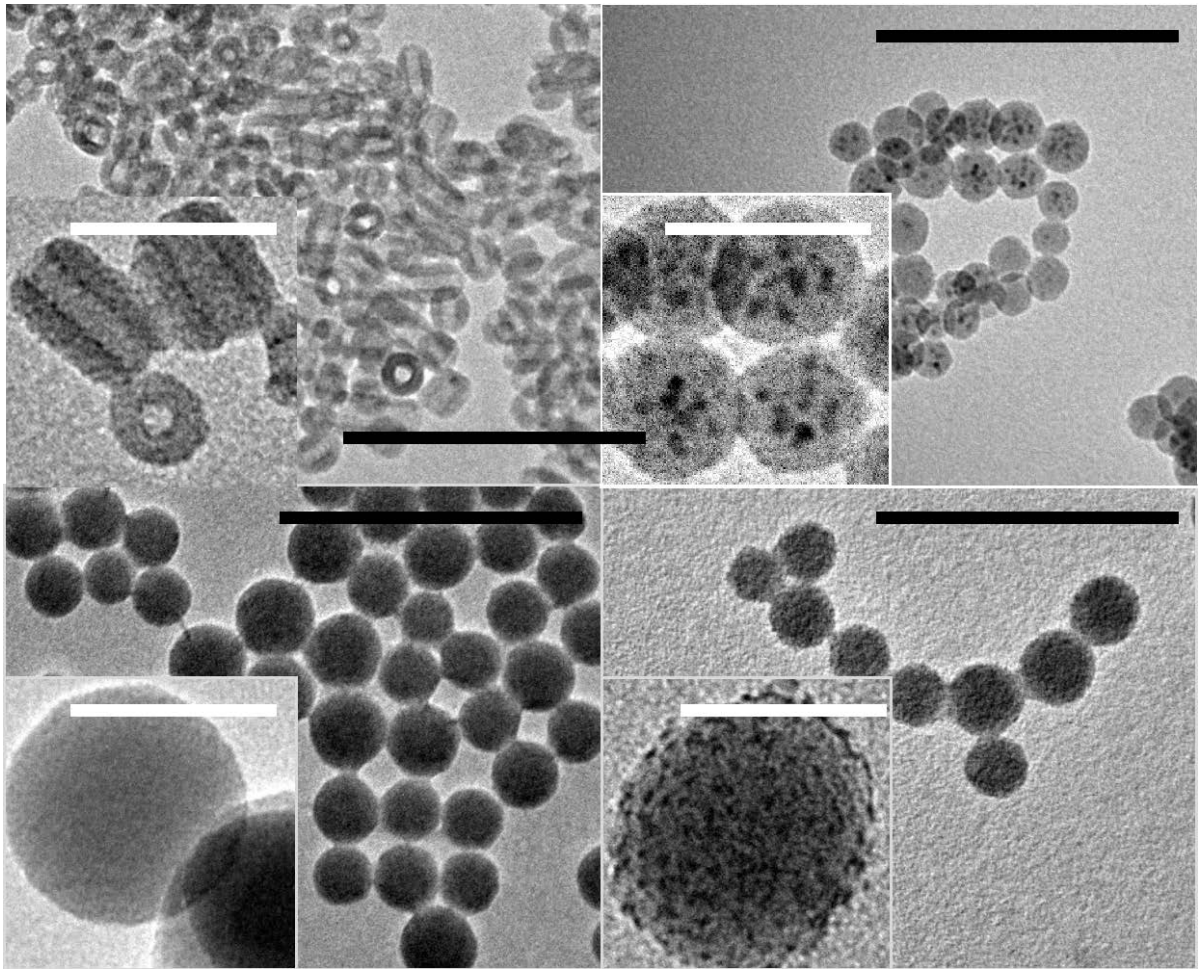

**Figure 4: hNi@$SiO_2$ (a.), nhNi@$SiO_2$ (b.), metal-free $SiO_2$ (c.), and Ni-$SiO_2$ (d.). Scale bars are 50 nm for insets (white) and 200 nm for larger images (black).**

**Table 1: Ni loading and dry powder size characteristics for hNi@$SiO_2$, nhNi@$SiO_2$, and Ni-$SiO_2$ nanomaterials shown in Figure 4.**

| Nanoparticle | Ni loading [wt% Ni] | $D_p$, Ni particle [nm], n= # particle | $D_p$, primary particle [nm], n= # particle |
|---|---|---|---|
| *h*Ni@$SiO_2$ | 9.0 ± 0.9 | < 2 | 25.9 ± 3.0, n=16 |
| *nh*Ni@$SiO_2$ | 5.1 ± 0.4 | 2.5 ± 0.4, n=11 | 46.2 ± 6.5, n=13 |
| Ni-$SiO_2$ | 11.9 ± 3.2 | 2.1 ± 0.4, n=23 | 56.5 ± 8.2, n=12 |

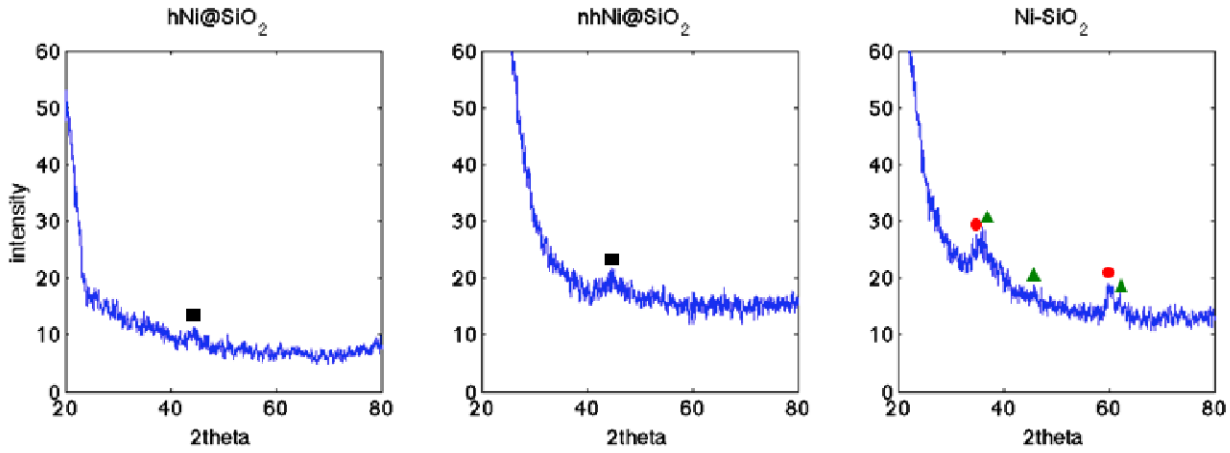


**Figure 5: X-ray diffraction patterns of hNi@$SiO_2$, nhNi@$SiO_2$, and Ni-$SiO_2$. Square=Ni (04-0850), circle=NiO (78-0643), triangle=$NiSiO_3$ (43-00664).**

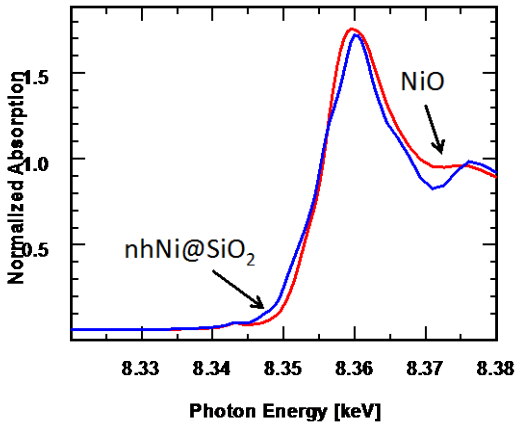


**Figure 6: EXAFS spectra for nhNi@$SiO_2$ material calcined at 500°C (edge energy=8.3423) compared with NiO standard (edge energy=8.3402). Curve is characteristic of NiO, but oscillations at high photon energy is characteristic of Ni silicate (*72*). Conducted at Argonne National Laboratory.**

Nanoparticles, in particular, are well-known to agglomerate in aqueous environments (*98*, *99*). This is because particles of smaller sizes have a lower repulsive strength, causing the particles to collapse into each other (*100*). Although agglomerates can be temporarily broken up by physical means (e.g., sonication), agglomerate size typically increases in aqueous environments with low ionic strengths such as media solutions or the cellular environment. The agglomerate size is the final determinant for diffusion and membrane transport and hence a critical indicator of the ultimate fate and toxic potential of nanoparticles. As-synthesized materials dispersed by sonication in E3 media solution were tested in DLS and the results are given in Figure 7. Three successive measurements (over ~10 min each) are shown which clearly indicate time-dependent agglomeration to largest hydrodynamics diameters of 0.5-1 μm for all the samples and only nhNi@$SiO_2$ showing any hint of agglomerates <300 nm by the third measurement. Since the detection of small particles can be masked by the presence of larger particles in DLS, analysis was repeated after filtration with a 0.45 μm-cellulosic filter. The resultant sampling population was too small for the instrument to measure, further confirming that large agglomerates populations dominated the dispersions.

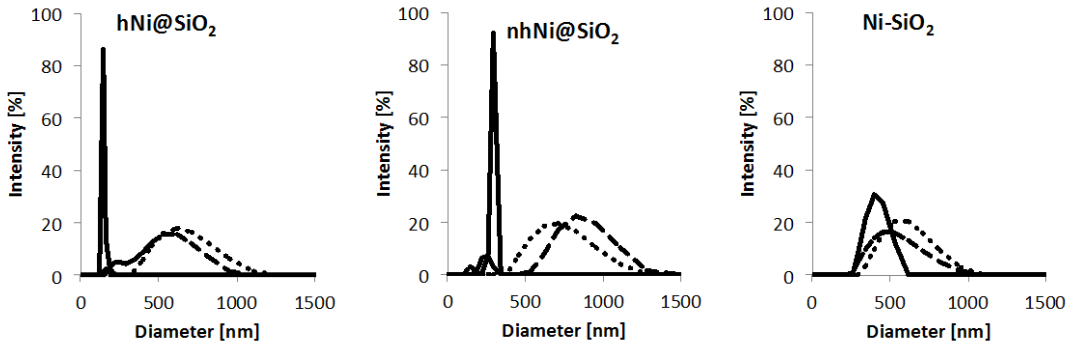


**Figure 7: Hydrodynamic diameter measured in DLS for hN@$SiO_2$, nhNi@$SiO_2$, Ni-$SiO_2$ directly after dispersion by sonication. Particle concentrations were 45-107 mg/L in E3 media (pH=7.4). Three successive measurements were done: 1st (solid line), 2nd (dashed line), 3rd (dotted line). Instability due to agglomeration is seen at low concentrations.**

Ideally, one would prefer to also characterize agglomerate size at higher concentrations since agglomeration is expected to increase at higher particle concentrations and since the allowable particle concentrations in DLS are often much lower than those of interest for nanoparticle exposure testing. However, multi-scattering and the gravitational settling that results at high concentrations leads to inaccuracies in DLS such that this technique is no longer appropriate.

Gravitational settling was readily visible in our samples within a few hours of preparing dispersions at higher concentrations of ~1 g/L. Given that agglomeration and sedimentation act as exposure modifiers, quantification of agglomerate size at higher concentrations can be important as well. Sedimentation was measured by UV-visible spectroscopy (Figure 8), demonstrating a significant amount of settling within 120 min. From sedimentation trends, settling velocities can be calculated at each time point. As described previously, each settling velocity can be related to the agglomerate size by Stoke's law and the corresponding population size can be estimate from the change in absorbance between time points. Figure 9 shows

estimated agglomerate size distributions based on this analysis. More large agglomerates were present for hNi@$SiO_2$ while nhNi@$SiO_2$ had the largest fraction of smaller agglomerates, which can readily be inferred from the sedimentation data as well.

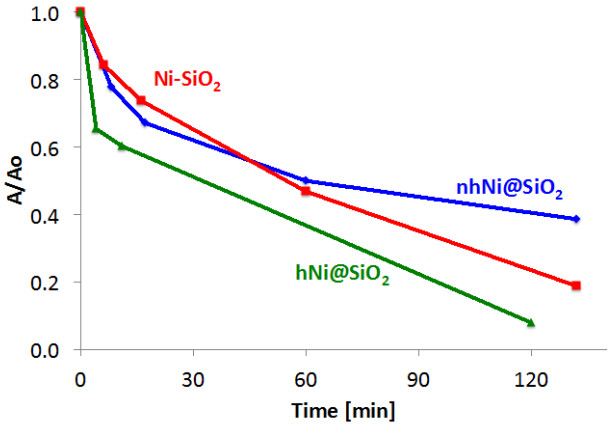


**Figure 8: Settling measured in UV-visible spectroscopy for Ni-containing nanomaterials (normalized to initial value for each material, $A_o$). Initial concentration is 150 mg Ni/L.**

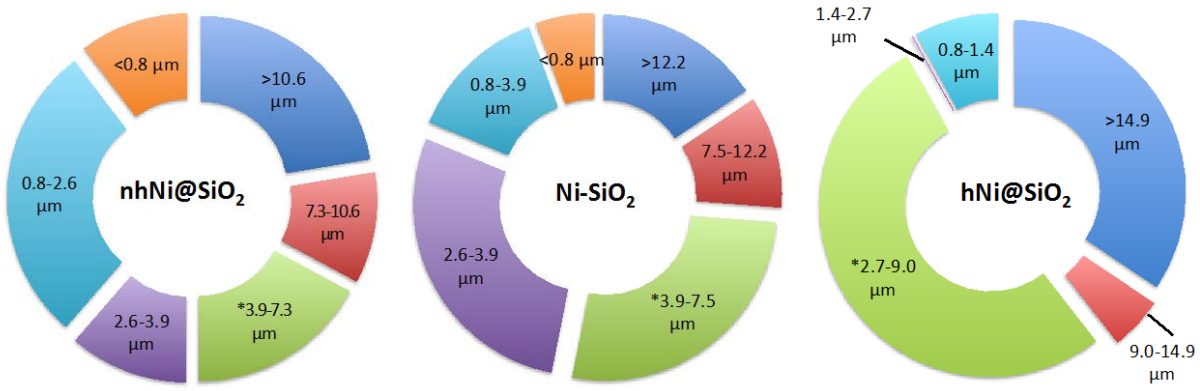


**Figure 9: Hydrodynamic diameter distribution estimates for Ni-containing nanoparticle dispersions based on calculations using Stoke's law for settling data collected in UV-Vis for 120 min. Initial concentration is 150 mg Ni/L for all materials.**

In a second study, normalized absorbance ($A/A_o$) after 24 hrs of settling was compared for a range of initial particle concentrations. Higher initial particle concentrations are expected to increase agglomeration and sedimentation since this would increase the amount of particle

interactions. Increased sedimentation was observed at higher initial concentrations for both hNi@$SiO_2$ and Ni-$SiO_2$ while nhNiNi@$SiO_2$ remained relatively stable in solution (Figure 10, left). Yet lower concentrations did result in more stable dispersions for hNi@$SiO_2$ compared to nhNi@$SiO_2$. This second observation is actually consistent with the behavior we expected given that the hollow center of hNi@$SiO_2$ should decrease the density and therefore slows sedimentation. It is important to also view these data as a function of particle concentration (a more realistic predictor of dispersion stability). Figure 10 (right) shows UV-vis trends based on particle concentration, further emphasizing a higher relative stability of nhNi@$SiO_2$ dispersion, even at particle concentrations >1.5 g/L. While the scope of this work did not include determination of the reasoning for this difference, it hypothesized that the surface chemistry of this material leads to the higher stability trends observed. The nhNi@$SiO_2$ is etched as part of the particle synthesis. It could be that the etching of extraneous nickel changes to surface morphology and composition to make it more easily solvated in aqueous solutions. Meanwhile, the exposed surface consisted mostly of non–hydroxylated or condensed silica for hNi@$SiO_2$ and NiO and nickel silicate for the Ni-$SiO_2$ material. We propose that these differences in surface chemistry lead to a lower tendency for the nhNi@$SiO_2$ to agglomerate and sediment compared to the other materials.

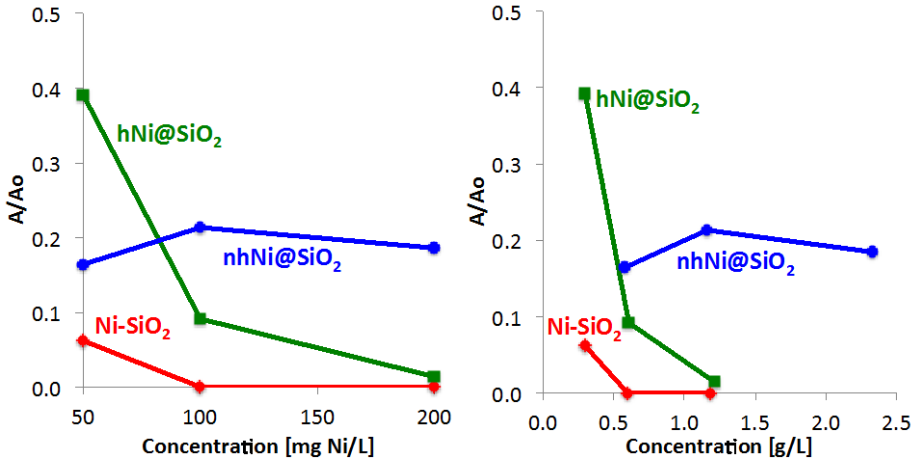


**Figure 10: Dependence of $A/A_o$ on initial concentration in UV-Vis at 287 nm for t=0 and t=24 hr for nanoparticle dispersions in E3 media. Data is displayed in terms of both nickel dosing [mg Ni/L] (left) and corresponding particle concentration [g/L] (right).**

Nickel dissolution from the Ni-containing nanomaterials is shown in Figure 11 for an initial concentration of 200 mg Ni/L in E3 media. For all materials, the rate of dissolution was initially fast and gradually slowed after the first 24 hrs. The final nickel ion concentrations were 3-15 mg Ni/L, and the highest dissolution occurred for Ni-$SiO_2$, where 8% of the initial nickel particle concentration was measured as ions in solution.

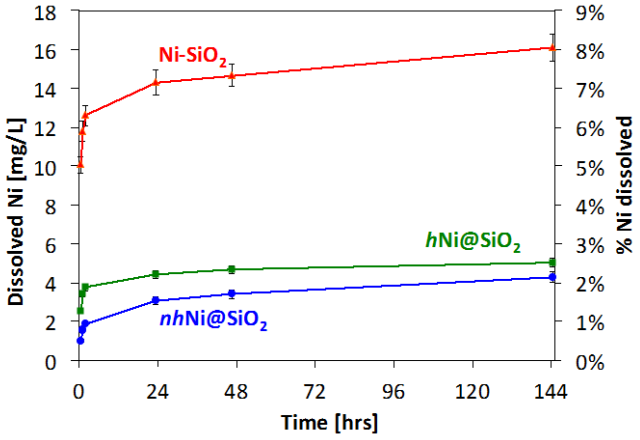


**Figure 11: Amount dissolved and percent dissolution of Ni-containing nanomaterials in E3 media at room temperature for 5 days. Error bars (only visible for Ni-$SiO_2$) reflect standard error of the estimate for the ICP calibration curve (3.9%) and the % relative standard deviation 3 ICP measurements.**

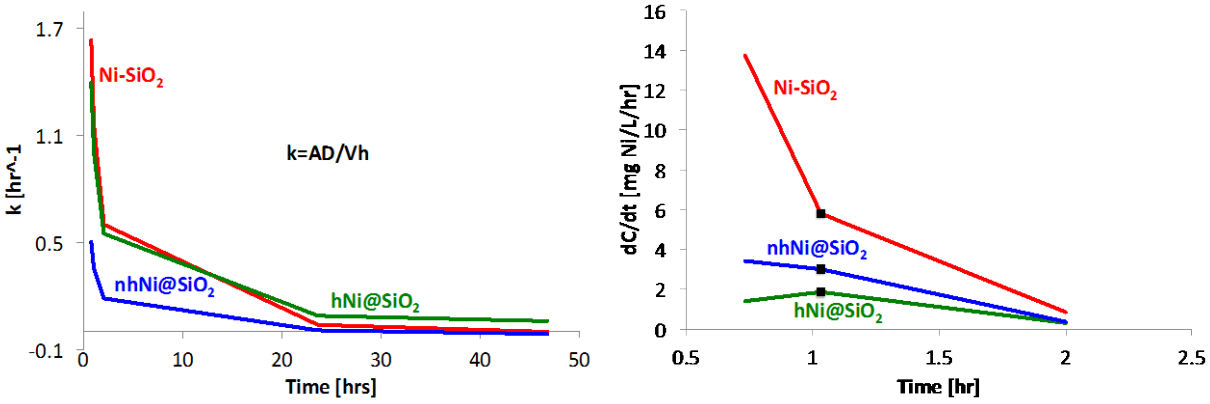


**Figure 12: Time dependence of dissolution constant (left) and dissolution rate at initial times (right).**

The concentration in the bulk is expected to vary according to:

$$\frac{dC}{dt} = k\left(C_s - C(t)\right) \quad (1)$$

where $C(t)$ is the concentration of $Ni^{2+}$ at time $t$, $C_s$ is the saturation concentration, and $k$ is the dissolution rate constant. The rate constant is defined as $k=AD*(Vh)^{-1}$, where $A$ is surface area,

*D* is diffusion coefficient, *V* is solution volume, and *h* is effective diffusion layer. This results in the following time-dependent expression for concentration:

$$C(t) = C_s\left(1 - e^{-kt}\right) \quad (2)$$

This equation can be transformed according to:

$$\ln\left(1 - \frac{C(t)}{C_s}\right) = -kt \quad (3)$$

Taking the dissolved concentration recorded at the end of the experiment to reflect the saturation concentration for each material, the value on the left-hand side of equation (3) can be estimated. A linear relationship for equation (3) would result from a constant rate constant (*k*). However, our analysis gave a non-linear trend, indicating either a time-dependent dissolution constant or saturation concentration. Assuming a time-dependent rate constant to be the more reasonable of the two cases, a polynomial data fit of according to equation (3) yields an estimate of the dissolution constant (shown in Figure 12). By this analysis the rate constant of Ni-$SiO_2$ and hNi@$SiO_2$ are fairly similar while that of nhNi@$SiO_2$ is much lower. It is interesting to think about this experiment in the context of the etching step used to prepare nhNi@$SiO_2$ material; this step might essentially remove loosely associated nickel to result in lower rate constants for this material. Meanwhile, the rate constant reduces dramatically over time for all materials. Based on the definition of the rate constant, this could be due to a progression towards a larger effective diffusion layer in particles embedded more deeply in the silica matrix. With a more embedded particle, one would expect a larger silica-nickel interaction, which may in turn prevent water solvation and subsequent dissolution of the particle.

Alternatively, when *t* is small, $C(t) \approx 0$ and the initial rates are simply proportional to $kC_s$. According to this analysis, Ni-$SiO_2$ also had the highest initial dissolution rate (i.e., to $k_{Ni\text{-}SiO_2}$).

By comparison, relative dissolution rates were 0.5 $k_{Ni\text{-}SiO_2}$ and 0.3 $k_{Ni\text{-}SiO_2}$ for hNi@$SiO_2$ and nhNi@$SiO_2$, respectively. If we assume the nickel surface area (*A*), diffusion coefficient (*D*), and volume (*V*) were similar based on the ~2 nm nickel particle size and identical experimental conditions, this also implies effective diffusion layers of $h_{nhNi@SiO_2} > h_{hNi@SiO_2} > h_{Ni\text{-}SiO_2}$. The differences in the effective dissolution layer agrees with what might be expected from the individual structures (illustrated in Figure 13): the nickel particle is almost entirely exposed to the media for Ni-$SiO_2$, is exposed only to the hollow interior in hNi@$SiO_2$, and is entirely surrounded by the porous silica matrix except for any adjacent pores in nhNi@$SiO_2$. Indeed, the diffusion layer is thought to increase as a result of bridging of primary particles into aggregates, formation of agglomerates, and coating of the particle surface (*50*).

**Figure 13: Schematic of Ni-$SiO_2$, hNi@$SiO_2$, and nhNi@$SiO_2$ materials, demonstrating a progressively lower Ni-surface accessible based on structural configuration.**

In the case of an even lower initial concentration, we suspected that a greater degree of nickel dissolution might occur given that $C_s$-*C(t)* (i.e., the driving force for dissolution) would be larger at a given time t. To test this, dissolution was measured at 50 mg Ni/L and compared by percent dissolution with the results from 200 mg Ni/L presented above. Shown in Figure 14, the nickel dissolution by percent for core-shell materials increased significantly at this lower concentration, but was largely unaffected for Ni-$SiO_2$. Meanwhile, the initial rate assessment was very similar ($0.8k_{Ni\text{-}SiO2}$ and $0.3k_{Ni\text{-}SiO2}$ for hNi@$SiO_2$ and nhNi@$SiO_2$, respectively). This

difference was surprising, suggesting an impendence to nickel dissolution for the Ni-$SiO_2$ only. To understand this difference, we should note that colloidal silica can also dissolve in aqueous environments to equilibrium concentrations of ~100 mg $SiO_2$/L (*96*). In our experiments with both nickel-free and Ni-containing nanomaterials, a pH increase of 0.5–1.0 from the initial value of 7.4 was often observed, consistent with observations for colloidal silica dissolution in early work by Iler and coworkers (*96*).

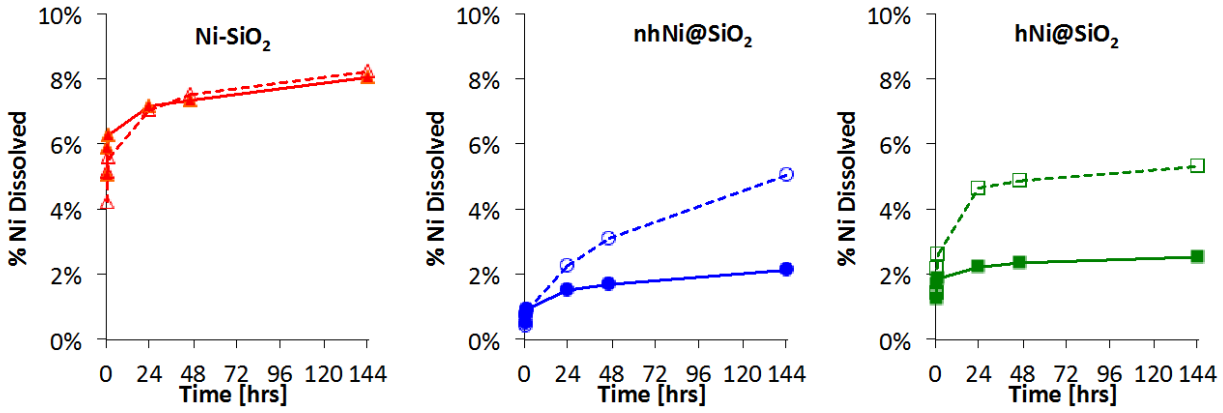


**Figure 14: Percent dissolution of nickel from of Ni-containing nanomaterials for 50 mg Ni/L (dashed, open symbols) and 200 mg Ni/L (solid, closed symbols) in E3 media at room temperature for 5 days. Lower initial concentration resulted in higher % dissolution for core-shell materials.**

Dissolution studies for silica were also conducted at the same concentrations tested previously for Ni (i.e., 50 mg Ni/L and 200 mg Ni/L). This corresponded with initial concentrations of ~500 and 2000 mg $SiO_2$/L, depending on the exact composition of each material. As shown in Figure 15, a much larger amount of dissolved silica was measured for core-shell materials (up to the ~100 mg/L) compared to only ~ 10 mg $SiO_2$/L for Ni-$SiO_2$ materials. Additionally, the percent of the silica that dissolved was much higher for the lower initial concentration (50 mg Ni/L), especially in core-shell materials, which was consistent with the experiments for nickel dissolution. This analysis is also consistent with the observation that

initial rates were similar for each initial concentration; i.e., a higher mobility of the nickel particle due is only expected after a time delay for silica dissolution to begin. TEM micrographs of all materials after 5 days of dissolution (Figure 16) indeed showed what appeared to be partial dissolution of silica compared to as-synthesized materials (Figure 4).

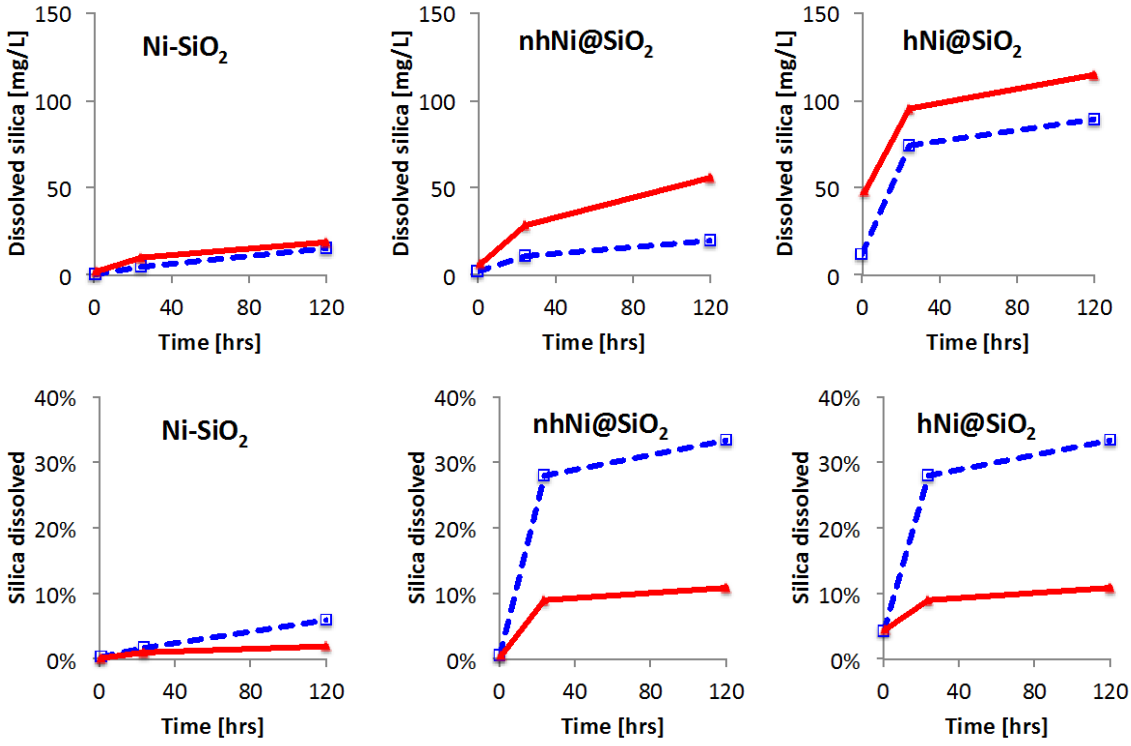


**Figure 15: Percent of silica dissolution for Ni-containing nanomaterials for initial concentration of 50 mg Ni/L (dashed, open symbols) and 200 mg Ni/L (solid, closed symbols). Low dose results in higher % dissolution, especially for core-shell materials.**

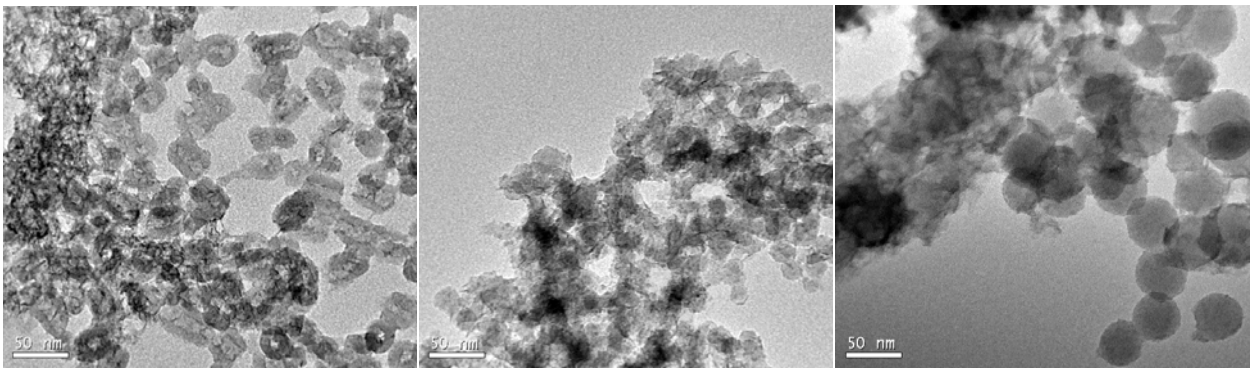


**Figure 16: TEM micrographs hNi@$SiO_2$ (left), nhNi@$SiO_2$ (middle), and Ni-$SiO_2$ (right) after 5 days dissolution in E3 media showing some re-structuring of silica in all three samples.**

## Discussion

Gravitational forces begin to dominate as nanomaterials in aqueous solutions agglomerate, causing measurable sedimentation to occur for many particle types (*98-101*). While gravitational settling can essentially modify the intended dose during toxicity exposure studies, it is nonetheless a realistic behavior for nanomaterials in aqueous environments. Artificial and even naturally occurring stabilizers like decomposed organic matter, can prevent agglomeration and settling. However, in this study we chose to characterize the dynamic behavior of as-synthesized nanomaterials in the absence of such stabilizers to establish a reference case comparison between the three materials of interest. The implication of agglomeration and sedimentation behavior in our study was that nhNi@$SiO_2$ particles could impart a greater toxic effect given that it was comprised of a larger population of smaller agglomerates compared to the other materials. This is especially true for in-vivo studies with free-swimming fish since they remain high in the water column throughout the majority of the exposure experiment, i.e. any sedimentation of particles will reduce the effective exposure dose. Furthermore, the fish would be exposed to the smallest particles in the population of nhNi@$SiO_2$, and thus the particles with the greatest potential of interacting with cellular

structures. Conversely, for in-vitro studies in which cells are settled in media solutions, a nanoparticle exposure above the intended dose would occur to a greater extent for the hNi@$SiO_2$ and Ni-$SiO_2$ materials. Yet this elevated exposure would essentially consist of large agglomerates that have preferentially settled, and hence interactions with cellular structures might be limited.

Dissolution of nanomaterials is thought to be a key mechanism for toxicity of silver (*102, 103*), nickel (*48, 49*), and zinc nanoparticles (*30, 104*). Metal ion shedding depend on the degree of crystallization, pH, temperature, particle size, and in our case, the stability of the support. Smaller particle sizes (i.e., nano-sized particles) are predicted to have higher rates of dissolution due to higher surface energies (*50*), hence giving rise to concern. Dissolution from nickel nanoparticles has been recorded as high at 3.7% of the initial concentration after 48 hrs for 6 nm nickel nanoparticles (*49*) and up to 2.5% of the initial concentration after 4 days for 30-60 nm nickel nanoparticles (*48*). For the latter the case a final nickel ion concentration of 25 mg Ni/L was measured (*48*). In our dissolution studies of ~2 nm Ni particles, dissolution of 8% of the initial concentration (up to 15 mg Ni/L) was observed for Ni-$SiO_2$ materials.

When hydrated the thin passivation layer of NiO on these materials will become hydroxylated according to NiO → $Ni(OH)_2$ (*105*). A transition to a slightly alkaline condition will quench dissolution because of low solubility of $Ni(OH)_2$ at high pH (*105*). However, the large excess of $Cl^-$ ions in the media (>50 nM) may enhance nickel solubility given the high solubility of $NiCl_2$ (64.2 g/100 mL). Finally, dissolution of silica can also occur to up to 100-140 mg $SiO_2$/L (*106*), as was observed in our experiments. The equilibrium reaction to form dissolved silicic acid from silica particles proceeds according to: $SiO_2 + 2H_2O <-> H_4SiO_4$.

While the dissolution kinetics is slow, amorphous silica has a higher rate of dissolution compared to crystalline forms.

**Figure 17: Schematic of effect of silica dissolution on enhancement Ni dissolution for nhNi@$SiO_2$ material.**

Hence, simultaneous dissolution of both nickel and silica are presumably possible for these materials. Silica encapsulation (such as in core-shell materials), silicates, and particle agglomeration are all expected to hinder nickel dissolution, but the small ~2 nm diameter of the nickel nanoparticle will enhance it. Finally, the dissolution of silica will progressively increase accessibility of the nickel nanoparticle. An example of this is depicted in Figure 17, where silica dissolution would enhance mobility and accessibility of the nickel nanoparticle once underway. Comparing initial concentrations 50 mg Ni/L (or ~500 mg $SiO_2$/L) with 200 mg Ni/L (~2000 mg Si/L), we might expect more dissolution (by percent) at the lower of the two concentrations. This is because a greater fraction of silica dissolution is required from each individual particle to approach the dissolved silica equilibrium concentration. Indeed, this effect was observed for the core-shell materials while silica dissolution for Ni-$SiO_2$ materials was low and unchanged by the initial concentration. Meanwhile, the change in the % nickel dissolution for Ni-$SiO_2$ was also minimal, presumably because the silica was less accessible for dissolution. This could be because of a more prominent population of crystalline nickel silicates, or simply that the silica is

less accessible due to surface deposition of nickel. Overall however, the highly accessible nickel nanoparticles of Ni-$SiO_2$ were observed to yield the highest nickel dissolution, and hence may be more capable of imparting a toxic effect. On the other hand, silica dissolution at a lower initial concentration was seen to dramatically increase the amount of nickel dissolution such that this difference between each of the materials became less pronounced.

**Conclusion**

Complex metal nanomaterials are currently being developed for a range of nanotechnology applications and it is likely that this class of supported (versus single component) materials will dominate the next generation of nano-enabled materials. Therefore, development of methods to study the environmental fate and exposure risk to these types of materials is of critical importance. A fundamental part of this assessment is an understanding their dynamic behavior in representative media solutions. Agglomeration, sedimentation, and dissolution are time-dependent modifiers of toxicity and are controlled in an entirely new ways in multi-component materials. Here, significant agglomeration and gravitational settling was observed for all of the materials, which would generally be expected to reduce toxicity. Indeed, although it is not the focus of this report, preliminary exposure screenings with zebrafish embryos to these materials do show low toxicity for end points of survival and developmental malformations. Despite this, the lower sedimentation of nhNi@$SiO_2$ and higher dissolution of Ni-$SiO_2$ has also allowed us to identify these two structures as having a higher potential for toxic effect.

Furthermore, measurement of dissolution of the silica demonstrated that poor stability of the support structure allows an altogether different environmental fate for core-shell materials by facilitating a delayed release of dissolved metal ions. In our case, the large agglomerates prevent

the possibility of any significant membrane interaction or cellular uptake. However, one could imagine a well-dispersed particle with a degradable support in a size range ideal for endocytotic uptake. In this scenario, uptake of the particle could result in a 'Trojan horse'-type effect in which the subsequent degradation of the support would allow enhanced dissolution of the second metal (e.g., nickel) within the cells. Indeed, this concept is already exploited in degradable supports for drug delivery and it could greatly enhance the toxicity of complex metal nanomaterials.

Overall we have observed very different behaviors for each silica-structured nanomaterial studied here. nhNi@$SiO_2$ stood out as more resistant to agglomeration, but was susceptible to an elevated release of nickel ions in more dilute solutions due to silica dissolution. Ni-$SiO_2$ was observed to yield the highest release of nickel ions, but appeared to be more stable and long-lived in solution compared to the other materials. hNi@$SiO_2$ was agglomerated to a larger extent compared to the other materials, but was also susceptible to a coupled silica and nickel dissolution, especially at lower concentrations. One can see by this how different strategies for the necessary structuring of the nanoparticles can entirely alter environmental fate. Clearly, continued work is necessary to understand the difference, of the toxic potential that could result from these varied behaviors in media solutions. Nonetheless, our results indicate that hollow Ni@$SiO_2$ may have a comparatively lower toxicity due to its tendency to agglomerate and settle and a minimal dissolution compared to Ni-$SiO_2$.

*Acknowledgment.* Jeff Miller and Tianpin Wu at Argonne National Laboratory are acknowledged for characterization of our materials in EXAFS.

## 2.4 THE USE OF DISPERSANTS FOR SILICA-STRUCTURED NANOMATERIALS IN AQUEOUS SOLUTIONS

Since the agglomeration of nanoparticles in aqueous solutions can present such a challenge for studying nanotoxicity, some researchers have attempted to address this by incorporating polymeric coatings that enhance colloid stability, such as PEI (*107*), bovine serum (*86*), PEG (*93*), PVP (*108*), natural organic matter (*109*), alginate (*110*), and humic acid (*111, 112*). For silica-based materials, incorporation of cationic, anionic, and neutral functional groups is also possible by modification of silica pre-cursor during synthesis (*113, 114*). In most cases the coatings are charged and hence will increase the repulsive forces between adjacent particles so as to prevent agglomeration. This can be beneficial for toxicity studies, in which agglomeration and settling will reduce the intended dose of the experiment. Yet while coatings can prevent agglomeration, they can also result in increased or decreased uptake of the particle by modifying the interaction of the particle with cellular membranes.

Silica, which is studied in the detail in this work, is expected initially to have a weakly negative surface charge (*98*). Positively charged coatings (such as PEI or any other amine-based coatings) will result in increased interaction between the particular and the negatively charged cell membrane, often leading to elevated uptake levels, or complete disruption of the cellular membranes (*115*). Neutrally charged PEG and negatively charged coatings, by contrast, are known to reduce interactions with negatively charged proteins, and hence can reduce cellular uptake (*93*). It is also expected that nanoparticles will interact with naturally occurring surface modifiers when they are released in the environment. In this way, an understanding of the effect

of these types of coatings is important in predicting the ultimate fate of nanoparticles released into the environment.

Alginate and humic acid are both considered environmentally relevant materials, and can also increase the dispersion of nanoparticles in aqueous solution. Alginate is a polysaccharide consisting of a randomly organized linear copolymers of beta D-mannopyranuronate (M) and alpha-L-gulopyranuronate (G) monomers (Figure 18). It is typically derived from brown algae, where it makes up the cell wall. Alginate has been recognized to adsorb divalent cations and hence there is a substantial amount of research in the area of alginate treatment for metal-contaminated environments (*116*). By comparison, humic substances are substantially more complex supramolecules that are made up of loosely associated constituents. Humic acid is essentially one component of decomposing organic matter, which also contains fulvic acid in varying amounts. While the effect of one humic material over another on nanoparticle dispersions will vary, it is nonetheless a highly relevant assessment given the prevalence of humic materials in the environment and the virtual guarantee that nanoparticles will interact with them. Polyethylene glycol (PEG) was also briefly assessed as part of this work. PEG is a neutrally charged FDA-approved food additive and used widely as a drug vehicle. Thus, although not relevant for environmental release of nanoparticles, PEG is a useful neutrally charged comparator for the field of bio-based applications of nanomaterials.

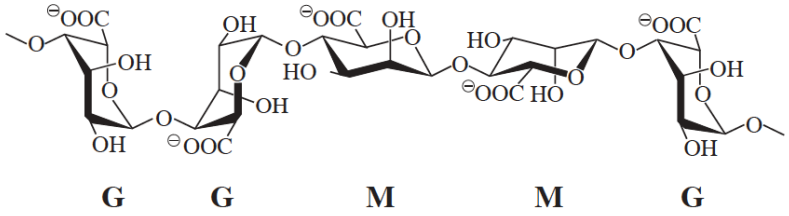


**Figure 18: Example of a segment of alginate, containing randomly order M and G blocks. (*116*)**

This part of the work consists of an exploratory look at the effects of these three stabilizers on agglomeration behavior. Among the three structures studied by us, hNi@$SiO_2$ was selected as the material with the greatest possible improvement for colloid stabilization, based on initial results from our sedimentation studies (2.4) and hence this material is studied in more detail in this section. Ni-free silica spheres were also used as test materials here, as they are expected to be fairly representative of our microemulsion-derived nanoparticles. Lastly, screening studies were done with zebrafish given that these materials might be useful in the future for stabilization of our particles during in-vivo exposure studies. These studies analyzed whether surfactants alone imparted any toxic effects on zebrafish development.

**Methods**

Dynamic light scattering was used measure agglomerate sizes of hNi@$SiO_2$ dispersed in media by sonication with alginate and humic dispersing agents (refer to methods section 2.2). Three successive measurements were done, allowing for the stability of the dispersion to be monitored. Settling studies of silica material dispersed with humic and alginate were done in UV-Vis. Exposure studies were done with zebrafish for a PEG materials with different chain lengths, humic acid, and alginate.

**Results**

Solutions of hNi@$SiO_2$ were prepared containing 50 mg Ni/L (~0.5 g/L particles, the lowest concentration used in toxicity studies in section 1.5) with either 100 ppm of alginate or humic acid. The dispersant concentrations were selected based on media concentrations used in nanotoxicological tests for zebrafish (*35*). Alginic acid and humic acid tested alone have a fairly large hydrodynamic radius at 400 nm and 250 nm, respectively, as denoted by the grey background curves in Figure 19. Successive tests done with dispersed hNi@$SiO_2$ show a clear

instability in the three successive measurements conducted, indicated by the large and unpredictable shifts in the peak center. We suspect that this instability is due to a combination of agglomeration and settling of the material immediately after the initial dispersion event. Still, from this data, one might conclude that humic acid imparts slightly more colloidal stability on the dispersion compared to alginate.

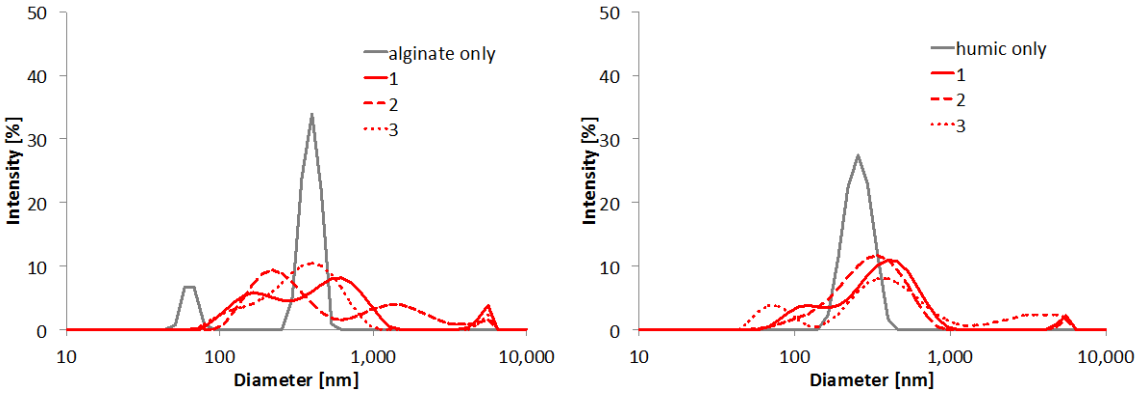


**Figure 19: DLS of hNi@$SiO_2$ dispersions in E3 containing 100 ppm alginate (left) or 100 ppm humic acid (right) as dispersing agents. (Concentration=50 ppm Ni, t=0). Solid=1st, dashed=2nd, dotted=3rd.**

Conversely, dispersions held for 24 hours exhibit better stability and more repeatable measurements, with hydrodynamic diameters of 200-600 nm and 200-400 nm in the presence of alginate and humic, respectively (Figure 20). However it is still difficult to discern whether these results can even be attributed to the nanoparticle given that the dispersant peaks align very well with the measured peaks. A small peak also occurs at near 5.5 μm, which is consistent for both materials. Finally, a comparison DLS at three time points is given (Figure 21). These data suggest that after 1 hour, the dispersion it nearly as stable as it is at 24 hours, presumably because most larger agglomerates as removed from solution by sedimentation within the first hour. Furthermore, though small, the 5.5 μm peak is consistently observed in all cases.

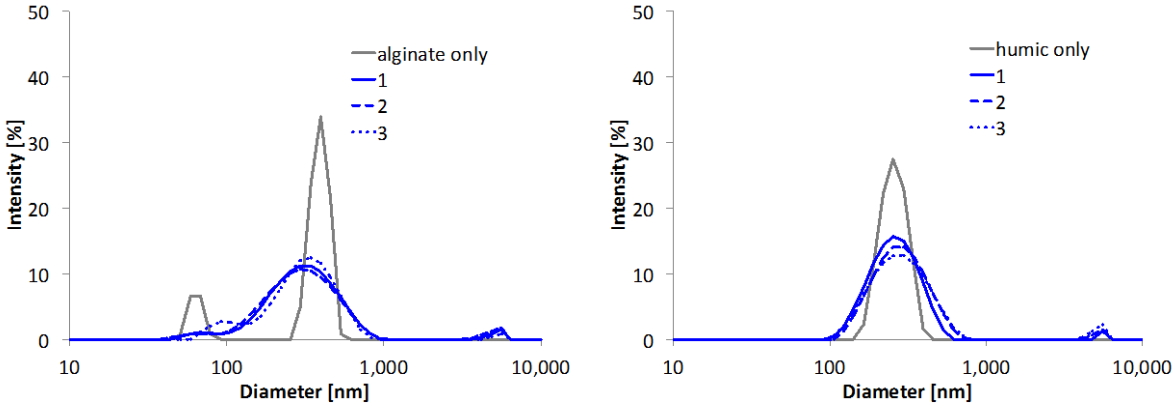


**Figure 20: DLS of hNi@$SiO_2$ dispersions in E3 containing 100 ppm alginate (left) or 100 ppm humic acid (right) as dispersing agents. (Concentration=50 ppm Ni, t=24 hr).**

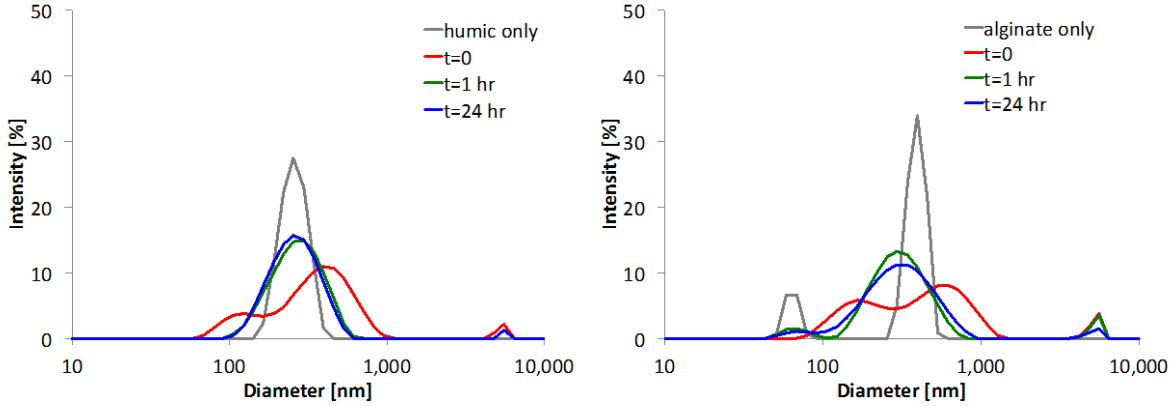


**Figure 21: Comparison of single DLS curve at time points of t=0, t=1 hr, and t=24 hr for dispersions of hNi@$SiO_2$ in E3 with 100 ppm alginate (left) or 100 ppm humic acid (right) as dispersing agents. (Ni concentration=50 ppm)**

Since settling was readily observed by the naked eye during DLS testing, additional studies were done to directly measure settling in UV-visible spectroscopy. In this case, silica was studied to gain a general perspective for each dispersant. Concentrations of 6 g/L silica and 0.5 g/L silica were tested since these also reflect the particle concentrations tested in toxicity studies in section 1.5. At 0.5 g/L there appears to be a larger population of smaller particles (<0.9 μm) in the alginate-dispersed material. Yet at 6 g/L, the populations at <0.9 μm are similar between both dispersants and the alginate-dispersed material has a larger population of >7μm

material. In material without surfactant, very large agglomerates are present and settling occur much more quickly. From this, we can gather that both surfactants improve dispersion, and that alginate may be a better dispersant at low concentrations while humic acid works better at high concentrations. However, this flip-flop behavior for the surfactants is somewhat surprising and not entirely consistent with our findings for hNi@$SiO_2$ in DLS. Hence, further studies with silica are recommended in DLS at concentration low enough that settling can be avoided.

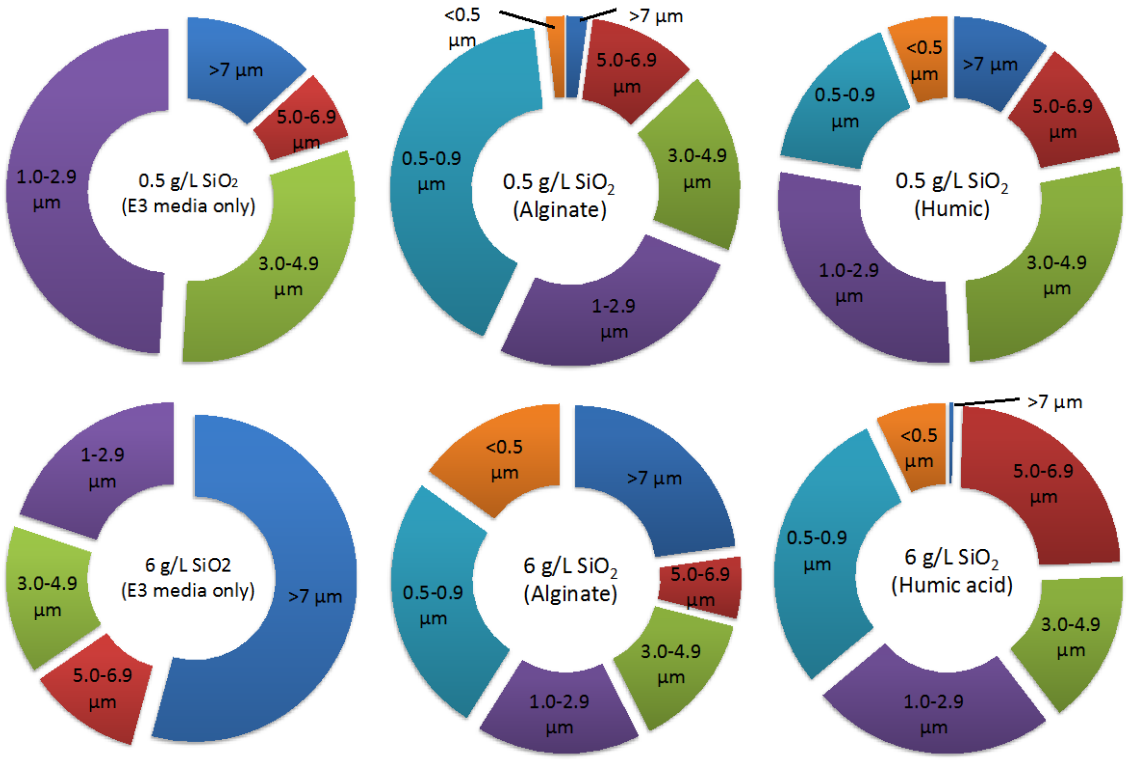


**Figure 22: Size distributions extracted from settling data measured in UV-Vis at initial concentration of 0.5 g/L and 6 g/L silica. These concentrations reflect maximum and minimum particle concentrations studied for Ni-containing nanomaterials.**

In parallel, negative control studies were done with zebrafish with a range of surfactant materials (Figure 23). Several PEG materials of different molecular weights were tested first. PEG-200 was found to have the lowest toxicity. PEG-100 and -8000 were found to be too toxic

to the fish for practical use. PEG-3000, had no effect in one study, but was observed to have a toxic effect in a follow-on test with the same material at a later date, possibly due to contamination or alternation of the material. This emphasizes the importance of regular testing of surfactant-only controls in future toxicity studies in order to avoid false interpretations of toxicity for nanoparticles dispersed with contaminated surfactants. By contrast, humic acid was found to have no adverse effect for a wide range of concentrations. Alginate was initially found to result in very low survival, but this was determined to be the result of decreased pH. In pH adjust alginate controls, no adverse effect were observed at the concentration of 0.1 g/L (or 100 ppm) used above for agglomeration settling studies.

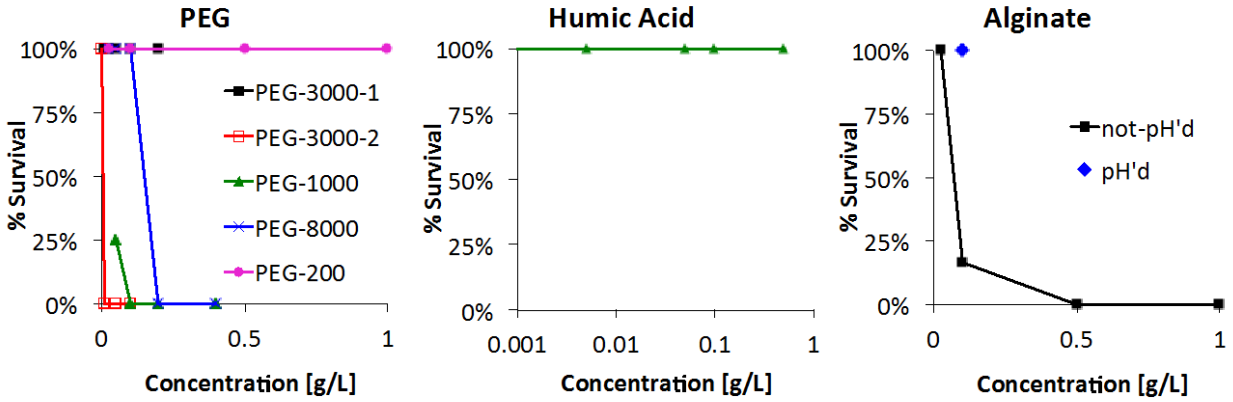


**Figure 23: Zebrafish larvae survival data from multiple surfactant and stabilizer screenings in 5-day studies conducted in 24 well plates.**

## Conclusion

Although using a surfactant or stabilizer in toxicity tests can alter the toxic effect of particles, analysis of environmentally relevant surfactants may still be important for assessment of the true fate of nanoparticles in the environment. Here, both humic acid and alginate were found to reduce the settling and agglomeration of nanoparticles in aqueous solutions in a way that would be expected to increase the amount of stable suspended nanoparticles during toxicity

tests with zebrafish. Hence, while these materials alone do not elicit a toxic effect in zebrafish, a combined effect of surfactant and particles could be possible. In this way, both humic acid and alginate are not only useful for ensuring delivery of a specific dose of nanoparticles but also relevant for predicting the fate and potential toxicity of particles in natural aqueous environments.

## 2.5 ASSESSMENT OF SILICA STRUCTURED NANO-ENVIRONMENTS FOR TOXICITY IN ZEBRAFISH


### Abstract

An *in vivo* toxicity study with 26 - 57 nm silica structured nanomaterials containing nickel nanoparticles <5 nm in diameter was conducted with zebrafish (*Danio rerio*) embryos. The results support our hypothesis that nanoparticles of toxic metals embedded within porous silica have a low toxicity. High survival as compared to analogous salt was observed for all materials tested. Although the small nickel particles are relatively resistant to dissolution in media, nickel uptake was still detectable at ng levels within the larvae tissues at the experimental endpoint despite the high survival observed. Finally, motility analysis was used as a screening tool, with an increased sensitivity compared to endpoints of survival and developmental deformations. Dose-dependent motility was observed in relation to exposure to hNi@$SiO_2$ while elevated variance was observed in the case of Ni-$SiO_2$ exposure.



***Keywords:*** nanomaterials, nanotoxicology, nanostructuring, zebrafish, nickel, motility

The emerging field of nanotoxicity continues to grapple with how to assess the potential risk of exposure to nanomaterials (*31-33*). Although environmental concentrations of nanomaterials have not been measured, the increase in production rates in recent years poses a growing exposure probability (*3, 25, 28, 117*). Meanwhile, evaluation of the toxicity of new nanomaterials consistently lags behind the development and commercialization of nano-enabled products. Nanomaterial components are often well-characterized in their bulk form, but the large surface areas, high surface energies, and unique transport and mobility at very small particle diameters present new challenges in toxicity evaluation (*25, 28, 29*). In fact, the very properties that make nanomaterials highly active and valuable in novel applications are the same properties that might impart new toxic effects at the nano-scale (*118*).

The tendency of unprotected bare nanoparticles to aggregate or sinter and deactivate necessitates the design of multi-component materials comprised of active nanoparticles embedded within a protective matrix, hence ensuring favorable dispersion and stability of the active particle (*119*). Extremely small particles, which are of special concern in the field of nanotoxicity, are also are the most likely to require such nano-structuring stabilization. Here we approach the problem of nanotoxicity from the perspective that nano-enabled products will most often be in this nano-supported form, and conduct a toxicity screening using zebrafish as a model. Our over-arching hypothesis is that silica structuring of metal nanoparticles will result in materials with a low toxicity, i.e. we aim to take a 'benign by design' approach to nanomaterial synthesis and development.

Nickel is a common material for industrial catalysis and considerable work has been done to develop nano-scale Ni-containing materials for various purposes (*120, 121*). Yet nickel is also a recognized even in its bulk form as toxin and its toxicity has been confirmed previously in

zebrafish studies, where soluble nickel has been shown to delay hatching of embryos (*45, 46*) and to decrease locomotive activity at levels of 7.5 – 15 mg Ni/L (*47*). Furthermore, Ispas and coworkers found that nickel nanoparticles with diameters of 30-100 nm had a lethal concentration 50 (LC50) in zebrafish of 221-361 mg Ni/L compared to 221 mg Ni/L for soluble nickel (*48*). A study with *Daphnia pulnex* (water flea) using sub-10 nm nickel particles (a size much more relevant to observe any nano-specific toxicity (*6*)), found that LC50 values after 48-hr exposures were slightly above those for soluble nickel (*49*). In a final study, an elevated toxicity from 5-20 nm nickel nanoparticles compared to other metals in multiple organisms was purported to be a result of a high dissolution of nickel ions into the media and not any nano-specific effect (*50*). These studies collectively indicate that nickel nanoparticles can be a useful starting point to develop a toxicity screening model since the toxicity was previously measured for multiple diameters of bare nickel nanoparticles and since nickel dissolution was cited as a possible underlying mechanism for toxicity.

We propose in this work the use of structuring with porous silicon dioxide ($SiO_2$) to mitigate toxicity. Structuring with silica is a highly transferable approach for particle stabilization that has relevance in many areas (*122*). Silica coatings are applicable to virtually any metal nanoparticle (*14, 56*), highly robust against thermal and mechanical stress, considered biocompatible (*59*), and can be resistant to biological degradation. These attributes have made them of interest for drug delivery, sensors, and catalysts (*67, 123-128*) and porous silica coatings have been already been reported in a few cases for the intended mitigation of nanoparticle toxicity (*57, 58*).

The growing use of nanomaterials is likely to lead to increased contamination of aquatic environments, thus emphasizing the importance of studying nanoparticle toxicity in these

systems. Zebrafish studies have emerged as a comparatively fast and well-developed toxicological assessment model (*25, 28, 129, 130*). Early embryogenesis in both zebrafish and mammals is governed by common molecular mechanisms, such that insights into normal vertebrate development can arise from studies using zebrafish (*131*). The zebrafish also offers a uniquely accessible model for experimental manipulations due external embryonic development, embryo transparency, and prolific breeding. These factors combine to make zebrafish studies well suited for accelerated screening purposes. We synthesized and characterized three different types of silica-structured nickel nanoparticles for a toxicity screening using zebrafish. Toxicity testing consisted of 5-day exposures to nanoparticles dispersed in fish media followed by measurement of nickel uptake and zebrafish motility.

**Methods**

*Hollow Ni@$SiO_2$ (hNi@$SiO_2$)* materials were made using a one-pot reverse microemulsion synthesis adapted from Takenaka, et al. (*68*), consisting of several step-wise additions. First, 50 mL of cyclohexane (≥99% Sigma-Aldrich) and 10.5 g surfactant Brij 58 (≥99% polyethylene glycol hexadecyl ether, $M_n$ ~1124, Sigma-Aldrich) was refluxed at 50$^oC$ until the surfactant was fully dissolved. 1.5 mL of 1 M $Ni(NO_3)_2 \cdot 6H_2O$ (99.999%, Sigma Aldrich) was then added dropwise, followed by 1.5 mL hydrazine hydrate (Sigma-Aldrich). Next, 3-5 g of tetraethylorthosilicate (TEOS, ≥99% Sigma-Aldrich) was added, followed by 3 mL of ammonium hydroxide (30%). After 2 hrs of aging for silica growth, particles were precipitated and washed three times with 2-propanol, and dried in air. Crushed powder was calcined in a Thermolyne 79300 tube furnace for 2 hrs at 500$^oC$ in air.

*Non-hollow Ni@$SiO_2$ (nhNi@$SiO_2$)* nanoparticles were made by a simple modification of the hNi@$SiO_2$ method by exclusion of hydrazine addition. Precipitated material was dried and

calcined as described above. In order to remove external nickel from these materials, calcined particles were reduced and etched in nitric acid. Specifically, 0.20 g of material was dispersed in a 1:1 volume dilution of nitric acid (Sigma, 70%) in DI water for 30 min. Etched materials were washed twice in water to neutral pH, dried, and calcined.

For surface-deposited *Ni-$SiO_2$*, nickel-free spherical silica spheres were first synthesized using the microemulsion hNi@$SiO_2$ procedure except 1.5 mL DI water was added in place of the aqueous salt and hydrazine was excluded. A deposition-precipitation method (modified from (*73*)) was used to deposit nickel nanoparticles on the surface of the silica spheres. 0.6 g of silica nanoparticles was dispersed in 15 mL of DI water by sonication, a nickel salt solution was added (0.55 g $NiCl_2$ in 10 mL DI water), and the mixture was again sonicated for 20 min. Ammonium hydroxide (30%, Sigma) was then added slowly dropwise (~5 mL) until the pH of the solution was ~9.5. The resulting material was mixed for 20 min, centrifuged, dried, calcined at 300$^{o}$C in air, rinsed two times in DI water, dried, and calcined again at 300$^{o}$C in air.

All materials were characterized for particle size and morphology with transition electron microscopy (TEM, JEOL-2000FX electron microscope). Typical sample preparation consisted of grinding the sample in a mortar, dispersed in ethanol, ~2 min sonication, and placement of 1-2 drops of the dispersion on copper type-B support grid (Ted Pella, Inc.) to dry in air. Particle measurements of TEM images were done using ImageJ software (http://rsb.info.nih.gov/ij/). Scanning Electron Microscopy (SEM) equipped with EDX Genesis was used to determine elemental composition of palladium-coated samples at beam voltage of 15kV, spot size 4 (typically). An average of at least 3 composition measurements was used for each sample. Catalyst surface area was determined by Brunauer Emmett Teller (BET) analysis (Micromeritics ASAP 2020 surface area and porosity analyzer), after a pre-treatment of 2-3 hr degas at 200$^{o}$C

under vacuum. Typically, a 6-point BET analysis was used for total surface area measurement. Media dispersion of nanoparticles were tested at room temperature by dynamic light scattering (DLS, Zetasizer Series Nano-ZS) to estimate the hydrodynamic diameters in E3 media (49 mM NaCl, 1.6 mM KCl, 3.3 mM$CaCl_2 \cdot 2\ H_2O$, 3.3 mM $MgSO_4 \cdot 7\ H_2O$, pH 7.4). The samples were first dispersed for ~2 min by sonication in media and then ~1 mL of dispersed solution was added to a plastic cuvette. A target of 5 mg Ni/L (~0.5 g/L particles) was used, which was adjusted if a higher particle count was needed for analysis of a particular material. Trace metal ion concentration was measured under radial detection by ICP-AES (Thermo Electron Corporation iCAP6500 Duo Series ICP-OES Spectrometer). A standard curve was generated with at least 3 standard solutions that captured the sampling range. Standards were formulated from an ICP standard solution (Fischer Scientific) with 3% $HNO_3$ in deionized water. Three measurements were collected for calculation of a mean and an internal blank and standard were used in each sampling period. The degree of nickel ion dissolution from the nanoparticles in E3 media was determined with ICP. Dispersions (typically, 50-200 mg Ni/L) were prepared in E3 media and separated into 10 mL aliquots for analysis at specific time points. Metal nanoparticles were removed from the dispersion by centrifugation followed by filtration (Amicon 10,000 molecular weight cut-off filters, ~3.1 nm). $HNO_3$ (Sigma, 70%) was added dropwise to the filtrate to a concentration of 3wt %. The amount of dissolved nickel available in each well [ng/well] (and hence available to each fish in each well) was calculated via:

*[mg Ni/well]=Dissolved Ni concentration [mg Ni/L] x 0.002 L/well*

For in-vivo zebrafish studies, metal nanoparticles and homologous salt solutions were prepared in E3 media at multiple concentrations. Dried nanoparticle powder was weighed according to a specific dose, added to E3 media, and sonicated ~20 min. Serial dilutions were

then prepared volumetrically using this first dispersion. To conduct exposures, 24 hours post fertilization (hpf) embryos were manually de-chorionated with tweezers and healthy fish was transferred to each well (1 fish/well) of 24-well polystyrene plates. Residual water was removed with a pipette. Dispersions were re-dispersed by sonication for 1-2 minutes just prior to addition to each well. Fish were incubated for 5 days at 28.5$^{o}$C and analyzed visually each day for survival and developmental deformations. 6 – 18 embryos were typically tested at each dose, depending on the embryos available in a given clutch. For selected materials motility analysis was done. For these cases, surviving fish were collected at day 4, washed three times to remove residual particles, and re-plated in 96-wells plates. Fish movement after nanoparticle exposure was then captured by video on day 5 after an overnight stabilization period. Zebrafish motility tracking included light exposure (1 hr) followed by 10 min light/dark cycles (1 hr). Each video file was processed using LSRTrack and LSRAnalyze. These are MATLAB scripts developed within the laboratory to quantify motility of zebrafish embryos from video files (*79*, *80*). The analysis allows calculation of the velocity for each fish or the mean velocity of fish at an exposure dose. Animals not analyzed for motility were collected upon termination of the experiment (day 5) to measure cumulative metal uptake. Larvae were transferred to clean 12 well plates in groupings by dose and fresh E3 media was added to rinse residual particles from the fish. Fish were sacrificed with a 10% bleach solution according to the operational protocol and again rinsed with E3 media. Residual media was removed and fish were dried in air. A digestion procedure by Borgmann et al., 2000 was used (*77*) beginning with addition of nitric acid (12.5 µL/fish, 70%, Fischer Scientific) followed by at least 1 week digestion and then addition of hydrogen peroxide (10 µL/fish, 30%, JTBaker), followed by 24 hrs digestion. Digestion reagents are not expected to contribute a significant amount of Ni to the sample and

polypropylene storage containers used are expected to resist nickel adsorption (*78*). Resulting solutions were diluted with deionized water for measurement of the nickel concentration in ICP. Uptake [ng/fish] was calculated as follows:

*Concentration [mg Ni/L]* x *Dilution volume [L]* x *(1E6 ng/mg)* x *(1well/1fish)* / *# of fish*

**Results**

The Ni-containing nanoparticles used for exposures included hollow core-shell Ni@$SiO_2$ (hNi@$SiO_2$), non-hollow Ni@$SiO_2$ (nhNi@$SiO_2$), and nickel-deposited Ni-$SiO_2$. TEM micrographs are given in Figure 24. hNi@$SiO_2$ materials consisted of an inner layer of particles within the hollow interior of a silica sphere with primary particle sizes of ~26 nm. The sub-2nm nickel nanoparticles in this material were too small to measure in TEM. nhNi@$SiO_2$ material contained ~3 nm Ni particles and ~50 nm primary particles. Lastly, Ni-$SiO_2$ had a primary particle size of ~57 nm, which was then decorated by ~2 nm nickel nanoparticles. Overall the materials vary slightly in particle size and composition but nickel nanoparticles are all ≤2 nm with primary particle sizes <60 nm. BET surface areas were 200-300 $m^2/g$ and the silica microstructures were confirmed to be porous, as shown in Figure 25.

These materials were observed to agglomerate and settle in aqueous solutions and hydrodynamic diameters measured in DLS were >300 nm (see section 2.3). Dissolution of nickel ions from the materials was measured in media solutions over the course of 5 days. 5-8% dissolution to nickel ions was recorded and Ni-$SiO_2$ materials were found to have the highest degree of dissolution. These material attributes are summarized in Table 2.

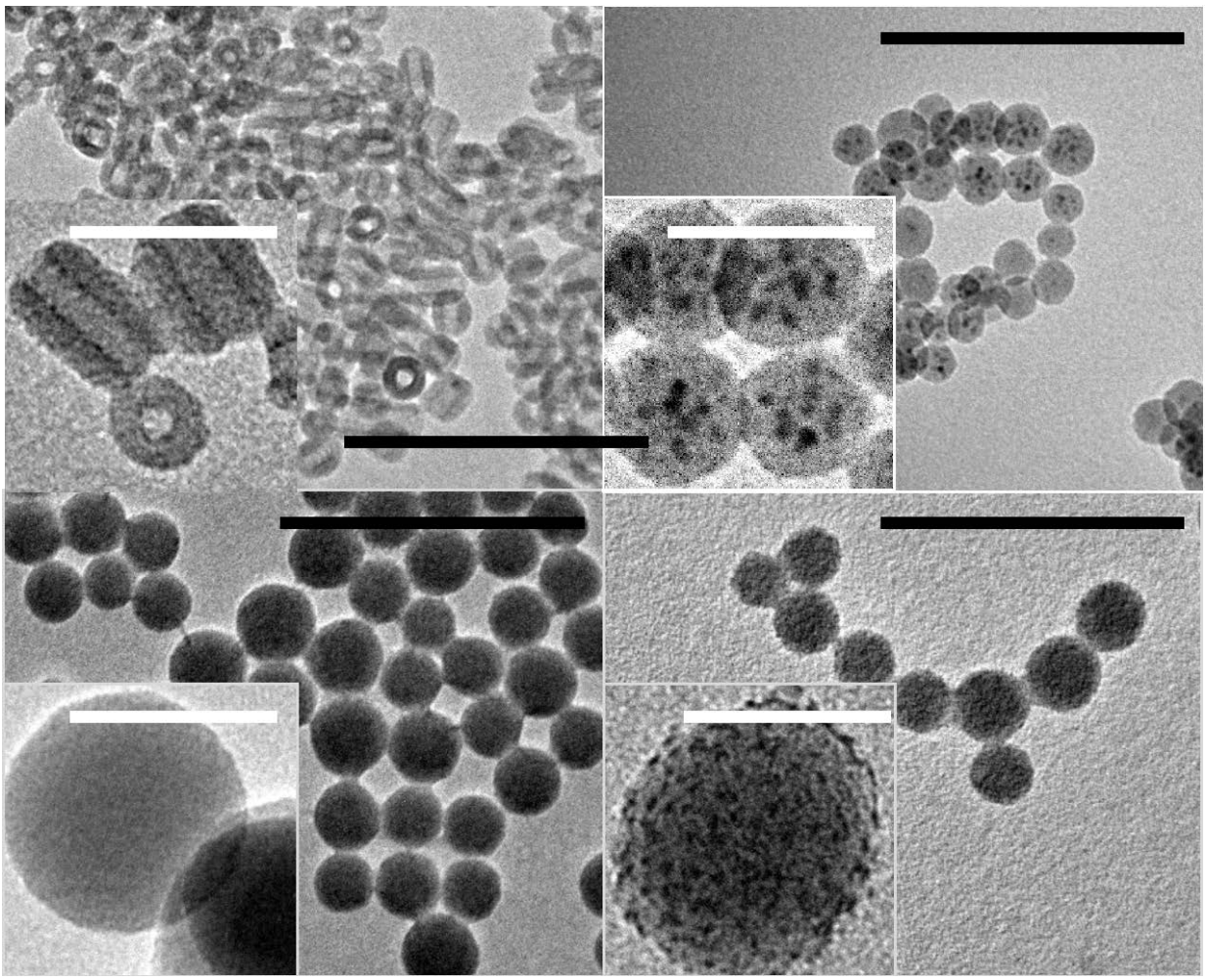

**Figure 24: *h*Ni@$SiO_2$ (top left), *nh*Ni@$SiO_2$ (top right), metal-free $SiO_2$ (bottom left), and Ni-$SiO_2$ (bottom right). Scale bars are 50 nm for insets (white) and 200 nm for larger images (black).**

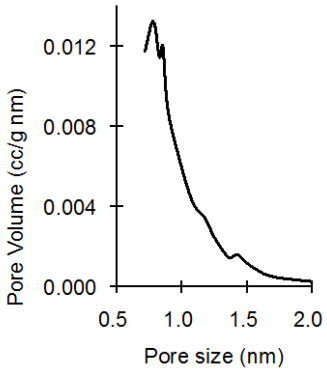


**Figure 25: Typically BET $N_2$ desorption curve showing ~0.7 nm pores**

**Table 2: Material attributes for as–synthesized Ni-containing nanomaterials**

| Material | Ni loading [wt% Ni] | $D_{Ni\ nanoparticle}$ n= # particle | $D_{primary\ particle}$ n=# particle | $D_{hydrodynamic}$ (main) in E3 at 5[1] or 20[2] mg Ni/L, PDI=polydispersity index | % Dissolution in E3 at 50 mg Ni/L |
|---|---|---|---|---|---|
| *h*Ni@$SiO_2$ | 9.0 ± 0.9 | <2 nm* | 25.9 ± 3.0 nm, n=16 | 641 nm, PDI=0.557[2] | 5% |
| *nh*Ni@$SiO_2$ | 5.1 ± 0.4 | 2.7 ± 0.4 nm, n=20 | 46.2 ± 6.5 nm, n=13 | 350 nm, PDI=0.630[2] | 5% |
| Ni-$SiO_2$ | 11.9 ± 3.2 | 2.1 ± 0.4 nm, n=23 | 56.5 ± 8.2 nm, n=12 | 514 nm, PDI=0.369[1] | 8% |

*resolution too low for measurement

5-day toxicity studies with zebrafish embryos for doses of 50-400 mg Ni/L yielded very high survival while the positive control of $NiCl_2$ caused high toxicity. (The 400 mg Ni/L dose was not tested for Ni-$SiO_2$ and hNi@$SiO_2$ due to insufficient amount of material). Survival rates in E3 media alone for all experimental control fish combined was 99% (n=202). Survival was marginally lower (95% and 96%, respectively) for nhNi@$SiO_2$ and Ni-$SiO_2$ at 50 mg Ni/L, but still within standard error of the media control. Additional control tests with nickel-free silica nano-spheres shows 100% survival up to 2 g/L, capturing the range of particle sizes expected in the tests with Ni-containing materials, as shown in Table 3.

**Table 3: Corresponding particle concentrations for representative batches of Ni-containing nanoparticles and silica control materials**

| Nanoparticle | Approx. Ni loading [wt% Ni] | Experimental Dosing [mg Ni/L] | Particle Concentration [g/L] |
|---|---|---|---|
| *h*Ni@$SiO_2$ | 10 | 50-200 | 0.5-2 |
| *nh*Ni@$SiO_2$ | 10 | 50-200 | 0.5-2 |
| Ni-$SiO_2$ | 12 | 50-200 | 0.4-1.7 |
| Silica | N/A | N/A | 0.5-2 |

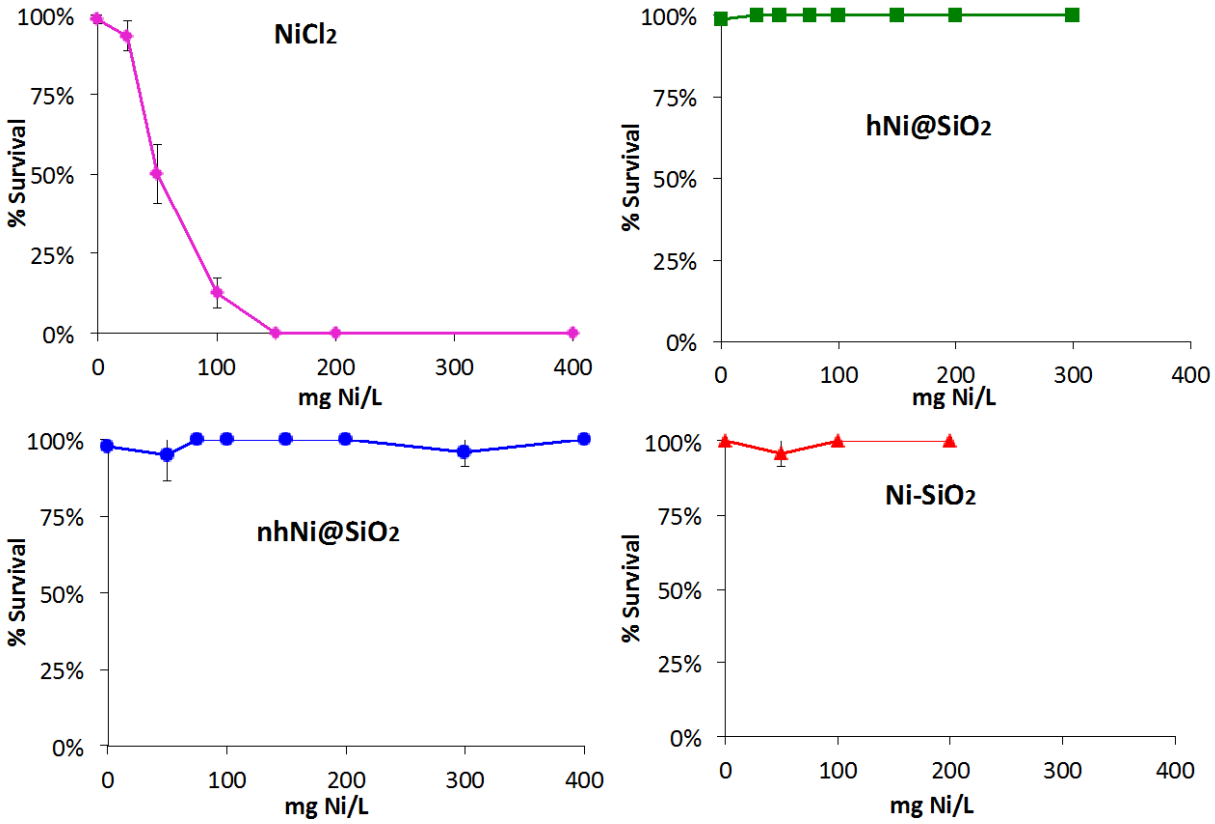


**Figure 26: Day 5 survival for 3 materials: $NiCl_2$, $hNi@SiO_2$, $nhNi@SiO_2$ and Ni-$SiO_2$. Error bars show standard error of the estimate.**

In parallel, uptake of nickel was measured for groupings of surviving fish at each exposure dose for each material type. Here, we observed ng/fish levels of nickel uptake with no obvious indication of dose-dependence (Figure 27). The uptake values are compared graphically with estimates of dissolved nickel ions in each well based on measurements from separate abiotic dissolution tests on nanoparticles at initial concentrations 50 and 200 mg Ni/L (see section 2.3). The amount of nickel ions available/well was roughly 2 orders of magnitude higher than the uptake observed for nanomaterials and roughly 3 orders of magnitude higher for $NiCl_2$. To see this effect more clearly, a value for 'uptake efficiency' was calculated, based on the ratio

between the uptake measured in fish and the estimated amount of nickel ions available in the wells by dissolution. This calculation was done at 50 mg Ni/L, the only concentration at which the uptake data for the $NiCl_2$ and the particles overlapped. As shown in Figure 28, the 'uptake efficiency' is slightly lower for the nickel salt versus the particles. This difference suggests that another mechanism of uptake (i.e, transport of nanoparticles or agglomerates into the fish tissues) could be active. However, we should note that the difference could also arise from a toxicity-induced biological difference. Finally, it is intriguing that the uptake values are similar at all doses (~20-80 ng/fish) with only a very slight upward trend at higher doses. One explanation for this could be that despite different dosing targets, material sedimentation leads to a similar effective exposure concentration within the upper water column for all concentrations. Recalling that nhNi@$SiO_2$ was slightly more resistant to sedimentation, the slightly higher uptake efficiency for this particular material is notable as well.

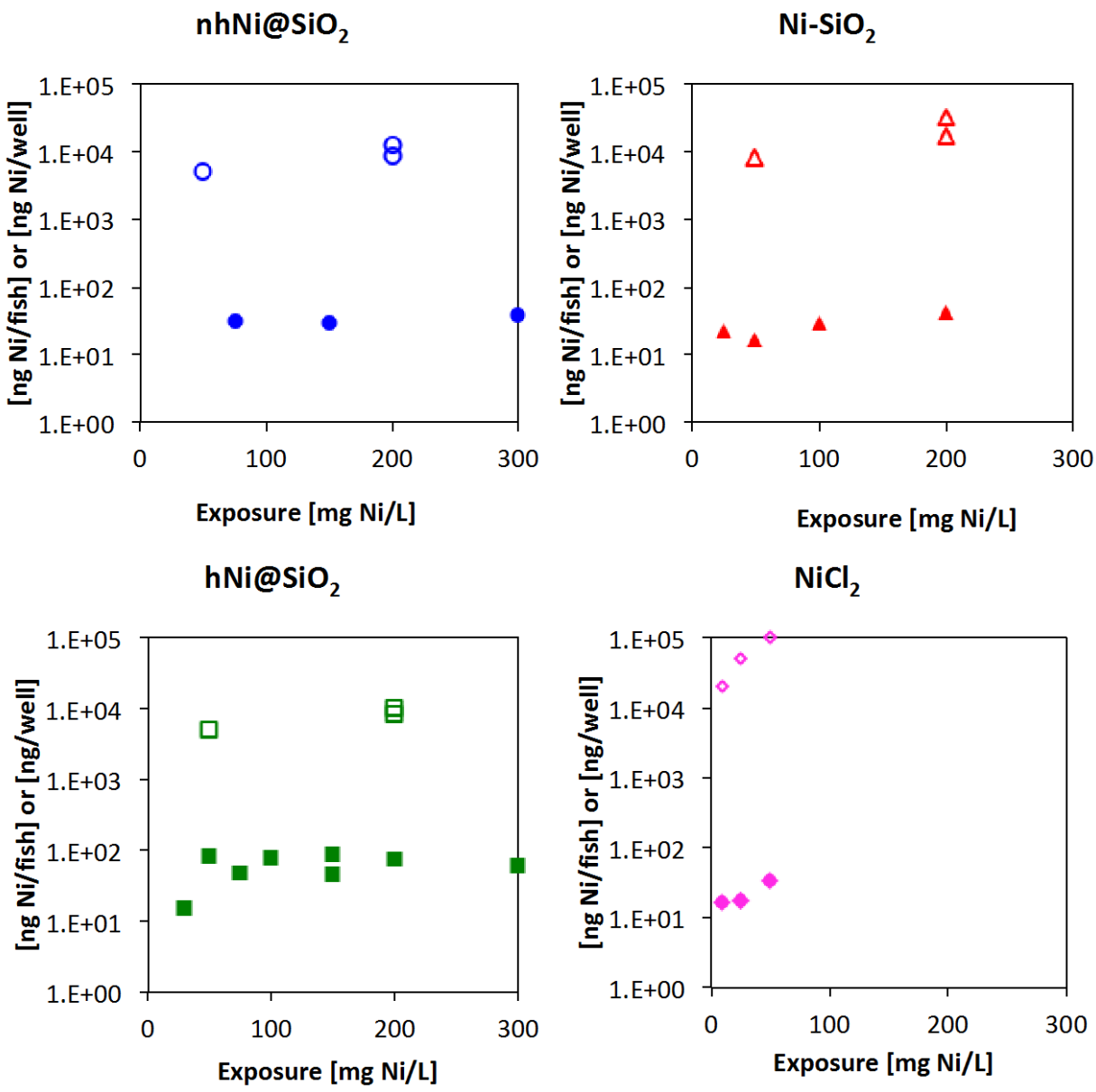


**Figure 27: Uptake of Ni into zebrafish following 5-day exposures (filled symbols) and available Ni/well according to dissolution testing at specific doses (open symbols).**

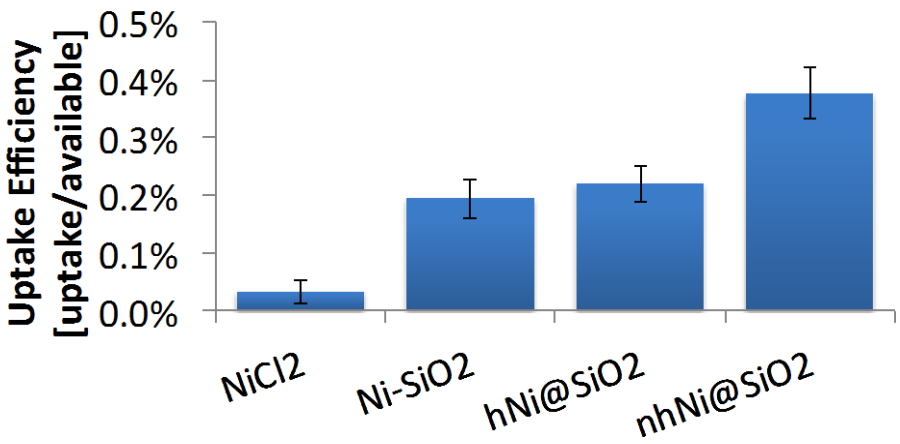


**Figure 28: Uptake efficiency of $NiCl_2$ compared to Ni-containing nanomaterials at 50 mg Ni/L exposure. Error bars reflect the combination of the standard error of the estimate from ICP standardization curve, % relative standard deviation from ICP measurement, and dilution error from centrifuge tubes.**

Fish were also monitored for malformations. Metal nanoparticles have been shown to cause a range of developmental defects in zebrafish (*18*) and bent spines, tissue necrosis, and edema of the head, heart, and gut are common Ni-related malformations (*132*). Although several incidences of these types of malformations were observed as a result of exposure to soluble nickel (see Figure 29 for an example), very few malformations were seen with all nanomaterials exposures (Figure 30). It should be noted that for very high doses of $NiCl_2$, a decrease in the percent of malformations is expected given that at these doses fish often do not survive until the first day for the experiment for the malformation to develop and be observed. An average malformations occurrence of 3% (n=184) and 5% (n=41) was determined for negative controls of E3 media and silica, respectively. Thus the number of malformations observed for Ni-$SiO_2$ and hNi@$SiO_2$ are roughly in line with the control observations while nhNi@$SiO_2$ malformations were slightly higher (near 10%) for several doses. Hence, by comparing our observations for survival and malformations, the latter endpoint emergences as a slightly more sensitive metric for detecting toxic effects between materials.

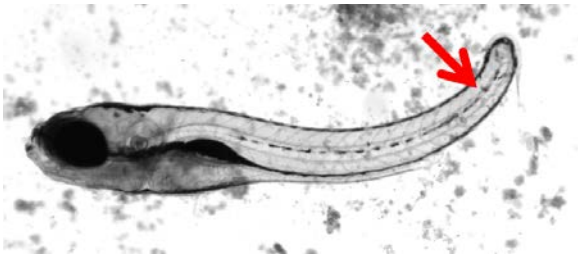

**Figure 29: Example of 'bent spine' malformation in zebrafish embryos**

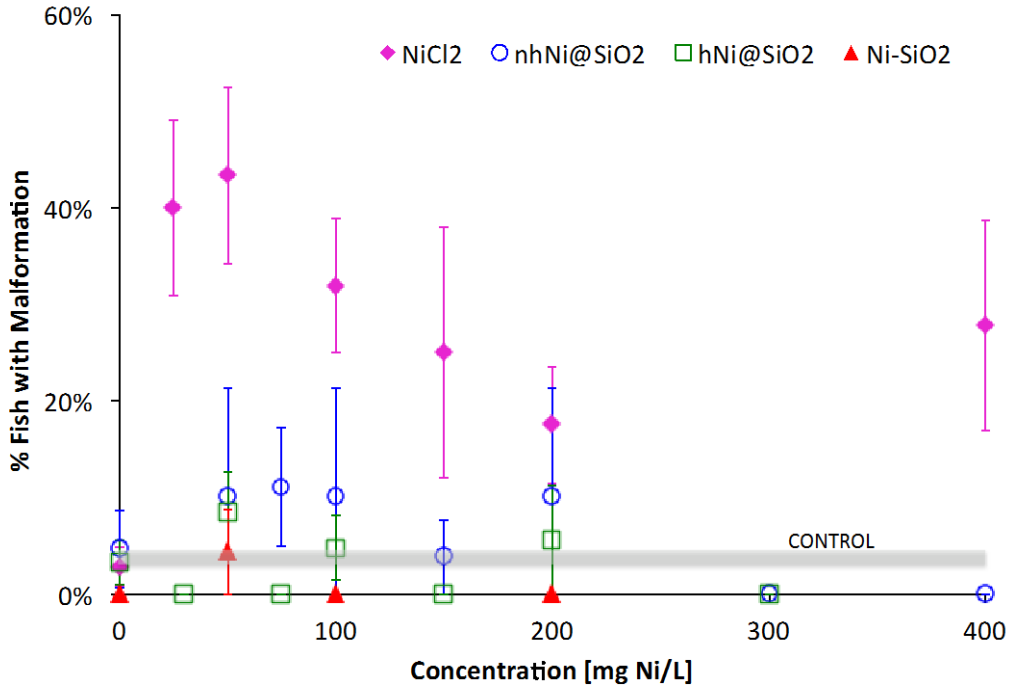


**Figure 30: Frequency of deformities at any time in 5-day study (#observed with deformations at a given dose/# fish test at a given dose)**

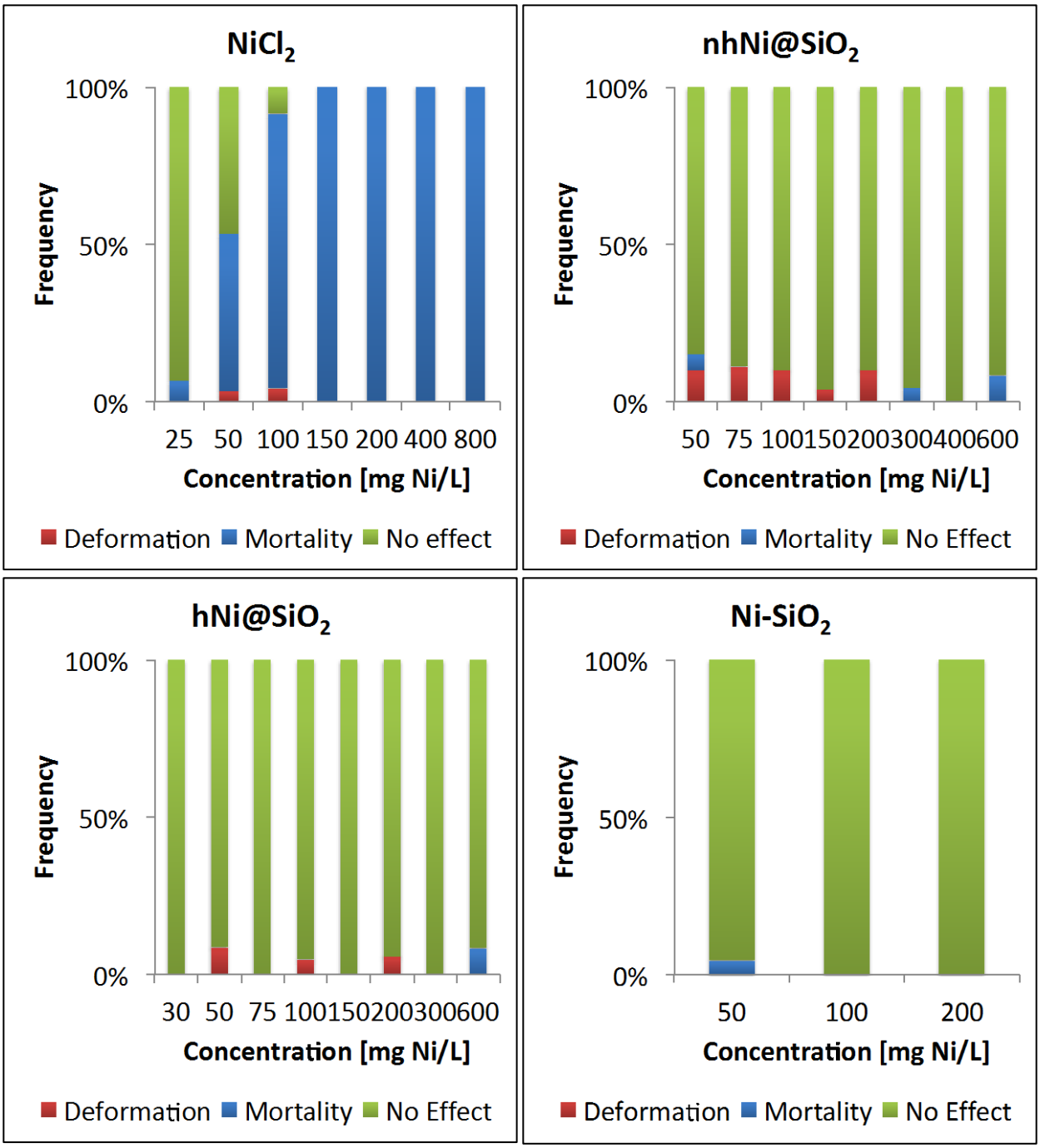


**Figure 31: Effect of nanomaterial exposure on frequency of malformations and mortality. Data reflects day 5 data for several exposure experiments at a range of doses. No effect designated that neither malformation of mortality was observed after 5-day exposure.**

The malformation results can be viewed a bit more clearly by comparing the frequency of malformations with the frequency of mortality at a given dose (Figure 31). For $NiCl_2$ exposure, more malformations are observed at lower doses (25-50 mg Ni/L). At higher doses, the higher mortality rate can prevent these deformations from being developed and observed prior to death of the fish, resulting in a lower incidence of malformations at higher doses. A similar trend is observed for the nhNi@$SiO_2$, where a higher frequency of malformations is seen at lower doses, but the mortality rate is not very high for the particles, as discussed previously. Again, recalling that the lower rate of sedimentation for this material would result in a higher effective dose in-vivo, it is interesting that the nhNi@$SiO_2$ material also had an elevated rate of deformation. Meanwhile, results for hNi@$SiO_2$ and Ni-$SiO_2$ are less conclusive, showing a low frequency of malformations that is near the frequency observed with control fish exposed to media or amorphous silica spheres alone.

To this point, we measured only a slight difference in the toxic response between materials based on deformations, and virtually no difference in terms of survival. And yet our studies of nickel uptake indicated that the amount of nickel exposure to fish tissues via nickel uptake was not necessarily dissimilar to that of the nickel salt, which did have an obvious toxic effect. Since previous studies had indicated an effect on motility following exposure to nickel salt (*47*), and we had seen evidence of significant variability in the nickel dissolution between each material and each dose, we decided to quantify the motility of the zebrafish larvae at the experimental endpoint. Motility studies were conducted on 2 of the 3 materials discussed in this study. Only 2 materials were selected since the analysis requires a sufficient number of fish for each dose (~7-8) and multiple controls groups were included for comparison. Ni-$SiO_2$ was selected for this analysis since this material exhibited the highest amount of dissolution, which

has previously been cited as a mechanism of toxicity of nickel particles. hNi@$SiO_2$ was selected as a suitable comparator for this material, since it exhibited less dissolution but had more similar agglomerate sizes compared to nhNi@$SiO_2$. Groups of 7-8 fish were used for each dose, and motility was measured first for 1 hr under light exposure and then 1 hr under 20 min light/dark cycles. Figure 32 shows mean velocities for each exposure group both as raw data and processed as time averages velocities to better allow for trend assessment. The axis is given as the video frames collected in the experiment, where 7200=1hr and 14400=2hrs according to the frame rate of 2 frames/sec. During the first hour of light exposure, swimming was expected to be relatively flat (refer to negative controls of E3 media and silica). Upon exposure to the first dark cycle, the swimming velocities increased and then re-stabilized, typically in a linear fashion. Similarly, at the start of a light cycle, the swimming velocity drops, and then recovers. By this, the strong response during the light/dark 'perturbation' cycles and the variance in the light exposure can be used as a metric in our study to inspect for a toxic effect.

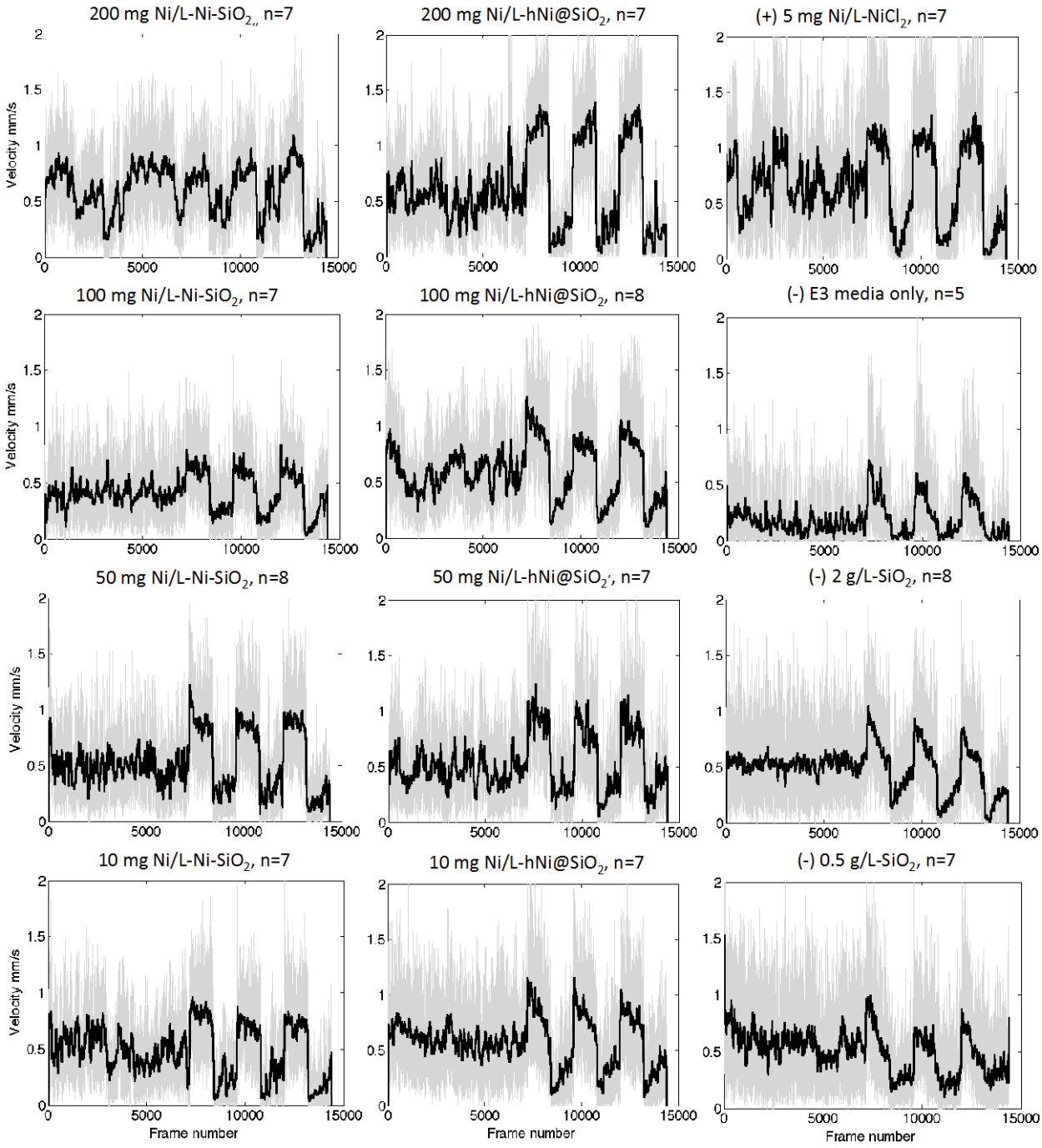


**Figure 32: Zebrafish motility in terms of group mean velocity for each video frame (2 frames/sec) after Ni-$SiO_2$ and hNi@$SiO_2$ exposures as compared to controls of (-) E3 media, (-) silica particles, and (+) analogous nickel salt**

A positive control of 5 mg Ni/L was selected as a value close to the Ni dissolution expected from the highest particle doses of during the experiment. Motility is relatively high for positive controls of nickel salt and low for E3 media and silica controls, while most of the motility data for nanoparticles (NP) fell somewhere in the middle of these control exposures. A higher degree of variability was also noted during the light exposure for the nickel salt. This particular phenotype is also reflected in the 200 mg Ni/L particle exposures, especially in the case of Ni-$SiO_2$. Finally for the hNi@$SiO_2$ materials a slight dose-dependence is apparent by the progressively more pronounced up-swings and down-swings in mean velocity at higher doses during perturbation cycles. In sum, the higher nickel dissolution for Ni-$SiO_2$ compared to hNi@$SiO_2$ did not directly lead to an obvious motility effect for this material. But clear differences were seen at higher doses that were similar to the positive control of nickel salt. Additional studies of fish motility are currently underway with to further elucidate the results of this initial study by testing for the reproducibility of the data and allowing for a more rigorous quantification of the motility effects observed.

**Conclusion**

Overall, our studies of Ni-containing nanostructured materials do suggest that incorporation of silica coatings can mitigate nanomaterial toxicity as demonstrated by the high survival measured in the range of 50-200 mg Ni/L. By comparison, LC50s concentrations of 200-300 mg Ni/L have been measured for much larger 30-100 nm nickel nanoparticles (*48*). However, since the majority of our silica nanostructured particles typically settled in <24 hrs during *in-vivo* exposure studies and fairly large agglomerate sizes were measured in DLS, we must also acknowledge that the effective exposure dose of dispersed particles were lower. Beyond survival, a greater incidence of malformations was observed for nhNi@$SiO_2$, the

material with the smallest agglomerates, and presumably the highest effective dose within the water column after settling. Next, dissolution and uptake studies revealed that the nickel uptake efficiency (uptake versus nickel ions available) for particle exposure was slightly higher than that of the analogous salt. In other work, there is evidence that uptake of nickel particles occurs up to 7.97 ± 3.76 ng Ni/embryo for 60 nm particles and 1.69 ± 1.29 ng/embryo for dendritic particle exposures, but our measurements of 20-60 ng/embryo were considerably higher (*48*). This higher level of uptake compared to previous work could be accomplished by a 'Trojan-horse' type mechanism of particle uptake across cell membranes followed by nickel particle dissolution, thereby concentrating nickel in the fish tissues. Since gill filtering and feeding do not develop until later, most of the exchange with the environment at this stage occurs across the epidermal, a more permeable membrane (*40*, *133*, *134*). Still, it is still not clear why our similar sized materials (~60 nm) might have more uptake than nickel particles and it is curious that these higher levels of uptake are not linked any strong toxic effects.

Finally, in studies of motility, which were introduced here as a more sensitive metric for toxicity compared to survival and malformation, slight dose-dependence was observed during light/dark perturbation cycles for hNi@$SiO_2$ exposures. For Ni-$SiO_2$, no clear dose-dependence was observed, but the higher variance seen at higher dose during light exposure could be an indicator of an adverse effect for this material. For both materials, similar behavior was seen compared to the positive control of nickel salt. However, further development of the motility metric is still needed to better quantify the statistical significance of these observations. Still, our use of motility studies to measure toxicity represents an important benchmark for zebrafish as a screening tool. Motility analysis could serve as a broadly applicable and sensitive toxicity detection tool in a way that might facilitate high-throughput toxicity screening. As

nanomaterials continue to be developed at an ever-increasing pace, these tools will be critical to meet the challenge of assessing complex nanostructures and identifying structural aspects that are important in mitigating toxic effects.

## 2.6 NANOTOXICITY CONCLUSION

In this work, we set out to synthesize Ni-containing silica-structured nanomaterials with inherently low-toxicity. While nickel particles are recognized as toxic, our goal was to incorporate silica in a way that mitigated this toxicity. Three nanomaterials were made: hollow Ni@$SiO_2$, non-hollow Ni@$SiO_2$, and Ni-$SiO_2$. The materials were first studied in detail in media solutions to determine upfront if specific structural aspects can act as predictors of environmental fate and, ultimately, nanomaterial toxicity. One common mechanism of toxicity is dissolution of metal ions into media solutions. Nickel dissolution was slightly elevated in our materials as compared to previous reports for larger Ni-only particles. Differences between the dissolution trends of our materials were attributed to concurrent dissolution of amorphous silica into the media solutions. Specifically, core-shell hNi@$SiO_2$ and nhNi@$SiO_2$ structures were found to be subject to a higher degree of silica dissolution, making the nickel particles within these materials more susceptible to dissolution over time. This was especially true if the initial particle concentration was low since this led to a greater driving force for silica dissolution. This is in contrast to Ni-$SiO_2$ materials, which were surprisingly resistant to silica dissolution, possibly due to a higher population of crystalline nickel silicate 'shields' on the surface of this material, which would be expected to prevent dissolution of the centrally located amorphous silica. Nonetheless, since Ni-$SiO_2$ contained externally located nickel nanoparticles, which were more accessible to solvation by the media, these nanomaterials ultimately had the highest nickel dissolution among all of the materials. However, we might expect that for lower doses, the

amount of nickel dissolution would be become more similar for each of the particle types, as was observed between initial doses of 200 mg Ni/L and 50 mg Ni/L.

Next, particle agglomeration and settling was studied. Large agglomerates were observed to develop in solution, even in the very dilution solutions studied in DLS. Agglomerate-driven settling was further characterized in UV-Vis, which in turn allowed an estimate of agglomerate sizes for larger particle concentrations as well. In this part of the work, dispersions of nhNi@$SiO_2$ stood out as the most stable and with the smallest agglomerate size. From this perspective we might hence predict a higher toxic effect from exposure studies with zebrafish to these materials given that a larger proportion of the target dose is expected to stay suspended in solution. A small study was also included on the effects of stabilizers on these materials. It was found that addition of both humic acid and alginate made nanoparticle dispersions more resistant to settling and reduced agglomerate size. Additionally, zebrafish exposures to media containing these environmentally relevant stabilizers exhibited no observable toxic effect. Therefore, future studies might benefit from incorporation of such stabilizers, which would be expected to increase the amount of suspended particles in solution and reduce the agglomerate sizes thereby achieving exposure closer to the nanoparticle dose intended for a given study.

Finally, 5-day exposure studies with zebrafish embryos were done with each of the three nanomaterials synthesized for this work. High survival was observed after exposure to doses of 50-400 mg Ni/L. Slightly higher malformations were observed as a result of exposure to nhNi@$SiO_2$ materials. Motility studies were introduced a new method for toxicity screening. Dose dependence during light/dark cycles was observed following exposure to hNi@$SiO_2$ and a higher variance during light exposure was seen for higher doses of Ni-$SiO_2$.

Lastly, a significant effort was put forth in this work to develop suitable methods to study complex nanomaterials from the perspective of environmental fate and toxicity. First, it was our experience that the commonly used technique of DLS provided only an initial estimate of agglomerate size and that higher concentrations reflected in exposure studies could not necessarily be assessed with this method. This is because the DLS particle size determination method assumes particles are undergoing only Brownian motion, so that gravitational settling at higher concentrations, as well as multi-scattering, can give an inaccurate result. An alternate method of direct measurement of settling was therefore incorporated to extract estimates of agglomerate size distributions for each particle type at a range of concentrations. Next, dissolution analysis for nickel alone was not sufficient to explain the differences we saw between each material at specific concentrations. Colorimetry-based testing for silica was therefore implemented, revealing the role of silica dissolution on nickel dissolution. While ICP is a powerful tool for detecting dilute concentrations of metal ions, it typically requires digestion of the sample. Measurement of dissolved silica via colorimetry is a convenient alternative to differentiate between polymeric silica (i.e., silica nanoparticles) and dissolved silica that avoids the cumbersome digestion required for ICP. In sum, in order to assess new complex nanomaterials, alternate and creative methods must be developed to pick apart the influence of different aspects of the materials (e.g. agglomeration vs sedimentation, nickel vs silica dissolution). In this way, necessary connections between structural aspects can be made with regard to the fate of nanomaterials in environment.

Beyond this, zebrafish were also implemented as a screening tool for nanotoxicity. While the use of zebrafish may not be the best screening method to directly quantify the potential toxicity of nanomaterial to humans, we do believe the zebrafish assay to be relevant from an environmental toxicity perspective. There are indeed many choices of potential screening models: in vivo versus in vitro models, and several animal models within the option of in-vivo organisms. Rodents are more often used to establish thresholds for chemical exposure, but we were attracted to the zebrafish model as one that seemed more versatile from a screening perspective. With a zebrafish experiment, all routes of exposure (dermal, respiratory, and gastrointestinal) are captured simultaneously, thereby giving the experimenter the means of having a broad look at potential toxicity in a single test. Additionally, the small size of the experimental set-up, large number of embryos available in a given clutch, and easy of viewing the transparent animal without the need of dissection, made the zebrafish model of interest from a cost and skill set minimization perspective as well. What we did not fully anticipate were the challenges of dynamic behavior of the nanoparticles in media solutions. The settling that was observed indicated that our agglomerate size was large, and the dissolution made it unclear whether the toxicity observed was due to the nanoparticles or simply dissolved nickel ions. From this perspective, screening these materials via more traditional respiratory exposure chambers with rodents at times seemed a more appropriate approach. And yet zebrafish are also recognized increasingly for their use as a high-throughput screening model, especially for hatching, survival, and oxidative stress end points. We were able to examine the effect of nanomaterials to thousands of fish in this work, but the value of the zebrafish model really became clear as we moved to a higher throughput assessment of motility as a toxicity end point. Although our initial results are fairly preliminary, this screening tool truly has an exciting

potential for analysis of toxicity in terms of its statistical power and easy of data collection. Future work is planned in our laboratory to expand these initial studies to range of nanomaterials and use data fitting schemes to quantify changes in zebrafish motility responses in relation to exposure dose and material type.

# 3.0 NANOMATERIALS FOR $CO_2$ UTILIZATION VIA CHEMICAL LOOPING DRY REFORMING

## 3.1 INTRODUCTION

Carbon dioxide ($CO_2$) is widely recognized as the primary anthropogenic GHG contributor to global warming. Combustion of fossil fuels is the leading cause of $CO_2$ emissions, constituting ~80% of the U.S. GHG emissions from all sources (*135*). Currently, the U.S. is deriving ~83% of total energy consumption from fossil fuels, and no significant change is anticipated for at least the next two decades (*136*) and international trends are similar to those in the U.S. (*137, 138*). The effects of climate change are predicted to exacerbate a multitude of other global issues in the near future (*139, 140*), with some economic estimates predicting up to 20% losses in GDP (*141*). Reducing $CO_2$ emissions is hence one of our most important and challenging problems of this century.

Chemical looping combustion (CLC) is a highly efficient carbon capture technology, which has been studied in recent years as a means to reduce anthropogenic levels of $CO_2$. In conventional CLC (Figure 33), an oxygen carrier, typically a metal (denoted 'M') is oxidized with air in the first reactor (oxidizer, or 'air reactor') and then reduced in contact with a fuel in a second reactor (reducer, or 'fuel reactor'). The effluent of the reducer is a virtually pure mixture of $CO_2$ and steam such that following condensation of steam a high-pressure, sequestration-ready $CO_2$ stream is obtained from this flameless $NO_x$-free combustion process (*142-144*). In addition

to capturing $CO_2$, CLC is recognized as a highly efficient process in comparison to conventional combustion. This stems from a reduction in entropic energy losses via the step-wise, less irreversible, and low-temperature combustion of CLC (*145-147*).

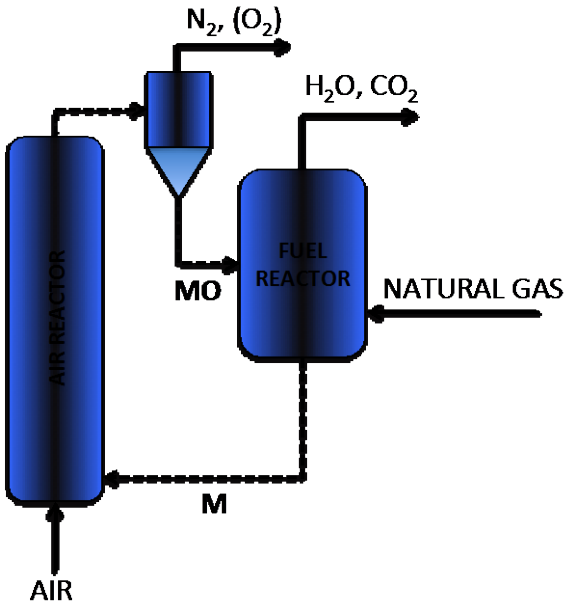


**Figure 33: Conventional Chemical Looping Combustion (CLC)**

In truth, the $CO_2$ capture achieved via CLC is really just an added bonus for the already elegant process. The two-reactor design integrates effluent gas separation into the process, resulting in a huge energy savings by elimination of downstream separation requirements. The fuel-flexibility of the process opens up the chemical looping processes to feedstocks of liquid fuels, syngas, biomass, and even solid carbon. Finally, alternate oxidants, such as steam or $CO_2$, can be used to conduct fuel reforming instead of combustion. Fuel reforming consists of chemical conversion of a fuel into useful chemical precursors, such as synthesis gas (i.e. CO and $H_2$). The term 'chemical looping reforming' or 'CLR' has been used to broadly described any chemical looping configuration in which a fuel is reformed to useful downstream chemicals, such as synthesis gas or pure hydrogen. CLR processes have been discussed to some extent in

recent reviews (*148-150*), but the technology is still in the early phases of development. Here, we will briefly discuss several approaches to chemical looping reforming, in relation to conventional fuel reforming and CLC.

**Chemical Looping Dry Reforming**

Chemical looping combustion (CLC) has been presented above as a promising $CO_2$ capture technology. However, despite the high efficiency of capture for CLC, the environmental benefit of CLC is limited because it does not offer a solution for $CO_2$ sequestration, which has not yet been developed at large scale. This lack of a secure and proven sequestration technology motivates our development a CLC-based process for the alternate purpose of $CO_2$ utilization.

$CO_2$ utilization has been explored in a number of ways (*151-154*), including both physical and chemical methods. $CO_2$ is a highly stable, low free energy molecule; its molecular transformation into chemical precursors or fuels (e.g. CO, formaldehyde, or methanol) requires energy input (*155*). Conventional dry reforming is an example of a $CO_2$ utilization process and it too requires energy input to drive the endothermic reaction. In typical methane dry reforming, methane (an even more potent greenhouse gas) and $CO_2$ react at elevated temperatures (> 700°C) over a catalyst (typically nickel or a noble metal) to produce syngas fuel with a $H_2$/CO=1 (*156-162*) according to:

(R1) $CH_4 + CO_2 \rightarrow 2\ CO + 2\ H_2$

However, conventional dry reforming is hindered by catalyst cost, deactivation due to coking, and poor selectivity for syngas (*155, 162*). An approach that is explored in this work consists of modifying CLC to instead perform dry reforming using the redox cycles of an oxygen carrier. The process is called Chemical Looping Dry Reforming (CLDR) and is depicted in Figure 34, with $CO_2$ as an oxidant instead of air. When using methane as the fuel, CLDR

produces a net reaction similar to dry reforming of methane, as shown below based on a metallic 'M' oxygen carrier:

(R2) oxidizer: $4\ M + 4\ CO_2 \rightarrow 4\ MO + 4\ CO$

(R3) reducer: $4\ MO + CH_4 \rightarrow 4\ M + CO_2 + 2\ H_2O$

(R4) net reaction: $CH_4 + 3\ CO_2 \rightarrow 4\ CO + 2\ H_2O$

This process differs from conventional catalytic dry reforming processes: While the target of conventional dry reforming (R1) is high syngas yield, CLDR (R4) results in different stoichiometry, with the target of maximum CO yield and no selectivity for $H_2$ by assuming complete combustion of $CH_4$, i.e. CLDR is a process optimized for $CO_2$ activation. Additionally, complete combustion of $CH_4$ minimizes the endothermicity of the overall process in order to ensure maximum utility for $CO_2$ activation.

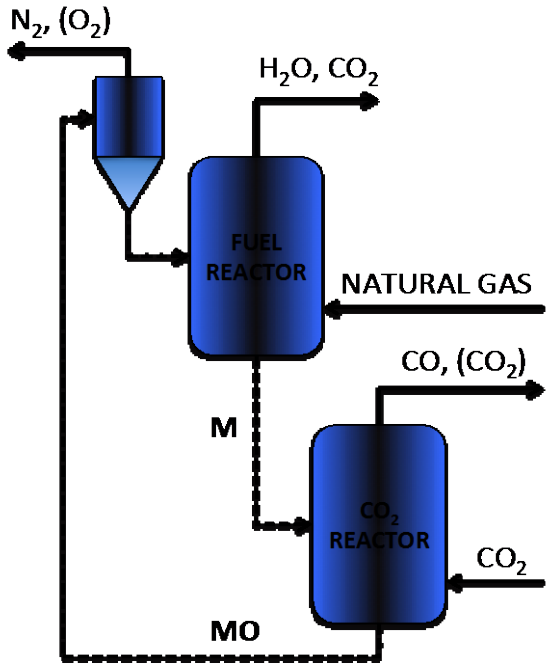


**Figure 34: Chemical Looping Dry Reforming (CLDR)**

This leads to production of CO for CLDR, a useful industrial gas (*154*, *159*, *163*). Hence, while the effluent stream from dry reforming of methane contains syngas (CO and $H_2$) combined with unreacted methane, the CLDR oxidizer effluent contains only CO and unreacted $CO_2$. This in-situ separated CLDR effluent of CO has altogether different uses: Most commonly, CO is used to an every increasing extent for fine chemical synthesis via carbonylation reactions, for substrates such as olefins, alkynes, and reactive aryl, vinyl or alkyl species (*164*). In terms of larger production chemicals, $CO/CO_2/H_2$ feed gas mixtures of 10:10:80 (such as might be made by a specific combination the CLDR effluent) are used to make methanol industrially over Cu/Zn catalysts (*165*). While $CO_2$ is the methanol pre-cursor, presence of CO ensures that the catalyst is in a more reduced form than is possible from the presence of $H_2$ alone. Finally, CO is also combined with methanol to produce acetic acid via the Monsanto process, by which the majority of acetic acid is made today (*166*). Hence, although CO is well recognized as a noxious gas and pollutant in the transportation sector, it is also important as a pre-cursor for chemical synthesis. In this way, CLDR might serve as an alternate source for CO by deriving it from $CO_2$ waste streams, in turn providing an environmental benefit by reducing $CO_2$ emissions. However, it is important to point out that for this process to be broadly feasible it would eventually require the use of an alternate fuel feedstock besides methane, a very high quality energy source. This is not an unreasonable requirement since conventional chemical looping processes have already been demonstrated to be fuel flexible, even for biomass and solid fuels. However, this particular report is limited to a proof-of concepts study using methane as a process fuel.

In terms of carrier selection, Fe-based chemical looping carriers are attractive in regard to their low cost and toxicity. Furthermore, $CO_2$ decomposition to CO or carbon has been previously demonstrated over ferrite material (*167-169*), making Fe-based carriers promising

candidates for CLDR specifically. However, it is also known that $CO_2$ is both a highly stable molecule and a weak oxidant. For this reason, the oxidizer reaction kinetics with $CO_2$ is expected to be slower than for the case with air. To address this, nanostructured oxygen carriers can be developed to minimize the diffusion limitations to hence improve reaction kinetics. Finally, such carriers also would require the incorporation of a high temperature stable support to abate sintering of the iron nanoparticles. Only a few approaches have been explored in nano-enabled capture technologies, mostly using sorbents (*170, 171*) and membranes (*172*). But chemical looping combustion has seen the use of some nano-scale oxygen carriers (*173, 174*) and our lab has done work with extremely high temperature stable Ni- and Cu-based nanocomposites (*83, 175*).

For the reactor configuration, circulating fluidized beds (CFBs) are typically preferred over the packed bed reactor (PBR) in conventional CLC due to the possibility of hot spot formation from exothermic reactions (*144*). But with CLDR, there is actually a need for very efficient heat integration between the two half reactions to drive the endothermic dry reforming process. Therefore, the use of $CO_2$ as an oxidant also presents an interesting opportunity to evaluate a chemical looping system in a PBR. Modeling and experimental work has been done previously on the bed temperature changes within a PBR reactor with both CLC (*176, 177*) and CLR (*178*), demonstrating that much milder bed temperature changes occur for CLR as a result in the reduced in exothermicity for this case.

CLDR is a novel concept that has been explored for the first time as part of this work. However, there are a few other chemical looping enabled reforming processes that also explore the possibility of using chemical looping concepts beyond conventional combustion. Two

additional chemical looping reforming processes and the important aspects of these processes in terms of CLDR will be discussed briefly below:

Chemical looping steam reforming (CLSR) consists of a chemical looping oxidizer that is fed with steam instead of air to result in formation of pure $H_2$ in the oxidizer effluent after consensation of the unreacted steam (Figure 35).

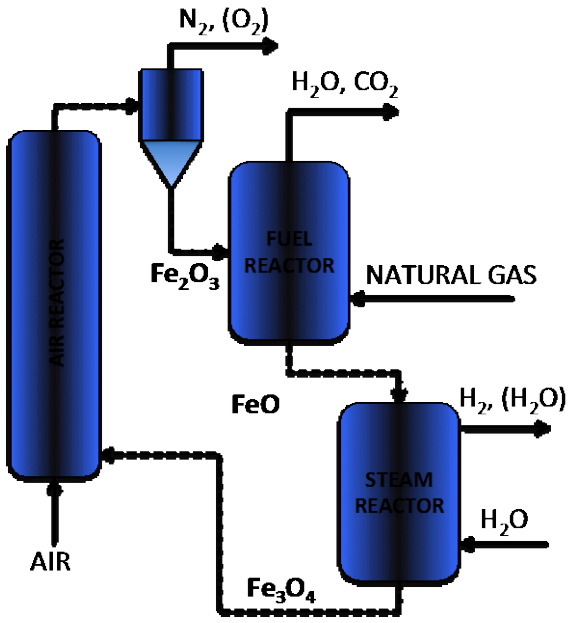


**Figure 35: CLR process, with an intermediate steam reactor added for pure $H_2$ production. Adapted from (*179*).**

Chiesa et al. first conceptualized the idea of CLSR (*179*). Using an iron carrier, fully oxidized $Fe_2O_3$ enters the fuel reactor and is reduced to FeO. FeO is then oxidized to $Fe_3O_4$ (the maximum oxidation state thermodynamically possible for an Fe-based carrier exposed to steam). Finally, $Fe_3O_4$ is re-oxidized by air to complete the loop. The effluent of this first oxidation reactor (i.e., the steam reactor) is hydrogen and any unreacted steam, which can be easily separated by condensation. Hence, the system acts as an integrated means of $CO_2$ capture (in the reducer) and pure hydrogen production (in the oxidizer). Chiesa's study focused on optimization

of thermal balancing of the model, while several later authors (*178*, *180*) demonstrated the feasibility of the process in experimental work. In many aspects, this process is quite similar to the CLDR process proposed above: Fe-based carriers are used, $H_2O$, like $CO_2$, is considered a weaker oxidant than air, and it is hoped that the exothermicity of the reducer will drive the overall endothermic reaction. However, since dry reforming is even more endothermic than steam reforming, CLDR is an even greater challenge energetically and downstream separation of unreacted $CO_2$ is not convenient as in CLSR. Nonetheless, given the overlap between the two processes, it is interesting to consider the possibility of a $CO_2/H_2O$ flexible process, in the same way that is highlighted below for solar-thermal processes.

As mentioned previously, the principle focus of this work is the CLDR processes, but lessons from CLSR processes provide useful insights for this work. Recent work in thermochemical splitting of $CO_2$ or $H_2O$ via a solar thermal process is also of great interest (*181-186*) since it too uses the oxidation states of a metal carrier in a cyclic manner. This process is comprised of an oxidation step with $CO_2$ or $H_2O$ or a combination of the two, followed by a metal oxide decomposition step. Concentrated solar power is used to reach very high temperatures (>2500 K) to drive the metal oxide decomposition. The carrier materials undergo the same transformations as CLSR and CLDR discussed above. Zn-, Fe-, and Ce-based carriers have been identified as suitable materials for the process, of which Fe and Ce material have also been identified as suitable for CLDR or CLSR. Although the metal reduction half-cycle is different than CLDR, the reactivity of $CO_2$ with an oxygen carrier and the impressive observation of Ce-based material stability after over 500 cycles (*184*) is instructive for the long-term stability of such materials during successive chemical looping oxidation-reduction cycles.

More importantly, there may be an opportunity to integrate CLDR and thermochemical splitting processes to allow for un-interrupted operation by alternating between sunlight and fuel during daylight and nighttime hours.

Overall, this work was comprised of several tasks designed to meet our goal to demonstrate the feasibility of the CLDR process and the flexibility of chemical looping for objectives beyond more conventional combustion. Specifically, this work includes:

- Analysis of thermodynamic feasibility of the CLDR process, including a screening of transition metals capable of reducing $CO_2$, quantification of conversion and selectivity for CLDR reactions, and selection of suitable operating temperatures.
- Evaluation of maximum temperature changes in a periodically operated PBR via reactor modeling.
- Synthesis of well-controlled, highly active, and high-temperature stable nanostructured oxygen carriers for use in the CLDR process, including material characterization with TEM, EDX, XRD, BET.
- Performance analysis of materials in TGA and PBR
- Evaluation of second law efficiencies of the CLDR process compared to conventional dry reforming of methane via exergy analysis.

## 3.2 METHODS

**NOTE: The methods presented here are a detailed compilation of all of the procedures used for this chapter. A more concise or specific methods description is included in selected subsections of this chapter that are proposed for manuscript submission.**

**Synthesis**

Fe@$SiO_2$ materials were made using a one-pot reverse microemulsion synthesis adapted from Takenaka, et al. (*68*), consisting of several step-wise additions. First, 50 mL of cyclohexane (≥99% Sigma-Aldrich) and 20 g surfactant Brij 58 (≥99% polyethylene glycol hexadecyl ether, $M_n$ ~1124, Sigma-Aldrich) were refluxed at 50$^o$C until the surfactant was fully dissolved. 1.5 mL aqueous $Fe(NO_3)_3 \cdot 9H_2O$ (≥99.99%, Sigma-Aldrich) was then added dropwise. The concentration of the aqueous salt was varied (0.5 – 1.3 M). Upon subsequent addition of 1.5 mL hydrazine hydrate (Sigma-Aldrich), the microemulsion turned from deep orange to black, and the solution was then allowed to age overnight. Next, 3 mL of ammonium hydroxide (30%) was added, followed by 3-5 g of tetraethylorthosilicate (TEOS, ≥99% Sigma-Aldrich), followed by another aging step for $SiO_2$ shell growth via base catalyzed hydrolysis and condensation ($Si(OCH_2H_5)_4 + 2\ H_2O \rightarrow SiO_2 + 4ROH$) (*70*). Finally, the particles were precipitated after 2 hrs aging with 2-propanol, collected via centrifugation, washed three times with 2-propanol, and dried in air. Crushed powder was calcined in a Thermolyne 79300 tube furnace for 2 hrs at 500$^o$C in air (flow rate 0.1 - 0.3 SLM).

Hollow Fe@$SiO_2$ (hFe@$SiO_2$) materials were synthesized using a two-step 'wrap bake' synthesis adapted from others (*187*). First, akagenite (β-FeOOH) spindle particles were made

via hydrolysis of 0.02 mmol of $FeCl_3 \cdot 6\ H_2O$ (>97%, Sigma-Aldrich) dissolved in 400 mL DI water. The solution was magnetically mixed and refluxed overnight (12-16 hrs) at 80°C. Alternatively, akagenite (β-FeOOH) spindle particles were made via hydrothermal synthesis of a 1 mM solution of $FeCl_3 \cdot 6\ H_2O$ for 16 hrs at 80°C. In either case, the resulting particles were centrifuged and dried. Typically, .04 g of iron particles (from either hydrolysis or hydrothermal synthesis) were dispersed with 1 g polyvinylpyrrolidone (PVP10, average mol wt 10,000, Sigma-Aldrich) via sonication (~20 min) and magnetically mixed for 24-30 hrs to coat the particles with PVP. Ethanol and 30% ammonium hydroxide were then added to the colloid according to the ratio of 10 mL EtOH : 0.6 mL $NH_3OH$ : 1 mL colloid mixture. 0.3-2 mL TEOS was added as the silica pre-cursor. After 12-15 hours of magnetic mixing, particles were centrifuged and dried in air. The crushed powder samples were calcined for 2 hr in air then reduced for 1 hr in $H_2$, leading to oxidation of β-FeOOH@$SiO_2$ to $Fe_3O_4/Fe_2O_3$@$SiO_2$ and reduction to hollow Fe@$SiO_2$, respectively.

Fe@$CeO_2$ materials were synthesized by a hydrothermal formation of $CeO_2$ particles with iron-based nanoparticle as seeds described above in a similar way as Pd@$CeO_2$ made by others (*188*). In our synthesis, 0.114g of akageneite (β-FeOOH) spindle particles were dispersed in 10mL DI water using sonication for 20 min. PVP-10 was then added in a ratio of 1g/0.04 g particles. The solution was then diluted to a final volume of 25 mL and mixed at room temperature for 24 hrs. Next, 1 mmol of $CeCl_3$ and 10 mol of urea were combined with 17 mL of the colloid mixture containing PVP-coated particles. The target in this synthesis is roughly Fe:Ce of 1:10. This solution was then mixed for 20 min and then transferred to a 50 mL hydrothermal reactor and held at 90°C for 24 hrs. The mixture was then cooled, centrifuged, dried, and calcined at 500°C.

Fe-BHA (BHA = Barium hexa-aluminate) was synthesized with a reverse microemulsion sol-gel process in which metal nanoparticles were synthesized simultaneously with a ceramic matrix via a one-pot approach developed by others (*83, 175, 189*). First, an aqueous metal salt solution of ($Fe(NO_3)_3 \cdot 9\ H_2O$ (≥99.99%, Sigma-Aldrich) was mixed with iso-octane (2,2,4-trimethylpentane, 99.7%), a surfactant (poly(ethylene oxide)-block-poly(propylene oxide)-block-poly(ethylene oxide), Aldrich) and a co-surfactant (1-pentanol, 99+%). Aluminum isopropoxide and barium isopropoxide (both 99.9%) were dissolved at a stoichiometric ratio of 1 to 12 under inert gas as precursors of BHA, a high temperature stabilized alumina (*190*). The isopropoxides were then added to the reverse microemulsion where they diffuse into the water micelles and hydrolyzed. In parallel, the metal salt formed metal nanoparticles, which remained embedded in the porous BHA framework. The reverse microemulsion was aged for ~48 hours, and then separated by temperature-induced phase separation. The collected product underwent several washing steps with acetone, followed by volatile removal via freeze-drying. The resulting dry powder was crushed and calcined in air for 2 hours at 500$^{o}$C.

**Characterization**

All materials were characterized for particle size and morphology with transition electron microscopy (TEM, JEOL-2000FX electron microscope). Typical sample preparation consisted of grinding the sample in a mortar, ethanol dispersion, ~2 min sonication, and placing 1-2 drops of dispersion on copper type-B support grid (Ted Pella Inc.) to dry in air. Particle measurements of TEM images were done using ImageJ software (http://rsb.info.nih.gov/ij/). Catalyst surface area and porosity were determined by Brunauer Emmett Teller (BET) analysis (Micromeritics ASAP 2020 surface area and porosity analyzer). Pre-treatment consisted of 2-3 hr degas at 200$^{o}$C under vacuum. Typically, a 6-point BET analysis was used for total surface area measurement

and an 84-point $N_2$ BJH analysis with Halsey thickness curve correction and Kruk-Jaroniec-Sayari BJH correction for pore size and volume determination. Crystal structure was determined with X-ray diffraction (XRD) (Phillips PW1830, USA). XRD was run in 'line focus' mode using a monochromatic Cu radiation at the wavelength of 1.54 Å. The beam voltage was 40kV at a current of 30mA. Diffraction patterns were recorded between 15 and 90° (2θ) in steps of 0.08° intervals with a 0.2 s counting time at each step. Scanning electron microscope energy dispersive X-ray spectroscopy (SEM EDX Genesis) was used to determine elemental composition of samples at beam voltage of 15kV, spot size 4 (typically), a collection time of 50-100 s, and a monitored dead times of 20-40%. Sample powders were first mounted with double-sided carbon tape and then coated with palladium for analysis. At least 3 measurements were taken for each sample, and at least 5 samples if measurements varied by more than 5%. Material composition values were used to estimate expected weight gains and losses for materials in chemical looping experiments.

**Thermodynamic Calculations**

A commercial software FACTSAGE was used to conduct a thermodynamic screening of transitions metals suitable for CLDR. The software performs a Gibbs free energy minimization of reactant and product mixtures at a fixed temperature and pressure to predict equilibrium values. Calculations were done at 300-1700$^{o}$C with a stoichiometric supply of $CO_2$ and methane for metal oxidation and reduction, respectively. The principle selection criteria were (1) conversion greater than 20% for all temperatures (2) operation below metal oxide melting point for high temperatures and (3) toxicity of transitions metals. In select cases, the effect of an overstoichiometric supply of $CO_2$ to oxidation was analyzed.

**Reactive Assessment**

Redox reactions for CLDR were observed via isothermal thermogravimetric analysis (TGA, Perkin Elmer TGA7) with sample purge and balance purge flow rates of 20-35 sccm and 60 sccm, respectively, controlled by MKS flow controllers calibrated for each gas.

Isothermal fixed bed reactor studies were conducted with a ¼" quartz tube reactor with effluent gas detection via mass spectrometry (Pfeiffer Omnistar QMS 200). The CO satellite signal from $CO_2$ was removed from the raw ion current data for 28 MW. Following this, molar flow rates were calculated based on calibration curves relating ion current to mole fraction in the presence of helium.

## 3.3 THERMODYNAMIC ANALYSIS FOR CLDR

**Note: The following results are published in Chemical Engineering Research and Design as part of a study on the feasibility of the CLDR process (*191*).**

### Introduction

A key issue in chemical looping processes is the selection of an appropriate oxygen carrier material. The reactivity of the carrier, its cost, toxicity, thermal stability, and attrition resistance (in the commonly used circulating fluidized bed reactor) are all critical selection criteria. For chemical looping reforming processes, reactivity is an even more stringent criterion than for conventional CLC, since the reactivity of $H_2O$ or $CO_2$ as oxidants is significantly lower than for air (i.e., oxygen).

### Thermodynamic calculations

Thermodynamic screening calculations were conducted as a first step to identify suitable metals as active oxygen carrier components. A broad range of metals was analyzed using commercial software (FACTSAGE 5.0) to determine the thermodynamic equilibrium limitations for carrier oxidation and reduction in CLDR. This analysis performs a Gibbs free energy minimization of the reactant and product mixture at specific temperature and pressure. To screen for suitable transition metal carrier materials, several factors were considered. First, although a significant number of transition metals can be oxidized by $CO_2$, many of these same metals fail to exhibit suitable equilibrium conversion for the reduction reaction with a range of fuels. Additionally, suitable equilibrium conversion was often only achieved at temperatures nearing

the melting points of the metals. Since chemical looping processes require stable oxygen carrier materials that can undergo extended high-temperature oxidation-reduction cycles with reproducible kinetics, materials that were only reactive above or near their melting points were eliminated. Lastly, cost and material toxicity were also considered in the selection.

Table 4 shows the results from $CO_2$ oxidation screening experiments for transition metals that were shown to have exhibited high thermodynamic carrier conversion (>20%) in both the forward and reverse reactions over a range of temperatures. The table lists the maximum capacity for $CO_2$ reduction to CO in g $CO_2$ per mole of metal based on reaction stoichiometry (i.e., the maximum reduction capacity in the absence of equilibrium limitations). The maximum and minimum reactor operating temperatures are also given. The maximum temperature represents either the metal melting point, as is the case for Cr-, Mo-, Nb-based carriers, or the lowest temperature at which full conversion was achieved for reduction of the carrier with methane for Co-, Zn-, Fe- based carriers. The minimum temperature is defined as the temperature at which equilibrium conversion for carrier reduction with methane drops to 20%. The reduction temperature was selected as the minimum temperature determinant because the minimum temperatures required for sufficient carrier reduction were consistently higher than for carrier oxidation. The minimum and maximum temperatures given in Table 4 define the effective operating range for a CLDR process based on the respective carrier.

**Table 4: Screening results for CLDR carriers**

| Carrier Oxidation Reaction | $CO_2$ Carrying Capacity [g $CO_2$/mol M] | Min. Temp. [C] | Max. Temp. [C] |
|---|---|---|---|
| Mo + 2 $CO_2$ -> $MoO_2$ + CO | 88 | 900 | 1000 |
| 2 $Cr_3O_4$ + $CO_2$ -> 3 $Cr_2O_3$ + CO | 66 | 1700 | 2400 |
| 3 Fe + 4 $CO_2$ -> $Fe_3O_4$ + 4 CO | 59 | 700 | 1800 |
| Fe + $CO_2$ -> FeO + CO | 44 | 700 | 1800 |
| Zn + $CO_2$ -> ZnO + CO | 44 | 1200 | 1600 |
| Co + $CO_2$ -> CoO + CO | 44 | 200 | 300 |
| 3 FeO + $CO_2$ -> $Fe_3O_4$ + CO | 15 | 700 | 1800 |
| 2 $NbO_2$ + $CO_2$- > $Nb_2O_5$ + CO | 11 | 1300 | 1500 |

While a number of metals give reasonable $CO_2$ reduction capacity, it is apparent that only iron gives high oxygen storage capacity from $CO_2$ over a wide temperature range. The very limited operating range for Mo makes its use impractical, Cr- and Nb-based carriers require temperatures well above those reasonable for reactor operation, and the very low temperature range for Co is prone to result in unacceptably slow kinetics. Iron-based carriers, which combine low cost, wide availability, and low toxicity, were thus selected for further analysis.

A general concern in $CO_2$ reduction processes is control of the degree of reduction. This is particularly true in any heterogeneously catalyzed $CO_2$ reduction process, or in a non-catalytic gas-solid reaction such as the presently considered. $CO_2$ reduction can result either in partial reduction to CO or deep reduction to elemental carbon (C). Since the formation of carbon can be expected to result in deposition and carrier deactivation due to active site occlusion, the reduction of $CO_2$ to C is undesirable. For this reason, the degree of $CO_2$ reduction, i.e. conversion and selectivity of the reduction process for the Fe-based carriers was studied. Figure 36 shows the equilibrium $CO_2$ conversion in the case of stoichiometric $CO_2$ supply for the oxidation of Fe to FeO, Fe to $Fe_3O_4$, and FeO to $Fe_3O_4$, respectively, along with the corresponding selectivity to CO over a temperature range of 200-1000$^oC$. Clearly, while $CO_2$

conversion remains incomplete at all conditions, consistently high conversions (>50% for Fe and >30% for FeO) show again the wide operating range of iron-based carriers. This data demonstrates the process flexibility of iron as a carrier through the accessibility of three different oxidation states of iron with similar $CO_2$ conversion trends, albeit with different oxygen carrying capacities. It should be noted that the highest oxidation state of iron, $Fe_2O_3$, was not obtained as a thermodynamically accessible phase at any of the investigated conditions with $CO_2$ as oxidant, indicating the reduced oxidation capability of $CO_2$ in comparison to air.

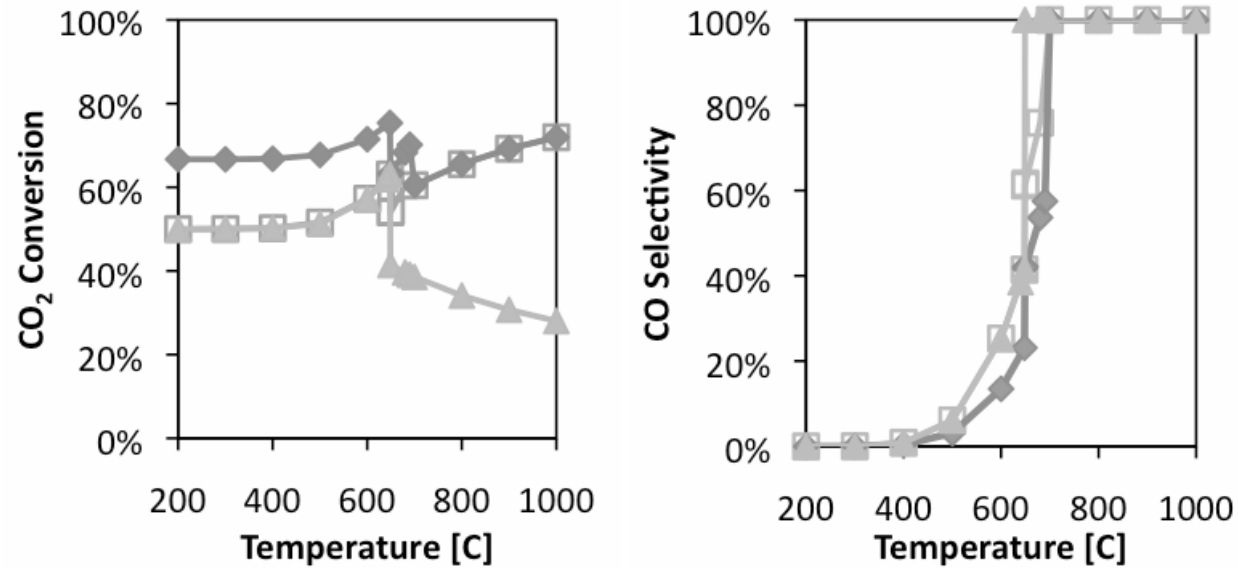


**Figure 36: Temperature dependence of conversion and selectivity for oxidation reactions Fe → FeO (diamonds), Fe → $Fe_3O_4$ (open squares), and FeO → $Fe_3O_4$ (triangles)**

Since incomplete carrier conversions are obtained at temperatures >700°C, where carbon formation is thermodynamically unfavorable, further analysis was performed to determine the amount of excess (i.e., over-stoichiometric) $CO_2$ feed required to shift the thermodynamic equilibrium in the oxidation reactor to 100% carrier conversion to $Fe_3O_4$. The equilibrium conversions calculations are also based a closed system, while calculations for an overstoichiometric supply would correspond to a more ideal reactor set-up (i.e. counter-current

gas and solid phases or a packed-bed reactor). Here, we define excess $CO_2$ as the percentage of $CO_2$ above the stoichiometric requirement to fully oxidize the carrier to $Fe_3O_4$: "0% excess" represents a stoichiometric feed of $CO_2$, while 100% excess indicates a two-fold stoichiometric supply of $CO_2$. Only temperatures >650$^oC$ are evaluated, where the selectivity for CO (over carbon) is predicted to be high. A large excess of $CO_2$ (~150-200%) is required to attain Fe conversion to $Fe_3O_4$, while more moderate values of <30% are needed for FeO conversion to $Fe_3O_4$ (Figure 37).

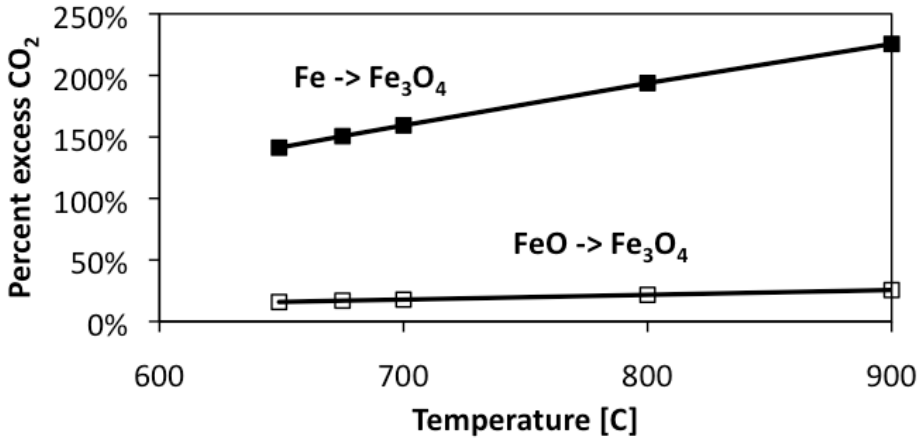


**Figure 37: Thermodynamic calculation for percent excess $CO_2$ required for full conversion to $Fe_3O_4$ with either Fe or FeO as the starting material for the CLDR oxidizer.**

Equilibrium calculations were also conducted for the reduction of $Fe_3O_4$ using methane as the fuel in the reducer at temperatures 600 – 1400$^oC$, selecting for full combustion to $CO_2$ and $H_2O$ and FeO or Fe as a reduced states of the carrier, according to the stoichiometries below:

*FeO as reduced state:* $CH_4 + 4\ Fe_3O_4 \rightarrow CO_2 + 2\ H_2O + 12\ FeO$

*Fe as reduced state:* $CH_4 + Fe_3O_4 \rightarrow CO_2 + 2\ H_2O + 3\ Fe$

For the reduction of $Fe_3O_4$ to FeO, the result shows an increasing conversion with increasing temperature (Figure 38). In this case, FeO is the only reduction product for the

carrier (i.e. $S_{FeO}$ = 100%). Conversely, supplying sufficient methane for stoichiometric reduction of $Fe_3O_4$ to Fe results in 100% carrier conversion at all temperatures, but with a less unfavorable *mixture* of FeO and Fe as the reduction products (i.e. $S_{FeO}$ ~60%). The gas phase conversion for $Fe_3O_4$ reacting with methane is >95% for all temperatures, but the selectivity for total oxidation products is poor (Figure 39). The calculation also shows that carbon formation is predicted at temperatures <650$^{o}$C for $Fe_3O_4$ reduction with methane.

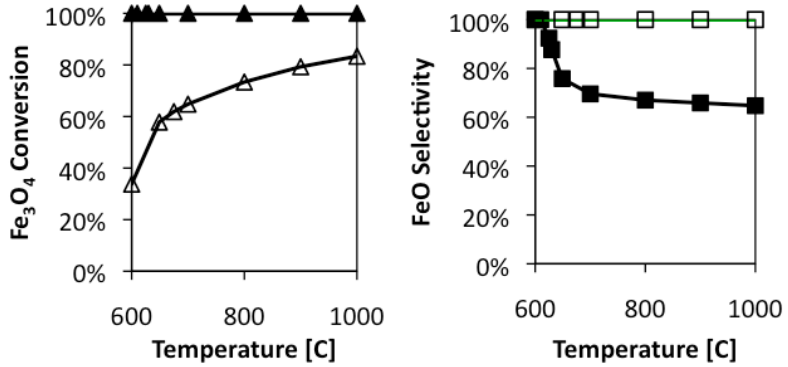


**Figure 38: Conversion and selectivity for reduction with methane. $Fe_3O_4$→Fe (closed symbols) and $Fe_3O_4$→ FeO (open symbols).**

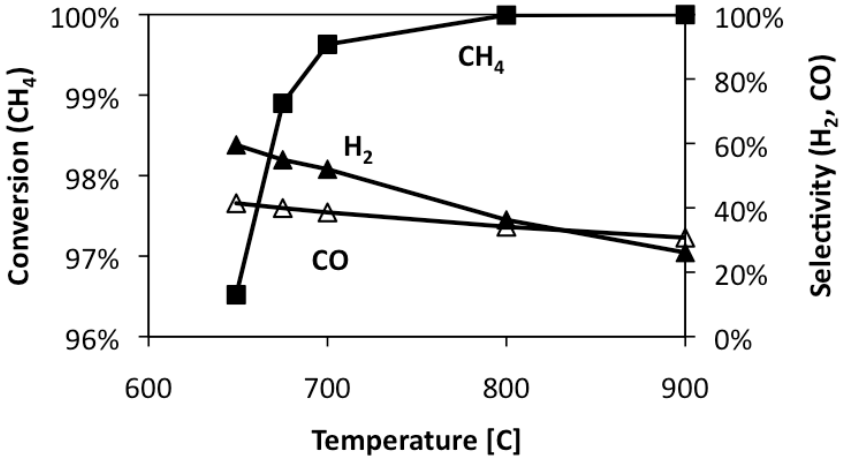


**Figure 39: Gas phase conversion and selectivity for reduction with stoichiometric supply of methane.**

In sum, the thermodynamic calculations indicate that the most efficient and straightforward methane-fueled CLDR process would operate >700$^{o}$C with $Fe_3O_4$ and FeO as oxidized and reduced carrier state, respectively. However, a process with an oxidized state of $Fe_3O_4$ and reduced state consisting of both Fe and FeO is also possible, allowing higher iron utilization. Overall, the thermodynamic screening calculations show that Fe-based carriers, despite some shortcomings, are the most promising carrier materials for CLDR.

**Reactor Modeling**

The most commonly discussed reactor configuration for chemical looping processes is a two-reactor circulating fluidized bed (CFB). Although CFB operation is known to provide excellent heat and mass transfer characteristics, which are critical for chemical looping, CFBs also present significant operational challenges with regard to oxygen carrier transport and particle attrition (*144*). Alternatively, CLC operation in a cyclically operated packed bed reactor (PBR) has also been proposed and tested, although heat management can be a problem in this case (*176, 177*). Conversely, in chemical looping reforming processes, the heat from the carrier oxidation reaction enthalpy is substantially reduced, therefore reducing the probability of obtaining hot spot formation in the packed bed, or an unacceptable temperature maxima in the cyclic operation of the reactor. In fact, since dry reforming is overall endothermic, the use of a PBR system is expected to be advantageous since the heat generated from the exothermic oxidation half-cycle is regeneratively transferred via the oxygen carrier to the subsequent endothermic reduction step, resulting in highly efficient heat integration between the two half cycles (*192-194*). Indeed, heat integration through the use of periodically operated packed bed reactor systems for endothermic reactions has been previously proposed by others for counter-

current flow configuration, and has been shown to result in super adiabatic temperatures at autothermal conditions (*195, 196*).

Here, we consider a simple packed-bed reactor operation in which the bed is operated periodically between oxidation with $CO_2$ and reduction with methane in a co-current configuration, giving rise to traveling gas and temperature waves through the reactor. Such a configuration entirely avoids carrier attrition and separation issues, which are the main concern in CFB process development. Still, the thermal dynamics of the system require consideration in order to avoid unacceptable maximum temperatures.

A simplified heat and mass transfer model for CLDR operations is analyzed in the following. The model was originally developed by Kuipers and coworkers for conventional CLC (*176*), and later adapted by Solunke and Veser for chemical looping steam reforming (CLSR) (*178*). The calculations presented here are based on a dynamic analysis of the pseudo-homogeneous energy balance for a packed-bed CLC process. Noorman et al. demonstrated that this energy balance can be solved analytically given several simplifying assumptions. Here we will briefly review the model derivation by Kuipers and coworkers, as adapted for our dry reforming process. The maximum temperature excursions in the bed can be directly derived from the energy balance given the following assumptions: it is assumed that the carrier in the packed-bed is initially in its reduced form (FeO), and reacts with the $CO_2$ instantaneously, i.e. with an infinitely fast reaction rate, until complete carrier conversion is attained. Similarly, instantaneous, complete reaction of $Fe_3O_4$ with methane during for the reduction phase is assumed. While neither assumption (infinite reaction rate or complete conversion) is strictly true in our case, as seen in the thermodynamic calculations above and reactor experiments (see

sections 3.3 and 3.5), the analysis based on these assumptions will yield a worst-case estimate for the maximum temperatures that can be expected in the process.

The coupling between the gas-solid reaction and the convective gas flow results in the formation of two spatially separated travelling wave fronts, which move through the reactor with different front velocities. Assuming all of the heat within the solid material is transferred to the gas phase at the heat front and all $CO_2$ in the feed reacts instantaneously with the solid carrier, these front velocities are given as:

$$(1) \quad v_h = \frac{\rho_g v_g C_{p,g}}{\varepsilon \rho_s C_{p,s}} \quad \text{and} \quad (2) \quad v_r = \frac{\rho_g v_g w_{g,CO_2}^{in} M_{act}}{\varepsilon_s \rho_s w_{act} M_{CO_2} \xi}$$

(for a full list of the variables definitions, see 'Nomenclature' below). The first expression is the velocity of the heat front ($v_h$), and the second is the velocity of the reaction front ($v_r$), where the oxidant ($CO_2$) reacts with the reduced oxygen carrier (FeO). It is assumed that the heat capacity of the gas and the solid ($C_{P,g}$ and $C_{P,s}$) and the solid density ($\rho_S$) are constant, and that the influence of pressure drop over the packed bed and the variation of the mass flow rate can be neglected. Since the heat capacity of the reactants ($C_{P,g}$) is only weakly dependent on temperature over the temperature range of interest, an average value $C_{P,g}$ was utilized and the calculations are not dependent on a specific reference temperature.

Assuming furthermore that the gas phase volumetric heat capacity is negligible, the heat produced by the oxidation of the oxygen carrier is taken up entirely by the solid carrier, and the energy balance can then be written as:

$$(3) \quad \frac{\rho_g v_g w_{g,CO_2}^{in}}{M_{CO_2}} \left(-\Delta H_R\right) = \varepsilon_s \rho_s C_{P,s} \left(v_r - v_h\right)\left(T_{\max} - T_0\right)$$

Finally, combining equations (1) and (2) into (3) and gives the maximum temperature rise in the bed:

$$(4) \quad \Delta T_{\max} = \left(T_{\max} - T_0\right) = \frac{-\Delta H_R}{\frac{C_{P,s} M_{act}}{w_{act} \xi} - \frac{C_{P,g} M_{CO_2}}{w_{g,CO_2}^{in}}}$$

As already pointed out by Noorman et al., the maximum temperature rise is independent of the gas flow velocity, due to the assumption that the heat capacity of the gas phase is small in comparison to the solid phase, which results in negligible convective heat transport with the gas flow. Furthermore, equation (4) does not account for the influence of the reaction rate on the maximum temperature rise, which is a result of the assumption of an essentially instantaneous reaction and will hold as long as the reaction rate is sufficiently fast (*176*). While the incomplete conversions observed in our experiments will result in significant dampening of the temperature maxima as compared to the model results, the fast onset of the reactions and high reaction rates, particularly during the first phase of reduction and oxidation, respectively, can be expected to satisfy the present assumption.

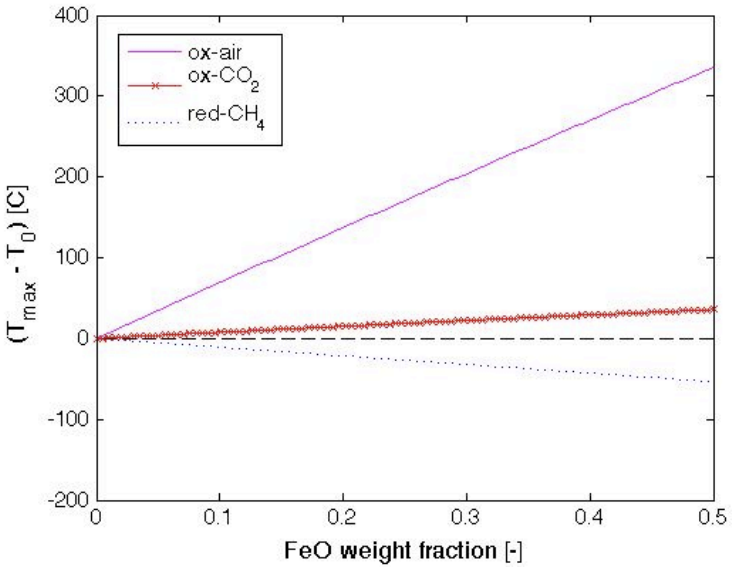


**Figure 40: Maximum temperature increase within the bed during each half-reaction in CLDR**

Figure 40 shows the maximum temperature change during the reduction of a iron-based carrier with methane as fuel along with the maximum temperature rise during oxidation of the carrier with $CO_2$ and, for comparison, with air as a function of the weight fraction of FeO in the oxygen carrier. As expected, the maximum temperature rise in the reactor during carrier oxidation is dramatically lowered for $CO_2$ compared to air as oxidant. While the temperature maxima for oxidation with air exceeds 300$^{o}$C, the temperature rise during oxidation with $CO_2$ never increases above 50$^{o}$C. Clearly, hot spots or temperature peaks are unlikely to pose a concern in a packed-bed CLDR process.

In fact, the temperature maxima in Figure 40 illustrate another important aspect of CLDR. Since the process yields methane dry reforming as overall reaction, it is a strongly endothermic process, as apparent in the fact that the temperature minima in the oxidizer exceed the maxima in the reducer (in terms of absolute values). In practice, the process could be operated via externally fired reactors, as done in industrial steam reforming of methane.

However, this would counter the intent of the process as a net $CO_2$ consumer, since this combustion process would again result in $CO_2$ emissions. Alternatively, the process could be rendered autothermal by co-feeding oxygen with $CO_2$ as co-oxidizer, in close analogy to industrial autothermal methane reforming (*197*). The overall reaction hence would give:

$$CH_4 + y\ CO_2 + (3\text{-}y)/2\ O_2 \rightarrow (1+y)\ CO + 2\ H_2O$$

A thermodynamic analysis yields y = 1.83 in order to attain a thermo-neutral reaction, i.e. in practice the process would require slightly lower values of y in order to attain a mildly exothermal process for autothermal operation.

In CLDR, several alternate schemes for this oxygen co-feed are possible: The oxygen could be directly co-fed with $CO_2$ to the oxidizer, or it could be fed with methane to the reducer. Clearly, the latter is the more favorable configuration, since it reduces the endothermicity of the reducer reaction, which minimizes the temperature swing between the oxidation and reduction half-cycles. Since the required methane/oxygen mixture would be well above the fuel-rich flammability limit, process safety would not be a significant concern. Furthermore, co-feeding oxygen with methane would allow an increase in fuel conversion and improve selectivity towards total oxidation products while aiding in removing any potential carbon residues, i.e. it would help to overcome some of the issues identified in our thermodynamic analysis and in the reactor experiments.

As for the oxygen source, oxygen could either be fed as air or as a pure $O_2$ stream. Feeding air would be preferable from a cost perspective. However, it would result in a strong dilution of the $CO_2$ stream from the reducer with ~70 vol% $N_2$ after steam condensation (assuming complete conversion of methane to total oxidation products), counter-acting the intent

of the process to yield sequestration-ready $CO_2$ streams on the reducer side. Hence, efficient process operation would require purified oxygen feed at the expense of process operating cost.

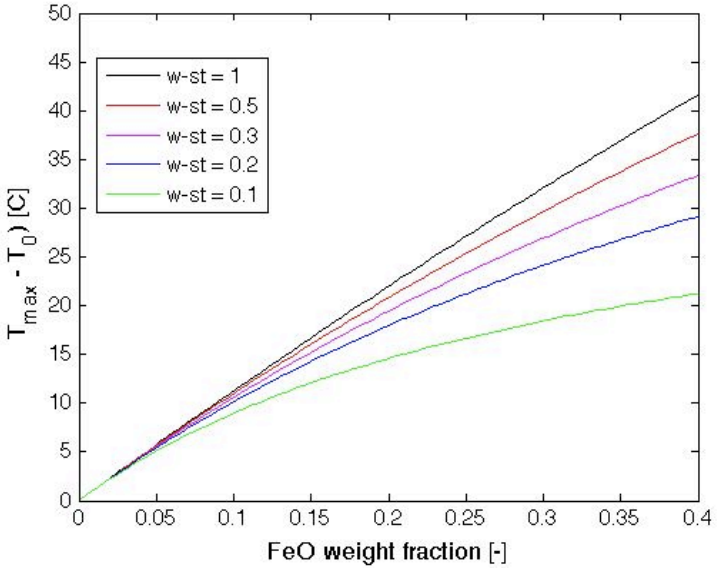


**Figure 41: The effect of $CO_2$ dilution and carrier weight fraction in temperature increase in the bed.**

As previously discussed, the operation of CLDR with dilute $CO_2$ streams also poses an intriguing possibility for utilization of such dilute $CO_2$ streams on the oxidizer side while producing highly concentrated, sequestration-ready $CO_2$ streams on the reducer side. In this case, however, the fraction of $CO_2$ in the oxidizing stream will impact the temperature rise in the system. This is shown in Figure 41, where the maximum temperature rise during oxidation with $CO_2$ is shown again as a function of the FeO weight loading of the carrier for a range of $CO_2$ mass fractions in the oxidizing feed stream (the balance is assumed to be inert gas). The maximum temperature is only weakly affected by the change in oxidizing gas composition, supporting the feasibility of a CLDR-based process that would be operated with dilute $CO_2$ feed streams. Beyond offering activation of $CO_2$ as alternative to $CO_2$ sequestration, CLDR hence opens the possibility to operate with dilute $CO_2$ streams (including, potentially, power plant flue

gases) that would otherwise require expensive separation for $CO_2$ concentration before being considered for sequestration.

***Nomenclature for packed-bed reactor model:***

$C_P$= heat capacity (J/kg·K)

$\Delta H_R$ = heat of reaction (J/ mol)

$M_{act}$= molecular weight of reactive component in solid carrier (kg/mol)

$M_{CO_2}$ = molecular weight of $CO_2$ (kg/mol)

$T_o$= initial temperature (C)

$T_{\max}$= maximum temperature (C)

$\Delta T_{\max}$ = maximum temperature rise (C)

$v_g$= gas velocity (m/s)

$v_h$= heat front velocity (m/s)

$v_r$= reaction front velocity (m/s)

$w_{act}$= weight fraction of reactive component in solid carrier

$w_{g,CO_2}^{in}$= weight fraction of $CO_2$ in the feed

$\rho$= density (kg/m$^3$)

$\varepsilon_s$= porosity

$\xi$ = stoichiometric factor (molar ratio gas to solid in the oxidation reaction)

## 3.4 EXERGETIC CONSIDERATIONS FOR CHEMICAL LOOPING DRY REFORMING

One key benefit of chemical looping is its innate flexibility for a range of fuels, carrier materials, reactor configurations, and oxidants. In addition, the exergetic benefits of the chemical looping process over conventional combustion are well established (*146, 198-200*). However, minimal analyses have been conducted on alternative chemical looping technologies that also take advantage of this process flexibility. Furthermore, previous work was only focused on alternative configurations for thermal balancing in the process (*201*). We are interested in several other alternative chemical looping processes which vary the oxidizing gas in the process, including chemical looping steam reforming and chemical looping dry reforming. These alternative approaches to CLC can result in either positive or negative impacts on process efficiency, and exergy losses are a major contributor to these efficiency losses. Furthermore, a detailed exergy analysis of the exact locations of entropic losses is a valuable tool when designing processes and comparing new technologies (*202-204*). For instance, Rosen et al. conducted an energetic and exergetic comparison of several $H_2$ production technologies, revealing a wide range of 19-83% for exergy efficiency for various scenarios (*205*). This type of analysis can hence provide insight for strategic selection and development of new or improvement of existing technologies.

As mentioned previously, one alternative chemical looping technology is Chemical Looping Dry Reforming (CLDR), where $CO_2$ is used as the oxidant instead of air. The focus of

this section is to conduct an exergetic study on the CLDR process as compared to conventional dry reforming of methane (DRM). As seen in Figure 42, the CLDR process consists two reactors: in the first reactor (the 'oxidizer'), $CO_2$ is used to oxidize an oxygen carrier metal to a metal oxide, and in the second reactor (the 'reducer') the metal oxide is reduced by a fuel. The net result is activation of $CO_2$ by its conversion to CO via combustion of a fuel. In previous work, we proposed the CLDR as a novel process for $CO_2$ activation and utilization (*191, 206*) and identified Fe/FeO or Fe/$Fe_3O_4$ carriers as well suited for the process.

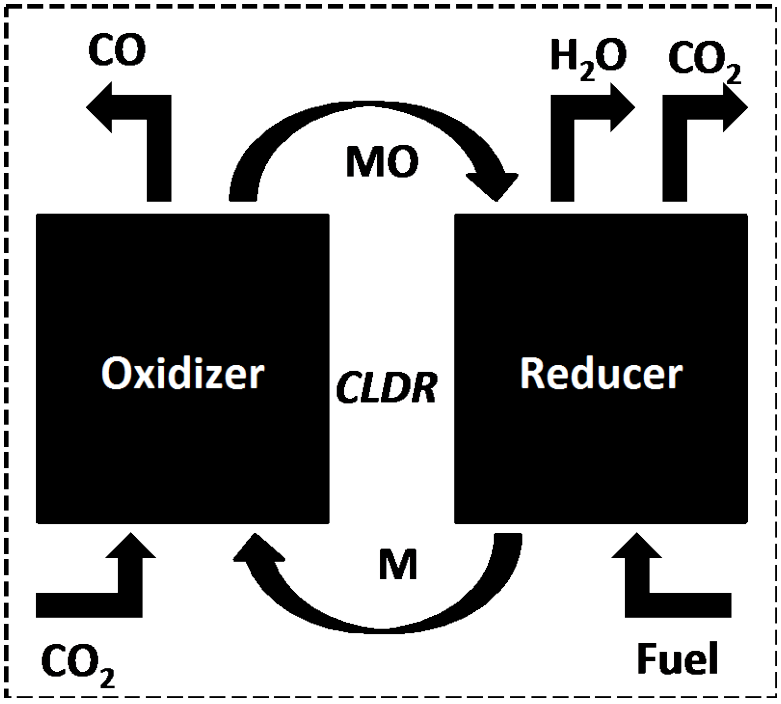


**Figure 42: Schematic of Chemical Looping Dry Reforming**

In order to study exergetic losses for CLDR, it is helpful to first step back and clearly define exergy and to consider it within the context of combustion. The exergy is a concept was introduced in the 1950s to describe the maximum usable energy that can be extracted from a system as is moves to equilibrium with its environment (*207*). In contrast to energy, which is always conserved in any process, exergy is destroyed by irreversible processes. Temperature

gradients, chemical mixing, friction, and chemical potential gradients are all recognized as sources of irreversibility in a thermodynamic system. Conventional combustion is fraught with irreversibility and is well-known to exhibit exergy losses of over 20% of the chemical exergy input (*146*).

Exergy (or usable energy) can enter a process in the form of either chemical or thermal exergy. The aim of this study was to calculate chemical exergy losses in CLDR since this was where a strong benefit has been seen for CLC and since it is these chemical reactions that have been modified for chemical looping reforming. Combustion and reforming processes have a chemical exergy input from the fuel (e.g., methane), which is defined as the Gibbs free energy of that material (E1). An exergetic loss is synonymous with an entropic loss during a process, as shown in Equation 2. For combustion and reforming processes specifically, this is proportional to the difference in entropy between reaction products ($CO_2$, CO, $H_2$, $H_2O$) and reactants ($CH_4$). Finally the % of chemical exergy lost can be calculated by relating the entropic (or exergetic) losses to the chemical exergy input.

(E1) Chemical Exergy into the System: $\Phi_{chem,in=}|\Sigma(G_i)_{in}|$ [cal/h]

(E2) Entropic Loss: $TdS = T(dS_{out}-dS_{in})$ [cal/h]

(E3) % lost = Entropic Loss/Chemical Exergy into the System

where G is Gibbs free energy, T is reactor temperature, and S is entropy

The chemical looping process is recognized as a more exergetically efficient process (*145*, *208*), with estimates of reaction exergy losses that are 1-3% lower than conventional combustion (*146*). This reduction in exergy losses stems from dividing the highly irreversible and unrestrained gas-phase combustion into two more reversible and more constrained solid-gas reactions (*145*). In fact, the CLC-concept was originally presented in the 1980s by Ritcher and

Knoche as a means for a more efficient combustion and has only very recently seen attention in the 21st century as a process for capturing $CO_2$.

The specific exergy, which is directly related to the Gibbs free energy, is a helpful metric for exergy analysis. High exergy molecules have a higher capacity to do work by driving chemical reactions forward, which then results in the evolution of molecules with lower chemical exergy. At the same time, any large changes in the chemical exergy between the reactants and products can result in irreversibility in the process. Methane has a high chemical exergy (as shown in Figure 43), which provides the chemical potential for both combustion and reforming reactions to occur. $CO_2$ and $H_2O$ from combustion are the lowest exergy products, but the formation of CO and $H_2$ by reforming is also possible. Meanwhile, the elevated exergy content of iron can allow reduction of $CO_2$ to CO. By this, one can see how the use of an iron-based carrier in CLDR might drive $CO_2$ reduction to CO.

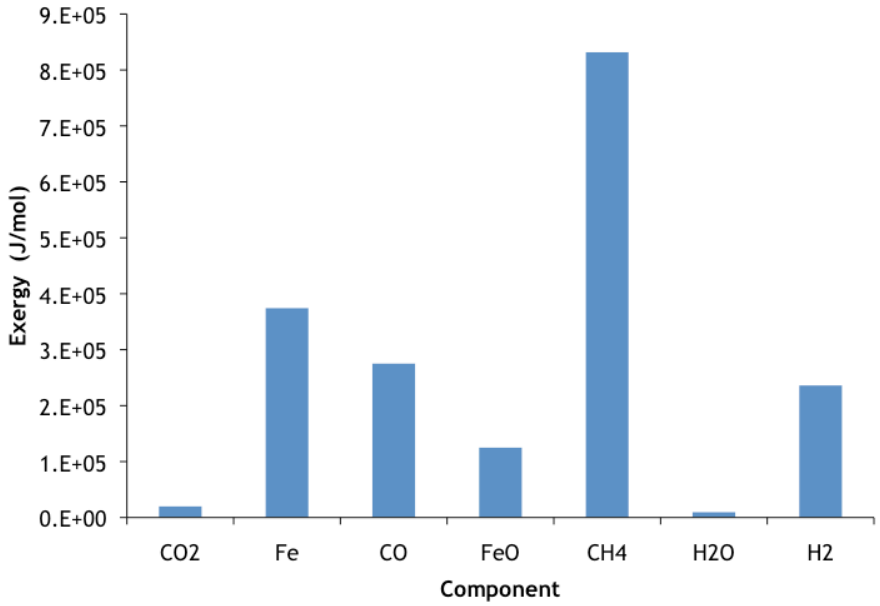


**Figure 43 Specific chemical exergy of DRM and CLDR reactants and products (*203*).**

Dry reforming of methane (DRM) is typically performed over a nickel or noble metal catalysts (*160, 209*). Reactor temperatures of 800-1000$^{o}$C are required to avoid carbon deposition and subsequent deactivation of the catalyst (*155, 162*). The process is endothermic, thus requiring a source of heat for the reactor that is above the reactor temperature. CLDR is also an endothermic process, and but the overall reaction enthalpy is comprised of the sum of the two half reactions. In previous work on CLDR, suitable reaction temperatures of 700-900$^{o}$C were identified based on a thermodynamic analysis (see section 2.3 and (*191*)). Since these temperatures are slightly lower than DRM and since entropic losses are proportional to temperature, this in turn contributed to reduced exergetic losses for CLDR.

Our study consists of first a reactor temperature optimization, followed by a simple exergy analysis in which the loss of initial chemical exergy is calculated.

**Methods**

Aspen plus was used to create process models of a single cycle of CLDR and a corresponding DRM reactor for a one mole of methane basis. For CLDR, an 'oxidizer' reactor was defined with $CO_2$ and Fe as the material stream inputs. The solid phase of the oxidizer effluent was used as an input feed for the 'reducer' via an Aspen flow sheet option variable. The 'reducer' also had an input stream of one mole of methane. For DRM, gas phase material streams of $CO_2$ and methane were fed to the single process reactor. All input streams were fed at the specified reaction temperature. In all cases isothermal Gibb's reactors were used for the analysis, which allows a free energy minimization to be performed to predict equilibrium compositions of product streams. The free energy minimization was performed with a user-specified constraint of possible molecules, which included the following: Fe, FeO, $Fe_3O_4$, $Fe_2O_3$, $FeCO_3$, $CO_2$, CO, C, $H_2$, $H_2O$, and $CH_4$. The Aspen model also calculated the necessary heat

duty for each reactor for the isothermal reactor condition. The Peng-Robinson property method was selected and material streams were designated as 'mixed' or 'cisolid' according to gas and solid and solid only phases, respectively. The studies were done at 1 atm.

**Results**

The process flow diagram for the CLDR model is shown in Figure 44.

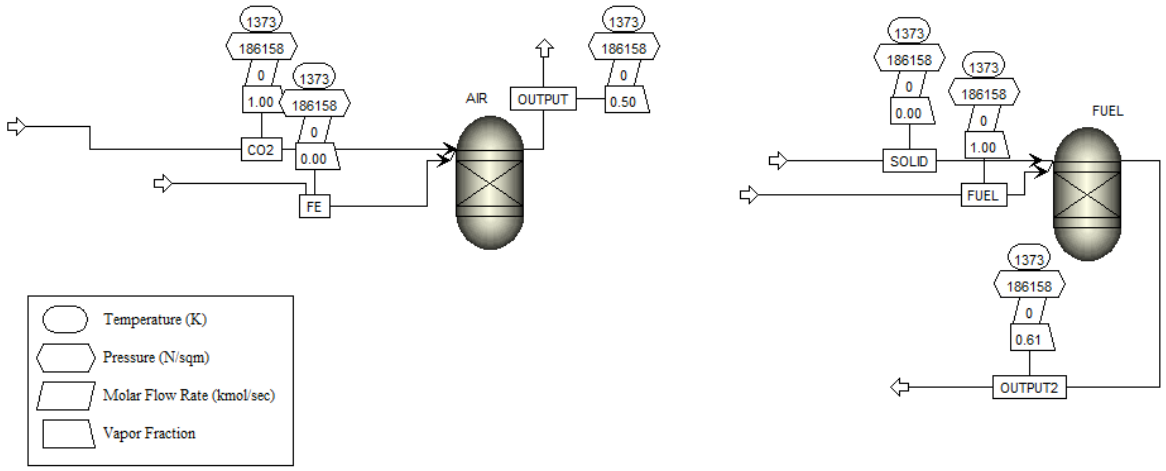


**Figure 44: Process flow diagram for CLDR Aspen model at T=1373 K and P=1 atm**

According to the reaction stoichiometry given in Table 5, the CLDR process is optimized for production of CO with an overall process feed ratio of $CO_2/CH_4$=3, or when full combustion of $CH_4$ to $CO_2$ and $H_2O$ occurs within the reducer. Alternatively, a feed ratio of $CO_2/CH_4$=1 reflects the case where partial oxidation of methane to CO and $H_2$ occurs in the reducer, and the reaction stoichiometry aligns directly with that of conventional dry reforming. While a larger amount of CO could be produced in the latter case, our analysis showed more favorable conversion for methane in the case for $CO_2/CH_4$=1, and selectivity for CO and $H_2$ were high despite changes in reactant feed ratios.

**Table 5: Feed ratios for CLDR process according to partial oxidation ($CO_2/CH_4$=1) or full oxidation ($CO_2/CH_4$=3) in the reduction reactor**

| Process | $CO_2/CH_4$=3 | $CO_2/CH_4$=1 |
|---|---|---|
| CLDR oxidizer | $4Fe+4CO_2 \rightarrow 4FeO+4CO$ $\Delta H_{298K}$=43.76 kJ/mol | $Fe+CO_2 \rightarrow FeO+CO$ $\Delta H_{298K}$=10.94 kJ/mol |
| CLDR reducer | $CH_4+4FeO \rightarrow 2H_2O+CO_2+4Fe$ $\Delta H_{298K}$=285.87 kJ/mol | $CH_4+FeO \rightarrow 2H_2+CO+Fe$ $\Delta H_{298K}$=236.38 kJ/mol |
| CLDR total | $CH_4+3CO_2 \rightarrow 2H_2O+4CO$ $\Delta H_{298K}$=329.63 kJ/mol | $CH_4 + CO_2 \rightarrow 2H_2 + 2CO$ $\Delta H_{298K}$=247.32 kJ/mol |
| DRM | $CH_4+3CO_2 \rightarrow 2H_2O+4CO$ $\Delta H_{298K}$=329.63 kJ/mol | $CH_4 + CO_2 \rightarrow 2H_2 + 2CO$ $\Delta H_{298K}$=247.32 kJ/mol |

An initial study of the reactor temperature was conducted in the range of 25-1100$^oC$ at $CH_4/CO_2$=1 (Figure 45). Carbon formation occurs in the oxidizer at up to 900$^oC$. For this reason, 900$^oC$ and 1100$^oC$ were selected as the possible process temperatures of interest for the study. At these temperatures, the model predicts FeO and Fe as the oxidized and reduced forms of the carrier, respectively. Carrier conversion was 80% at 900$^oC$ and 100% at 1100$^oC$ in both reactors. Virtually no $CO_2$ was formed at all temperatures studied in the reducer, demonstrating selectivity for partial oxidation products.

Percent conversion of reactants (left) and mole fraction of products (right) are given in Figure 46 for both the oxidizer and reducer combined. A slightly lower methane conversion was observed for CLDR compared to DRM. As expected according the reducer stoichiometry, the $H_2/CO$ ratio is closer to 2 for CLDR and 1 for DRM. This last result emphasizes another potential benefit of CLDR over DRM in that a higher $H_2/CO$ (preferred for downstream processes such as Fischer-Trophe) results without an additional processing step.

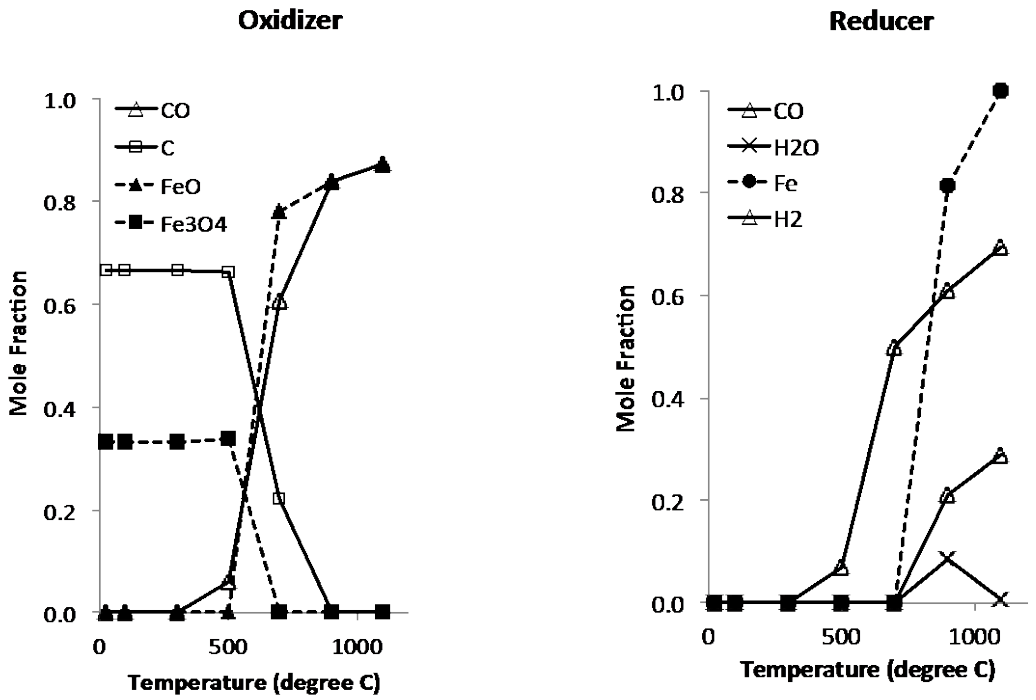


**Figure 45: Selectivity of products in the reducer reaction in oxidizer (left) and reducer (right). $CO_2$~0 at all temperatures in the reducer.**

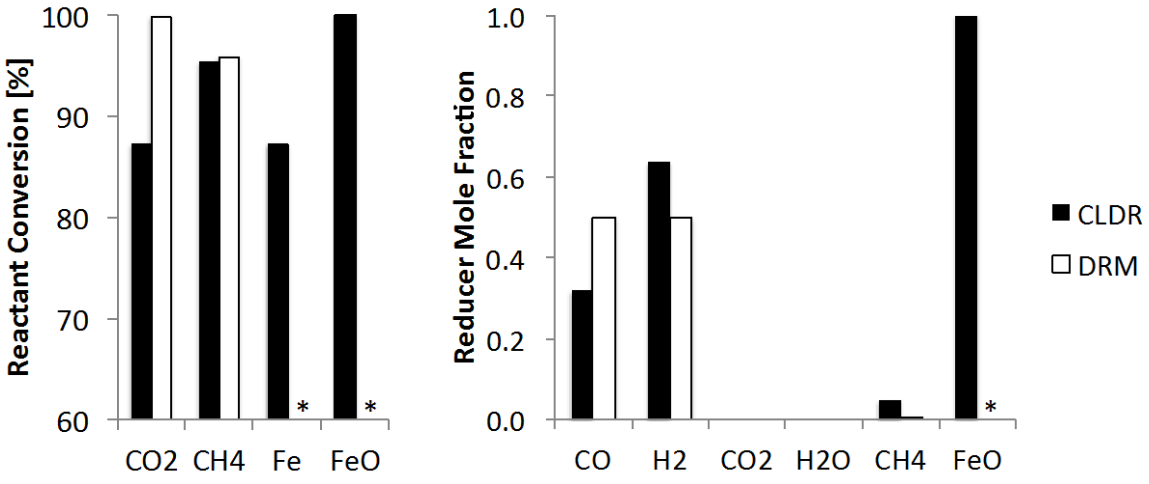


**Figure 46: Conversion of reactants (left) and mole fraction (right) of products predicted in Aspen for CLDR (filled bars) and DRM (open bars). * indicates not applicable for DRM.**

Finally, chemical exergy losses were found to be 1% lower for CLDR (59% versus 60%), which was calculated for the case of $CO_2/CH_4$=1 at 1100$^oC$ according to equations 1-3 and detailed in Table 6.

**Table 6: Relevant quantities for exergy analysis of CLDR and DRM, according to equations 1-3**

| Property | $CLDR_{tot}$ | DRM |
|---|---|---|
| Entropy out [cal/h] | 3.0E+08 | 2.8E+08 |
| Entropy in [cal] | 2.1E+08 | 1.8E+08 |
| Entropy Loss TdS [cal] | 9.1E+07 | 9.2E+07 |
| $\Phi_{chem,in=}\lvert\Sigma(G_i)_{in}\rvert$ [cal/h] | 1.5E+08 | 1.5E+08 |
| $\Phi_{chem,out=}\lvert\Sigma(G_i)_{out}\rvert$ [cal/h] | 2.0E+08 | 1.4E+08 |
| % $destruction_{chem}=TdS/\Phi_{chem}$ | 59% | 60% |
| Q [cal/h] | 4.6E+07 | 6.1E+07 |

## Conclusion

Here we have quantified the expected entropic loss of the CLDR process compared to that of dry reforming of methane. There is a slight reduction (1%) in entropic loss for CLDR and there is also a lower net heat duty for the CLDR reactors. According to $\Delta H=Q$ for the energy balance of the system, this second observation is at least partially reflected by the lower methane conversion for CLDR. Despite the minimal improvement in entropic efficiency for CLDR, a more pronounced efficiency improvement might be found in an analysis envelope larger than that of just the reactors. More importantly, the analysis of entropic losses does not account for the benefit of the higher $H_2/CO$=2 for CLDR, which is obtained at no cost to process efficiency.

This ratio is viewed as an ideal feed for Fischer-Tropsch and hence makes the CLDR reducer effluent a more convenient feedstock for the process. In sum, while our analysis shows little benefit for CLDR on the basis of reactor energetics, the process still holds promise for efficiency improvement in terms of a process intensification over the conventional dry reforming.

## 3.5 FE-BHA CARRIER FOR CHEMICAL LOOPING DRY REFORMING

**Note: The following results can be found published in Chemical Engineering Research and Design (*191*) and in Chemical Engineering Technology (*206*).**

Fe-BHA nanostructured carriers were characterized by transmission electron spectroscopy (TEM, JEOL 200), x-ray diffraction (XRD), and nitrogen sorption (BET). A typical TEM image of calcined material is shown in Figure 47, where an amorphous BHA matrix surrounds Fe particles with diameters of 15-20 nm. The $N_2$ adsorption isotherm in Figure 48 shows a typical hysteresis corresponding to type-IV mesoporous material with a broad pore distribution and pore sizes between 10-50 nm. These large pores are expected to facilitate ample access to the active carrier material by the reactive gases. BET surface area after calcination at 600$^o$C was 100-150 $m^2$/g. All Fe-BHA carriers had a weight loading of 33 wt% Fe. XRD analysis shows that oxidized material contains $Fe_2O_3$ while reduced material has peaks for Fe (*189*).

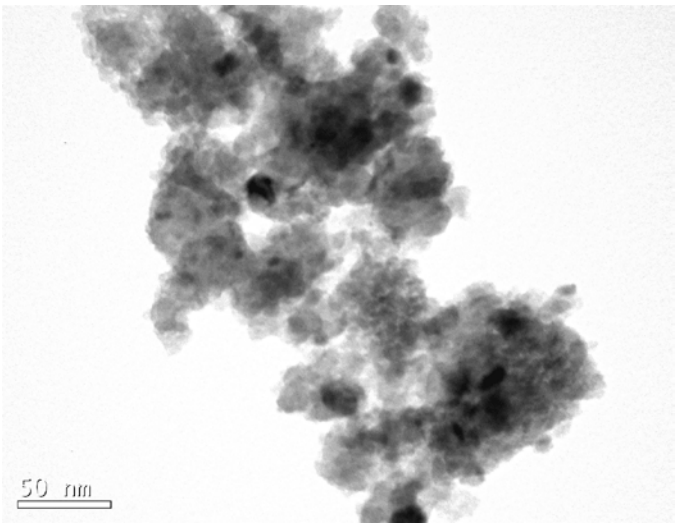


**Figure 47: TEM of Fe-BHA after calcination in air and then reduction in $H_2$ at 500°C.**

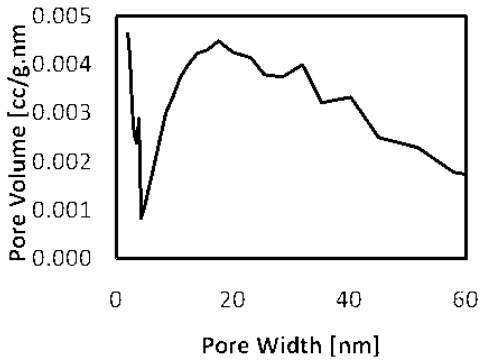


**Figure 48: Typical $N_2$ BET isotherm for Fe-BHA, showing large open pore structure for the material.**

To test the reactivity of the nanostructured Fe-BHA carrier materials, thermogravimetric analysis (TGA) and fixed-bed reactor studies were conducted using hydrogen as a model fuel. $H_2$ was chosen to avoid complications due to competition between partial vs. total oxidation pathways when using methane as fuel (as identified in the thermodynamic analysis above), and hence to focus on the oxidation of the carrier using $CO_2$ as an oxidant as well as on the stability of the carrier in cyclic redox operation. Coincidentally, using hydrogen as fuel in CLDR results

effectively in reverse water-gas shift (RWGS) as net reaction: $CO_2 + H_2 = CO_2 + H_2O$. While this reaction is of some industrial interest, the use of hydrogen is based entirely on the fact that it is a convenient, highly reactive model fuel with a single oxidation pathway.

Initial reactivity tests consisted of thermogravimetric analysis (TGA) of Fe-BHA material with $CO_2$ (20 sccm) as the oxidant, $H_2$ (20 sccm) as the reducing gas, and an Ar (60 sccm) gas purge phase between oxidation and reduction phases. It should be noted that unlike for CLC, where the purge phase is critical in order to avoid uncontrolled mixing of oxygen with fuel upon switching between oxidation and reduction phases, CLDR does not require such a purge phase and it is added in the experiments purely for the purpose of attaining separated gas phase signals from each half-cycle.

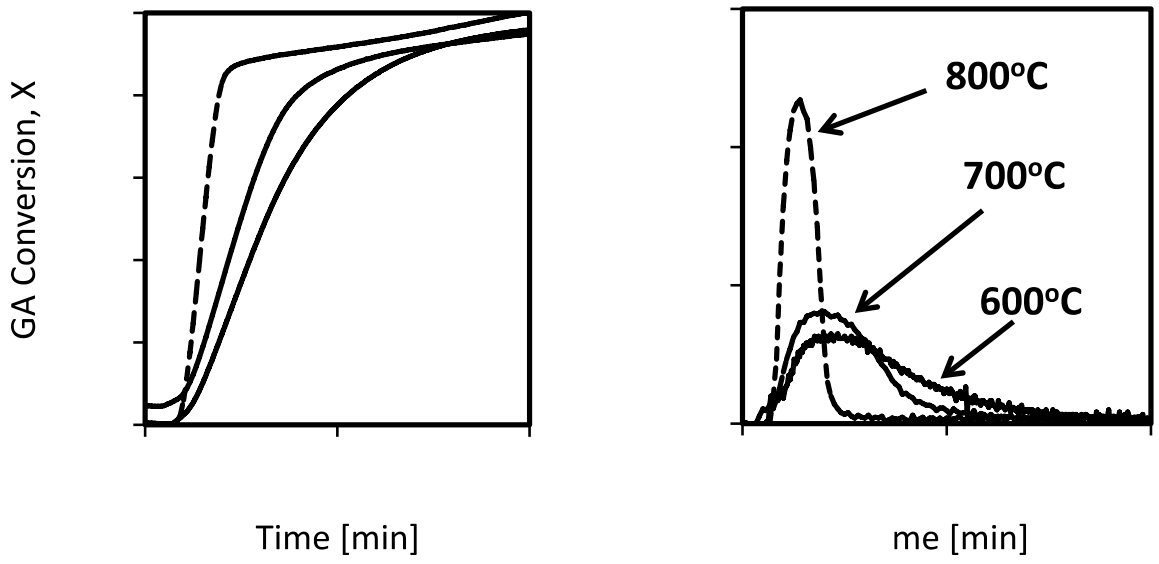


**Figure 49: TGA conversion of Fe-BHA carrier during $CO_2$ oxidation at 600, 700 and 800°C (left) and time derivation of TGA conversion, dX/dt (right).**

Carrier conversion in TGA can be defined as $X = (M_t-M_{red})/(M_{ox}-M_{red})$, where $M_t$ represents the sample mass at time *t*, $M_{red}$ is the mass of the fully reduced sample, and $M_{ox}$ the mass of the fully oxidized sample. Hence, X= 0 corresponds to the fully reduced carrier (Fe) and

X=1 corresponds to a fully oxidized carrier ($Fe_3O_4$). This renormalizes TGA weight curves, and allows calculation of a conversion rate, dX/dt, by computing the time derivative of the conversion time traces.

Figure 49 (left) shows the sample conversion (X) versus time during oxidation of a 33 wt% Fe-BHA carrier sample at three temperatures (600, 700, and 800$^o$C). One can see that the reduced and oxidized sample weights (i.e. lowest and highest sample weights, respectively) agree within experimental error between all three experiments, indicating that the same degree of conversion is achieved in all cases. Furthermore, the sample weight increases initially very rapidly, and then slows down before reaching the final value. This is particularly pronounced at the lower two temperatures, while the kinetics at the highest temperature of 800$^o$C show a much faster, almost step-wise transition from the reduced to the oxidized state within ~2-3 min. Finally, carrier utilization was calculated to be 84% for Fe-BHA in TGA cycles with $H_2/CO_2$ cycling, i.e., 84% of the iron available in the material reduces to Fe and re-oxidizes to $Fe_3O_4$.

Figure 49 (right) shows the results of these calculations as rate dX/dt versus time t. Again, the fast initial rate of oxidation is apparent with a subsequent slow-down of the oxidation rate. Strikingly, however, the rate is only mildly increased upon raising the temperature from 600 to 700$^o$C, and then shows a very strong increase from 700 to 800$^o$C. It is interesting to review this observation in connection with the thermodynamic calculations given in section 3.3. The temperature range between 600-800$^o$C corresponds to a range where thermodynamics predicts a transition in the selectivity of the oxidation reaction from carbon to CO as the main product. Thus, the transition to the much faster oxidation at 800$^o$C may be associated with this switch in the reaction path. This could be due to either the reduction of CO to C being much slower than the first oxygen abstraction such that overall carrier oxidation is slower, or because the formation

of carbon at lower temperatures results in carbonaceous residues on the sample surface that introduce mass transfer limitations. Observations from the fixed-bed reactor experiments discussed below suggest that small amounts of carbonaceous deposits are indeed present, supporting the second explanation. However, the fact that the sample weight is essentially unchanged with temperature indicates that the amount of these carbon deposits must be small.

Following the cyclic TGA experiments, the Fe-BHA samples were subjected to cyclic reduction-oxidation in a fixed bed reactor configuration. 220 mg of Fe-BHA were loaded into a quartz-glass tube (1/4" I.D.) and placed horizontally in an electric oven. This system was heated to 700$^{o}$C in Ar and then alternating phases of $H_2$ and $CO_2$ were contacted with the Fe-based carrier at a flow rate of 5 sccm at 700$^{o}$C for six ~30 min. oxidation and reduction cycles. Reduction and oxidation half-cycles were again separated by an Ar purge phase. The product gases were monitored via mass spectrometry (Pfeiffer Omnistar QMS 200).

Figure 50 shows all 6 cycles (top) along with a more detailed breakout of a single cycle below. The results show stable cyclic operation of the carrier as apparent from the unchanged product gas traces for the entire duration of the experiment (~10 hrs.). Review of a single cycle shows a fast onset of CO formation in the reactor effluent as a result of $CO_2$ reduction during the oxidation half-cycle, followed by a slow decay for the CO signal over the next ~20 min. of operation. Similarly, $CO_2$ conversion is very high over the first ~10 min. of the oxidation phase, and then decreases in parallel with the decreasing CO formation. Clearly, in order to attain high CO yields, the oxidation phase should be stopped after ~10 min. of operation and the reactor should be switched to the reduction phase.

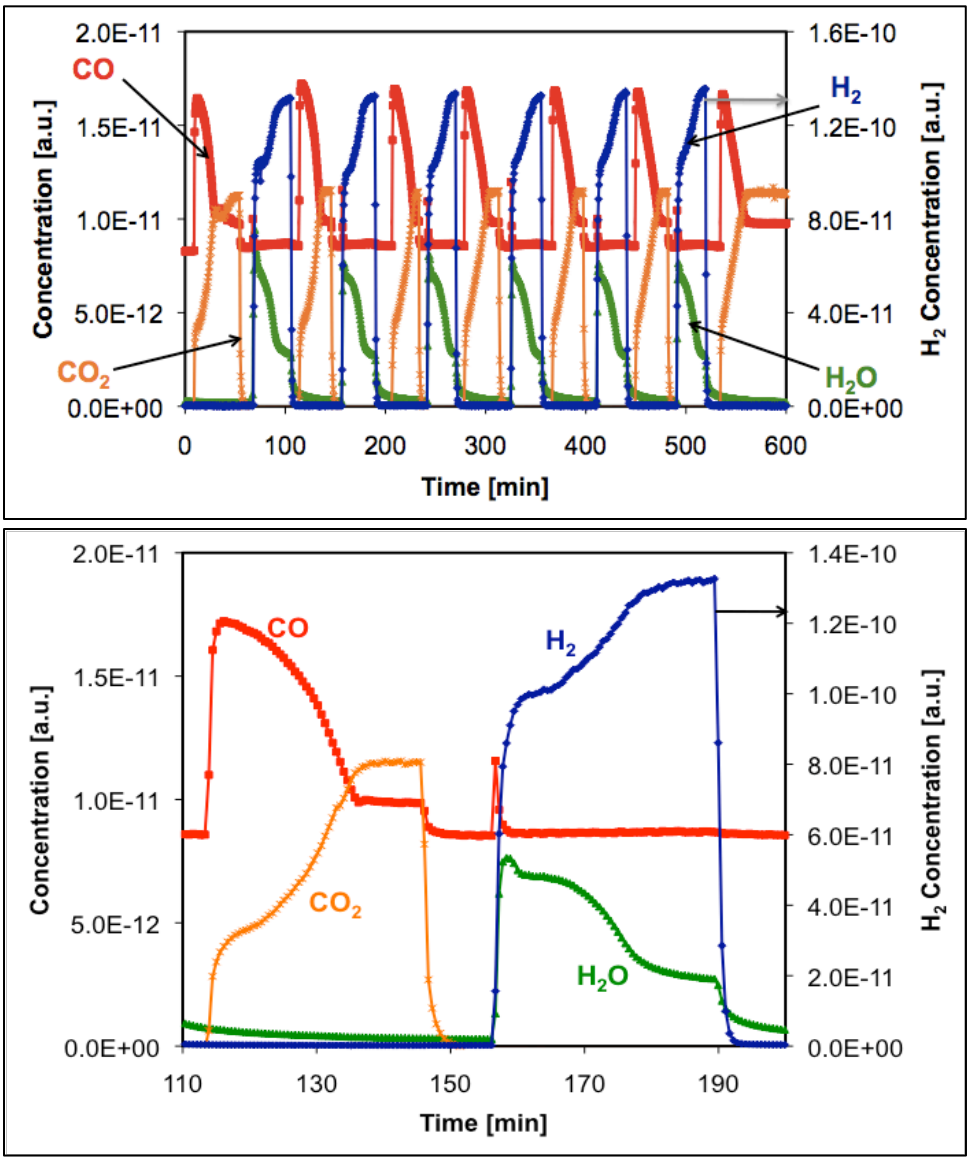


**Figure 50: 6 cycles with Fe-BHA with $H_2$ (as a model fuel). Inset shows a single cycle with CO production during oxidation half reaction and $H_2O$ production during reducer half reaction.**

During the reduction half-cycle, one can see similar trends as during oxidation: A very fast onset of $H_2O$ formation indicates fast reduction of the carrier, transitioning to slower reduction after ~15 min., i.e. halfway through the cycle. Interestingly, continued water formation indicates that even after 30 min., i.e. at the end of the reduction half-cycle, the carrier is not yet completely reduced. Hydrogen conversion remains incomplete at all times throughout

the reduction half-cycle, indicating that slower flow rates, i.e. increased contact times, and would be preferable for efficient reactor operation. By limiting the oxidation and reduction half-cycles to the first ~10 min. each, and by adjusting the feed flow rates, CO yields and $H_2$ conversion could potentially be maximized, however, at the expense of carrier utilization.

Finally, a small, but reproducible, CO pulse at the very onset of the reduction cycle indicates the presence of a small amount of carbon on the sample, which is gasified by the steam formed during carrier reduction. This is in agreement with the interpretation of the TGA experiments, discussed above, as well as with the results of the thermodynamic analysis indicating that 700$^o$C is roughly the upper temperature range at which carbon formation must be expected.

This experiment was repeated several times with different operating conditions (*206*). 50 mg of carrier were used with 5 vol% $H_2$ (5 sccm) in Ar for reduction an 20% $CO_2$ (20 sccm) in Ar for oxidation with 10 min reduction/oxidation phases and 15 min purge phases. An assessment of multiple temperatures was done in which an Arrhenius-type increases in reaction kinetics with temperature was observed. Estimates for carrier conversion were calculated at 13%, 34%, and 51% for 600, 700, and 800$^o$C. Since improved kinetics were observed at higher temperature, 11 cycles were run at 800$^o$C, showing stable operation for all cycles.

Overall, the TGA and fixed-bed reactor experiments indicate that CLDR with Fe-based carriers could potentially be a feasible process. However, the relatively low reactivity of both $CO_2$ as well as Fe, and the potential for carbon formation will require careful design and operation of such a process. Additionally, this data only represents studies done with $H_2$ as a model fuel, which still does not demonstrate the ability of the material to operate under the proposed CLDR process scheme with methane as the fuel to complete dry reforming.

Testing of the reduction of Fe-BHA in methane was in fact attempted in the TGA (Figure 51). Although some reduction was observed, oscillatory behavior in the weight trend suggested the formation of coke. Elemental analysis (EDX) of Fe-BHA (a 33 wt% Fe as-synthesized sample) on a copper plate after methane reduction shows just 29 wt% Fe and a surprising 22 wt% carbon, confirming significant coking even though weight gains were not observed during reduction operations. Coke whisker formation was also seen in TEM micrographs after TGA with methane, which is also shown in Figure 51 (right). Elemental analysis of the effluent gas was done for this particular TGA test by connecting a mass spectrometer to the outlet stream of the TGA. In Figure 52, a decrease methane ion current and strong increase in $H_2$ ion current is observed after 30 min, corresponding with the weight perturbations seen in TGA. This is indicative of the methane decomposition reaction according to $CH_4 \rightarrow 2H_2 + C$.

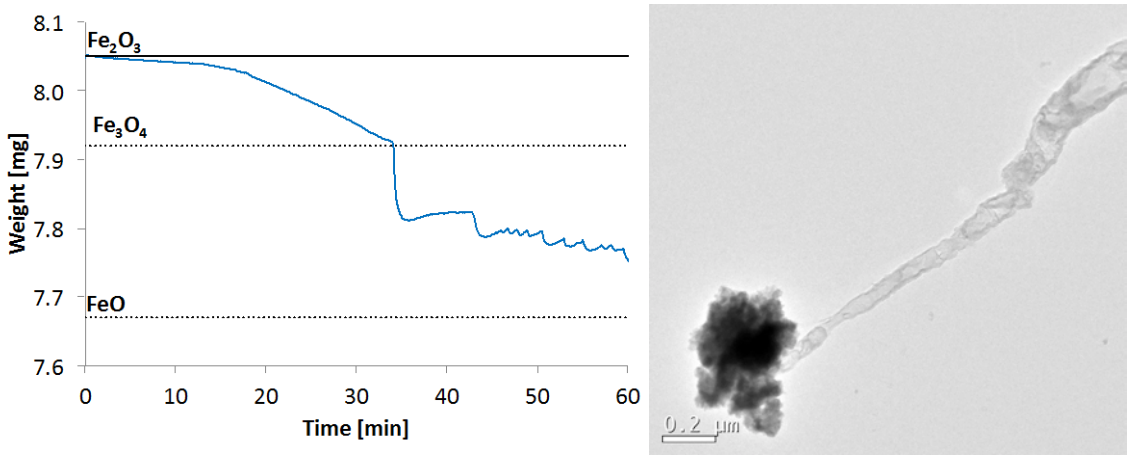


**Figure 51: TGA curve during reduction with $CH_4$ ($CH_4$=20 sccm, purge=60 sccm) and TEM of Fe-BHA after reduction in methane at 700°C, showing carbon whiskers.**

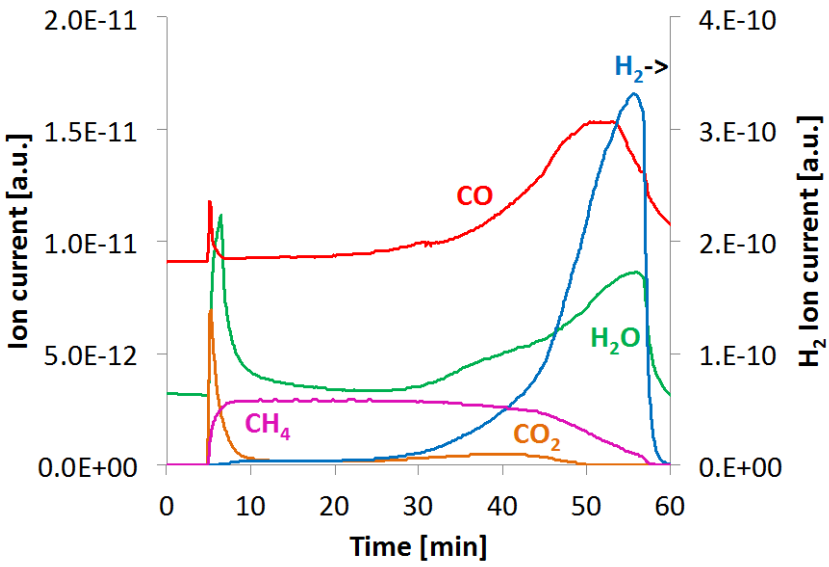


**Figure 52: Mass spectrometry data of TGA effluent gas stream during reduction of Fe-BHA with methane. Show transition to methane decomposition after 30 min.**

Overall, the analysis of Fe-BHA has led to the following conclusions: superior performance of Fe-BHA over materials with other supports (such as silica) in terms of fast redox kinetics, high carrier utilization, high material stability, and *yet* significant carbon formation with $CH_4$ reduction for Fe-BHA materials.

## 3.6 DEVELOPMENT OF HIGHLY-TUNABLE IRON CORE-SHELL STRUCTURES FOR OXIDATION-REDUCTION CHEMISTRY

Several types of core-shell nanostructures were developed for chemical looping applications as part of this work. In this section, we will discuss various synthesis modifications used to tune the material properties of these nanostructures. From a basic nanomaterials perspective, the importance of developing novel core-shell materials extends beyond our focus of gas-phase redox reactions; core-shell iron materials have also been studied for a range of applications, including drug delivery (*65*), biological imaging (*15, 210*), sensors (*211*), environmental remediation (*66*), and sorbents (*212*). Thus, a detailed understanding of the critical 'tuning knobs' available during material synthesis is a key aspect that can govern whether these nanomaterials have a broader application. In all cases, iron served as the core while silica and ceria were incorporated as thermally and mechanically stable supports.

**Silica-Supported Materials**

Fe@$SiO_2$ materials (i.e., iron core surrounded by a silica shell) are shown in Figure 53. In each case, the amount of iron precursor added to the synthesis was modified (0.4-2 mmol) to result in slightly different iron core diameters. These modifications were done to discern the robustness of the synthesis method as well as the tunability of the iron content and silica shell thickness of the materials. The median diameter of the Fe cores and the silica shell thickness is shown in Figure 54 for varying Si:Fe molar ratios. The median core diameter is fairly constant at ~8 nm for the higher iron loadings emphasizing that the surfactant/water ratio governs the iron

core diameter. Put another way, an increase in iron loading within the capacity of the system leads only to an increase in the number of micelles and not larger cores. The silica shell thickness is also smaller at higher iron loadings, again indicating the formation of more micelles within the microemulsion system, and hence reducing the amount of TEOS available for each individual micelle. Yet smaller cores can be easily be formed (4-7 nm) by decreasing the Fe loading.

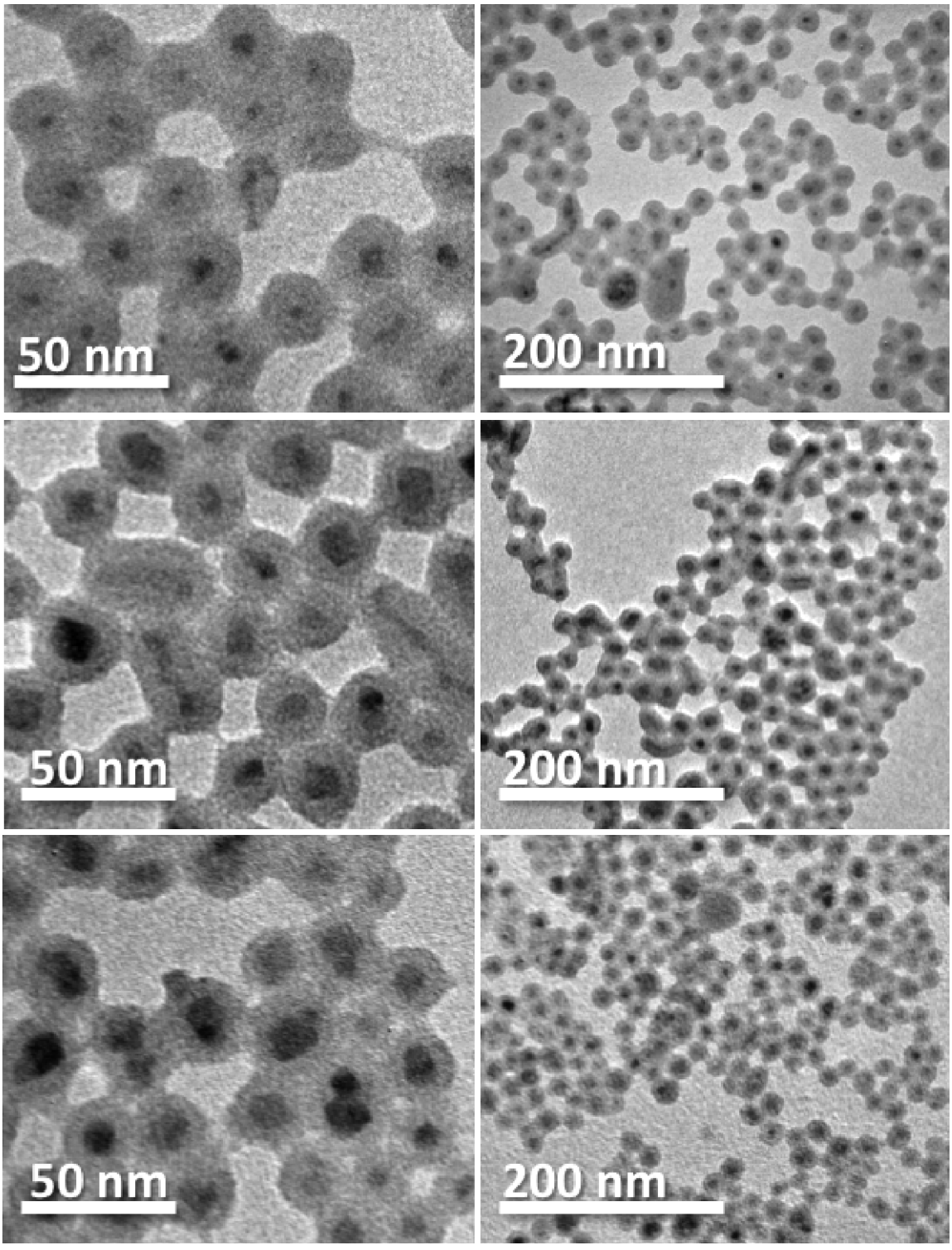


**Figure 53: Core-shell Fe@$SiO_2$ materials at high magnification (left images) and lower magnification (right images). Iron addition amounts as follows: 0.4 mmol Fe (top), 1.5 mmol Fe (middle), and 2 mmol Fe (bottom).**

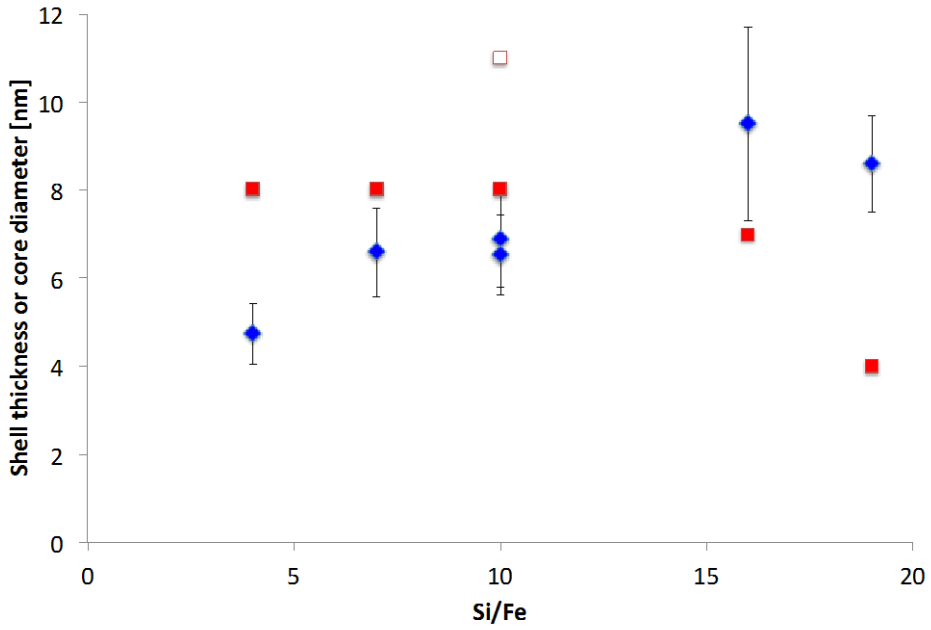


**Figure 54: Relationship between Si:Fe molar ratio and mean shell thickness (diamonds) and median iron core diameter (squares). Open square indicates a synthesis in which a lower surfactant to water ratio was used, resulting in a larger diameter iron core.**

A high-resolution image of the Fe@$SiO_2$ is shown in Figure 55, in which the lattice structure of the iron can easily be seen within the amorphous silica shell. Finally, in SEM (Figure 56) the spherical surface expected for microemulsion synthesis is observed.

BET surface areas for these material are typically 250-290 $m^2/g$ and porosity is ~0.7 nm (NETL, micropore analyzer, Figure 57). Following oxidation in air and reduction in $H_2$ of the fresh sample at 500$^o$C, crystal structures were identified in XRD to be $Fe_3O_4$ and Fe, respectively. A more detailed XRD analysis done in conjunction with reactive tests (see section 3.7), revealed $Fe_2O_3$ as an accessible phase as well. Overall, this demonstrates that the iron core

is active in redox reactions while protected within the silica shell. The typical synthesis yield is ~1.2 g after calcination.

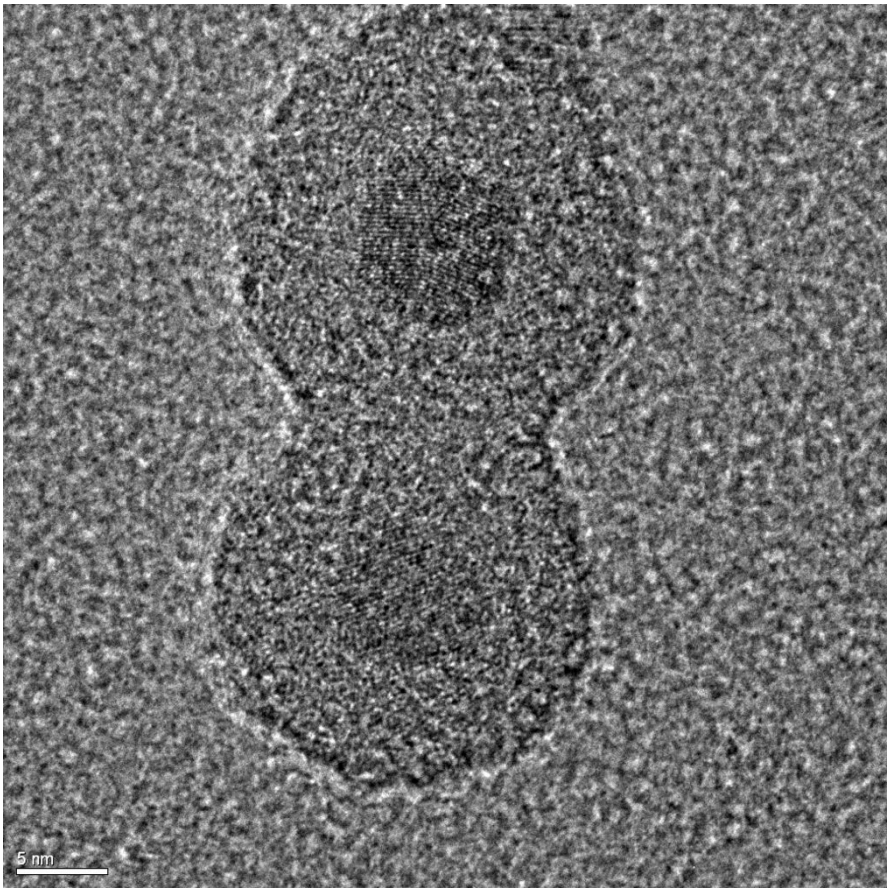


**Figure 55: High resolution TEM of $Fe@SiO_2$ for iron addition amount of 2.5 mmol Fe.**

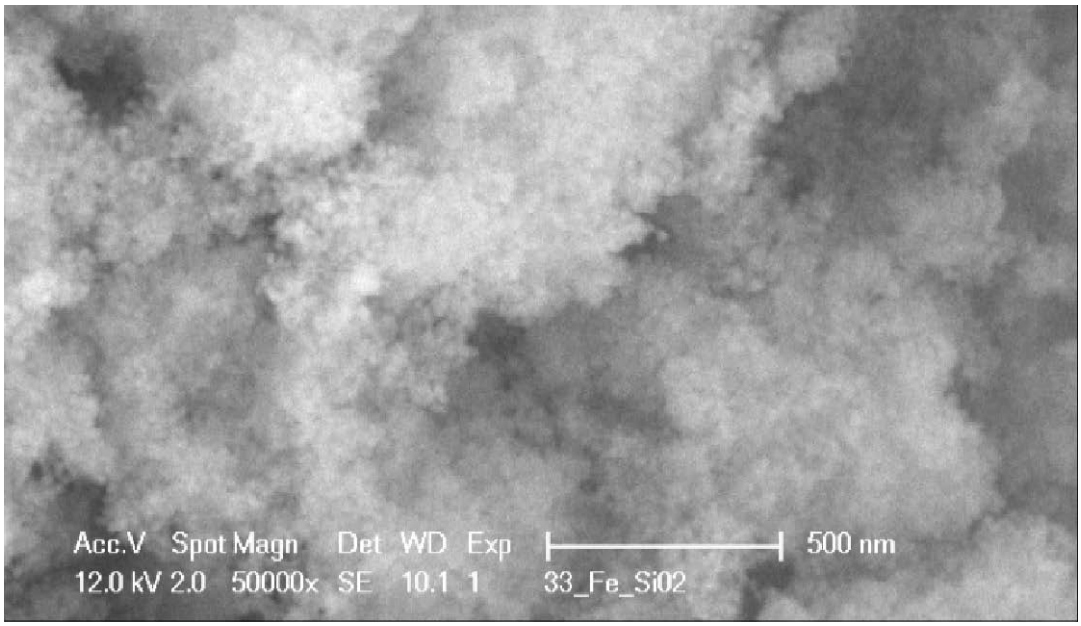


**Figure 56: Typical SEM image of spherical Fe@$SiO_2$ material.**

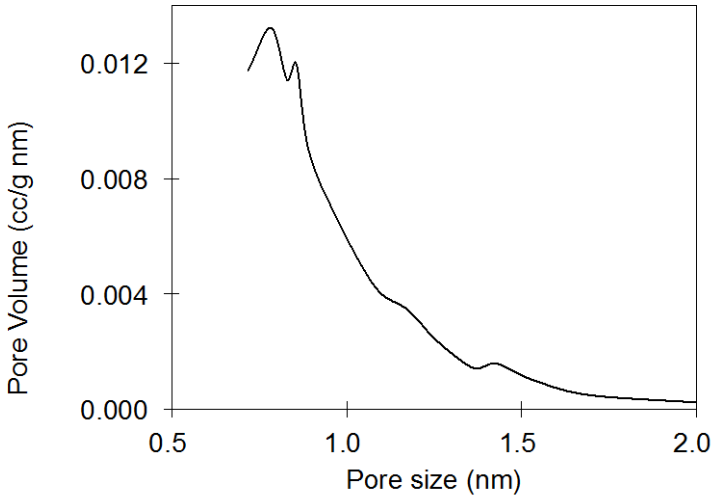


**Figure 57: BET pore distribution for core-shell material made from microemulsion, showing typical pore size near 0.7 nm.**

Previous work in our laboratory has indicated that these types of materials can suffer from mass transfer limitations, which might be avoided by incorporating thinner silica shells (*69*). This motivated us to design material with the highest possible loading and thinnest

possible silica shell. Yet at high metal loadings, the core-shell morphology is more susceptible to collapse and irregularity. An example is shown in Figure 58, with an iron loading of 41 wt%. While this thin-shelled material was found to respond well in high temperature oxidation-reduction reactions (see section 3.7), the synthesis itself was not reproducible, probably due to an instability that the high iron content contributes to the microemulsion.

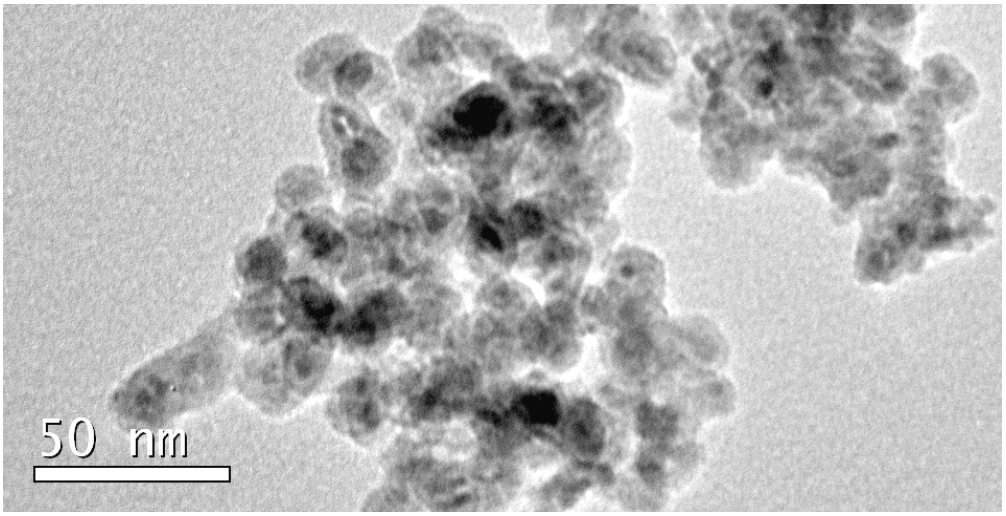


**Figure 58: Poorly defined core-shell material with 41 wt % Fe and very thin silica shell (~4 nm).**

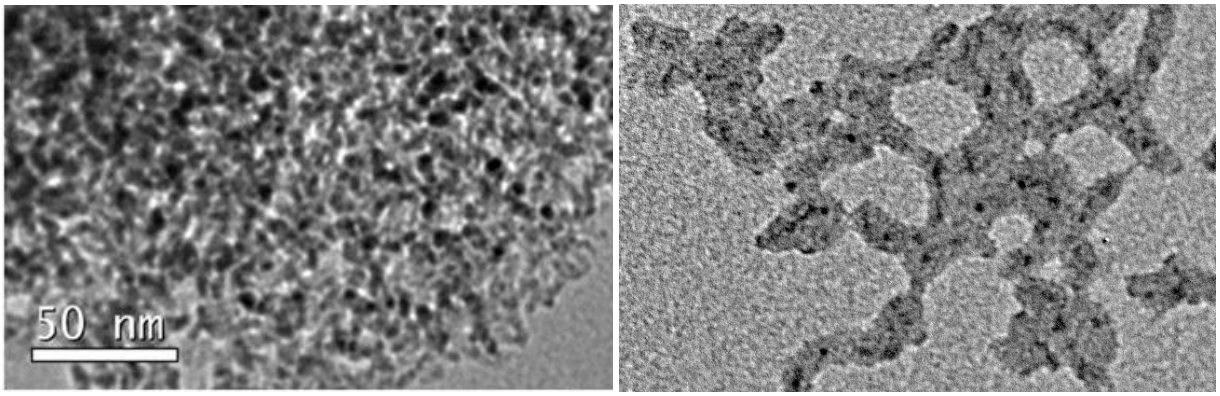


**Figure 59: Materials resulting from synthesis modifications of excluding hydrazine with 1 hr (left) and 2 hr (right) silica hydrolysis time. 50 nm scale bar applies to both images.**

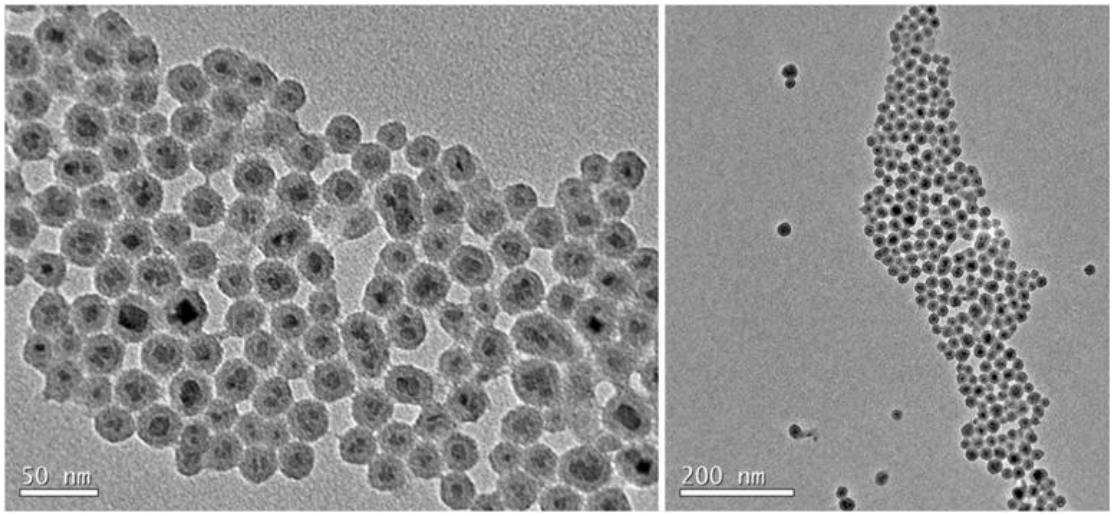


**Figure 60: TEOS and $C_{18}$TMS used as silica precursor in microemulsion synthesis to obtain a more open pore structure.**

Lastly, we made other modifications aiming to either decrease the iron particle size or increase the accessibility of the iron core within the silica shell, i.e. to facilitate increased activity of the material. First, exclusion of the hydrazine reduction step results in a composite-like structure instead of the core-shell morphology, with iron dispersed within a silica matrix. With a 1 hr hydrolysis step, the material is 52.3 ± 8.2 wt% Fe with a high surface area of 331 $m^2g^{-1}$, and the iron particles are too small to even measure accurately (Figure 59, left). If the hydrolysis time is 2 hr, the loading is just 11.53 ± 0.33 wt % Fe, with 2-3 nm dispersed Fe particles (Figure 59, right).

Alternatively, octadecyltrimethoxysilane ($C_{18}$TMS, 90%, Sigma-Aldrich), a silica precursor with a bulky side chain, can be supplemented with TEOS (4.7 mol TEOS: 1 mol $C_{18}$TMS) to create a modified silica structure in which a pore size of ~2-3 nm is expected (*58, 124*). A similar core-shell structure was achieved (Figure 60) with a BET surface area of 185 $m^2g^{-1}$, but there was in fact no discernable difference in pore distribution compared to TEOS alone. These final structures all represent interesting potential pathways for nanomaterial

applications. However, initial testing showed that they were not active for our application and henceforth will not be discussed further.

**Hollow Fe@$SiO_2$**

The highest possible oxidation state of core-shell iron structures can be $Fe_3O_4$ with smaller amount of $Fe_2O_3$ (*173*), even after extended air exposure. Indeed, XRD analysis of our calcined Fe@$SiO_2$ material has aligned with either $Fe_3O_4$ or $Fe_2O_3$ in different instances, demonstrating that there may be some kinetic impedance to complete oxidation of the core. Yet some researchers have made $Fe_2O_3$ core-shell structures by coating pre-formed iron oxide particles with silica (*123, 187, 213*). For our redox application, $Fe_3O_4$ core-shell structures do not directly impose any limitation given that this is the highest oxidation state achievable with $CO_2$ as an oxidizing gas. However, the space confinement of the nanoparticle within the silica shell may still limit the oxidation susceptibility of the nanoparticle whereas a hollow structure might facilitate a larger region for oxidation. Additionally, oxide overlayers on particles can limit the extent of iron oxidation (*189*) and thus a smaller critical particle dimension could alleviate this limitation.

With this in mind, hollow Fe@$SiO_2$ (hFe@$SiO_2$) materials were developed, based on the work of Hyeon and coworkers (*187*), and are illustrated briefly in the schematic shown in Figure 61. The first part of the procedure involves the synthesis of rod-shaped β-FeOOH structures. Next, the rods are wrapped in a silica shell to form β-FeOOH@$SiO_2$. Extended oxidation of this material leads to hollow $Fe_3O_4$@$SiO_2$ or $Fe_2O_3$@$SiO_2$ due to a density decrease from β-FeOOH to $Fe_3O_4$ or $Fe_2O_3$ (3 g $cm^{-3}$ versus 5 g $cm^{-3}$). The hollow cavity can be opened up further with $H_2$ reduction to form Fe@$SiO_2$.

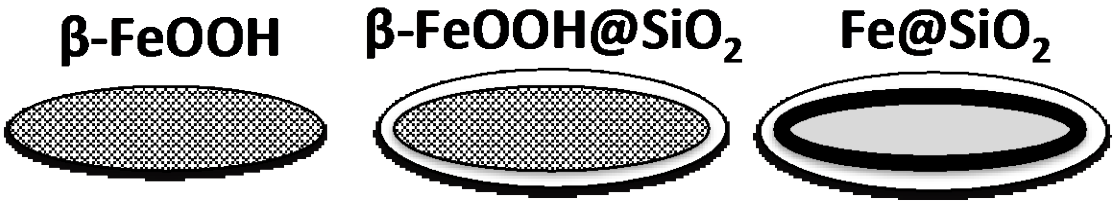


**Figure 61: Schematic of hFe@$SiO_2$ synthesis, involving fabrication of rod-shaped low density iron precursor, followed by wrapping in silica and calcination in air or reduction in hydrogen to result in a hollow center.**

Control over the morphology of the β-FeOOH precursor is perhaps the most critical and challenging part of the synthesis, as it dictates the morphology and polydispersity in the final silica-coated material. The β-FeOOH rods can be made by either hydrolysis (*187, 214-216*) or hydrothermal synthesis (*217, 218*).

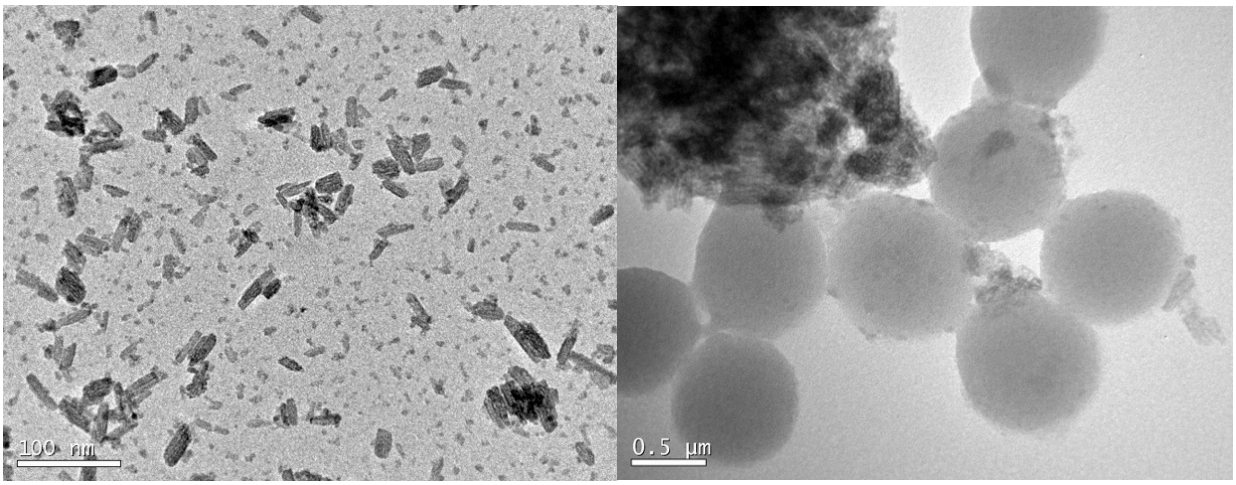


**Figure 62: Fe-based material made with hydrolysis synthesis route, exhibiting both β-FeOOH rods and small spherical $Fe_2O_3$ particles in both TEM (left), ineffective wrapping of $Fe_2O_3$ particles (right).**

For synthesis via hydrolysis, we found it difficult to avoid formation of $Fe_2O_3$, an example of which is shown in Figure 62. $Fe_2O_3$ structures were found in turn to not be accessible to silica wrapping via this synthesis route and furthermore are not suitable for making

hollow materials. Figure 62 shows the resultant material, consisting of Stober-type silica spheres co-mingled with the $Fe_2O_3$ structures.

Still, the hydrolysis synthesis route is not without value. In fact, we found also one interesting result with the addition of urea in accordance with Music et al. (*218*), resulting in more pointed β-FeOOH spindles that adopted a unique anti-parallel orientation (Figure 63), but unfortunately had a strong bimodal particle size distribution as seen by the tiny particles in the image background. Additionally, Piao and coworkers, who originally developed this synthesis route, successfully used a hydrolysis method to obtain their β-FeOOH precursor particles for wrapping (*187*). And finally, we were also able to achieve silica-wrapped hFe@$SiO_2$ (discussed more below) at least once with this method, although the silica thickness of these structures was far too large to be practical for our application.

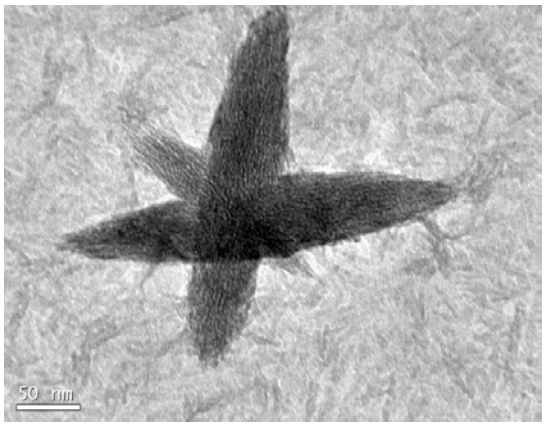


**Figure 63: Fe-based precursor particles synthesized via hydrolysis with urea additive, resulting in spindles in anti-parallel alignment and a background population of spindle structures that are much smaller in size (right).**

Despite our marginal success with hydrolysis synthesis, hydrothermal synthesis was found to exhibit better reliability for our purposes. The synthesis was held for 16 hrs at 80°C, and the resultant structures are shown in Figure 64 and Figure 65. Some optimization was

required to identify these conditions; shorter synthesis times (<8 hrs) appeared to result in incompletely formed or truncated rod structures while extended synthesis times led to dense square structures (likely consisting of $Fe_2O_3$), which were not suitable for this synthesis route (Figure 66).

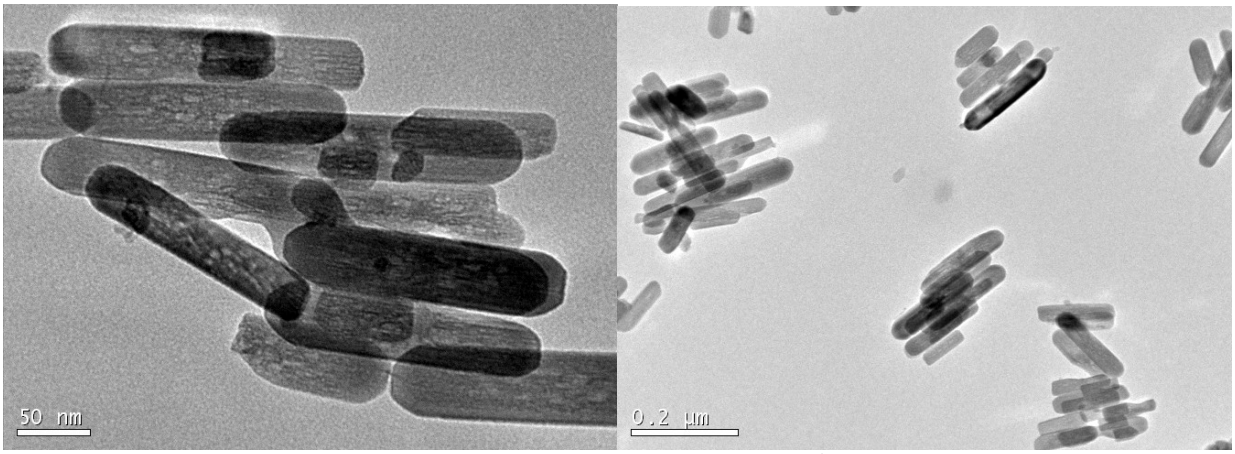


**Figure 64: β-FeOOH rods synthesized via hydrolysis (16 hrs, 80°C).**

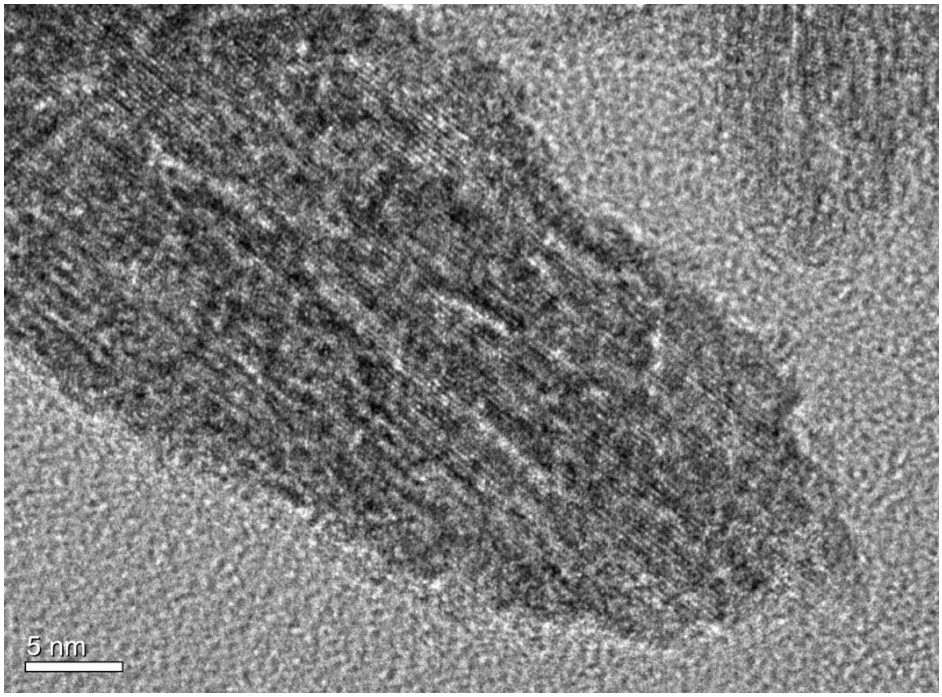


**Figure 65: High resolution TEM of β-FeOOH rods.**

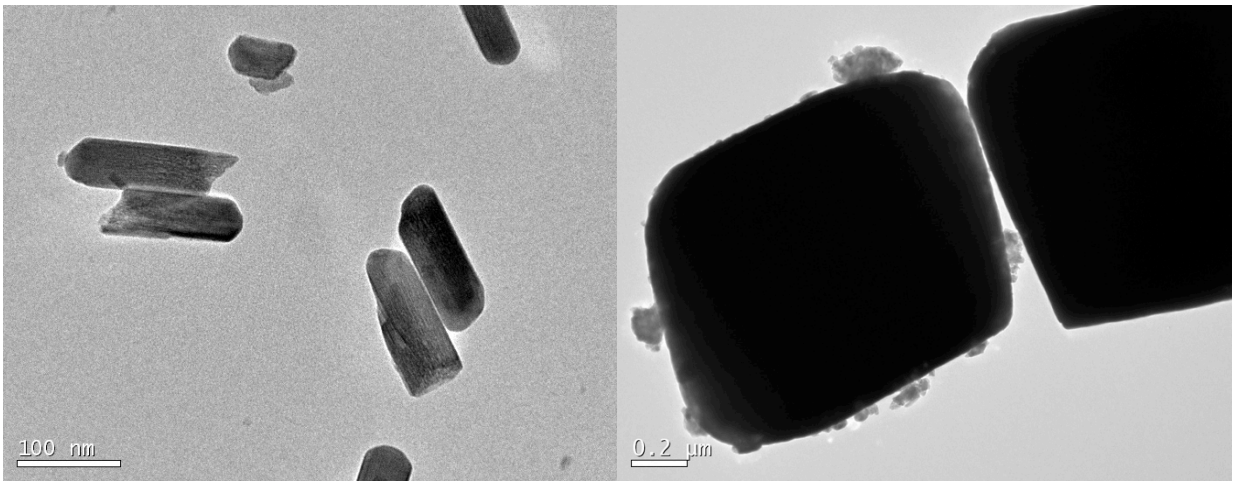


**Figure 66: Hydrothermal synthesis products after 5 hr (left) with truncated rods, and after 48 hr (right) with large square structures.**

Although the 16 hr hydrothermal synthesis was optimized according to observed β-FeOOH rods in TEM, XRD analysis revealed that $Fe_2O_3$ is not avoided entirely (Figure 67). Hence, finer control and further optimization over the synthesis of the iron pre-cursor might further improve the final morphology of the silica-coated material described below.

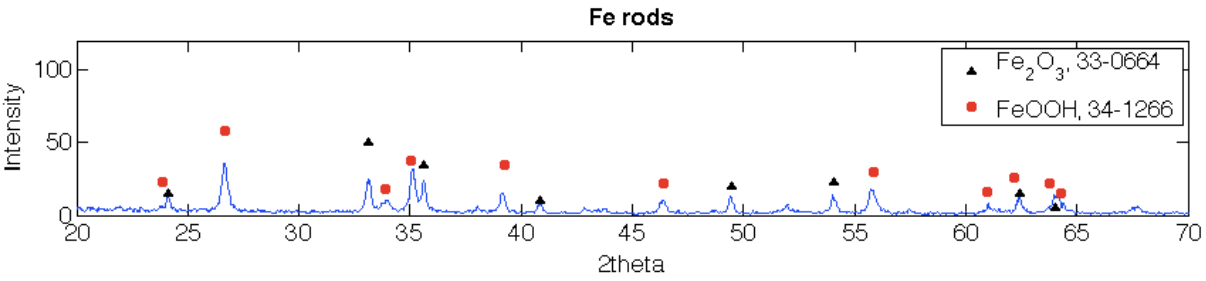


**Figure 67: XRD of Fe rods synthesized hydrothermally (16 hrs, 80°C)**

After optimization of the iron rod synthesis, the next step of wrapping with silica was assessed in more detail. Iron precursors were coated with silica via a modified Stöber synthesis, as depicted in TEM in Figure 68. Here one can clearly see the material is comprised of a hollow interior surrounded by a dark shell of iron, which in turn is surrounded by a light grey amorphous silica shell. The fresh calcined material had a BET surface area of 23 $m^2/g$ and an iron content of

~20 wt %. As described by (*187*), the materials were accessible to gas-phase oxidation, and XRD analysis showed oxidation up to $Fe_2O_3$ and reduction in $H_2$ led to formation of Fe (not shown). In terms of the silica coating, systematic modifications were made to the synthesis to reduce the silica shell thickness, as was done with the non-hollow Fe@$SiO_2$ materials. This was done by incrementally reducing the amount of TEOS added or by increasing the mass of β-FeOOH particles used in each synthesis, thereby decreasing the Si:Fe ratio. The relationship between the Si:Fe ratio and silica shell thickness for these materials is shown in Figure 68 (right). SEM images (Figure 69) of the material are also shown with distinct capsule shapes.

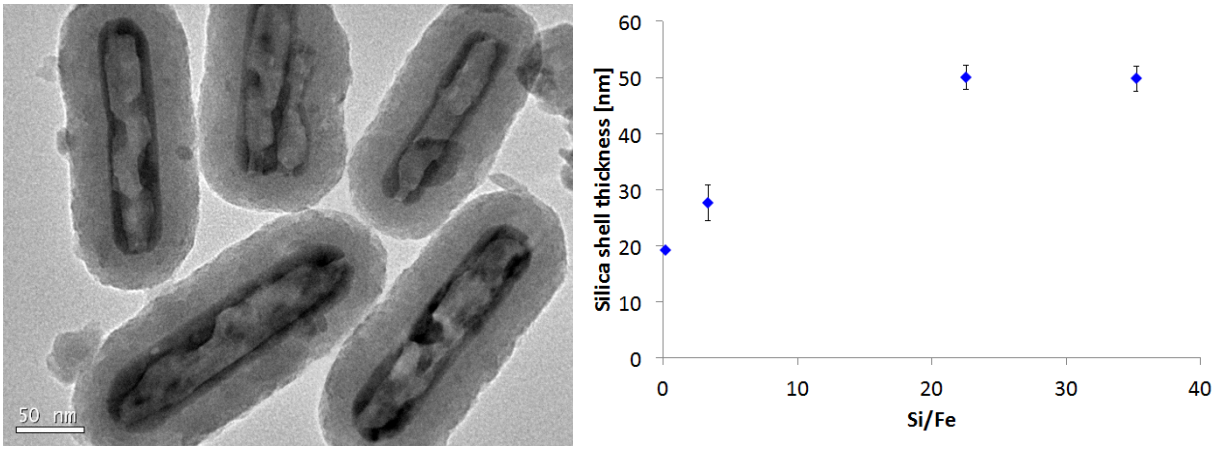


**Figure 68: hFe@$SiO_2$ materials with a Si/Fe=3.4 and silica shell of 28 ± 2 nm (left) and effect of Si/Fe on silica thickness for hFe@$SiO_2$ materials (right).**

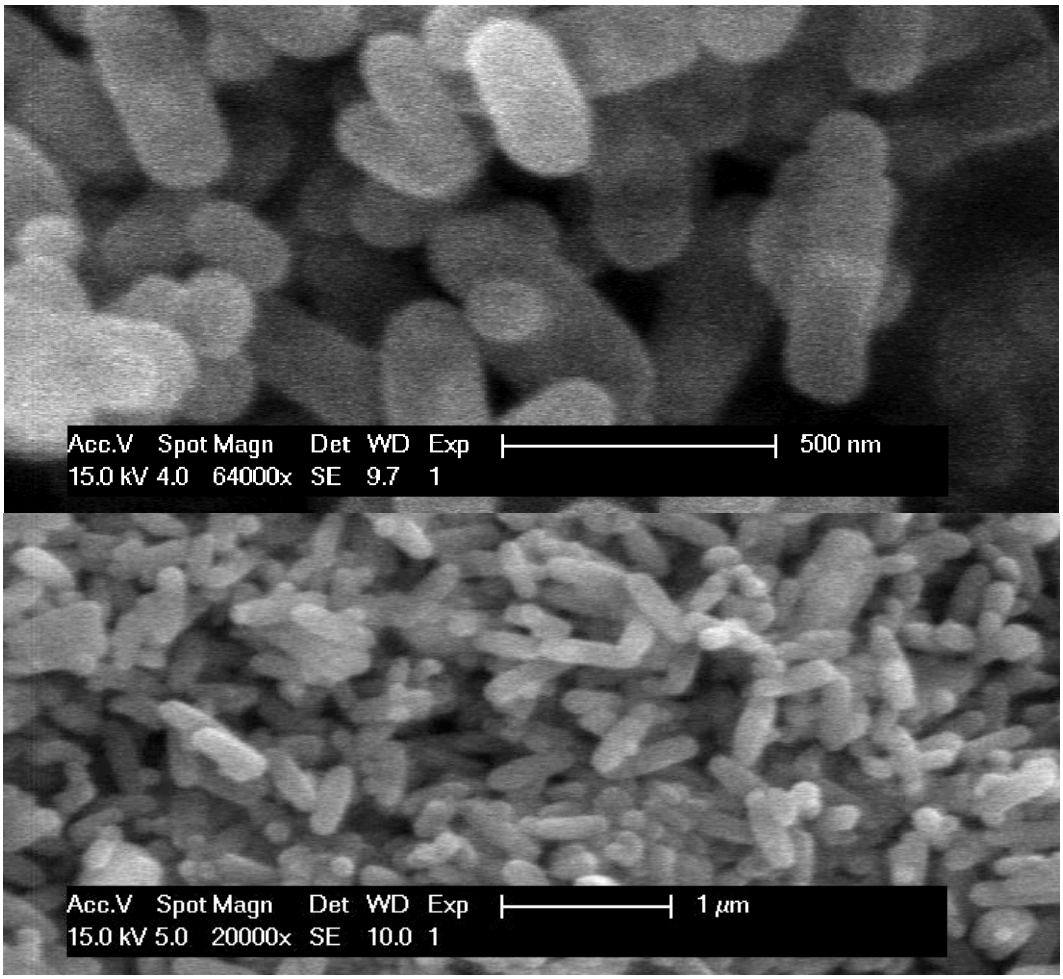


**Figure 69: High and low magnification SEM of hFe@$SiO_2$, showing elongated rod structure of the coated iron materials.**

Unfortunately, maintaining homogeneity of the particles in this synthesis was a constant challenge, especially as the Si:Fe decreased. An example of this is shown in Figure 70, where a silica shell thickness of <20 nm was achieved, and yet significant particle size polydispersity was seen in conjunction with extraneous material that was not confined within the core-shell structure at all. One reason for this could be that the Teflon sealing can fail in the hydrothermal reactors resulting in pressure loss. Since the reactor pressure dictates morphology this in turn introduces variability in the β-FeOOH spindles, which carries forward to the final silica-wrapped material.

Residual particles in the hydrothermal reactor can also influence nanoparticle nucleation and henceforth the resultant crystal structure.

Another consideration is scale-up. In order to achieve the batch sizes of 10-100 mg required for reactive testing, more iron nanoparticles must be dispersed within a limited solvent volume due to available laboratory vessel volumes and centrifugation equipment. Hyeon and coworkers were able to generate well-formed particles but worked with much larger batch volumes (~6 fold) (*187*).

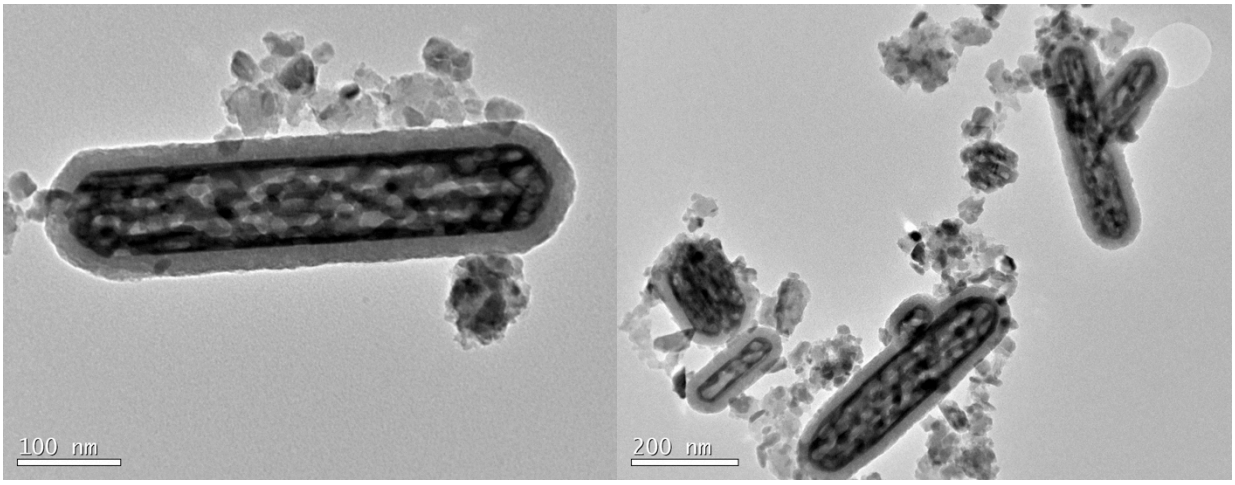


**Figure 70: hFe@$SiO_2$ with silica shell of 19 ± 2 nm using a Si/Fe of 0.2, but with significant polydispersity and extraneous material persistent throughout sample.**

Another challenge was that the centrifugation separation of the iron rod precursor from solution was time-consuming, sometimes requiring solvent exchange to acetone, and hence a poorly controlled synthesis step that could add to polydispersity. In fact, we hypothesized that cumbersome centrifugal separation and the subsequent re-dispersion step of the iron precursor were the most likely contributors to the poorly formed silica wrapped materials. To test this, in one instance the intermediate isolation step of the rod-shaped iron particles was eliminated. Instead, the solution containing hydrothermally synthesized β-FeOOH particles was immediately

pH adjusted to ~8.5, as required for silica growth. Next, PVP was added as the dispersant as before and held mixing for 24 hours. This was followed by addition of ethanol, ammonia, and TEOS, scaled by 2.5x in accordance with the larger volume of water present as a result of eliminating the centrifugation step. The result is shown in Figure 71, where a very thin silica shell is seen in the as-synthesized material. However, it seems this silica shell is insufficient to support the large iron interior since large amounts of extraneous material appear when it is calcined. Consequently, although a thinner shell is achievable, the stability of the material is compromised.

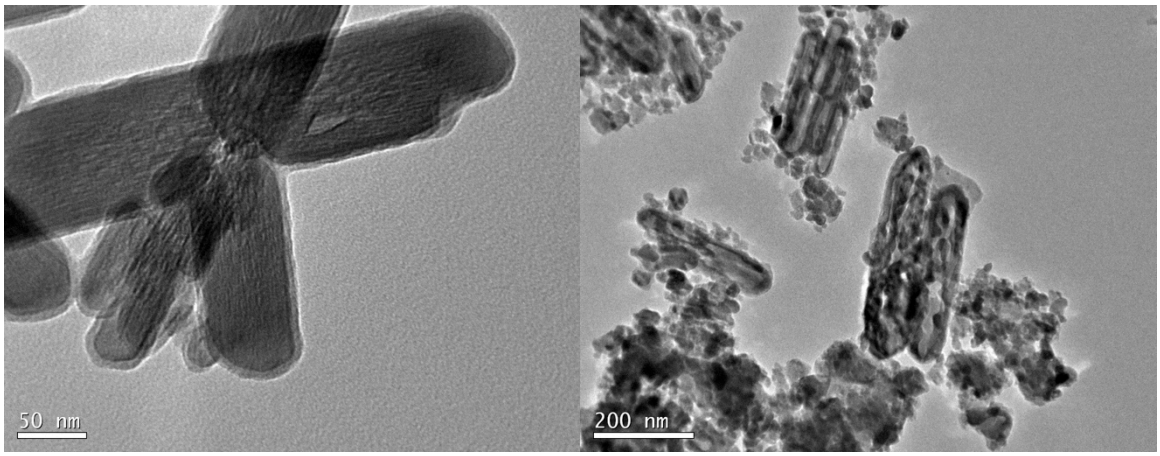


**Figure 71: β-FeOOH@$SiO_2$ material made from 'straight-through' synthesis (left) with very thin 5 nm silica shell, and the same material after calcination at 500$^o$C, demonstrating thermal instability with the very thin shell.**

As a final note, although both Fe@$SiO_2$ and hollow Fe@$SiO_2$ were found to be active in reactive tests, a formation of iron silicates this testing (3.7 and (*206*)) reduced the redox capacity of the materials, thus limiting their value for our particular application. To address this, an alternate $CeO_2$-based material was explored.

**Fe@$CeO_2$**

Compared with silica, ceria supports are considered more active in the sense that they can participate in redox chemistry. $CeO_2$ is a reducible support, allowing oxygen vacancies with the lattice structures according to $Ce_{1-\delta}O_2$. In addition it is a useful material for improving oxygen mobility within a structure due to its planar crystal structure (*219*).

For Fe@$CeO_2$ materials the previous discussed β-FeOOH rod structures used for hFe@$SiO_2$ where also used as a pre-cursor for a $CeO_2$ wrapping step. TEM and SEM images are shown for this material in Figure 72 and Figure 73. From TEM, we see that the individual iron rods are decorated by a loosely organized ceria structures. In SEM, these ceria-decorated spindles can easily be seen, in addition to bowtie-like structures that are presumably made of ceria. EDX analysis revealed that the material was only 10 wt % iron (and over 70 wt % ceria), while redox cycles in TGA (see section 3.8) suggested that the iron content was closer to 14 wt %. Results from a more detailed study in HRTEM are displayed in Figure 74, showing iron-rich rod structures (42.5 wt % Fe) and ceria-rich structures (25.5 wt % ceria). This analysis confirmed previous reasoning that the large amounts of extraneous material could be attributed to ceria.

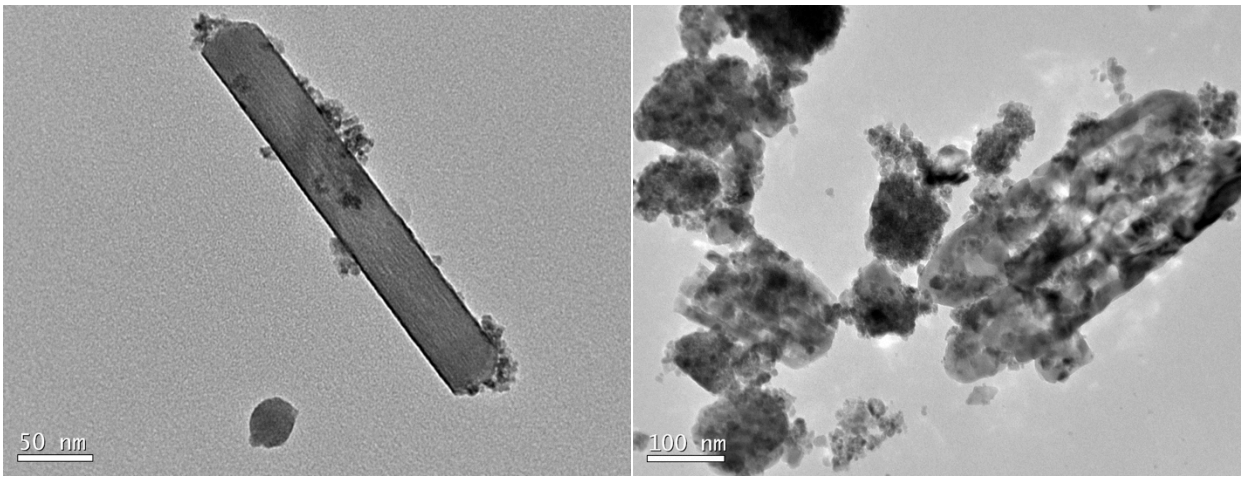


**Figure 72: TEM of uncalcined Fe@$CeO_2$ (left) and after calcination (right).**

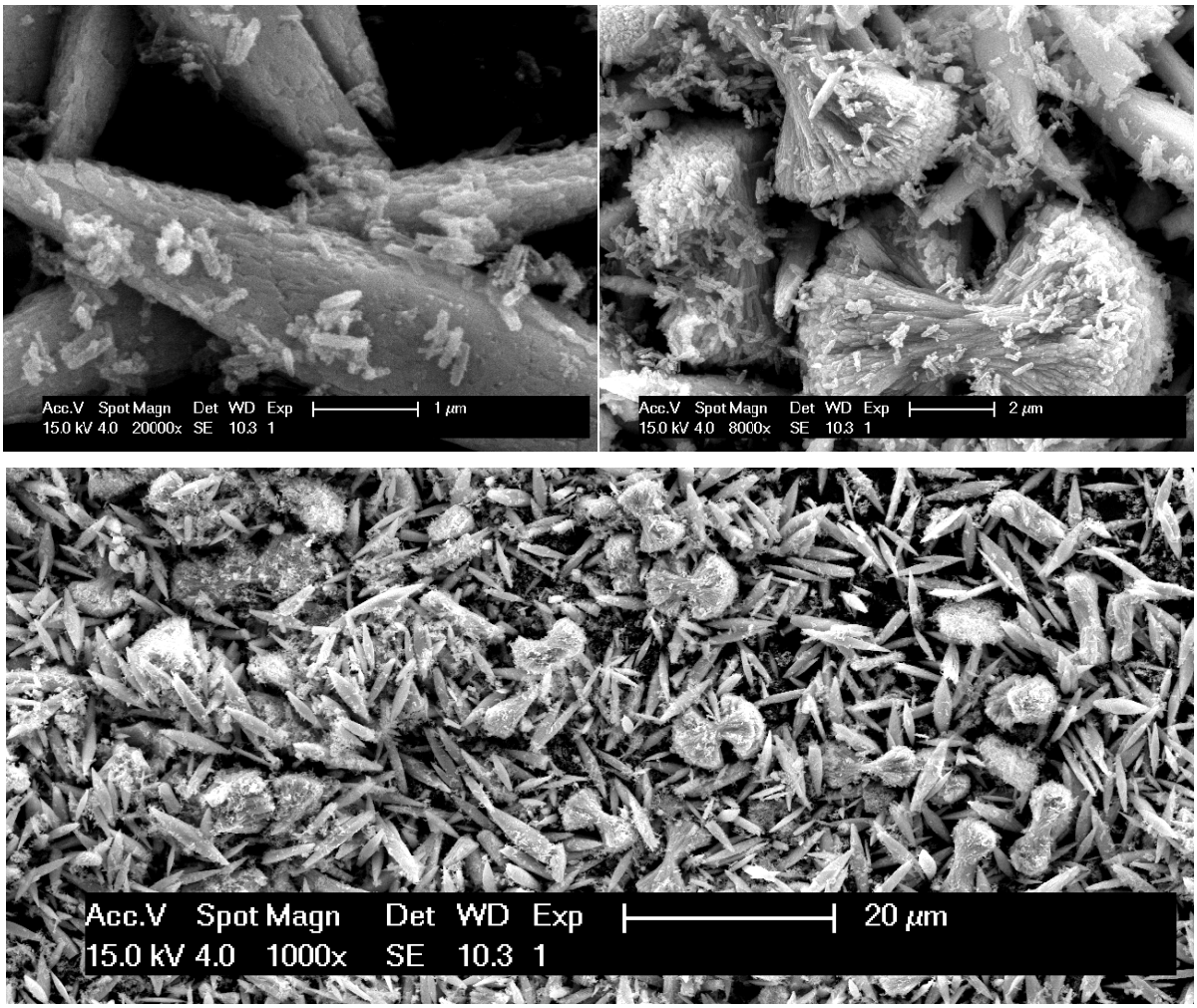


**Figure 73: SEM of Fe@$CeO_2$, showing individual $CeO_2$-decorated rods (left, top) and bowtie structures of aligned $CeO_2$ rods (right, top), and low magnification image of the well-ordered sample.**

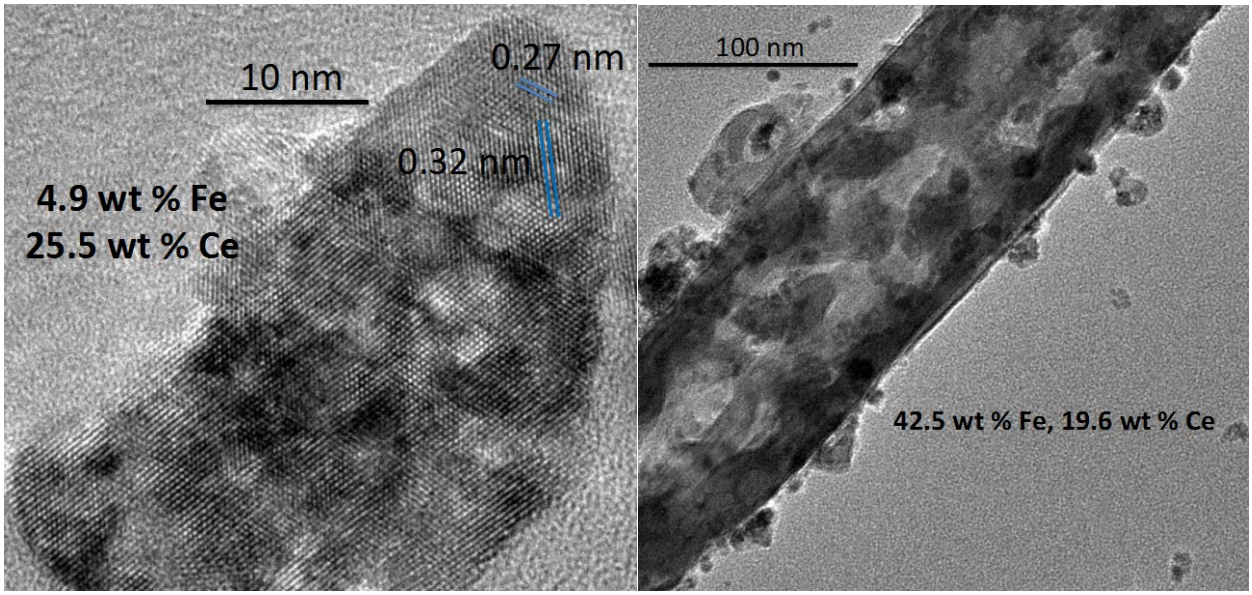


**Figure 74: HRTEM of ceria-rich and iron-rich structures. Lattice spacing 0.32 and 0.27 of the ceria rich sample corresponded with ceria 111 and 200 surfaces (*220*)**

XRD analysis showed $Fe_2O_3$ as the oxidation state of the fresh calcined material (Figure 75). After reduction in $H_2$, the iron is reduced to elemental iron. No $Ce_{1-\delta}O_2$ phase was detected, despite the indication in TGA (discussed later in section 3.8) that this support was reduced. Yet it is likely that the brief room temperature air exposure between reduction and XRD analysis was enough to re-oxidize the ceria material.

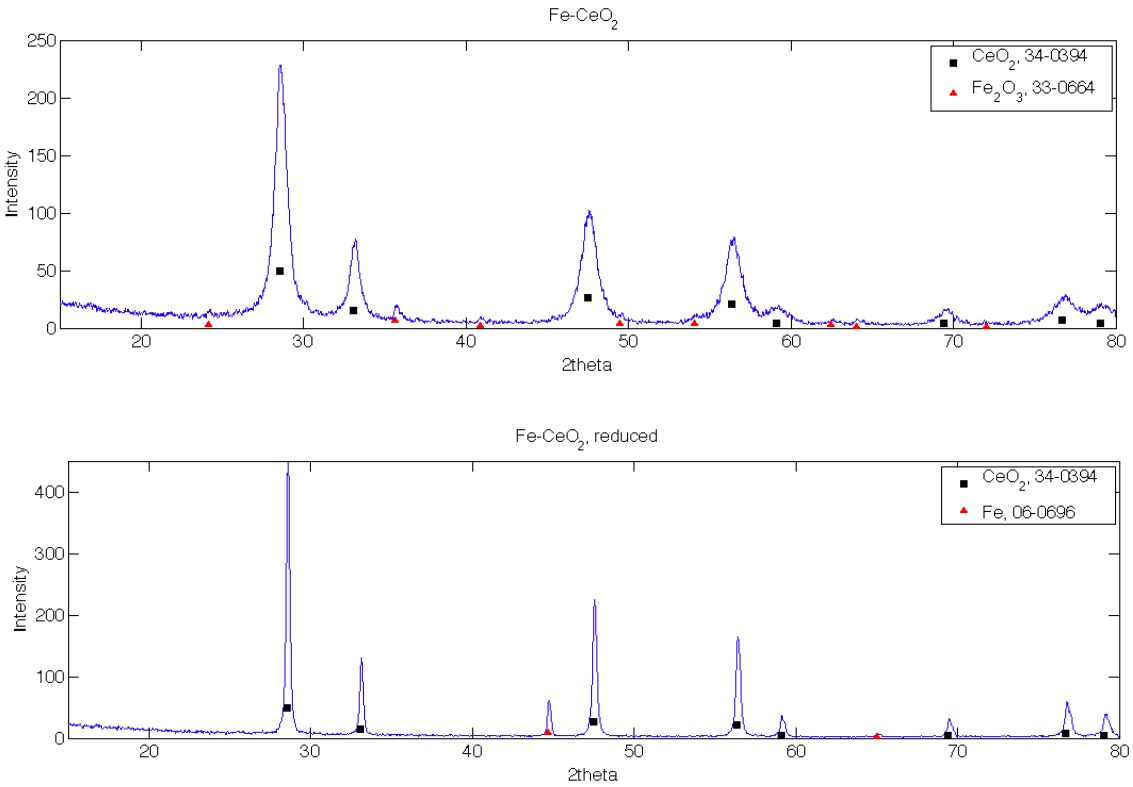


**Figure 75: XRD of fresh calcined Fe@$CeO_2$ material and reduced material, showing $Fe_2O_3$ as the Fe as the pertinent oxidation states, respectively.**

## Conclusion

To summarize, the several structures were developed with a core-shell morphology. In all cases, our target was to achieve a small iron core, which was protected within an amorphous support yet active in gas-phase oxidation-reduction chemistry. Although all materials were found to be accessible for oxidation and reduction as seen in XRD, reactive studies prompted us to make specific modifications: shell thickness was modified in silica materials to minimize mass transfer limitations and a hollow iron core was developed to eliminate any possible oxidation limitations of the iron core due to confinement. Finally, $CeO_2$ supports were explored as a means to avoid undesirable metal-support interaction seen in the silica materials. Beyond our own development for gas-phase redox chemistry, these materials may in fact be excellent

candidates for other applications. Several interesting studies have been published on the elevated magnetic susceptibility of $Fe_3O_4$ iron nanoparticles (*125*). Hollow and biocompatible $Fe@SiO_2$ core-shell structures with magnetic susceptibility are excellent candidates for drug delivery (*221*). Zero-valent iron also has promise for remediating water contaminants, and hence the liquid phase activity of coated iron materials may be of interest, especially if they exhibit favorable magnetic susceptibility for post-treatment separation (*66*). Finally, excellent reactivity and selectivity has been shown for epoxidation of cyclohexene with $FeCeO_2$ catalysts (*222*).

## 3.7 ACTIVITY OF FE@$SIO_2$ OXYGEN CARRIERS IN OXIDATION-REDUCTION CHEMISTRY FOR CLDR

Following the development of tunable iron-in-silica core-shell materials, reactivity studies were done to analyze the use of these materials in Chemical Looping Dry Reforming (CLDR). According to our thermodynamic studies, the highest attainable oxidation state of the carrier is $Fe_2O_3$ in air and $Fe_3O_4$ in $CO_2$. Meanwhile, reduction to both FeO and Fe can occur in either hydrogen or methane. Thermogravimetric analysis (TGA) was used to determine the activity of core-shell materials by measurement of weight gains and losses during carrier oxidation and reduction, respectively. Four oxidation states are available for iron (Fe, FeO, $Fe_3O_4$, and $Fe_2O_3$) and transitions through these oxidation states can often be readily observed in TGA. Initially, a test cycle of $H_2/CO_2$ was performed in order to allow more direct comparison between materials. $H_2$ exposure allows for the maximum possible extent of reduction to be assessed under carbon-free conditions. This fully reduced carrier can then be tested for maximize possible oxidation in the presence of $CO_2$. Next, methane was tested as the reducing gas in accordance with the CLDR process scheme.

***Fe@$SiO_2$***

Reduction of Fe@$SiO_2$ in $H_2$ proceeded slowly to a weight that corresponds to an oxidation state slightly below that of FeO (Figure 76, left). After reduction with $H_2$, the subsequent oxidation with $CO_2$ was minimal (Figure 76, right), proceeding only to weights which corresponded to formation of FeO, and no further oxidation was observed within the next

~40 min. This was somewhat surprising, given that our thermodynamic analysis predicted that formation of $Fe_3O_4$ is possible in the presence of $CO_2$. After 120 min, the gas inlet was switched to air and the carrier easily re-oxidized to near the original weight. By comparison, reduction with $CH_4$ was minimal (Figure 76, left), corresponding with reduction to $Fe_3O_4$ only. Furthermore, an oscillatory behavior was observed with $CH_4$ reduction, indicative of coke formation on the carrier surface as it is reduced. Additionally, the $CH_4$ reduction was not deep enough to allow a subsequent oxidation with $CO_2$ to complete the $CH_4/CO_2$ CLDR cycle.

XRD analysis of fresh calcined $Fe@SiO_2$ material revealed phases of $Fe_2O_3$, while analysis of fresh material reduced in $H_2$ showed dominant Fe phases (Figure 77). However, material oxidized in $CO_2$ after several cycles in TGA consisted of iron silicate ($Fe_2SiO_4$). Iron silicates have also been observed by us for $Fe@SiO_2$ reduced in $H_2$ after extended redox operation (*206*) and by others for $Fe\text{-}SiO_2$ carrier materials in conventional CLC (*223*). It is also useful to point out that the expected weight in TGA for FeO is equivalent to that for iron silicate (i.e. $2\ FeO + SiO_2 = Fe_2SiO_4$), and hence the slow-down of redox behavior can be directly connected with the formation of the iron silicate phase. Ultimately, during exposure to an oxygen-poor atmosphere, $Fe_2SiO_4$ was formed, which in turn reduced the overall carrier capacity by limiting the availability of iron for participation in the CLDR redox reactions.

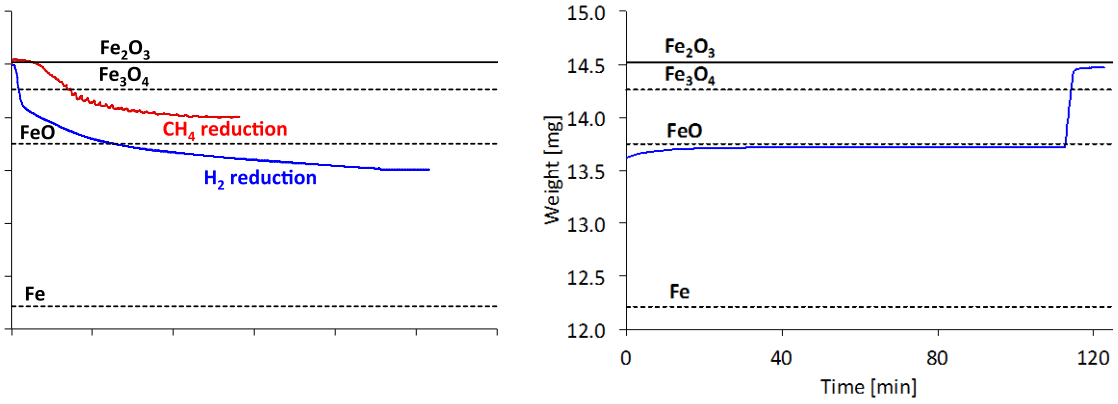


**Figure 76: Reduction of Fe@$SiO_2$ in TGA ($H_2$=20 sccm or $CH_4$=20 sccm, purge=60 sccm, left) and $CO_2$ oxidation ($CO_2$=20 sccm, purge 60 sccm, right), followed by oxidation in air (air=20 sccm, purge=60 sccm). T=700°C.**

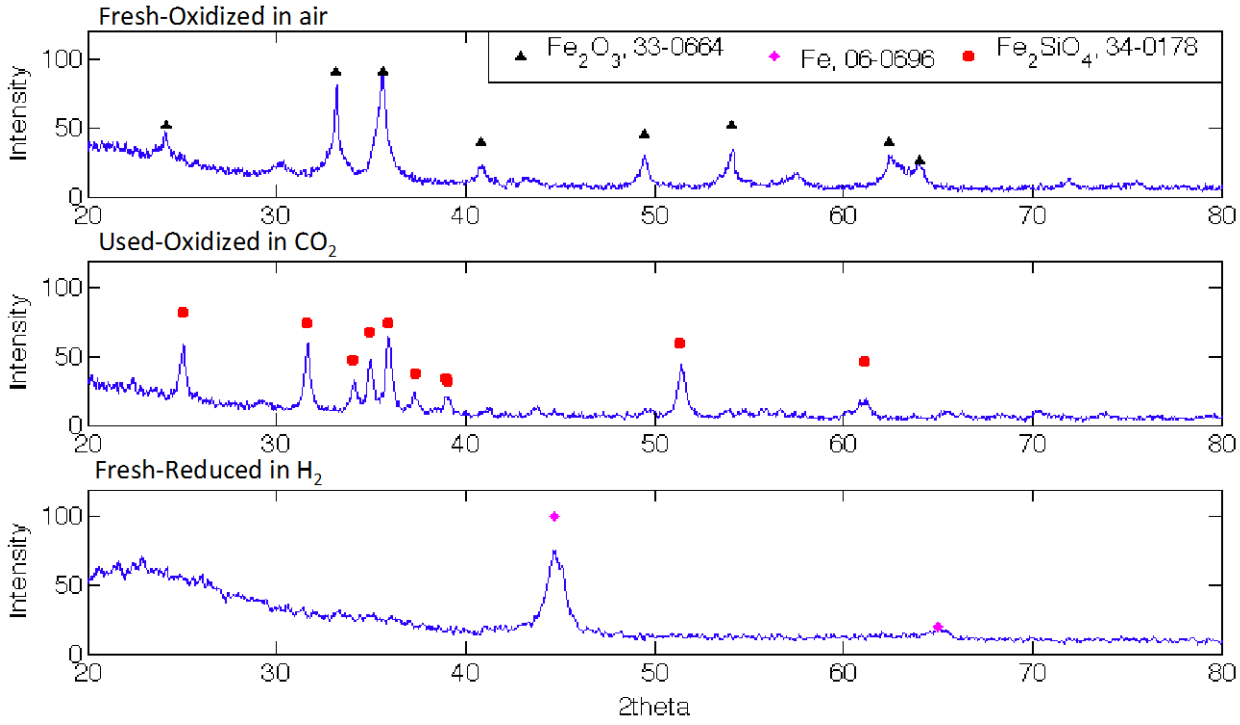


**Figure 77: XRD of Fe@$SiO_2$ for fresh calcined sampled (top), sample oxidized in $CO_2$ after many redox cycles in TGA (middle), and fresh reduced sample (bottom).**

We had previously also tested this material in a packed bed reactor configuration at 800$^{o}$C. In accordance with these TGA results, very little CO was formed during oxidation with $CO_2$ (*206*). Hence, this material had a poor capacity for CLDR redox cycles.

While iron silicates were a clear contributor to the limitations of the Fe@$SiO_2$ carrier, it was unclear whether this was the only factor. For Fe@$SiO_2$ materials, the iron core is confined within a high temperature stable silica shell. As the iron core becomes oxidized, it will need to occupy a larger space and hence there is some question regarding whether this space confinement could also have an impact on oxidizability. In some instances, $Fe_3O_4$ peaks were also observed in XRD analysis of fresh material after calcination in air (not shown). This indicated to us that indeed some inhibition to complete oxidation to $Fe_2O_3$ might exist. For this reason, it was hypothesized that a hollow Fe@$SiO_2$, while not alleviating iron silicate formation effects, might still yield improved carrier performance in the CLDR process.

**Hollow Fe@$SiO_2$**

Similar TGA studies were done with hollow Fe@SiO2 (hFe@$SiO_2$), shown in Figure 78. With $H_2$ exposure, the reduction proceeded further compared to the non-hollow material, i.e., more Fe was formed. Although the $CO_2$ oxidation still proceeded only to the formation of FeO, the deeper reduction enabled higher iron utilization. Hence, it was only the reduced phase in $H_2$ that was improved by incorporation of a hollow core. This is perhaps due to increased accessibility of the iron during the slower reduction step, achieved by incorporating a silica-free interface at the hollow interior. Meanwhile a slow down of oxidation was still present at the weight corresponding to FeO (or $Fe_2SiO_4$). Air oxidation following the $CO_2$ oxidation (at >30 min in Figure 78, right) resulted in a near complete re-oxidation of the carrier to a weight corresponding with formation of $Fe_2O_3$.

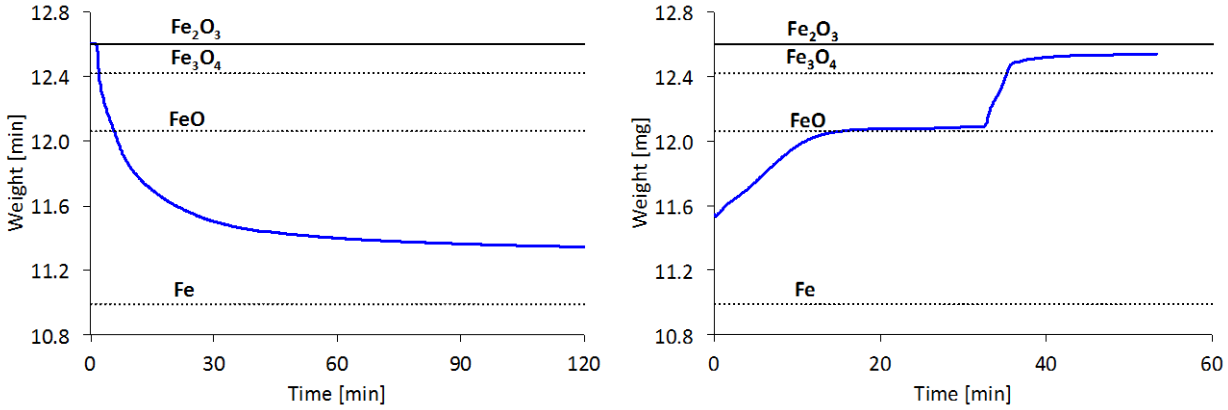


**Figure 78: Reduction of hFe@$SiO_2$ in TGA ($H_2$=20 sccm, purge=60 sccm, left) and oxidation ($CO_2$=20 sccm, purge 60 sccm, right), followed by oxidation in air (Air=20 sccm, purge=60 sccm). T=700°C.**

Next, reduction in $CH_4$ was tested (Figure 79). While the oscillatory behavior interpreted as coking with Fe@$SiO_2$ was not observed, the reduction did not proceed below the weight for FeO. As observed with Fe@$SiO_2$, the inadequate reduction in $CH_4$ limited the subsequent oxidation in $CO_2$, although a slight weight gain was actually observed for this material. The subsequent air oxidation was relatively fast at first, but was followed by a period of slow oxidation to the final weight.

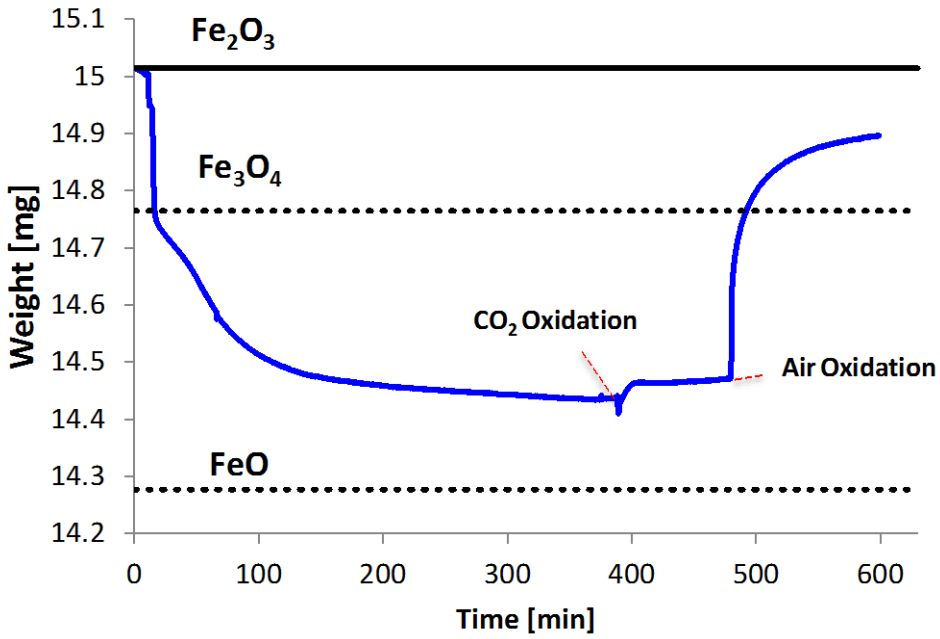


**Figure 79: Reduction for hFe@$SiO_2$ in TGA ($CH_4$=20 sccm, purge=60 sccm, left) and oxidation ($CO_2$=20 sccm, purge=60 sccm, right), followed by oxidation in air (Air=20 sccm, purge=60 sccm). T=700°C.**

XRD analysis showed that the material formed $Fe_2O_3$ when oxidized in air (Figure 80). Following a reduction in $H_2$ (after several redox cycles) both elemental iron and iron silicate ($Fe_2SiO_4$) were detected, whereas Fe alone was detected in fresh reduced samples (not shown). This observation brought us to a similar explanation as that made for non-hollow Fe@$SiO_2$; the silicate formation contributed to impedance of the reduction and hence the limited the utilization of iron in the oxygen carrier. A sample collected after oxidation in $CO_2$ was also analyzed. In this case, only $Fe_3O_4$ and $Fe_2O_3$ were detected, indicating that silicates in the sample had become oxidized during the brief air exposure prior to XRD analysis. This second explanation is also consistent with the observation of $Fe_2O_3$ in the sample, an oxidation state not attainable in the presence of $CO_2$.

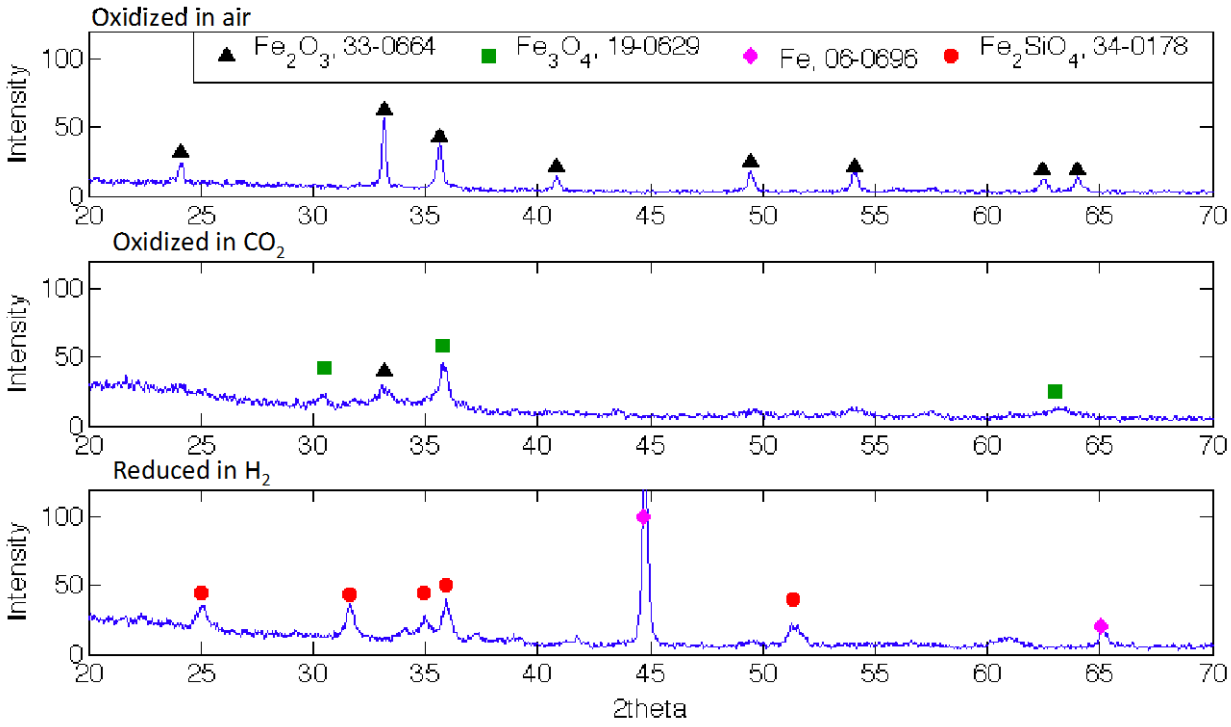


**Figure 80: XRD analysis of hFe@$SiO_2$ material. Fresh calcined sample (top), after oxidation in $CO_2$, and reduced sample after many cycles in TGA.**

Given the improved carrier utilization that was seen with the hollow structure, TEM analysis was performed after several cycles to determine whether the hollow center was stable in these structures. We expected a softening of the nano-sized silica shell at temperatures near 800$^{o}$C. Figure 81 in fact shows that the silica was partially collapsed. The hollow centers were not nearly as large as in the original structure, but they did remain somewhat intact.

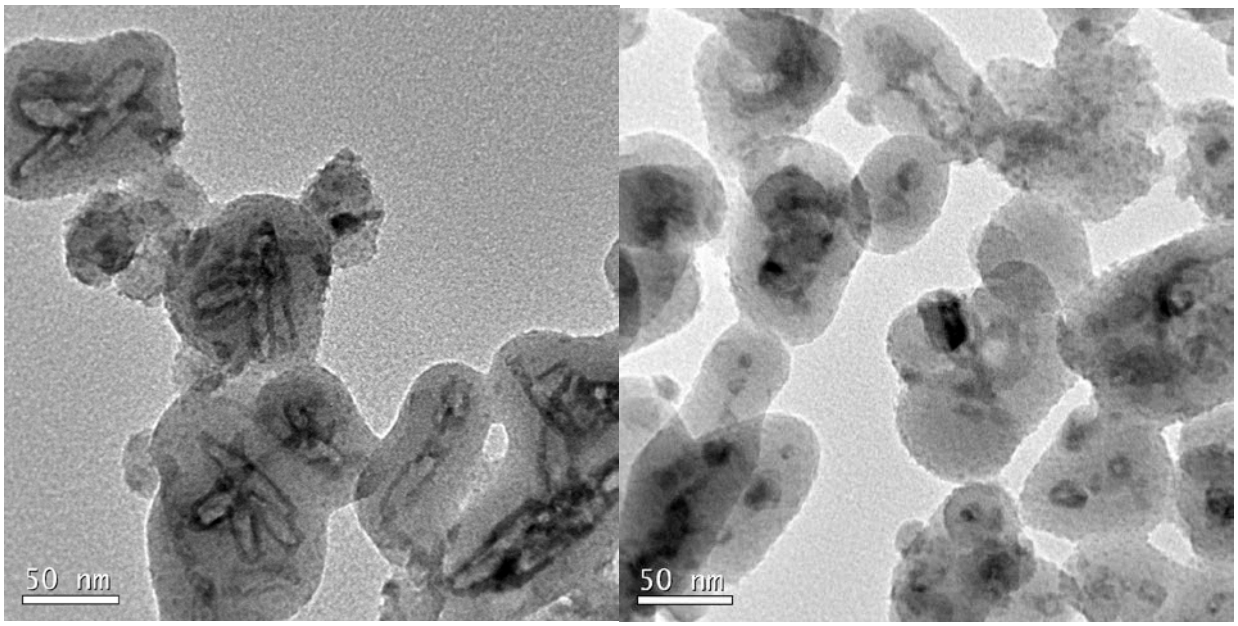


**Figure 81: Hollow Fe@$SiO_2$ (~35 nm shell) as-synthesized (left) and after several cycles at 700$^o$C in TGA (right).**

## Discussion

Iron silicate formation during the reduction half-cycle consistently limited the performance of the silica-structured carriers for this process. Despite this, we did observe that the formation of iron silicates was reversible by exposure to air to obtain $Fe_2O_3$. In this way, a 3-part CLDR process scheme comprised of reduction in a fuel, $CO_2$ oxidation, and finally air regeneration, has been proposed as a work-around for silicate formation (*206*). In this respect, reducibility is the most important metric for redox capacity for both of these materials given that the $CO_2$ oxidation has a rigid upper limit, even in this 3-part cycle. Three different batches of both non-hollow and hollow Fe@$SiO_2$ material were ultimately tested in TGA, of which one example has already been presented in detail above. Modifications were made with regard to iron core and silica shell thickness (see section 3.6) with the aim of improving redox performance.

TGA weight trends can be normalized by calculating the maximum possible weight loss between the oxidized and reduced material, based on iron composition. This results in a measure of iron utilization, X, defined by: $X = (M_t-M_{red})/(M_{ox}-M_{red})$, where $M_t$ represents the sample mass at time t, $M_{red}$ is the mass predicted for reduction to Fe, and $M_{ox}$ the mass of the oxidized material. Hence, X=0 corresponds to the fully reduced carrier (Fe) and X=1 corresponds to a fully oxidized carrier ($Fe_2O_3$ or $Fe_3O_4$). Several normalized TGA reductions in $H_2$ are shown below for Fe@$SiO_2$ (Figure 82) and hFe@$SiO_2$ (Figure 83) carriers with varying material properties. Here, some caution must be taken with regard to making conclusions on reaction kinetics since slightly different sample weights were used in these experiments (11.4-12.6 mg) and hence different gas contacting patterns are expected. However, differences in the final degree of reduction achieved may still provide a general insight of structural aspects that lead to improved iron utilization, and these values have been summarized from the normalized TGA reduction trends in Figure 82 and Figure 83.

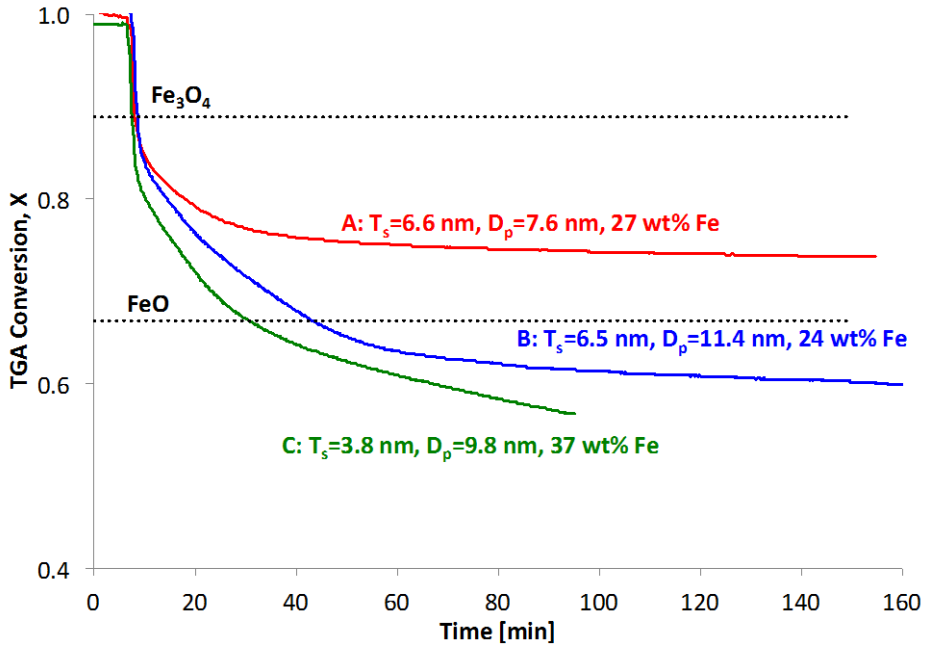


**Figure 82: Normalized TGA reduction in $H_2$ at 700°C for three different Fe@$SiO_2$ materials (A, B, and C).**

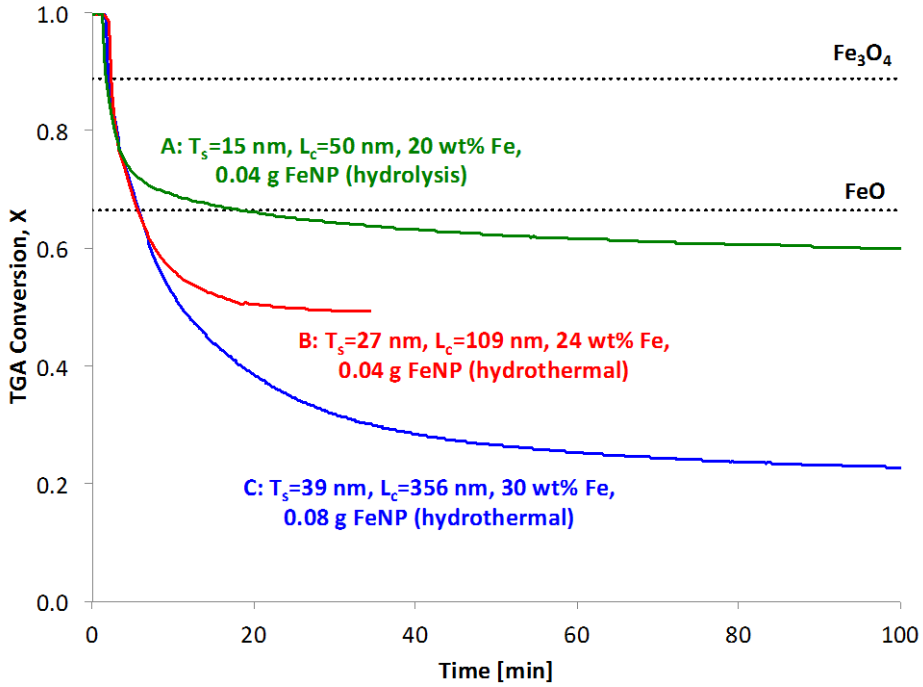


**Figure 83: Normalized TGA reduction in $H_2$ at 700°C for three different hFe@$SiO_2$ materials (A, B, and C).**

**Table 7: Iron utilization in hollow and non-hollow Fe@$SiO_2$ carriers**

| Material Type | Silica shell [nm] | Fe content [wt% Fe] | Fe Utilization, $H_2$ reduction only ($Fe_2O_3$/Fe) | Fe Utilization, $H_2/CO_2$ cycle ($Fe_3O_4$/Fe) |
|---|---|---|---|---|
| A: hFe@$SiO_2$ | 39 | 30 | 78 | 52% |
| B: hFe@$SiO_2$ | 27 | 24 | 50 | - |
| C: hFe@$SiO_2$ | 15 | 20 | 47 | - |
| A: Fe@$SiO_2$ | 3.8 | 37 | 43 | - |
| B: Fe@$SiO_2$ | 6.6 | 24 | 40 | - |
| C: Fe@$SiO_2$ | 6.5 | 27 | 26 | 2% |

The best iron utilization among Fe@$SiO_2$ carriers was seen for 3.8 nm silica shells (43 wt % Fe), compared to 6.6 nm (40 wt % Fe) and 6.5 nm (26 wt % Fe), i.e., the material with the thinnest silica shell and the highest iron loading.

As discussed previously, the iron utilization of the hFe@$SiO_2$ was much greater than the non-hollow material. For these materials, the use of larger iron precursors led to an increase in the internal length of the hollow cores ($L_c$). As a result, higher iron contents were observed as the synthesis progressed to thicker shells since the shells were built around progressively larger cores. For this material, the sample with both the thickest silica shell (39 nm) and the highest iron content (30 wt %) was observed to have the greatest reducibility. This suggested that diffusion through the silica shell or the size of the iron core was not limiting, at least in the hollow material. Rather, the material with the highest iron content again was found to perform the best.

Considering these two cases, we hypothesize that the higher iron content is linked to higher reducibility because it simply leads to a material with less silica available to form iron silicates. Indeed we can calculate that at >54 wt% iron, there will be free iron present even if all of the silica is incorporated into silicates. Hence, as the material composition approached this

54% threshold, perhaps even at values as low as 30%, the likelihood of segregated silica-free iron becomes greater. This is demonstrated in the best and worst performing sample given in Table 7, where iron utilization (referenced to $Fe_3O_4$/Fe redox cycles) is 52% and 2%.

To study this in more detail, further XRD analysis (Figure 84) was done on reduced samples of two hFe@$SiO_2$ samples after extensive cycling in TGA (since a more obvious trend was observed for this structure). Both iron and iron silicate phases were observed. A clear difference was seen in the iron peak intensities for the first and third samples (i.e., the least and most reducible in TGA). Analysis by the Sherrer equation (Figure 85) showed smaller elemental iron and larger iron silicate crystals material with the higher iron content. This might explain the deeper reduction that occurred with this material since the smaller iron particles may be more susceptible to reduction. Overall these results suggest that the amount of free iron in the sample may contribute to improved reducibility for these materials for the CLDR test cycle.

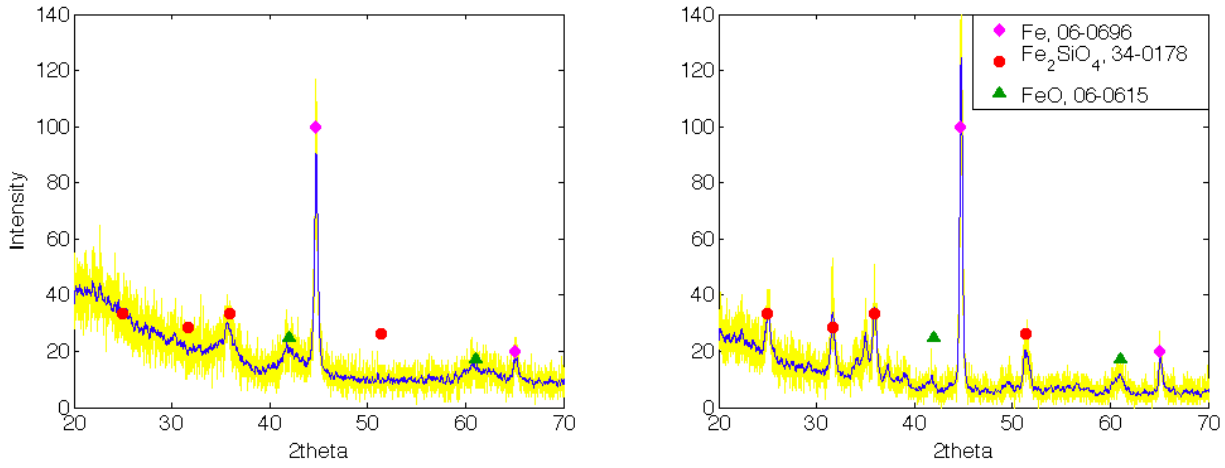


**Figure 84: XRD of reduced hFe@$SiO_2$ materials (C-worst, left and A-best, right) after several cycles in TGA.**

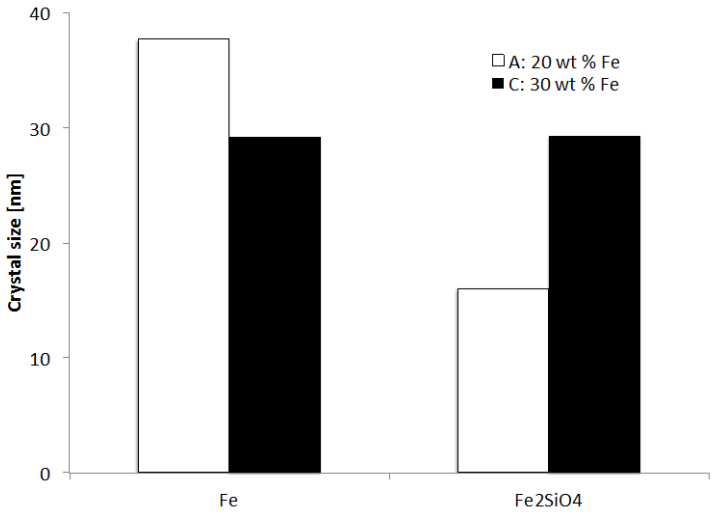


**Figure 85: Crystal size as determine via Sherrer equations of iron and iron silicate in hFe@$SiO_2$ containing 30 wt % and 20 wt % iron.**

## Conclusion

This study demonstrated the advantage of hFe@$SiO_2$ over non-hollow Fe@$SiO_2$ materials for oxidation-reduction chemistry. Since the extent of reduction was much greater for hFe@$SiO_2$ materials, a larger oxidation in $CO_2$ occurred for these materials in $H_2/CO_2$ test cycles. However, for actual application to CLDR (i.e., $CH_4/CO_2$ cycles), reduction in methane was not adequate enough to allow a subsequent oxidation in $CO_2$ to occur. Furthermore, the formation of iron silicates limited the availability of iron for all redox reactions, hence impeding the performance of the carriers. Several material modifications were made to improve redox performance and the materials were compared in TGA. The results suggested that iron utilization was not limited by silica shell thickness or iron particle size, but instead materials with a higher iron content were associated with better performance. It was hence hypothesized that a greater amount of free iron (i.e., not in the form of iron silicate) in these materials is partially responsible for improved carrier utilization.

## 3.8 ENHANCEMENT OF OXIDATION-REDUCTION CHEMISTRY IN CHEMICAL LOOPING DRY REFORMING USING CERIA-SUPPORTED IRON CARRIERS

### Introduction

Chemical Looping Combustion (CLC) is an emerging technology that offers an elegant and highly efficient route towards clean fossil fuel combustion (*142, 224*). In CLC, a fuel is combusted in a 'fuel' reactor by contact with a metal oxide carrier, which then enables capture of $CO_2$ in the fuel reactor effluent. After combustion of the fuel, the reduced metal oxide is circulated to an 'oxidizer' reactor where it is regenerated via oxidation with air. CLC results in clean, $NO_x$-lean, flameless combustion of fuels with inherent $CO_2$ capture without major energy penalty.

While the focus of CLC is fuel conversion for energy production with simultaneous $CO_2$ capture, alternative processes that incorporate fuel reforming within the framework of chemical looping have also been developed. We have recently proposed Chemical Looping Dry Reforming (CLDR), where $CO_2$ replaces air as an oxidant to regenerate the metal oxide (Figure 86) (*191, 206*). As in CLC, the oxidized carrier is fed back to the 'fuel reactor' where it is reduced by a fuel. When using methane as the fuel, CLDR can result in a net reaction similar to that of dry reforming of methane, as shown below:

| | | |
|---|---|---|
| Reducer: | $4\ MO + CH_4 = 4\ M + CO_2 + 2\ H_2O$ | (1) |
| Oxidizer: | $4\ M + 4\ CO_2 = 4\ MO + 4\ CO$ | (2) |
| Net Reaction: | $CH_4 + 3\ CO_2 = 4\ CO + 2\ H_2O$ | (1) + (2) |

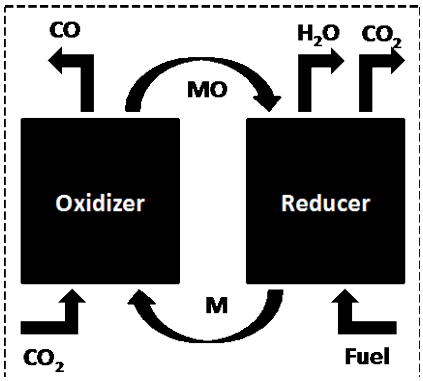


**Figure 86: Schematic of Chemical Looping Dry Reforming (CLDR) process**

Overall, CLDR results in $CO_2$ activation via conversion of $CO_2$ to CO. Consequently, while the environmental benefit of $CO_2$ capture via CLC depends upon development of large-scale sequestration solutions, CLDR instead opens a pathway for $CO_2$ utilization. $CO_2$ decomposition to CO or carbon has been demonstrated over ferrite material (*167-169*) and we have previously presented nanostructured Fe-based materials as suitable carriers for CLDR (*191, 206*). To address the slow kinetics expected for oxidation with $CO_2$ (a weak oxidant), nano-scale carriers were synthesized in these previous studies to improve reactivity. The carriers were also designed with a thermally stable support to avoid nanoparticle sintering at the elevated temperatures.

In the initial work, a composite-type Fe-Barium Hexa-Aluminate (Fe-BHA) material exhibited fast redox activity and stable operation, but reduction in methane was susceptible to coking (*178, 191*). Meanwhile, core-shell Fe@$SiO_2$ material suffered from slow reaction kinetics and utilization of the iron was partially limited by the formation of iron silicates during oxygen-lean reaction phases (*206*). While minimal coking was observed on the Fe@$SiO_2$ carriers during reduction with methane, the extent of reduction was not enough (i.e. to FeO or Fe) to allow a subsequent oxidation in $CO_2$ to proceed. Finally, hollow Fe@$SiO_2$ was developed

in order to improve accessibility of the iron in the core. Although significant improvement was seen in the reducibility of this material, this structure modification did not directly address the formation of iron silicates, and hence cyclic CLDR operation with methane reduction was still not achieved.

The aim of this work was to design a new carrier material by incorporation of ceria into the Fe-based carriers. $CeO_2$ has emerged as an excellent support material for oxidation-reduction chemistry given its reducibility and high oxygen mobility (*225-227*). We synthesized nanostructured $Fe@CeO_2$ materials via a hydrothermal synthesis and compared these with our previous materials and a more conventional $Fe\text{-}CeO_2$ material in the CLDR process.

**Methods**

***Hollow $Fe@CeO_2$.*** First, akageneite (β-FeOOH) nano-rods were made via hydrothermal synthesis of a 1 mM solution of $FeCl_3 \cdot 6\ H_2O$ for 16 hrs at 80°C. The resulting particles were centrifuged and dried. These akageneite particles were used as seeds for $Fe@CeO_2$ materials in a second hydrothermal process use a method similar to that used to make $Pd@CeO_2$ by Zhang et al. (*188*). In our synthesis, 0.114g of akageneite particles were dispersed by sonication in 10 mL DI water for 20 min. PVP-10 was then added in a ratio of 1g/0.04 g particles. The solution was diluted to a final volume of 25 mL and mixed for 24 hrs at room temperature. Next, 1 mmol of $CeCl_3$ and 10 mol of urea were combined with 17 mL of the colloid mixture containing PVP-coated particles. The solution was mixed for 20 min and transferred to a 50 mL hydrothermal reactor and held at 90°C for 24 hrs. The resulting mixture was then cooled, centrifuged, and dried. Crushed powder samples were calcined for 2 hr in air, leading to oxidation of β-$FeOOH@SiO_2$ to hollow $Fe_2O_3@CeO_2$.

***Fe-$CeO_2$.*** Fe-based carriers (14 wt% Fe, EDX) were synthesized via simple deposition-precipitation technique. Briefly, $Fe(NO_3)_3.9H_2O$ (99+%, Sigma-Aldrich) was dissolved in DI water, and 40 mL of the 0.02 M precursor solution was precipitated by 0.5 M NaOH at pH of 9 – 9.5 on 300 mg of the desired support powder suspended in 100 mL DI water. After aging for 2h, the resulting slurry was centrifuged, vacuum dried at 80 – 100$^oC$, crushed, and finally calcined in air at 800$^oC$ for 2h.

***Characterization.*** All materials were characterized for particle size and morphology with transition electron microscopy (TEM, JEOL-2000FX electron microscope). Typical sample preparation consisted of grinding the sample in a mortar, ethanol dispersion, ~2 min sonication, and placing 1-2 drops of dispersion on copper type-B support grid (Ted Pella Inc.) to dry in air. Particle measurements of TEM images were done using ImageJ software (http://rsb.info.nih.gov/ij/). Catalyst surface area and porosity were determined by Brunauer Emmett Teller (BET) analysis (Micromeritics ASAP 2020 surface area and porosity analyzer). Pre-treatment consisted of 2-3 hr degas at 200$^oC$ under vacuum. Typically, a 6-point BET analysis was used for total surface area measurement and an 84-point $N_2$ BJH analysis with Halsey thickness curve correction and Kruk-Jaroniec-Sayari BJH correction for pore size and volume determination. Crystal structure was determined with X-ray diffraction (XRD) (Phillips PW1830, USA). XRD was run in 'line focus' mode using a monochromatic Cu radiation at the wavelength of 1.54 Å. The beam voltage was 40kV at a current of 30mA. Diffraction patterns were recorded between 15 and 90° (2θ) in steps of 0.08° intervals with a 0.2 s counting time at each step. Scanning electron microscope energy dispersive X-ray spectroscopy (SEM EDX Genesis) was used to determine elemental composition of samples at beam voltage of 15kV, spot size 4 (typically), a collection time of 50-100 s, and a monitored dead times of 20-40%. Sample

powders were first mounted with double-sided carbon tape and then coated with palladium for analysis. At least 3 measurements were taken for each sample, and at least 5 samples if measurements varied by more than 5%. Material composition values were used to estimate expected weight gains and losses for materials in chemical looping experiments.

***Thermogravimetric analysis (TGA).*** TGA was used to test the carriers for oxidation and reduction reactivity. The highest oxidation state achievable for the Fe-based carriers is $Fe_2O_3$ in air and $Fe_3O_4$ in $CO_2$ (*191*). During reduction of the fully oxidized carrier, weight loss was clearly observed in association with oxidation states in the order of $Fe_3O_4$ and FeO. Flow rates in TGA were 60 sccm for the purge gas and 20 sccm for the reactive gases except for $CH_4$, which was fed at 5-10 sccm to avoid coking. 700$^oC$ was chosen as the operating temperature for TGA tests to avoid carbon formation thermodynamically predicted at lower temperatures and to limit the possibility of carrier sintering at higher temperatures.

***Reactivity tests in fixed-bed reactor.*** Fixed-bed reactor studies were conducted in order to analyze fuel conversion and selectivity during the reducer half-cycle and CO production during the oxidation half-cycle. 80 mg of carrier was loaded into a quartz-glass tube (1/4" I.D.) and placed horizontally in an electric oven. This system was heated to the desired reaction temperature in Ar (700-900$^oC$), pretreated in air for 30 min, and then alternating phases of reducing gas ($H_2$ or $CH_4$) and $CO_2$ were contacted with the carrier. Reduction and oxidation half-cycles were separated by an Ar purge phase to enable well-defined transitions during reactive phases. The product gases were monitored via mass spectrometry (Pfeiffer Omnistar QMS 200).

**Results**

TEM and SEM micrographs are given in Figure 87 and Figure 88 for Fe@$CeO_2$ material, including an image of the akageneite pre-cursor prior to wrapping with $CeO_2$. In this material, a loosely organized 'shell' of ceria nanoparticle clusters decorates the centrally located and elongated iron spindles. The iron content was found to be 10 wt % via EDX. However, further inspection of breakpoints during $H_2$ reduction in TGA (which correspond with each oxidation state of iron) suggested a value of 14 wt % iron. BET surface area was 55.77 $m^2/g$. Finally, XRD analysis indicated that the material was accessible for gas-phase oxidation and reduction by the detection $Fe_2O_3$ (JCPDS 33-064) and Fe (JCPDS 06-0696) crystals after oxidation in air and reduction in $H_2$, respectively.

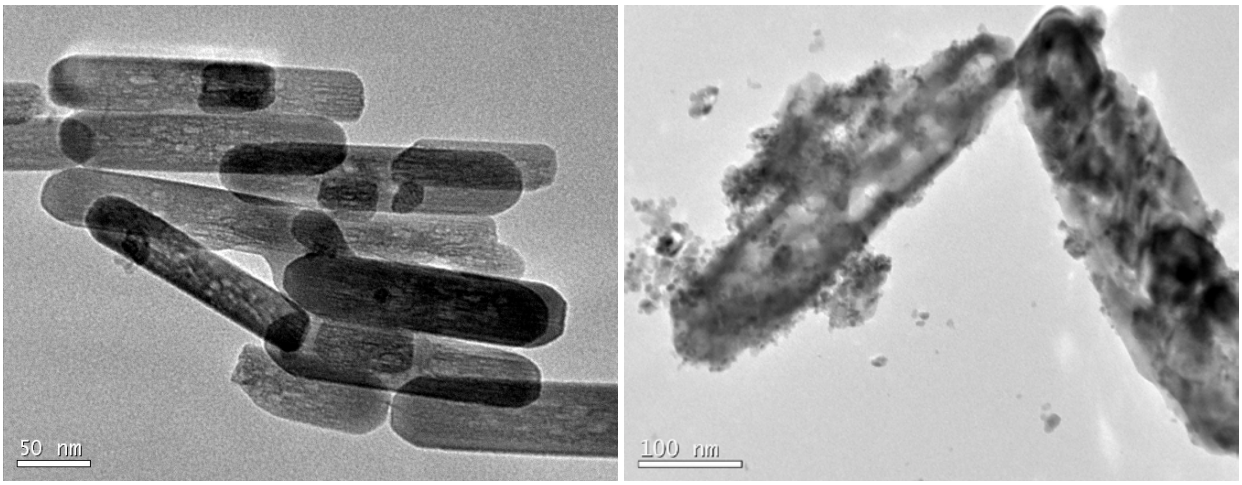


**Figure 87: TEM micrographs of rod-shape akageneite (β-FeOOH) precursor (left) and as-synthesized Fe@$CeO_2$ (right).**

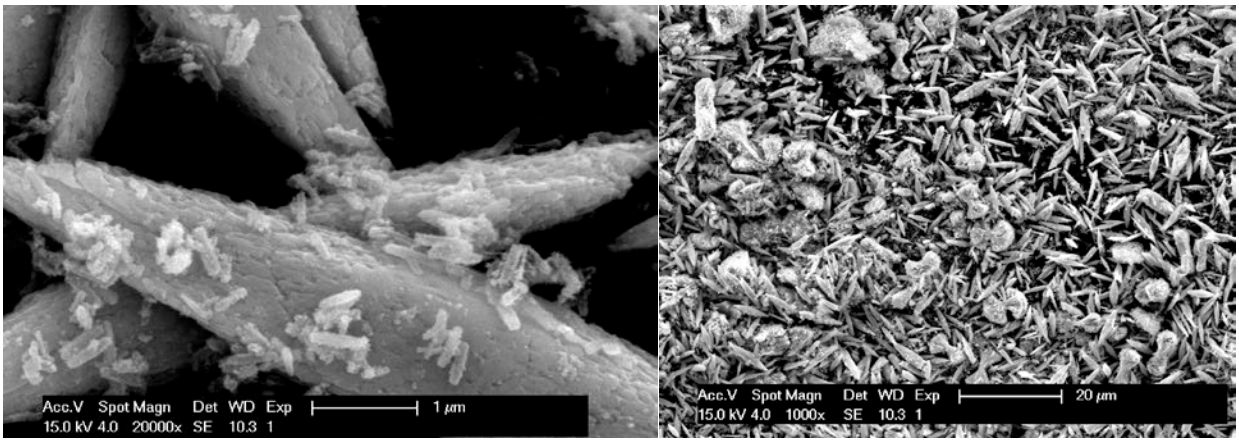


**Figure 88: SEM of Fe@$CeO_2$ material.**

Fe-$CeO_2$ materials made by the deposition-precipitation method were very different, consisting of ceria rod structures decorated with iron. The surface area for this material was 80 $m^2/g$ by BET and the composition was 14 wt % iron by EDX. With this material as well, inspection of TGA breakpoints suggest a higher composition of 19 wt % iron.

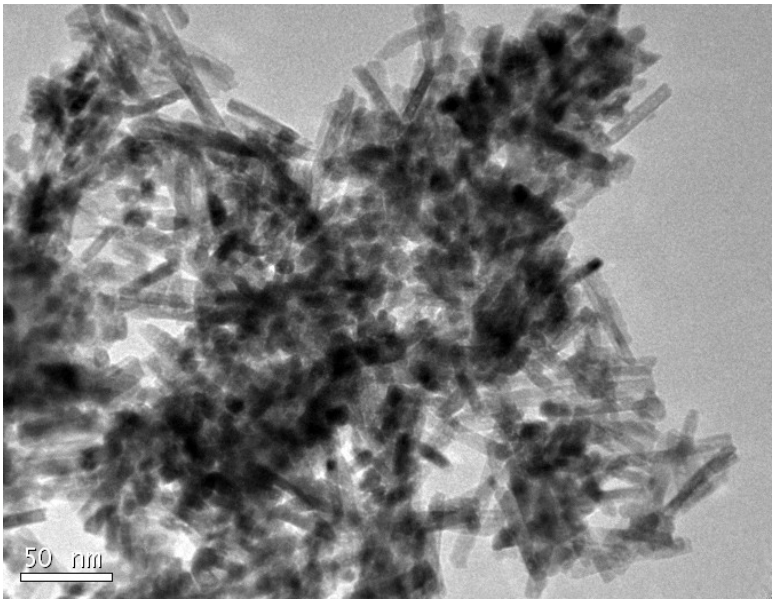


**Figure 89 TEM micrograph of Fe-$CeO_2$ material.**

In TGA studies with Fe@$CeO_2$, reduction in $H_2$ occurred within ~ 200 min with distinct bends in the weight curve that corresponded with the successive oxidation states of $Fe_3O_4$ and

FeO (Figure 90), as previously described. The weight then proceeded below the minimum calculated weight for the material based on complete reduction to iron. Although no $Ce_{1-\delta}O_2$ phases were detected in XRD analysis of the material directly after reduction, $CeO_2$ is recognized as a reducible support (*225*) at the $\delta$ value corresponding to the extra weight loss in TGA in this case is quite small. Subsequent oxidation of the material in air was fast (<5 min) and proceeded completely to $Fe_2O_3$, which demonstrates favorable accessibility of the iron core for oxidation despite it being embedded within the ceria. A second cycle was done with $H_2$ reduction followed oxidation with $CO_2$; oxidation to $Fe_3O_4$ was nearly complete within 50 min (Figure 91). In this case, a distinct bend in the oxidation trend was seen at the weight corresponding to FeO. The cause for this is still undetermined. We believe the most likely cause to be that the weaker oxidant of $CO_2$ exhibits slower and altered oxidation kinetics compared to air due to the presence of residual $H_2$ in the TGA system (which would quickly be consumed in the presence of air). We should also note that $FeCeO_3$ (which would correspond to the weight as FeO in TGA) has been observed in studies of the cyclic oxidation-reduction chemistry of $Fe/CeO_2$ materials (*228*). This material can be formed at high temperatures from materials containing $Fe_2O_3$, Fe, and $CeO_2$ (*229, 230*). However, XRD analysis of our sample after oxidation in TGA with $CO_2$ at the weight corresponding with FeO showed only $Fe_3O_4$ (Figure 92).

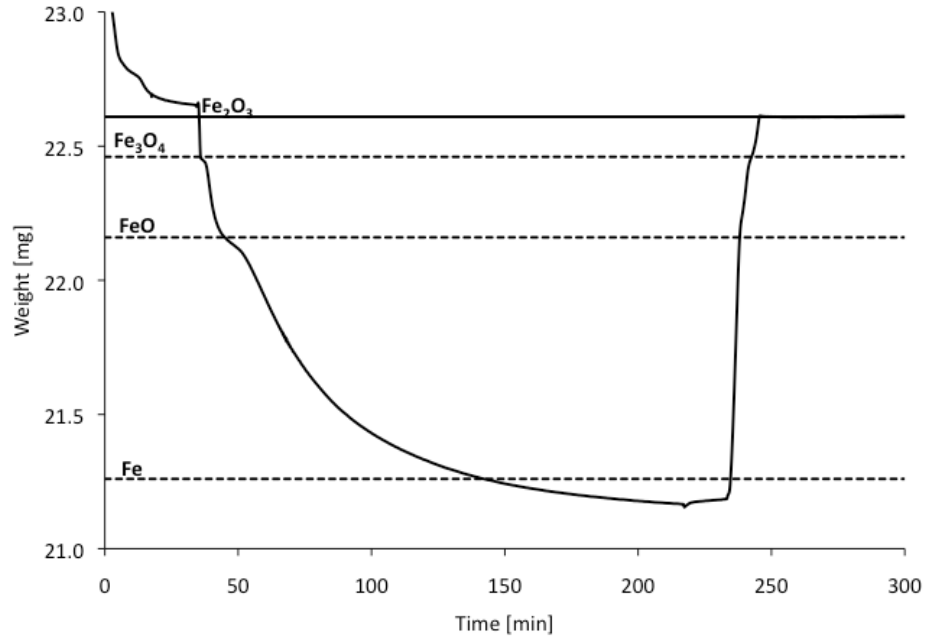


**Figure 90: $H_2$ reduction and air oxidation in TGA ($H_2$, Air=20 sccm, purge= 60 sccm, T=700°C). Break points in reduction and oxidation curves correspond well with weights for each successive iron oxidation state.**

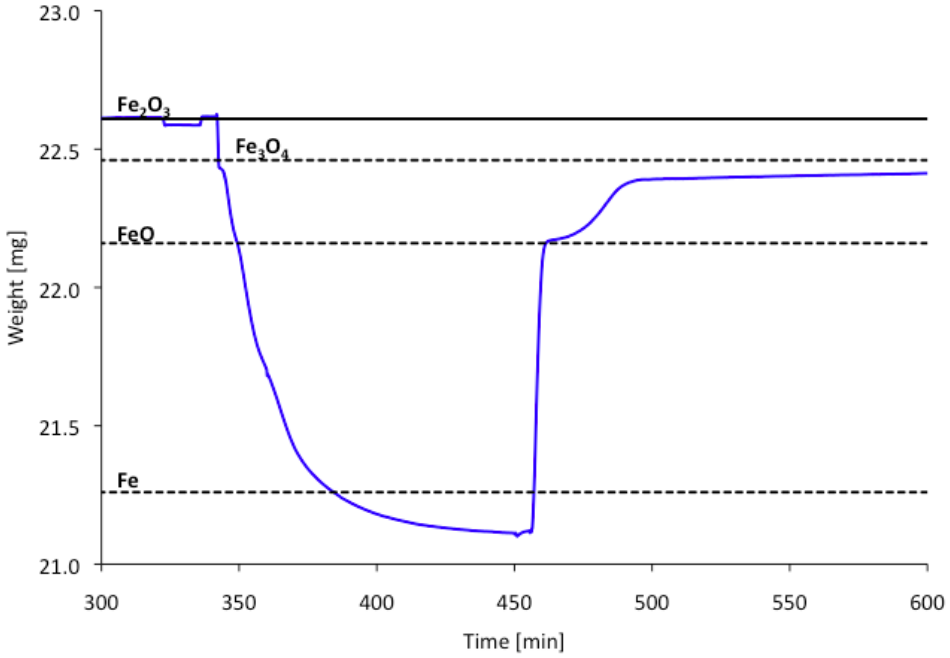


**Figure 91: $H_2$ reduction and $CO_2$ oxidation in TGA ($H_2$, $CO_2$=20 sccm, purge= 60 sccm, T=700°C).**

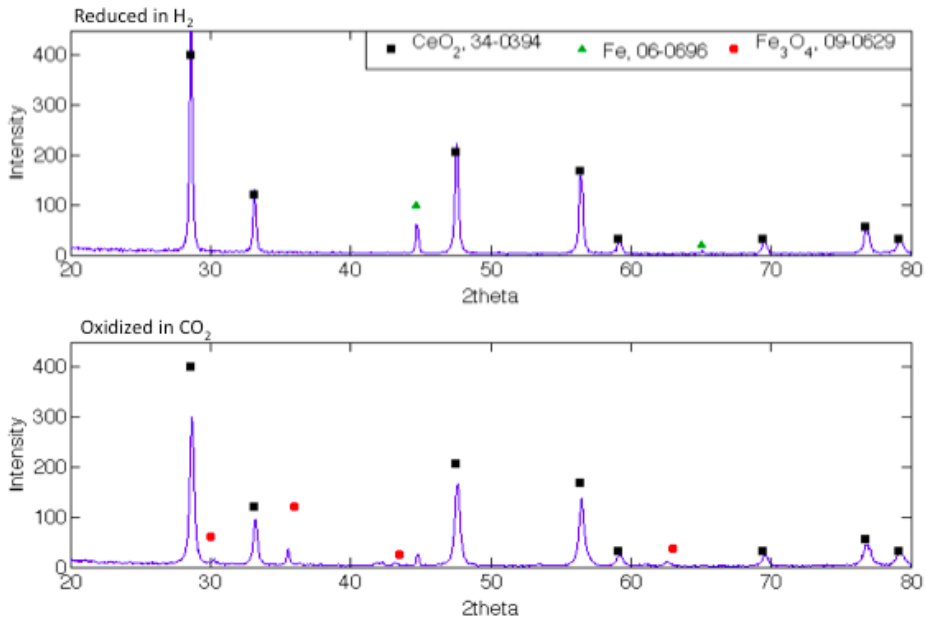


**Figure 92: XRD of Fe@$CeO_2$ material after reduction in $H_2$ (top) and oxidation in $CO_2$ (bottom)**

Next, $CH_4/CO_2$ cycles were tested in accordance with the CLDR process scheme. Reduction in methane was slow but progressed almost completely to Fe (Figure 93). Next, oxidation in $CO_2$ was fast (<10 min) and quickly reached the weight of the maximum possible oxidation state of $Fe_3O_4$, with no indication of a slow down at the weight corresponding to FeO as seen with hydrogen. Importantly, no obvious sign of coking was observed in this particular case, although strong coking occurred for higher methane flow rates (20 sccm) and if the reduction was allowed to proceed below weights corresponding with Fe. An example of the latter case is shown in Figure 94.

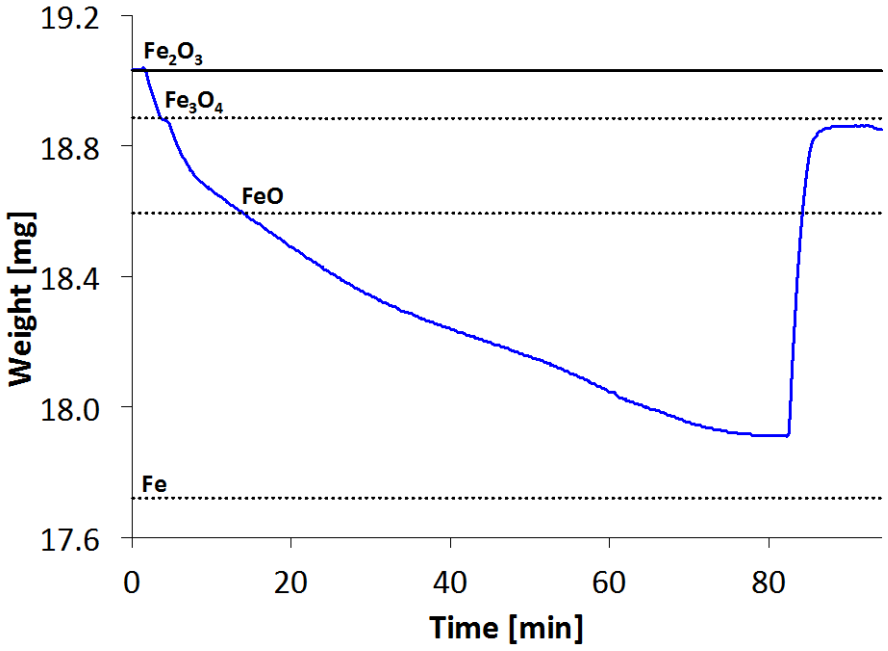


**Figure 93: $CH_4$ reduction and $CO_2$ oxidation in TGA ($CH_4$=10 sccm, $CO_2$=20 sccm, purge= 60 sccm, T=700°C). Sample flow was switched to inert at t=60 min to avoid coke formation. $CO_2$ oxidation proceeded to $Fe_3O_4$.**

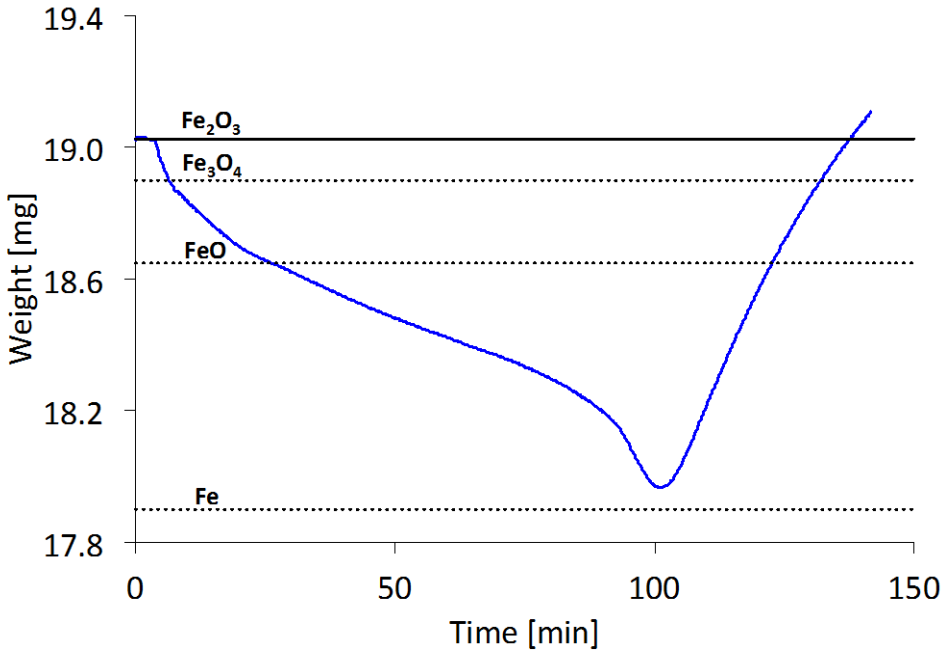


**Figure 94: $CH_4$ reduction in TGA with coking observed ($CH_4$=10 sccm, purge= 60 sccm, T=700°C). Coking began at t=100 min, resulting in fast weight gain above initial oxidized weight.**

TGA studies were repeated with Fe-$CeO_2$ material and the results were strikingly similar. Coking was also observed in TGA for this material if the reduction cycle was allowed to proceed too long. A summary of the iron utilization measured in TGA with previously studied materials (Fe@$SiO_2$, hFe@$SiO_2$, Fe-BHA) and material in this study (Fe@$CeO_2$ and Fe-$CeO_2$) is given in Figure 95. While an improvement was seen for the $H_2/CO_2$ test cycle for more open structures of hFe@$SiO_2$ and Fe-BHA, operation with methane was found to only be achievable with iron-ceria materials. The performance of Fe@$CeO_2$ and Fe-$CeO_2$ materials in TGA was nearly equivalent, perhaps suggesting that it is merely the presence of ceria and not the location of the iron particles that contributes to its activity for CLDR cycles.

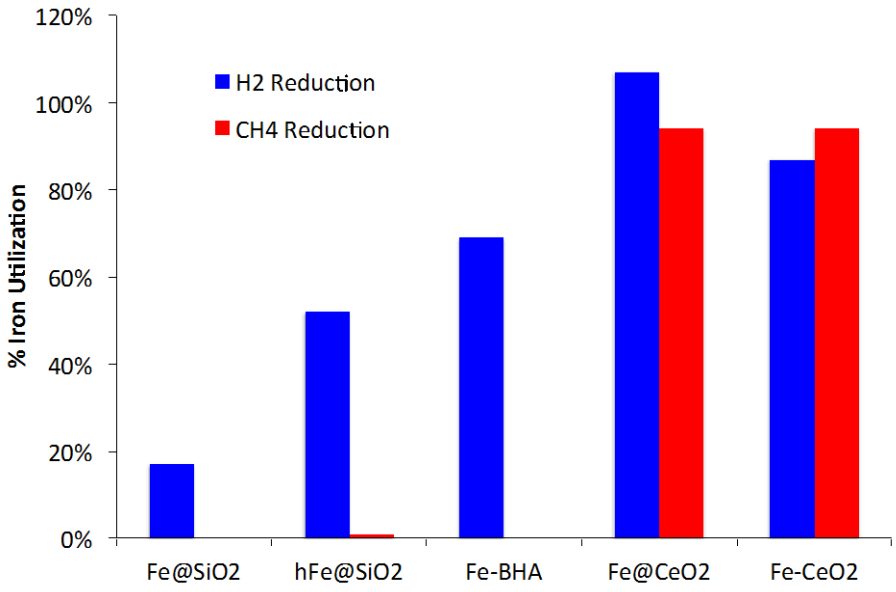


**Figure 95: Fe utilization for several carrier materials during testing in TGA with $H_2/CO_2$ test cycles and $CH_4/CO_2$ CLDR cycles**

Finally, the Fe@$CeO_2$ and Fe-$CeO_2$ materials were viewed in TEM after cycling operating in TGA at 700°C (Figure 96). The Fe@$CeO_2$ shows a collapse of the deposited ceria onto the iron rod while the Fe-$CeO_2$ showed sintering of rod-shaped ceria support.

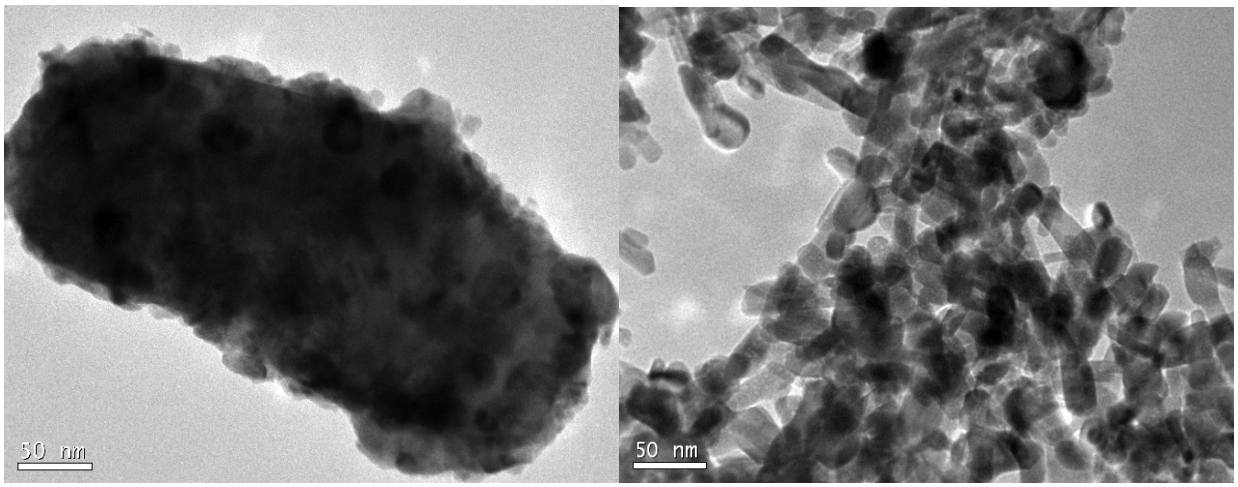


**Figure 96: TEM of Fe@$CeO_2$ (left) and Fe-$CeO_2$ after 2-5 cycles in TGA at 700°C.**

Next, fixed bed reactor studies were conducted to further characterize these materials for CLDR. First, seven $H_2/CO_2$ test cycles were run with Fe@$CeO_2$ at 800°C to determine whether stable and reproducible oxidation-reduction behavior could be achieved. The dry gas compositions of the reactor effluent streams were determined by mass spectrometry (Figure 97). Data from a single cycle of this experiment is also shown. A slightly higher temperature of 800°C was selected for this part of the work since better carrier activity was observed with this temperature within the desired cycle times for the fixed bed set-up. During the oxidation cycle, conversion of $CO_2$ to CO is indeed observed, as indicated by the spike in CO at the beginning of the oxidation half-cycle. Cumulative CO production during the oxidation half-cycle corresponded quantitatively to 100% oxidation of Fe to $Fe_3O_4$ in the first 2 min of operation. A final carrier conversion of 120% was reached after 10 min, indicating that the $CeO_2$ support (partially reduced after the reduction half-cycle) also participated in the $CO_2$ reduction to CO. This last observation is consistent with our TGA studies in which the $CeO_2$ support also enabled carrier conversions >100%. Similar behavior was observed for Fe-$CeO_2$ materials with $H_2$/CO cycles.

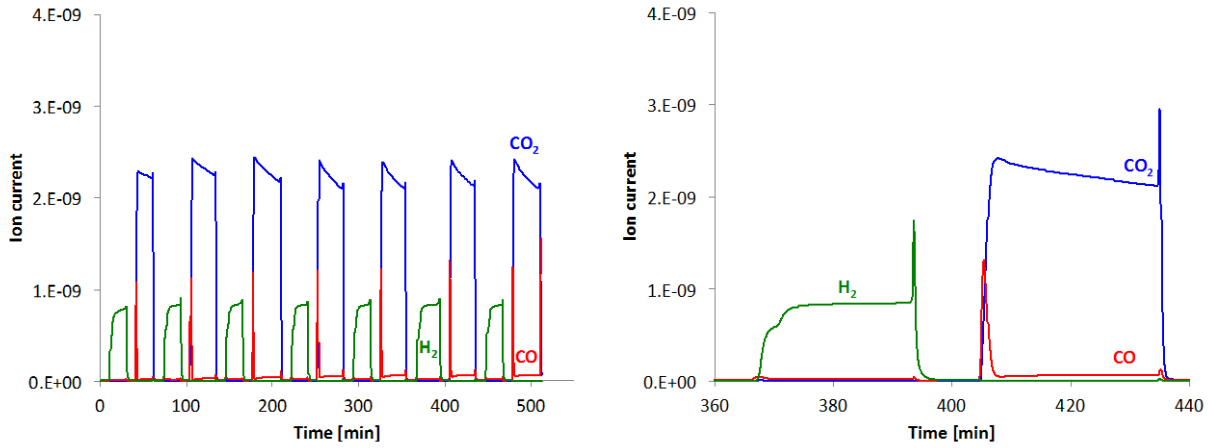


**Figure 97: $H_2/CO_2$ test cycles, showing stable oxidation-reduction operation for Fe@$CeO_2$ [80 mg, 13.8% Fe] in fixed bed reactor. T=800°C, He=25 sccm, $H_2$=2.5 sccm, $CO_2$=10 sccm.**

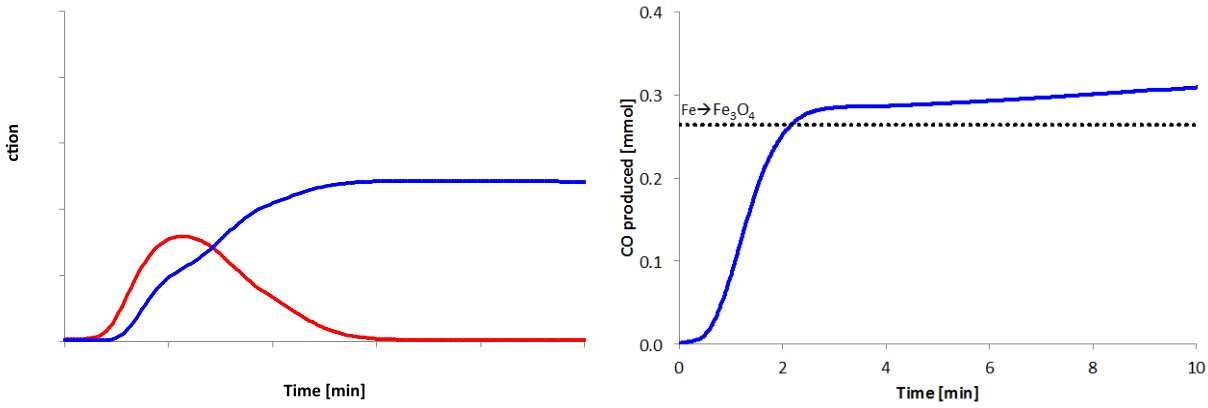


**Figure 98: Composition of effluent gases during oxidation half-cycle with Fe@$CeO_2$ [80 mg, 13.8 wt % Fe] in fixed bed reactor (left) and carrier conversion (right). Carrier conversion at 10 min is ~120% indicating the contribution of the reduced ceria support in the oxidation half-cycle. T=800°C, He=25 sccm, $H_2$=2.5 sccm, $CO_2$=10 sccm.**

Determination of activity during methane reduction was an essential next step to compare the ceria-based materials. While conditions that avoided coking were identified in TGA, different gas contacting patterns in fixed bed reactor could preclude this. For reduction in methane, several results are possible:

(1) Complete combustion: $CH_4 + Fe_3O_4 \rightarrow CO_2 + 2\ H_2O + 3Fe$

(2) Partial oxidation: $4CH_4 + Fe_3O_4 \rightarrow 4CO + 8\ H_2 + 3\ Fe$

(3) Catalytic methane decomposition: $CH_4 \rightarrow C + 2H_2$.

In Figure 99 and Figure 100, experimental data are compared for both Fe@$CeO_2$ and Fe-$CeO_2$ materials during reduction with methane. Contrary to TGA studies, strong coking was observed after ~20 min time-on-stream. Prior to coking, methane conversions up to ~40% were observed for both materials. A more stable and higher $H_2$/CO ratio of ~1 was measured for the Fe-$CeO_2$ carrier. Although complete combustion of methane to $CO_2$ and $H_2O$ is the desired reaction for this step, this more stable selectivity for the Fe-$CeO_2$ material is preferred since the more homogenous reducer gas effluent is more easily processed in downstream operations. Carrier conversions after 30 min of operation were nearly 100% and over 100% for Fe@$CeO_2$ and Fe-$CeO_2$, respectively. Given that the reactor loading amount and compositions were equivalent for each of these tests, we can infer from this that a slightly better utilization was possible for Fe-$CeO_2$.

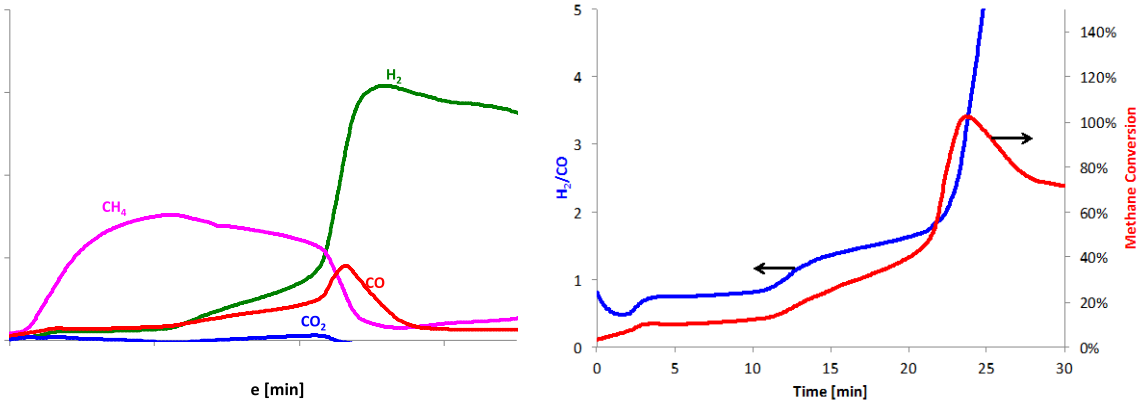


**Figure 99: Gas-phase compositions in reactor effluent (left) and $H_2$/CO ratio and methane conversion (right) during FBR reduction of Fe@$CeO_2$ [80 mg, 13.8 wt % Fe] in methane, showing coking at t=20 min. T=800°C, He=10 sccm, $CH_4$=1 sccm.**

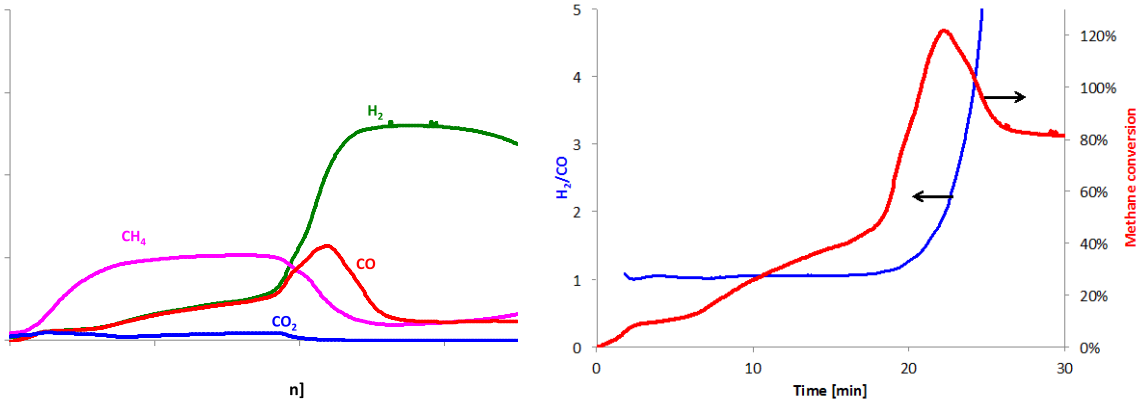


**Figure 100: Gas-phase compositions in reactor effluent (left) and $H_2$/CO ratio and methane conversion (right) during FBR reduction of Fe-$CeO_2$ [80 mg, 19 wt % Fe] in methane, showing coking at t=20 min. T=800°C, He=10 sccm, $CH_4$=1 sccm.**

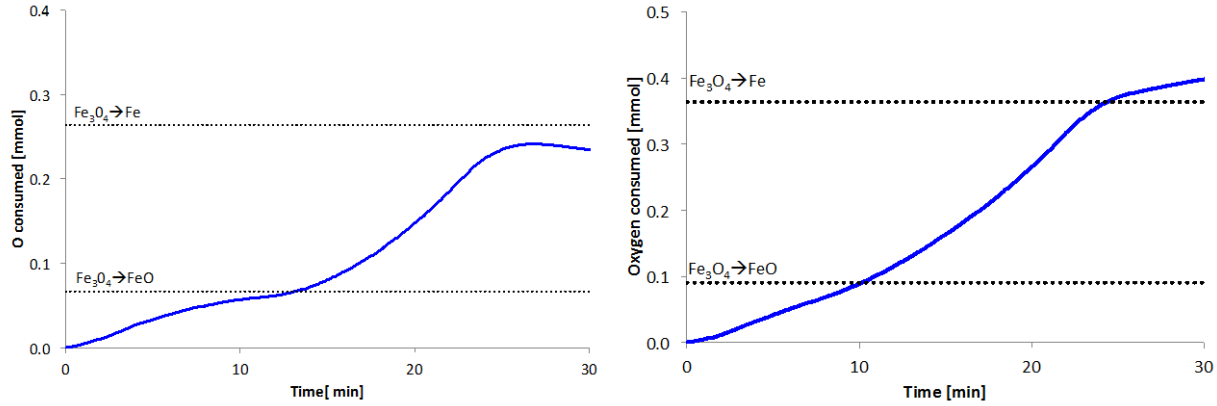


**Figure 101: Oxygen consumed by Fe@$CeO_2$ (left) and Fe-$CeO_2$ carriers during reduction with methane. Conversion is <100% and 108% after 30 min for Fe@$CeO_2$ and Fe-$CeO_2$ carriers, respectively.**

After t=30 min, the $H_2$ production subsided for both materials and methane breakthrough was observed, indicating that coke formation did not plug the reactor in either case. Following reduction in methane, oxidation in $CO_2$ was tested. Here, the CO measured was much greater than the case after reduction in hydrogen due to $CO_2$ gasification of the deposited carbon. The more oxidized carrier and longer methane reduction (150 min versus 40 min) for the Fe-$CeO_2$ materials resulted in more CO production during this test. In total, the cumulative CO equates to gasification of 0.9 mmol and 2.9 mmol carbon for Fe@$CeO_2$ and Fe-$CeO_2$, respectively. This carbon in turn amounts to ~40-50% of the methane fed to the reactor during each of the reduction half-cycles.

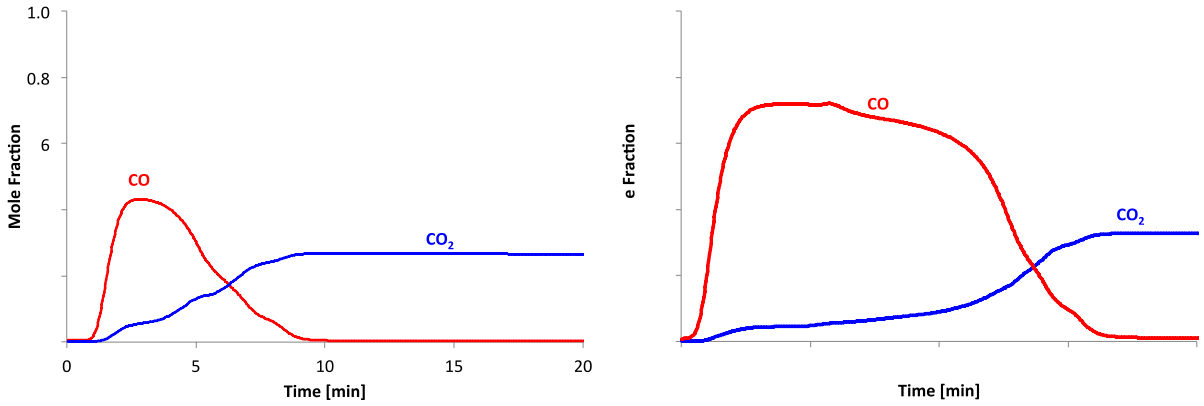


**Figure 102: $CO_2$ oxidation after 40 min $CH_4$ reduction (left) and 150 min $CH_4$ reduction (right), showing gasification of carbon formed during $CH_4$ reduction to CO. T=800°C, He=10 sccm, $CO_2$=5 sccm.**

## Discussion

Ceria-supported iron carriers were synthesized and evaluated for CLDR. TGA studies indicated complete iron utilization without significant carbon formation, even during reduction with methane. This is in contrast to previously tested materials, which suffered from either insufficient extent of reduction ($Fe@SiO_2$) or coking (Fe-BHA). Furthermore, during subsequent oxidation with $CO_2$, formation of $Fe_3O_4$ was achieved. By contrast, the oxidation for $Fe@SiO_2$ was limited to weights corresponding with FeO, and the strong coking of Fe-BHA materials prevented us from ever examining the $CO_2$ oxidation detail following reduction in methane. Hence, as indicated by Figure 95, the iron utilization measured in TGA was greatly enhanced as a result of incorporation of ceria as a carrier support.

Despite this, in fixed bed reactor studies, coking was still a challenge and methane decomposition was the dominant reaction after 20 min time-on stream for both carrier materials. This can be addressed in several ways. Since over 50% of the carrier reduction was achieved in <20 min, shorter reduction cycles could be used, hence avoided coking on the carrier. However,

during this time carrier conversion was <40% and hence higher space times or more carrier material are recommended.

Fortunately, the coking observed appeared to be fairly reversible and was removed during the subsequent oxidation half-cycle by gasification with $CO_2$. In fact, one can even imagine a process that takes advantage of the reversible coking observed with these materials given that the overall result is a phase of high $H_2$ production in the reducer effluent and high CO production from the oxidizer. This alternative CLDR selectivity (i.e. to instead produce $H_2$ and CO) would be most convenient with the Fe-$CeO_2$ materials given the initial production of syngas ($H_2$/CO~1) during the reducer half-cycle. Hence, the end result would be production of distinct, in-situ separated effluents of $H_2$ from the reducer and CO from the oxidizer by use of the iron/ceria material as a carbon carrier. In preliminary studies in which we have limited the oxidation of the carrier, we have observed an immediate onset of coking at high methane conversion, which is self-quenched after a sustained period of $H_2$ production. Obviously, there are still important obstacles for this scenario such as avoidance of reactor plugging during methane decomposition and ensuring high conversion and selectively during each of these phases. However, this configuration would also allow capture and utilization of carbon fed to both reactors and allows a convenient work-around for the case of carbon formation.

**Conclusion**

Overall-ceria based carriers have been shown to dramatically improve CLDR feasibility. For the first time, reduction with $CH_4$ and subsequent oxidation in $CO_2$ were observed in a fixed bed reactor system for this process. A comparison of core-shell (Fe@$CeO_2$) versus simpler deposition-precipitation (Fe-$CeO_2$) materials was completed. Both materials performed much better than previously test silica supported and ceramic supported iron-based carriers. Based on

this analysis, we found no benefit from using the nanostructured core-shell Fe@$CeO_2$ material. Cost and scale-up are typically more challenging for such complex nanostructures. Hence, this observation is a benefit, demonstrating that the CLDR process is not dependent on delicately designed and expensive carrier materials. We plan to continue this work by performing extended cycling studies with shortened cyclic times using Fe-$CeO_2$ materials with a range of iron contents to determine specific compositions for synergetic improvements in redox performance of iron-ceria carriers for CLDR.

## 3.9 CLDR CONCLUSION

Overall this work involved the conceptualization of a new type of chemical looping process in CLDR, assessment of its thermodynamic feasibility and energetics, development of several multi-component and nano-tailored materials, and reactive testing with these materials for the process.

We demonstrated that among transition metals iron is the most suitable candidate given its low toxicity, many oxidation states, susceptibility of oxidation in $CO_2$, and high oxygen carrying capacity at a wide range of temperatures. However, later studies revealed that CLDR might be accomplished with other materials as well. For instance, $CeO_2$ was later selected as a support because it was known to have excellent oxygen mobility. In addition, it was found to participate in oxygen-reduction chemistry, enhancing the carrier performance beyond that from iron alone. Indeed, the field of solar-thermal $CO_2$ and $H_2O$ splitting (a process very similar to CLDR) seems to be well aware of this; $CeO_2$ is used extensively and even exclusively as an oxygen carrier for this process. Yet in our experience with Fe-$CeO_2$ carriers, poor selectivity was observed for complete oxidation of the fuel, and the reaction was very susceptible to coking. Zinc was excluded from our studies given the very high temperatures required for zinc oxide reduction. However, zinc has also been proposed as a carrier for the solar-thermal process, and hence its used in the CLDR process may remain (*231*). Alternatively, the use of bimetallic carriers, such as Fe/Ni, might improve selectivity for complete oxidation during the reduction phase while the presence of reduced Fe or FeO would still allow reduction of $CO_2$ to CO in

oxidizer half-cycle of CLDR. In this way, a synergy between the high reactivity and preferred selectivity of Ni for the reduction and reactivity of iron with $CO_2$ might be gained. Finally, CLDR was originally conceptualized with full combustion in mind for the reducer reactor in order to close the heat balance and thereby produce enough energy to drive the endothermic CLDR reaction. However, time and again we observed selectivity for partial oxidation of the carrier. Although this would result in an even more endothermic process, it may be worthwhile to test carriers for this reaction pathway.

Another more unconventional approach might be to allow coking of the carrier in the reduction phase to form a high purity effluent of hydrogen from the reducer by the methane decomposition reaction. In our experiments, strong carbon formation was observed with $Fe/CeO_2$ carriers, but the coking did not plug the reactor and was self-quenched after ~30 min. In the subsequent $CO_2$ phase, an elevated CO effluent was observed, indicating gasification of the coke by the Boudouard reaction. In our development of the CLDR process, we specifically aimed to avoid coke formation. However, operation within a regime of 'controlled and self-quenched coking' may actually open up a new pathway for de-carbonization of methane by cyclic decomposition and gasification cycles. Obviously this proposal introduces high risk of reactor complexities due to reactor clogging and flow disturbance, but the idea is tempting nonetheless.

To summarize, a progression of several carriers were synthesized and tested for this work. Worth mentioning is the excellent redox kinetics of Fe-BHA during test reactions with $H_2/CO_2$ compared to other materials. Although this material was not realistic when methane was used as the reducer, it nonetheless was an excellent CLC carrier, which has also been reported previously for Ni-BHA carriers (*175*). Specifically, Fe-BHA exhibited fast and stable redox

kinetics for many cycles. By contrast, Fe@$SiO_2$ suffered from poor iron utilization and kinetics due to formation of iron silicates. Design of hollow Fe@$SiO_2$ showed an improvement in iron utilization, but still suffered from slow kinetics due to silicates and coking when using methane as the fuel. Despite this, our observation of improved reducibility by implementation of a hollow, more accessible core, could have use in other chemical looping carriers, or in other processes that require cyclic redox of a material. Finally, both Fe@$CeO_2$ and Fe-$CeO_2$ materials showed for the first time activity for CLDR with methane. While no significant difference was found between the performances of these two carriers, the simpler synthesis of Fe-$CeO_2$ is advantageous for scale-up of the process. Due to the use of ceria, iron utilization was at or near 100% for these materials, even during operation with methane. Further cycling studies are proposed with the Fe-$CeO_2$ material to further characterize the stability of the material during high-temperature operation in CLDR.

# REFERENCES


1. NSF, "The Societal Implications of Nanoscience and Nanotechnology" (Arlinton, VI, 2001).

2. D. Rejeski. (2009), vol. 2011.

3. NNI. (National Nanotechnology Institute).

4. G. A. Somorjai, A. M. Contreras, M. Montano, R. M. Rioux, Clusters, surfaces, and catalysis. *Proc. Natl. Acad. Sci. U. S. A.* **103**, 10577 (2006).

5. G. A. Somorjai, Y. M. Li, Impact of surface chemistry. *Proc. Natl. Acad. Sci. U. S. A.* **108**, 917 (2011).

6. D. Uzio, G. Berhault, Factors Governing the Catalytic Reactivity of Metallic Nanoparticles. *Catal. Rev. - Sci. Eng.* **52**, 106 (2010).

7. S. Jeong *et al.*, Controlling the thickness of the surface oxide layer on Cu nanoparticles for the fabrication of conductive structures by ink-jet printing. *Adv. Funct. Mater.* **18**, 679 (2008).

8. P. Poizot, S. Laruelle, S. Grugeon, L. Dupont, J. M. Tarascon, Nano-sized transition-metaloxides as negative-electrode materials for lithium-ion batteries. *Nature* **407**, 496 (2000).

9. S. A. Maier *et al.*, Plasmonics - A route to nanoscale optical devices. *Adv. Mater.* **13**, 1501 (2001).

10. H. Wang, D. W. Brandl, P. Nordlander, N. J. Halas, Plasmonic nanostructures: Artificial molecules. *Acc. Chem. Res.* **40**, 53 (2007).

11. L. S. Zhong *et al.*, Self-assembled 3D flowerlike iron oxide nanostructures and their application in water treatment. *Adv. Mater.* **18**, 2426 (2006).

12. J. Y. Bottero, J. Rose, M. R. Wiesner, Nanotechnologies: tools for sustainability in a new wave of water treatment processes. *Integrated Environmental Assessment and Management* **2**, 391 (2009).

13. A. Sanchez *et al.*, When gold is not noble: Nanoscale gold catalysts. *J. Phys. Chem. A* **103**, 9573 (1999).

14. J. Kim, Y. Piao, T. Hyeon, Multifunctional nanostructured materials for multimodal imaging, and simultaneous imaging and therapy. *Chem. Soc. Rev.* **38**, 372 (2009).

15. T. J. Yoon *et al.*, Specific targeting, cell sorting, and bioimaging with smart magnetic silica core-shell nanomateriats. *Small* **2**, 209 (2006).

16. Y. Xia, Nanomaterials at work in biomedical research. *Nature materials* **7**, 758 (2008).

17. L. T. Rosenblum, N. Kosaka, M. Mitsunaga, P. L. Choyke, H. Kobayashi, In vivo molecular imaging using nanomaterials: General in vivo characteristics of nano-sized reagents and applications for cancer diagnosis (Review). *Molec. Membr. Biol.* **27**, 274 (2010).

18. K. J. Lee, P. D. Nallathamby, L. M. Browning, C. J. Osgood, X. H. N. Xu, In vivo imaging of transport and biocompatibility of single silver nanoparticles in early development of zebrafish embryos. *ACS Nano* **1**, 133 (2007).

19. J. Lee, S. Mahendra, P. J. J. Alvarez, Nanomaterials in the construction industry: A review of their applications and environmental health and safety considerations. (2010).

20. in *The Economist*. (The Economist Newpaper Limited, London, 2007).

21. V. L. Colvin, The potential environmental impact of engineered nanomaterials. *Nat. Biotechnol.* **21**, 1166 (2003).

22. A. D. Maynard *et al.*, Safe handling of nanotechnology. *Nature* **444**, 267 (2006).

23. M. R. Gwinn, V. Vallyathan, Nanoparticles: Health effects - Pros and cons. *Environ. Health Perspect.* **114**, 1818 (2006).

24. W. H. De Jong, P. J. A. Borm, Drug delivery and nanoparticles: Applications and hazards. *Inter. J. of Nanomedicine* **3**, 133 (2008).

25. G. Oberdorster, E. Oberdorster, J. Oberdorster, Nanotoxicology: An emerging discipline evolving from studies of ultrafine particles. *Environ. Health Perspect.* **113**, 823 (2005).

26. T. Xia, M. Kovochich, A. E. Nel, Impairment of mitochondrial function by particulate matter (PM) and their toxic components: implications for PM-induced cardiovascular and lung disease. *Front Biosci* **12**, 1238 (2007).

27. C. D. Klaassen, J. B. Watkins, *Casarett & Doull's Essentials of Toxicology*. (Mc Graw Hill, New York, 2003), pp. 533.

28. A. Nel, T. Xia, L. Madler, N. Li, Toxic potential of materials at the nanolevel. *Science* **311**, 622 (2006).

29. W. Jiang, B. Y. S. Kim, J. T. Rutka, W. C. W. Chan, Nanoparticle-mediated cellular response is size-dependent. *Nat. Nanotechnol.* **3**, 145 (2008).

30. M. Auffan, J. Rose, M. R. Wiesner, J. Y. Bottero, Chemical stability of metallic nanoparticles: A parameter controlling their potential cellular toxicity in vitro. *Environ. Pollut.* **157**, 1127 (2009).

31. A. D. Maynard, D. B. Warheit, M. A. Philbert, The New Toxicology of Sophisticated Materials: Nanotoxicology and Beyond. *Toxicol. Sci.* **120**, S109 (2011).

32. C. R. Thomas *et al.*, Nanomaterials in the Environment: From Materials to High-Throughput Screening to Organisms. *ACS Nano* **5**, 13 (2011).

33. D. B. Warheit, P. J. A. Borm, C. Hennes, J. Lademann, Testing strategies to establish the safety of nanomaterials: Conclusions of an ECETOC workshop. *Inhalation Toxicol.* **19**, 631 (2007).

34. A. M. Voutchkova *et al.*, Towards rational molecular design: derivation of property guidelines for reduced acute aquatic toxicity. *Green Chem.* **13**, 2373 (2011).

35. S. Lin *et al.*, High Content Screening in Zebrafish Speeds up Hazard Ranking of Transition Metal Oxide Nanoparticles. *ACS Nano* **5**, 7284 (2011/09/27, 2011).

36. A. J. Hill, M. Jones, A. Dodd, H. Diekmann, A Review of Developmental Toxicity Screening Using Zebrafish Larvae. *Int. J. Toxicol.* **30**, 105 (2011).

37. B. Fraysse, R. Mons, J. Garric, Development of a zebrafish 4-day toxicity of embryo-larval bioassay to assess chemicals. *Ecotoxicol. Environ. Saf.* **63**, 253 (2006).

38. J. P. Ryman-Rasmussen, J. E. Riviere, N. A. Monteiro-Riviere, Penetration of intact skin by quantum dots with diverse physicochemical properties. *Toxicol. Sci.* **91**, 159 (2006).

39. J. M. McKim, S. P. Bradbury, G. J. Niemi, Fish Acute Toxicity Syndromes and Their Use in the Qsar Approach to Hazard Assessment. *Environ. Health Perspect.* **71**, 171 (1987).

40. A. Baun, N. B. Hartmann, K. Grieger, K. O. Kusk, Ecotoxicity of engineered nanoparticles to aquatic invertebrates: a brief review and recommendations for future toxicity testing. *Ecotoxicology* **17**, 387 (2008).

41. M. N. Moore, Do nanoparticles present ecotoxicological risks for the health of the aquatic environment? *Environ. Int.* **32**, 967 (Dec, 2006).

42. U.S.E.P.A. (2007).

43. D. Beyersmann, A. Hartwig, Carcinogenic metal compounds: recent insight into molecular and cellular mechanisms. *Arch. Toxicol.* **82**, 493 (2008).

44. K. Das, S. Das, S. Dhundasi, Nickel, its adverse health effects & oxidative stress. *The Indian journal of medical research* **128**, 412 (2008).

45. V. Scheil, H. R. Kohler, Influence of Nickel Chloride, Chlorpyrifos, and Imidacloprid in Combination with Different Temperatures on the Embryogenesis of the Zebrafish Danio rerio. *Arch. Environ. Contam. Toxicol.* **56**, 238 (2009).

46. G. Dave, R. Q. Xiu, Toxicity of Mercury, Copper, Nickel, Lead, and Cobalt to Embryos and Larvae of Zebrafish, Brachydanio-Rerio. *Arch. Environ. Contam. Toxicol.* **21**, 126 (1991).

47. C. Kienle, H. R. Kohler, A. Gerhardt, Behavioural and developmental toxicity of chlorpyrifos and nickel chloride to zebrafish (Danio rerio) embryos and larvae. *Ecotoxicol. Environ. Saf* **72**, 1740 (2009).

48. C. Ispas *et al.*, Toxicity and Developmental Defects of Different Sizes and Shape Nickel Nanoparticles in Zebrafish. *Environ. Sci. Technol.* **43**, 6349 (2009).

49. R. J. Griffitt, J. Luo, J. Gao, J. C. Bonzongo, D. S. Barber, Effects of particle composition and species on toxicity of metallic nanomaterials in aquatic organisms. *Environ. Toxicol. Chem.* **27**, 1972 (2008).

50. P. Borm *et al.*, Research strategies for safety evaluation of nanomaterials, Part V: Role of dissolution in biological fate and effects of nanoscale particles. *Toxicol. Sci.* **90**, 23 (2006).

51. A. Muñoz, M. Costa, Elucidating the mechanisms of nickel compound uptake: A review of particulate and nano-nickel endocytosis and toxicity. *Toxicol. Appl. Pharmacol.*, (2011).

52. M. Costa, H. H. Mollenhauer, Carcinogenic activity of particulate nickel compounds is proportional to their cellular uptake. *Science* **209**, 515 (1980).

53. M. Auffan *et al.*, Towards a definition of inorganic nanoparticles from an environmental, health and safety perspective. *Nat. Nanotechnol.* **4**, 634 (2009).

54. M. Mahmoudi, A. Simchi, M. Imani, A. S. Milani, P. Stroeve, An in vitro study of bare and poly(ethylene glycol)-co-fumarate-coated superparamagnetic iron oxide nanoparticles: a new toxicity identification procedure. *Nanotechnology* **20**, (2009).

55. M. Mahmoudi, A. Simchi, M. Imani, Cytotoxicity of Uncoated and Polyvinyl Alcohol Coated Superparamagnetic Iron Oxide Nanoparticles. *Journal of Physical Chemistry C* **113**, 9573 (2009).

56. C. Graf, D. L. J. Vossen, A. Imhof, A. van Blaaderen, A general method to coat colloidal particles with silica. *Langmuir* **19**, 6693 (2003).

57. G. A. Sotiriou *et al.*, Non-Toxic Dry-Coated Nanosilver for Plasmonic Biosensors. *Adv. Funct. Mater.* **20**, 4250 (2010).

58. Y. Chen *et al.*, Core/Shell Structured Hollow Mesoporous Nanocapsules: A Potential Platform for Simultaneous Cell Imaging and Anticancer Drug Delivery. *Acs Nano* **4**, 6001 (2010).

59. T. J. Brunner *et al.*, In vitro cytotoxicity of oxide nanoparticles: Comparison to asbestos, silica, and the effect of particle solubility. *Environ. Sci. Tech.* **40**, 4374 (2006).

60. K. Fent, C. J. Weisbrod, A. Wirth-Heller, U. Pieles, Assessment of uptake and toxicity of fluorescent silica nanoparticles in zebrafish (Danio rerio) early life stages. *Aquat. Toxicol.* **100**, 218 (2010).

61. L. K. Limbach *et al.*, Exposure of engineered nanoparticles to human lung epithelial cells: Influence of chemical composition and catalytic activity on oxidative stress. *Environmental Science & Technology* **41**, 4158 (2007).

62. K. O. Yu *et al.*, Toxicity of amorphous silica nanoparticles in mouse keratinocytes. *J. Nanopart. Res.* **11**, 15 (2009).

63. W. S. Lin, Y. W. Huang, X. D. Zhou, Y. F. Ma, In vitro toxicity of silica nanoparticles in human lung cancer cells. *Toxicol. Appl. Pharmacol.* **217**, 252 (2006).

64. M. A. Maurer-Jones, Y. S. Lin, C. L. Haynes, Functional Assessment of Metal Oxide Nanoparticle Toxicity in Immune Cells. *ACS Nano* **4**, 3363 (2010).

65. J. Kim *et al.*, Multifunctional Uniform Nanoparticles Composed of a Magnetite Nanocrystal Core and a Mesoporous Silica Shell for Magnetic Resonance and Fluorescence Imaging and for Drug Delivery. *Angew. Chem. Int. Ed.* **47**, 8438 (2008).

66. X. Li, D. W. Elliott, W. Zhang, Zero-valent iron nanoparticles for abatement of environmental pollutants: Materials and engineering aspects. *Crit. Rev. Solid State Mater. Sci.* **31**, 111 (2006).

67. S. H. Joo *et al.*, Thermally stable Pt/mesoporous silica core-shell nanocatalysts for high-temperature reactions. *Nat. Mater.* **8**, 126 (2009).

68. S. Takenaka, H. Umebayashi, E. Tanabe, H. Matsune, M. Kishida, Specific performance of silica-coated Ni catalysts for the partial oxidation of methane to synthesis gas. *J. Catal.* **245**, 392 (2007).

69. L. Z. Whaley, PhD Proposal, University of Pittsburgh (2010).

70. C. L. Chang, H. S. Fogler, Kinetics of silica particle formation in nonionic W/O microemulsions from TEOS. *AlChE J.* **42**, 3153 (1996).

71. H. Irving, R. J. P. Williams, The Stability of Transition-Metal Complexes. *J. Chem. Soc.*, 3192 (1953).

72. J. Yang, Y. Shul, C. Louisb, M. Che, In situ EXAFS study of the nucleation and crystal growth of Ni particles on SiO2 support. *Catal. Today* **44**, 315 (1998).

73. X. Y. Deng, Z. Chen, Preparation of nano-NiO by ammonia precipitation and reaction in solution and competitive balance. *Mater. Lett.* **58**, 276 (2004).

74. R. Bird, W. Stewart, E. Lightfoot, *Transport Phenomena*. (John Wiley and Sons, New York , NY, 2007).

75. I. Chowdhury, Y. Hong, S. L. Walker, Container to characterization: Impacts of metal oxide handling, preparation, and solution chemistry on particle stability. *Colloids and Surfaces A: Physicochemical and Engineering Aspects* **368**, 91 (2010).

76. G. Dave, Effect of pH on pentachlorophenol toxicity to embryos and larvae of zebrafish (Brachydanio rerio). *Bulletin of environmental contamination and toxicology* **33**, 621 (1984).

77. U. Borgmann, R. Neron, W. P. Norwood, Quatification of bioavailable nickel in sediments and toxic thresholds to Hyalla azteca. *Environ. Pollut.* **111**, 189 (2000).

78. P. Gaines. (2012).

79. C. L. Cario, T. C. Farrell, C. Milanese, E. A. Burton, Automated measurement of zebrafish larval movement. *The Journal of Physiology* **589**, 3703 (August 1, 2011, 2011).

80. T. C. Farrell *et al.*, Evaluation of spontaneous propulsive movement as a screening tool to detect rescue of Parkinsonism phenotypes in zebrafish models. *Neurobiology of Disease* **44**, 18 (2011).

81. D. B. Warheit, C. M. Sayes, K. L. Reed, K. A. Swain, Health effects related to nanoparticle exposures: Environmental, health and safety considerations for assessing hazards and risks. *Pharmacol. Ther.* **120**, 35 (2008).

82. T. Xia, N. Li, A. E. Nel, Potential health impact of nanoparticles. *Annu. Rev. Public Health* **30**, 137 (2009).

83. M. Kirchhoff, U. Specht, G. Veser, Engineering high-temperature stable nanocomposite materials. *Nanotechnol.* **16**, S401 (2005).

84. Y. Shang, T. Zhu, Y. Li, J. C. Zhao, Size-dependent hydroxyl radicals generation induced by SiO 2 ultra-fine particles: The role of surface iron. *Sci. China Ser. B: Chem.* **52**, 1033 (2009).

85. D. Napierska *et al.*, Oxidative Stress Induced by Pure and Iron-Doped Amorphous Silica Nanoparticles in Subtoxic Conditions. *Chem. Res. Toxicol.* **25**, 828 (2012).

86. A. Nel *et al.*, Nanomaterial Toxicity Testing in the 21st Century: Use of a Predictive Toxicological Approach and High-Throughput Screening. *Acc. Chem. Res.* **46**, 607 (2012).

87. G. Oberdorster *et al.*, Principles for characterizing the potential human health effects from exposure to nanomaterials: elements of a screening strategy. *Part. Fibre Toxicol.* **2**, 8 (2005).

88. S. M. Hussain *et al.*, Toxicity Evaluation for Safe Use of Nanomaterials: Recent Achievements and Technical Challenges. *Adv. Mater.* **21**, 1549 (2009).

89. J. W. Card, B. A. Magnuson, A Method to Assess the Quality of Studies That Examine the Toxicity of Engineered Nanomaterials. *Inter. J. Toxicol.* **29**, 402 (2010).

90. D. B. Warheit, How meaningful are the results of nanotoxicity studies in the absence of adequate material characterization? *Toxicol. Sci.* **101**, 183 (2008).

91. J. G. Teeguarden, P. M. Hinderliter, G. Orr, B. D. Thrall, J. G. Pounds, Particokinetics in vitro: dosimetry considerations for in vitro nanoparticle toxicity assessments. *Toxicol. Sci.* **95**, 300 (2007).

92. C. P. Johnson, X. Li, B. E. Logan, Settling velocities of fractal aggregates. *Environ. Sci. Technol.* **30**, 1911 (1996).

93. A. Verma, F. Stellacci, Effect of Surface Properties on Nanoparticle–Cell Interactions. *Small* **6**, 12 (2010).

94. S. Nangia, R. Sureshkumar, Effects of Nanoparticle Charge and Shape Anisotropy on Translocation through Cell Membranes. *Langmuir* **28**, 17666 (2012/12/21, 2012).

95. M. Zhu *et al.*, Physicochemical Properties Determine Nanomaterial Cellular Uptake, Transport, and Fate. *Acc. Chem. Res.*, (2012).

96. G. B. Alexander, W. Heston, R. Iler, The solubility of amorphous silica in water. *J. Phys. Chem.* **58**, 453 (1954).

97. R. K. Iler, *The Chemistry of Sillica: Solubiity, Polimerization, Surface Properties, and Biochemistry*. (John Wiley and Sons, New York, NY, 1979), pp. 866.

98. L. K. Limbach *et al.*, Oxide Nanoparticles Uptake in Human Lung Fibroblasts: Effects of Particle Size, Agglomeration, and Diffusion at Low Concentrations. *Environ. Sci. Technol.* **39**, 9370 (2005).

99. T. Phenrat, N. Saleh, K. Sirk, R. D. Tilton, G. V. Lowry, Aggregation and sedimentation of aqueous nanoscale zerovalent iron dispersions. *Environ. Sci. Technol.* **41**, 284 (2007).

100. L. V. Stebounova, E. Guio, V. H. Grassian, Silver nanoparticles in simulated biological media: a study of aggregation, sedimentation, and dissolution. *J. Nanopart. Res.* **13**, 233 (2011).

101. K. Wittmaack, Excessive Delivery of Nanostructured Matter to Submersed Cells Caused by Rapid Gravitational Settling. *ACS Nano* **5**, 3766 (2011/05/24, 2011).

102. C. M. Powers, J. Yen, E. A. Linney, F. J. Seidler, T. A. Slotkin, Silver exposure in developing zebrafish (Danio rerio): Persistent effects on larval behavior and survival. *Neurotoxicol. Teratol.* **32**, 391 (2010).

103. E. J. Park, J. Yi, Y. Kim, K. Choi, K. Park, Silver nanoparticles induce cytotoxicity by a Trojan-horse type mechanism. *Toxicol. In Vitro* **24**, 872 (Apr, 2010).

104. X. S. Zhu *et al.*, Comparative toxicity of several metal oxide nanoparticle aqueous suspensions to Zebrafish (Danio rerio) early developmental stage. *ENVRAL* **43**, 278 (2008).

105. N. Hernández, R. Moreno, A. J. Sánchez-Herencia, J. L. G. Fierro, Surface behavior of nickel powders in aqueous suspensions. *J. Phys. Chem. B* **109**, 4470 (2005).

106. K. B. Krauskopf, Dissolution and precipitation of silica at low temperatures. *Geochim. Cosmochim. Acta* **10**, 1 (1956).

107. J. E. Fuller *et al.*, Intracellular delivery of core–shell fluorescent silica nanoparticles. *Biomaterials* **29**, 1526 (4//, 2008).

108. X. Y. Yang *et al.*, Mechanism of Silver Nanoparticle Toxicity Is Dependent on Dissolved Silver and Surface Coating in Caenorhabditis elegans. *Environmental Science & Technology* **46**, 1119 (Jan, 2012).

109. A. A. Keller *et al.*, Stability and Aggregation of Metal Oxide Nanoparticles in Natural Aqueous Matrices. *Environmental Science & Technology* **44**, 1962 (2010/03/15, 2010).

110. S. George *et al.*, Surface Defects on Plate-Shaped Silver Nanoparticles Contribute to Its Hazard Potential in a Fish Gill Cell Line and Zebrafish Embryos. *Acs Nano* **6**, 3745 (2012/05/22, 2012).

111. A. Deonarine, B. L. Lau, G. R. Aiken, J. N. Ryan, H. Hsu-Kim, Effects of humic substances on precipitation and aggregation of zinc sulfide nanoparticles. *Environmental Science and Technology-Columbus* **45**, 3217 (2011).

112. G. R. Aiken, H. Hsu-Kim, J. N. Ryan, Influence of dissolved organic matter on the environmental fate of metals, nanoparticles, and colloids. *Environmental science & technology* **45**, 3196 (2011).

113. W.-K. Oh *et al.*, Cellular Uptake, Cytotoxicity, and Innate Immune Response of Silica‚àíTitania Hollow Nanoparticles Based on Size and Surface Functionality. *ACS Nano* **4**, 5301 (2010/09/28, 2010).

114. S. Legrand *et al.*, Controlling silica nanoparticle properties for biomedical applications through surface modification. *New J. Chem.* **32**, 588 (2008).

115. A. Davila-Ibanez *et al.*, Magnetic Silica Nanoparticle Cellular Uptake and Cytotoxicity Regulated by Electrostatic Polyelectrolytes-DNA Loading at Their Surface. *ACS Nano* **6**, 747 (2012).

116. T. A. Davis, B. Volesky, A. Mucci, A review of the biochemistry of heavy metal biosorption by brown algae. *Water Res.* **37**, 4311 (11//, 2003).

117. N. C. Mueller, B. Nowack, Exposure Modeling of Engineered Nanoparticles in the Environment. *Environmental Science & Technology* **42**, 4447 (2008).

118. H. Meng *et al.*, Ultrahigh reactivity provokes nanotoxicity: Explanation of oral toxicity of nano-copper particles. *Toxicol. Lett.* **175**, 102 (2007).

119. A. Cao, R. Lu, G. Veser, Stabilizing metal nanoparticles for heterogeneous catalysis. *Phys Chem Chem Phys* **12**, 13499 (2010).

120. D. L. Trimm, Catalysts for the control of coking during steam reforming. *Catal. Today* **49**, 3 (Feb, 1999).

121. W. Keim, Nickel: An element with wide application in industrial homogeneous catalysis. *Angewandte Chemie International Edition in English* **29**, 235 (2003).

122. X. Du, J. H. He, Spherical silica micro/nanomaterials with hierarchical structures: Synthesis and applications. *Nanoscale* **3**, 3984 (2011).

123. J. H. Zhang, A. Thurber, C. Hanna, A. Punnoose, Highly Shape-Selective Synthesis, Silica Coating, Self-Assembly, and Magnetic Hydrogen Sensing of Hematite Nanoparticles. *Langmuir* **26**, 5273 (2010).

124. W. R. Zhao *et al.*, Uniform Rattle-type Hollow Magnetic Mesoporous Spheres as Drug Delivery Carriers and their Sustained-Release Property. *Adv. Funct. Mater.* **18**, 2780 (2008).

125. S. L. Tie *et al.*, Monodisperse Fe3O4/Fe@SiO2 core/shell nanoparticles with enhanced magnetic property. *Colloids Surf., A* **293**, 278 (2007).

126. M. Ikeda, T. Tago, M. Kishida, K. Wakabayashi, Thermal stability of an SiO2-coated Rh catalyst and catalytic activity in NO reduction by CO. *Chem. Commun.*, 2512 (2001).

127. X. Gao, K. M. K. Yu, K. Y. Tam, S. C. Tsang, Colloidal stable silica encapsulated nano-magnetic composite as a novel bio-catalyst carrier. *Chem. Commun.*, 2998 (2003).

128. Y. H. Deng *et al.*, Multifunctional Mesoporous Composite Microspheres with Well-Designed Nanostructure: A Highly Integrated Catalyst System. *JACS* **132**, 8466 (2010).

129. B. Fadeel *et al.*, There's plenty of room at the forum: Potential risks and safety assessment of engineered nanomaterials. *Nanotoxicology* **1**, 73 (2007).

130. K. Donaldson, V. Stone, C. L. Tran, W. Kreyling, P. J. A. Borm, Nanotoxicology. *Occup. Environ. Med.* **61**, 727 (Sep, 2004).

131. G. E. Lyons, Vertebrate heart development. *Curr. Opin. Genet. Dev.* **6**, 454 (1996).

132. V. Scheil, A. Zurn, H. R. Kohler, R. Triebskorn, Embryo Development, Stress Protein (Hsp70) Responses, and Histopathology in Zebrafish (Danio rerio) Following Exposure to Nickel Chloride, Chlorpyrifos, and Binary Mixtures of Them. *Environ. Toxicol.* **25**, 83 (Feb, 2010).

133. W. Burggren, T. Blank, Physiological study of larval fishes: challenges and opportunities. *Sci. Mar.* **73**, 99 (Oct, 2009).

134. C. Nusslein-Volhard, R. Dahm, *Zebrafish: A Practical Approach*. (Oxford University Press, Oxford, 2002).

135. U.S.E.P.A., "Greenhouse Gas Inventory Report" *U.S. EPA # 430-R-1-006* (2010).

136. U.S.E.I.A., "Monthly Energy Review" (2010).

137. E.S.R.L. (2011).

138. IEA, "CO2 Emissions from Fuel Combustion" (International Energy Agency, Paris, France, 2009).

139. T. R. Karl, K. E. Trenberth, Modern global climate change. *Science* **302**, 1719 (2003).

140. IPCC, "Climate Change 2007, Synthesis Report. Contribution from Working Groups I, II, and III to the Fourth Assesment" (IPCC, Geneva, Switzerland, 2007).

141. N. Stern, The economics of climate change. *American Economic Review* **98**, 1 (2008).

142. M. Ishida, H. G. Jin, A New Advanced Power-Generation System Using Chemical-Looping Combustion. *Energy* **19**, 415 (1994).

143. M. M. Hossain, H. I. de Lasa, Chemical-looping combustion (CLC) for inherent CO2 separations-a review. *Chem. Eng. Sci.* **63**, 4433 (2008).

144. A. Lyngfelt, B. Leckner, T. Mattisson, A fluidized-bed combustion process with inherent CO2 separation; application of chemical-looping combustion. *Chem. Eng. Sci.* **56**, 3101 (2001).

145. H. J. Richter, K. F. Knoche, Reversibility of Combustion Processes. *ACS Symp. Ser.* **235**, 71 (1983).

146. M. Anheden, G. Svedberg, Exergy analysis of chemical-looping combustion systems. *Energy Convers. Manage.* **39**, 1967 (1998).

147. J. Dewulf *et al.*, Exergy: Its potential and limitations in environmental science and technology. *Environmental Science & Technology* **42**, 2221 (2008).

148. B. Moghtaderi, Review of the Recent Chemical Looping Process Developments for Novel Energy and Fuel Applications. *Energy & Fuels* **26**, 15 (2012/01/19, 2011).

149. H. Fang, L. Haibin, Z. Zengli, Advancements in development of chemical-looping combustion: A review. *International Journal of Chemical Engineering* **2009**, (2009).

150. L. S. Fan, L. Zeng, W. Wang, S. Luo, Chemical Looping Processes for CO2 Capture and Carbonaceous Fuel Conversion–Prospect and Opportunity. *Energy & Environmental Science*, (2012).

151. C. S. Song, *CO2 Conversion and Utilization*. (Oxford University Press, Incorporated, New York, 2002), pp. 440.

152. M. Aresta, *Carbon dioxide recovery and utilization*. M. Aresta, Ed., (Kluwer Academic Publishers, Boston, 2003), pp. 407.

153. J. Ma *et al.*, A short review of catalysis for CO2 conversion. *Catal. Today* **148**, 221 (Nov, 2009).

154. G. Centi, S. Perathoner, Opportunities and prospects in the chemical recycling of carbon dioxide to fuels. *Catal. Today* **148**, 191 (2009).

155. C. S. Song, Global challenges and strategies for control, conversion and utilization of CO2 for sustainable development involving energy, catalysis, adsorption and chemical processing. *Catal. Today* **115**, 2 (2006).

156. A. T. Ashcroft, A. K. Cheetham, M. L. H. Green, P. D. F. Vernon, Partial Oxidation of Methane to Synthesis Gas-Using Carbon-Dioxide. *Nature* **352**, 225 (1991).

157. P. D. F. Vernon, M. L. H. Green, A. K. Cheetham, A. T. Ashcroft, Partial Oxidation of Methane to Synthesis Gas, and Carbon-Dioxide as an Oxidizing-Agent for Methane Conversion. *Catal. Today* **13**, 417 (1992).

158. M. S. Fan, A. Z. Abdullah, S. Bhatia, Catalytic Technology for Carbon Dioxide Reforming of Methane to Synthesis Gas. *Chemcatchem* **1**, 192 (2009).

159. M. M. Halman, M. Steinberg, *Greehhouse Gas Carbon Dioxide Mitigation*. (CRC Press LLC, Boca Raton, 1999), pp. 568.

160. M. C. J. Bradford, M. A. Vannice, CO2 reforming of CH4. *Catalysis Reviews-Science and Engineering* **41**, 1 (1999).

161. J. R. H. Ross, A. N. J. vanKeulen, M. E. S. Hegarty, K. Seshan, The catalytic conversion of natural gas to useful products. *Catal. Today* **30**, 193 (1996).

162. S. Wang, G. Lu*, G. J. Millar, Carbon dioxide reforming of methane to produce synthesis gas over metal-supported catalysts: state of the art. *Energy & Fuels* **10**, 896 (1996).

163. S. Teuner, Make CO from CO2. *Hydrocarb. Process.* **64**, 106 (1985).

164. M. Beller, B. Cornils, C. D. Frohning, C. W. Kohlpaintner, Progress in hydroformylation and carbonylation. *J. Mol. Catal. A: Chem.* **104**, 17 (1995).

165. K. Waugh, Methanol synthesis. *Catal. Today* **15**, 51 (1992).

166. N. Yoneda, S. Kusano, M. Yasui, P. Pujado, S. Wilcher, Recent advances in processes and catalysts for the production of acetic acid. *Applied Catalysis A: General* **221**, 253 (2001).

167. Y. Tamaura, M. Tabata, Complete reduction of carbon-dioxide to carbon using cation excess magentite. *Nature* **346**, 255 (1990).

168. E. Yamasue, H. Yamaguchi, H. Nakaoku, H. Okumura, K. N. Ishihara, Carbon dioxide reduction into carbon by mechanically milled wustite. *J. Mater. Sci.* **42**, 5196 (2007).

169. C. S. Hwang, N. C. Wang, Preparation and characteristics of ferrite catalysts for reduction of CO2. *Mater. Chem. Phys.* **88**, 258 (2004).

170. X. C. Xu, C. S. Song, J. M. Andresen, B. G. Miller, A. W. Scaroni, Novel polyethylenimine-modified mesoporous molecular sieve of MCM-41 type as high-capacity adsorbent for CO2 capture. *Energy & Fuels* **16**, 1463 (2002).

171. F. S. Su, C. S. Lu, W. F. Cnen, H. L. Bai, J. F. Hwang, Capture of CO2 from flue gas via multiwalled carbon nanotubes. *Sci. Total Environ.* **407**, 3017 (2009).

172. R. Bredesen, K. Jordal, A. Bolland, High-temperature membranes in power generation with CO2 capture. *Chem. Eng. Process.* **43**, 1129 (2004).

173. J. N. Park, P. Zhang, Y. S. Hu, E. McFarland, Synthesis and characterization of sintering-resistant silica-encapsulated Fe3O4 magnetic nanoparticles active for oxidation and chemical looping combustion. *Nanotechnology* **21**, (2010).

174. H. J. Tian *et al.*, Chemical-looping Combustion of Coal-derived Synthesis Gas Over Copper Oxide Oxygen Carriers. *Energy & Fuels* **22**, 3744 (2008).

175. R. D. Solunke, G. Veser, Nanocomposite Oxygen Carriers for Chemical-Looping Combustion of Sulfur-Contaminated Synthesis Gas. *Energy & Fuels* **23**, 4787 (2009).

176. S. Noorman, M. V. Annaland, H. Kuipers, Packed bed reactor technology for chemical-looping combustion. *Industrial & Engineering Chemistry Research* **46**, 4212 (2007).

177. S. Noorman, M. V. Annaland, J. A. M. Kuipers, Experimental validation of packed bed chemical-looping combustion. *Chem. Eng. Sci.* **65**, 92 (2010).

178. R. D. Solunke, G. Veser, Hydrogen Production via Chemical Looping Steam Reforming in a Periodically Operated Fixed-Bed Reactor. *Industrial & Engineering Chemistry Research* **49**, 11037 (2010).

179. P. Chiesa, G. Lozza, A. Malandrino, M. Romano, V. Piccolo, Three-reactors chemical looping process for hydrogen production. *Int. J. Hydrogen Energy* **33**, 2233 (May, 2008).

180. K. S. Go, S. R. Son, S. D. Kim, K. S. Kang, C. S. Park, Hydrogen production from two-step steam methane reforming in a fluidized bed reactor. *Int. J. Hydrogen Energy* **34**, 1301 (Feb, 2009).

181. A. Stamatiou, P. G. Loutzenhiser, A. Steinfeld, Solar Syngas Production from H2O and CO2 via Two-Step Thermochemical Cycles Based on Zn/ZnO and FeO/Fe3O4 Redox Reactions: Kinetic Analysis. *Energy & Fuels* **24**, 2716 (2010).

182. W. C. Chueh, S. M. Haile, A thermochemical study of ceria: exploiting an old material for new modes of energy conversion and CO2 mitigation. *Philos. Trans. R. Soc. A-Math. Phys. Eng. Sci.* **368**, 3269 (2010).

183. C. Graves, S. D. Ebbesen, M. Mogensen, K. S. Lackner, Sustainable hydrocarbon fuels by recycling CO2 and H2O with renewable or nuclear energy. *Renew. Sust. Energ. Rev.* **15**, 1 (2011).

184. W. C. Chueh *et al.*, High-Flux Solar-Driven Thermochemical Dissociation of CO2 and H2O Using Nonstoichiometric Ceria. *Science* **330**, 1797 (2010).

185. J. E. Miller *et al.*, Metal oxide composites and structures for ultra-high temperature solar thermochemical cycles. *J. Mater. Sci.* **43**, 4714 (2008).

186. P. G. Loutzenhiser, A. Meier, A. Steinfeld, Review of the Two-Step H2O/CO2-Splitting Solar Thermochemical Cycle Based on Zn/ZnO Redox Reactions. *Materials* **3**, 4922 (2010).

187. Y. Piao *et al.*, Wrap-bake-peel process for nanostructural transformation from beta-FeOOH nanorods to biocompatible iron oxide nanocapsules. *Nature Materials* **7**, 242 (2008).

188. N. Zhang, S. Q. Liu, X. Z. Fu, Y. J. Xu, A Simple Strategy for Fabrication of "Plum-Pudding" Type Pd@CeO2 Semiconductor Nanocomposite as a Visible-Light-Driven Photocatalyst for Selective Oxidation. *Journal of Physical Chemistry C* **115**, 22901 (Nov, 2011).

189. R. D. Solunke, University of Pittsburgh (2011).

190. H. Inoue, K. Sekizawa, K. Eguchi, H. Arai, Preparation of hexa-aluminate catalyst thick films on alpha-SiC substrate for high temperature application. *J. Mater. Sci.* **32**, 4627 (1997).

191. M. Najera, R. Solunke, T. Gardner, G. Veser, Carbon capture and utilization via chemical looping dry reforming. *Chem. Eng. Res. Des.* **89**, 1533 (9//, 2011).

192. G. Neumann, G. Veser, Catalytic Partial Oxidation of Methane in a Reverse Flow Reactor. *AIChE J.* **51**, 210 (2005).

193. T. F. Liu, H. Temur, G. Veser, Autothermal Reforming of Methane in a Reverse-Flow Reactor. *Chemical Engineering & Technology* **32**, 1358 (2009).

194. G. Veser, Multiscale Process Intensification for Catalytic Partial Oxidation of Methane: From Nanostructured Catalysts to Integrated Reactor Concepts. *Catal. Today* **in press**, (2010).

195. B. Glockler, A. Gritsch, A. Morillo, G. Kolios, G. Eigenberger, Autothermal reactor concepts for endothermic fixed-bed reactions. *Chemical Engineering Research & Design* **82**, 148 (2004).

196. G. Kolios, J. Frauhammer, G. Eigenberger, Autothermal fixed-bed reactor concepts. *Chem. Eng. Sci.* **55**, 5945 (2000).

197. J. R. Rostrup-Nielsen, Syngas in Perspective. *Catal. Today* **71**, 243 (2002).

198. M. Ishida, D. Zheng, T. Akehata, Evaluation of a chemical-looping-combustion power-generation system by graphic exergy analysis. *Energy* **12**, 147 (1987).

199. O. Brandvoll, O. Bolland, Inherent CO2 capture using chemical looping combustion in a natural gas fired power cycle. *Transactions of the ASME-A-Engineering for Gas Turbines and Power* **126**, 316 (2004).

200. H. Jin, M. Ishida, A novel gas turbine cycle with hydrogen-fueled chemical-looping combustion. *Int. J. Hydrogen Energy* **25**, 1209 (2000).

201. V. K. Chakravarthy, C. S. Daw, J. A. Pihl, Thermodynamic Analysis of Alternative Approaches to Chemical Looping Combustion. *Energy & Fuels* **25**, 656 (2011).

202. J. Szargut, *Exergy Method: Technological and Ecological Applications*. (WIT Press, 2005).

203. I. Dincer, M. Rosen, *Exergy: Energy, Environment and Sustainable Development*. (Elvesier Science, 2007).

204. S. Norio, *Chemical Energy and Exergy: An Introduction to Chemical Thermodynamics for Engineers*. (Elvesier Science and Technology, 2004).

205. M. A. Rosen, D. S. Scott, Comparative efficiency assessments for a range of hydrogen production processes. *Int. J. Hydrogen Energy* **23**, 653 (1998).

206. S. Bhavsar, M. Najera, G. Veser, Chemical Looping Dry Reforming as Novel, Intensified Process for CO2 Activation. *Chemical Engineering & Technology* **35**, 1281 (Jul, 2012).

207. N. Sato, *Chemical Energy and Exergy: An Introduction to Chemical Thermodynamics for Engineers*. E. Science, Ed., (2004).

208. N. R. McGlashan, Chemical Looping combustion-a thermodynmic study. *Journal of Mechanical Engineering* **222**, 1005 (2008).

209. X. E. Verykios, Catalytic dry reforming of natural gas for the production of chemicals and hydrogen. *Int. J. Hydrogen Energy* **28**, 1045 (2003).

210. Y. Qiang *et al.*, Iron/iron oxide core-shell nanoclusters for biomedical applications. *J. Nanopart. Res.* **8**, 489 (2006/08/01, 2006).

211. L. Zhang, B. Liu, S. Dong, Bifunctional Nanostructure of Magnetic Core Luminescent Shell and Its Application as Solid-State Electrochemiluminescence Sensor Material. *The Journal of Physical Chemistry B* **111**, 10448 (2007/09/01, 2007).

212. X.-q. Li, W.-x. Zhang, Iron Nanoparticles: the Core−Shell Structure and Unique Properties for Ni(II) Sequestration. *Langmuir* **22**, 4638 (2006/05/01, 2006).

213. X. X. Yu, S. W. Liu, J. G. Yu, Superparamagnetic gamma-Fe2O3@SiO2@TiO2 composite microspheres with superior photocatalytic properties. *Appl. Catal. B-Environ.* **104**, 12 (2011).

214. M. Chen, B. Tang, D. E. Nikles, Preparation of iron nanoparticles by reduction of acicular β-FeOOH particles. *Magnetics, IEEE Transactions on* **34**, 1141 (1998).

215. K. Kauffman, F. Hazel, Infrared and Mössbauer spectroscopy, electron microscopy and chemical reactivity of ferric chloride hydrolysis products. *J. Inorg. Nucl. Chem.* **37**, 1139 (1975).

216. M. Ohyabu, Y. Ujihara, Study of the chemical states of chlorine and fluorine in akaganétte. *J. Inorg. Nucl. Chem.* **43**, 3125 (1981).

217. X. Fang *et al.*, pH-Induced Simultaneous Synthesis and Self-Assembly of 3D Layered

β-FeOOH Nanorods. *Langmuir* **26**, 2745 (2009).

218. S. Musić, M. Maljković, I. Czakó-Nagy, Effect of urea on the hydrolysis of Fe3+ ions in aqueous solutions at elevated temperature. *Mater. Lett.* **31**, 43 (5//, 1997).

219. C. T. Campbell, C. H. F. Peden, Oxygen vacancies and catalysis on ceria surfaces. *Science* **309**, 713 (2005).

220. H. X. Mai *et al.*, Shape-selective synthesis and oxygen storage behavior of ceria nanopolyhedra, nanorods, and nanocubes. *The Journal of Physical Chemistry B* **109**, 24380 (2005).

221. T. Neuberger, B. Schopf, H. Hofmann, M. Hofmann, B. von Rechenberg, Superparamagnetic nanoparticles for biomedical applications: Possibilities and limitations of a new drug delivery system. *J. Magn. Magn. Mater.* **293**, 483 (2005).

222. A. S. Reddy *et al.*, Synthesis and characterization of Fe/CeO< sub> 2</sub> catalysts: Epoxidation of cyclohexene. *J. Mol. Catal. A: Chem.* **318**, 60 (2010).

223. Q. Zafar, T. Mattisson, B. Gevert, Integrated hydrogen and power production with CO2 capture using chemical-looping reforming-redox reactivity of particles of CuO, Mn2O3, NiO, and Fe2O3 using SiO2 as a support. *Industrial & Engineering Chemistry Research* **44**, 3485 (May, 2005).

224. J. Adanez, A. Abad, F. Garcia-Labiano, P. Gayan, L. F. de Diego, Progress in Chemical-Looping Combustion and Reforming technologies. *Prog. Energy Combust. Sci.* **38**, 215 (Apr, 2012).

225. F. He, Y. Wei, H. Li, H. Wang, Synthesis Gas Generation by Chemical-Looping Reforming Using Ce-Based Oxygen Carriers Modified with Fe, Cu, and Mn Oxides. *Energy & Fuels* **23**, 2095 (2009/04/16, 2009).

226. W. C. Chueh, S. M. Haile, Ceria as a Thermochemical Reaction Medium for Selectively Generating Syngas or Methane from H2O and CO2. *Chemsuschem* **2**, 735 (2009).

227. S. Liang, G. Veser, Mixed Lanthana/Ceria Nanorod-Supported Gold Catalysts for Water–Gas-Shift. *Catal. Lett.*, 1 (2012).

228. X. Zhu, H. Wang, Y. G. Wei, K. Z. Li, X. M. Cheng, Hydrogen and syngas production from two-step steam reforming of methane over CeO2-Fe2O3 oxygen carrier. *Journal of Rare Earths* **28**, 907 (Dec, 2010).

229. F. J. Berry, S. Jobsen, S. L. Jones, An in situ iron-57 Mössbauer spectroscopic investigation of the reduction of ironcerium oxide catalysts in different gaseous reducing agents. *Hyperfine Interact.* **46**, 613 (1989).

230. M. Robbins, G. Wertheim, A. Menth, R. Sherwood, Preparation and properties of polycrystalline cerium orthoferrite (CeFeO< sub> 3</sub>). *J. Phys. Chem. Solids* **30**, 1823 (1969).

231. M. E. Galvez, P. G. Loutzenhiser, I. Hischier, A. Steinfeld, CO2 splitting via two-step solar thermochemical cycles with Zn/ZnO and FeO/Fe3O4 redox reactions: Thermodynamic analysis. *Energy & Fuels* **22**, 3544 (Sep-Oct, 2008).